AN ABSTRACT OF THE DISSERTATION OF

Ali Malek for the degree of Doctor of Philosophy in Geography presented on March 19, 2019.

Title: Empirical Analysis of Processes Affecting Drainage Flows and Inversions in a Forested Mountain Landscape.

Abstract approved:

____

Julia Jones

The objective of this dissertation was to understand the physical mechanisms affecting inversion events in a complex forested mountain landscape. This work was motivated by the long-term studies of climate at the Andrews Forest, short-term studies of vertical temperature, light, wind, and moisture gradient in old-growth trees, and interest in the role of inversions in moderating the effects of climate change. Regional atmospheric conditions and local topographic conditions (i.e., topographic depressions) are known to influence the formation and dissipation of inversions. However, relatively little is known about the effect of the forest canopy on the dynamics of inversion events in mountainous landscapes. Although a few studies have examined this topic through simulation modeling, to the knowledge of this author, no studies have used high temporal resolution climate data to study inversions in forested mountain landscapes. Therefore, the novelty of this Ph.D. research is conducting empirical analysis using long-term meteorological data in a complex forested landscape in the Western Cascades, Oregon.

Chapter 1 examined the main published ideas on the cold air drainage and inversion events since 1949.

Chapter 2 examined the effect of different sun angles on radiation, air temperature, wind speed and direction in Discovery Tree, a 66-m tall tree located on the valley floor of a forested mountain basin, in the H.J. Andrews Experimental Forest, and related those patterns to processes of cold air drainage and pooling on clear, cloudless days at different times of year. The study developed a conceptual model of the energy budget of a hypothetical Douglas-fir tree in an old-growth forest stand as a function of sun angle under clear sky conditions. This conceptual model used a simple radiation budget to establish predictions about the vertical temperature profile in the canopy at various sun angles. Data from four two-week periods centered around the solstices and equinoxes of 2016 and 2017 were evaluated to test hypotheses and predictions about heat and energy exchange within the canopy and the surrounding landscape. Data on air temperature, wind speed and direction, radiation, relative humidity, and leaf wetness were analyzed from heights ranging from 1.5 to 56 m in the tree, along with data on radiation from a nearby meteorological station (Primet). In addition, the proportion of the nearby landscape that was shaded was calculated for sun angles at pre-dawn, local noon, and local dusk on the solstices and equinoxes. Predictions based on the simple radiation budget were generally consistent with observations at local noon on solstices and equinoxes. However, most observations did not match predictions during pre-dawn and dusk, because other elements of the energy budget, such as upward ground heat flux, canopy heat storage, and subsidence (advection) also play a role in controlling temperature, wind, and moisture in the forest canopy. As a result of landscape shading, the Discovery Tree is in high shade in the morning and illuminated in the afternoon. In general, inversions occurred more frequently during the day than at night. Drainage flow and down-valley flow may create turbulence and mixing during the night. In addition, intermittent gusts may create turbulence at canopy top and mix the boundary layer during the night. Moreover, upward soil heat flux and outgoing longwave radiation from the canopy during the night may contribute to a mixed nighttime mixed boundary layer. Overall, at low sun angles, other elements than net radiation, including shading of the surrounding landscape, influenced the energy budget of the tree, producing conditions opposite to those predicted by radiation alone.

Chapter 3 examined the influence of seasonal and daily topographic shading and weather variability on inversions in a forested mountain watershed, H.J. Andrews Forest, Oregon. The objective of this study was to investigate how solar illumination affects topography-induced shading, local winds, and the frequency of inversions (when the temperature increases with height) in a forested mountain landscape. The study site is the H.J. Andrews Experimental Forest in the western Cascades, Oregon. It was expected that the frequency of stable conditions, i.e. when the lapse rate is more positive than the environmental lapse rate, and the strength of inversions would be greatest when the landscape is less illuminated, and vice-versa. The study used digital elevation data as well as hourly data from a low elevation (Primet) and a high elevation (Vanmet) meteorological station in the Andrews Forest during months near the solstices and equinoxes (October, January, April, and July) of 2003, 2011, and 2014, which were years with the second highest, the lowest, and the highest average temperature over the period 1989-2015, when matched records are available from these two stations. In addition, the proportion of the Andrews Forest landscape that was shaded was calculated for sun angles at pre-dawn, local noon, and local dusk on the solstices and equinoxes. Landscape shading was greatest at 0900 hours on all four dates, and least at 1200 at the winter solstice and at 1500 h at the summer solstice and the spring and fall equinoxes. The highest frequency of stable conditions and the strongest inversions occurred in January of all three years. The frequency of inversions was related to solar radiation and the amount of the landscape in high shade. Inversions were more frequent during nighttime than daytime hours. In many cases, up-valley winds dominate in the daytime and down-valley winds dominate at night. When synoptic (upper-elevation, i.e., Vanmet) wind speeds were high, the wind speeds at valley floor (i.e., Primet) were low since Primet was decoupled from the synoptic wind conditions. Thus, the interaction of sun angle with landscape shading strongly influenced the strength and persistence of inversions in this forested mountain landscape.

Chapter 4 examined the effect of light, wind, and humidity, and sensor type on the measurement of air temperature in the Discovery Tree, Andrews Forest, Oregon. The temperature difference between HOBO and aspirated sensors was significantly related to the HOBO light intensity at 40m and 56 m height in the tree. These relationships indicate that at 30 m and above, an increase of 1000 lux is associated with an increase of 0.10 to 0.18 °C in the temperature difference between the HOBO sensor and the aspirated one. At these heights, and at wind speeds < 1 m/s, an increase of 1000 lux is associated with an increase of 0.17 °C in the temperature difference between the HOBO sensor and the aspirated sensor, whereas at wind speed ≥ 1 m/s, an increase of 1000 lux is associated with an increase of only 0.1°C (at 56 m) or 0.13°C (at 40 m) in the temperature difference between the HOBO sensor and the aspirated sensor. These relationships can be used to correct HOBO sensor measurements in locations lacking aspirated sensors.

Chapter 5 summarizes the main findings of the dissertation. Chapter 2 showed that at low sun angles, other elements than net radiation, including shading of the surrounding landscape, influenced the energy budget of the tree, producing conditions opposite to those predicted by radiation alone. Chapter 3 demonstrated that the interaction of sun angle with landscape shading strongly influences the strength and persistence of inversion events in the Andrews Forest. Chapter 4 showed that at 30 m and above in the Discovery Tree, an increase of 1000 lux is associated with an increase of 0.10 to 0.18 °C in the temperature difference between the HOBO sensor and the aspirated one, and the radiation-induced temperature error is reduced when the wind speed is high.

Empirical Analysis of Processes Affecting Drainage Flows and Inversions in a Forested Mountain Landscape

by

Ali Malek

A DISSERTATION

submitted to

Oregon State University

in partial fulfillment of
the requirements for the
degree of

Doctor of Philosophy

Presented March 19, 2019
Commencement June 2019

Doctor of Philosophy dissertation of Ali Malek presented on March 19, 2019

APPROVED:

Major Professor, representing Geography

Dean of the College of Earth, Ocean, and Atmospheric Sciences

Dean of the Graduate School

I understand that my dissertation will become part of the permanent collection of Oregon State University libraries. My signature below authorizes release of my dissertation to any reader upon request.

Ali Malek, Author

ACKNOWLEDGEMENTS

I would like to expresses my sincere appreciation to my advisor Prof. Julia Jones for her continuous support of my Ph.D. research during the last five years. Her guidance helped me in all the time of research and writing of this thesis. I could not have imagined a better advisor and mentor for my Ph.D. study.

In addition, the author would like to thank the rest of the committee: Dr. Chad Higgins, my minor professor, for his astute comments and guidance on the theoretical part of the research, Dr. Mark Schulze, for his support in providing me with Discovery tree meteorological data, and also his constructive comments on the sensor types used in this research, Dr. Robert Kennedy, for his insightful comments and encouragements, and also Dr. James Liburdy, my GCR, for his ultimate support and guidance.

My sincere thanks also goes to Dr. David Whiteman for his insightful comments on the progress of knowledge in studying thermally developed wind systems in Mountainous terrains since the early 20th century until now, Dr. Mike Unsworth, for his constructive comments on the valley cooling rate theory, Dr. Larry Mahrt, for his insightful comments and guidance on the Physics of drainage and along-valley flows in complex terrain, Dr. Eric Skyllingstad and Dr. Simon de Szoeke for their comments and guidance on turbulence and atmospheric stability in complex landscape, and the last but not the least, Dr. Holly Oldroyd, for her guidance on understanding boundary layer stability at local scale.

CONTRIBUTION OF AUTHORS

The author would like to thank my advisor, Dr. Julia Jones for her contribution in preparing the manuscripts for Ch2, Ch3, and Ch4 and also Dr. Mark Schulze for his contribution in preparing the manuscript for Ch4.

TABLE OF CONTENTS

Page

Chapter 1_ Cold air drainage and inversion, background and literature review… 1

Chapter 2_ Effects of sun angle and topographic shading on vertical gradients of air temperature, wind, and humidity in an old-growth forest, Andrews Forest, Oregon……………………………………………………………………….. 12

2.1. Introduction...…………………………………………………………..13

2.2 Study site ………………………………………………………………16

2.3. Methods ……………………………………………………………….17

2.3.1. Energy budget of a tree………………………………………………18

2.3.2. Radiation balance of a tree ………………………………………..20

2.3.3. Thesis statement………………………………………………………22

2.3.4. Hypothesis…………………………………………………………….22

2.3.5. Predictions……………………………………………………………..24

2.3.6. Data…………………………………………………………………… 24

2.3.7. Analysis………………………………………………………………. 25

2.3.8. Landscape shading analysis………………………………………….. 25

2.4. Results ………………………………………………………………… 26

2.4.1. Two-week periods…………………………………………………… 26

2.4.1.1. December 14-31, 2016……………………………………. 26

2.4.1.2. March 14-31, 2017………………………………………... 26

TABLE OF CONTENTS (Continued)

Page

2.4.1.3. June 14-30, 2017 …… 26

2.4.1.4. September 14-30, 2017 …… 27

2.4.1.5. Comparison of predictions to results …… 27

2.4.2. One-day periods …… 28

2.4.2.1. Winter solstice (December 21, 2016) …… 28

2.4.2.2. Spring equinox (March 21, 2017) …… 29

2.4.2.3. Summer solstice (June 21, 2017) …… 31

2.4.2.4. Fall equinox (September 21, 2017) …… 32

2.4.2.5. Comparison of predictions to results …… 33

2.4.3. Landscape shading around Discovery tree …… 34

2.4.3.1. One-day periods on solstices and equinoxes …… 35

2.4.3.2. Two-week periods surrounding solstices and equinoxes …… 36

2.5. Discussion …… 36

2.5.1. Simple predictions of the energy budget considering net radiation, sensible heat flux, and canopy storage …… 37

2.5.1.1. Sensible heat …… 37

2.5.1.2. Convection …… 39

2.5.1.3. Ground heat flux …… 41

2.5.1.4. Latent heat flux …… 42

2.5.2. Landscape shading …… 43

2.6. Conclusion …… 46

Bibliography …… 48

TABLE OF CONTENTS (Continued)

Page

Chapter 3_ The influence of seasonal and daily topographic shading and weather variability on inversions in a forested mountain watershed, H.J. Andrews Forest, Oregon………………………………………………………………. 113

3.1. Introduction..……………………………………………………………… 113

3.1.1. Mechanisms of atmospheric heat exchange that cause inversions……… 114

3.1.2. Factors that produce and disperse temperature inversions……………… 117

3.1.2.1. Synoptic factors (anticyclonic, cyclonic, and zonal flow) ….. 117

3.1.2.2. Weather: warm fronts, cold fronts, precipitation, and wind…. 117

3.1.2.3. Topographic shading and cold air drainage and pooling …… 118

3.1.2.4. Relative importance of synoptic vs. topographic factors…… 119

3.1.3. Gaps in knowledge ……………………………………………………. 120

3.1.4. Study objectives and research questions……………………………… 120

3.2. Study site ………………………………………………………………….. 121

3.3. Methods … ……………………………………………………………….. 123

3.3.1. Thesis statement……………………………………………………….. 123

3.3.2. Hypothesis and predictions……………………………………………. 123

3.3.3. Data……………………………………………………………………. 124

3.3.4. Analyses……………………………………………………………….. 126

3.4. Results …………………………………………………………………….. 127

3.4.1. Landscape illumination………………………………………………… 127

3.4.2. Daytime lapse rates…………………………………………………….. 127

3.4.3. Nighttime lapse rates…………………………………………………… 128

3.4.4. Wind speeds and directions, valley floor site (Primet)………………… 128

3.4.5. Wind speeds and directions, near ridge site (Vanmet)………………… 130

3.5. Discussion ………………………………………………………………… 133

3.5.1. Solar illumination and inversions……………………………………… 134

TABLE OF CONTENTS (Continued)

Page

3.5.2. Solar illumination and local winds…………………………………….. 136

3.6. Conclusion ………………………………………………… ………………… 140

Bibliography ……………………………………………………………………... 141

Chapter 4_ The effect of light, wind, humidity, and sensor type on the measurement of air temperature in Discovery Tree, Andrews Forest, Oregon……………………........160

4.1. Introduction...…………………………………………………………………...160

4.2. Study site… … ………………………………………………………………...164

4.2.1. Configurations of temperature sensors on Discovery Tree……………….. 166

4.2.2. Data……………………………………………………………………... 166

4.3. Methods……………………………………………………………………………… 167

4.3.1. Assessing the effects of light on air temperature measurements………….. 167

4.3.2. Assessing the effects of wind and light on air temperature measurements…167

4.4. Results……………………………………………………………………………167

4.4.1. vertical distribution of light intensity as a function of height…………….....167

4.4.2. vertical distribution of wind speed as a function of height……………….. ..168

4.4.3. Temperature difference as a function of light intensity…………………… ..168

4.4.4. Temperature difference as a function of wind speed………………………..168

4.4.5. Temperature difference as a function of relative humidity……………….. 169

4.4.6. Wind speed and relative humidity…………………………………………170

4.5. Discussion ………………………………………………………………………….. 171

Bibliography …………………………………………………………………..........175

TABLE OF CONTENTS (Continued)

Page

Chapter 5_ Main findings and implications of the dissertation……………………….191

5.1. Objective of the dissertation……………………………………………………191

5.2. Effects of sun angle and topographic shading on vertical temperature profile in an old-growth Douglas-fir tree………………………………………………191

5.3. Effects of sun angle and topographic shading on inversion dynamics in a mountain landscape…………………………………………………………192

5.4. Effects of light and wind on air temperature measurement in low-cost temperature sensors……………………………………………………………………..192

5.5. Overall conclusions…………………………………………………………193

LIST OF FIGURES

Figure Page

2.1. Location of the Discovery Tree in the Andrews Forest……………………………… 61

2.2. Arrangement of sensors on the Discovery Tree……………………………………….62

2.3. The conceptual model of radiation balance in an old-growth conifer tree (a) pre-dawn (no incoming solar radiation); (b) local noon (maximum sun angle); (c) local dusk (sun falling below the horizon) ……………………………………………………………63

2.4. The conceptual model of energy balance in an old-growth conifer tree (a) pre-dawn (no incoming solar radiation); (b) local noon (maximum sun angle); (c) local dusk (sun falling below the horizon)………………………………………………………………………66

2.5. Elements of the energy balance at Primet and the Discovery Tree, December 14-30, 2016. (a) incoming and outgoing shortwave radiation at Primet (6 m), (b) incoming and outgoing longwave radiation at Primet (6 m), (c) air temperature at 1.5, 30, and 50 m on the Discovery Tree, (d) wind speed at 1.5 m, (e) wind speed at 50 m, (f) wind direction at 1.5 m, (g) wind direction at 50 m, (h) relative humidity at 0, 30 and 50 m, (h) leaf wetness at 0, 30, and 50 m. ……………………………………………………………………………………………..69

2.6. Elements of the energy balance at Primet and the Discovery Tree, December 21, 2016. (a) incoming and outgoing shortwave radiation at Primet (6 m), (b) incoming and outgoing longwave radiation at Primet (6 m), (c) air temperature at 1.5, 30, and 50 m on the Discovery Tree, (d) wind speed at 1.5 and 50 m, (e) wind direction at 1.5 and 50 m, (f) relative humidity at 0, 30 and 50 m, (g) leaf wetness at 0, 30, and 50 m……………………………………….72

2.7. Air temperature by height and time of day on the Discovery Tree on (a) afternoon and evening of December 20 and pre-dawn on December 21, 2016 (b) pre-dawn through local noon and dusk on December 21, 2016………………………………………………………………75

2.8. Elements of the energy balance at Primet and the Discovery Tree, March 14-30, 2017. (a) incoming and outgoing shortwave radiation at Primet (6 m), (b) incoming and outgoing longwave radiation at Primet (6 m), (c) air temperature at 1.5, 30, and 50 m on the Discovery Tree, (d) wind speed at 1.5 m, (e) wind speed at 50 m, (f) wind direction at 1.5 m, (g) wind direction at 50 m, (h) relative humidity at 0, 30 and 50 m, (h) leaf wetness at 0, 30, and 50 m ……………………………………………………………………………………………..76

2.9. Elements of the energy balance at Primet and the Discovery Tree, March 21, 2017. (a) incoming and outgoing shortwave radiation at Primet (6 m), (b) incoming and outgoing

LIST OF FIGURES (Continued)

Figures Page

longwave radiation at Primet (6 m), (c) air temperature at 1.5, 30, and 50 m on the Discovery Tree, (d) wind speed at 1.5 and 50 m, (e) wind direction at 1.5 and 50 m, (f) relative humidity at 0, 30 and 50 m, (g) leaf wetness at 0, 30, and 50m……………………………………79

2.10. Air temperature by height and time of day on the Discovery Tree on (a) afternoon and evening of March 20 and pre-dawn on March 21, 2017 (b) pre-dawn through local noon and dusk on March 21, 2017……………………………………………………………………82

2.11. Elements of the energy balance at Primet and the Discovery Tree, June 14-30, 2017. (a) incoming and outgoing shortwave radiation at Primet (6 m), (b) incoming and outgoing longwave radiation at Primet (6 m), (c) air temperature at 1.5, 30, and 50 m on the Discovery Tree, (d) wind speed at 1.5 m, (e) wind speed at 50 m, (f) wind direction at 1.5 m, (g) wind direction at 50 m, (h) relative humidity at 0, 30 and 50 m, (h) leaf wetness at 0, 30, and 50 m …………………………………………………………………………………………..83

2.12. Elements of the energy balance at Primet and the Discovery Tree, June 21, 2017. (a) incoming and outgoing shortwave radiation at Primet (6 m), (b) incoming and outgoing longwave radiation at Primet (6 m), (c) air temperature at 1.5, 30, and 50 m on the Discovery Tree, (d) wind speed at 1.5 and 50 m, (e) wind direction at 1.5 and 50 m, (f) relative humidity at 0, 30 and 50 m, (g) leaf wetness at 0, 30, and 50 m……………………………………..86

2.13. Air temperature by height and time of day on the Discovery Tree on (a) afternoon and evening of June 20 and pre-dawn on June 21, 2017 (b) pre-dawn through local noon and dusk on June 21, 2017………………………………………………………………………………89

2.14. Elements of the energy balance at Primet and the Discovery Tree, September 14-30, 2017. (a) incoming and outgoing shortwave radiation at Primet (6 m), (b) incoming and outgoing longwave radiation at Primet (6 m), (c) air temperature at 1.5, 30, and 50 m on the Discovery Tree, (d) wind speed at 1.5 m, (e) wind speed at 50 m, (f) wind direction at 1.5 m, (g) wind direction at 50 m, (h) relative humidity at 0, 30 and 50 m, (h) leaf wetness at 0, 30, and 50 m. …………………………………………………………………………………………90

2.15. Elements of the energy balance at Primet and the Discovery Tree, September 21, 2017. (a) incoming and outgoing shortwave radiation at Primet (6 m), (b) incoming and outgoing longwave radiation at Primet (6 m), (c) air temperature at 1.5, 30, and 50 m on the Discovery Tree, (d) wind speed at 1.5 and 50 m, (e) wind direction at 1.5 and 50 m, (f) relative humidity at 0, 30 and 50 m, (g) leaf wetness at 0, 30, and 50 m…………………………………………93

LIST OF FIGURES (Continued)

Figure Page

2.16. Air temperature by height and time of day on the Discovery Tree on (a) afternoon and evening of September 20 and pre-dawn on September 21, 2017 (b) pre-dawn through local noon and dusk on September 21, 2017………………………………………………………… 96

2.17. Proportion of the landscape surrounding the Discovery Tree that is in high, moderate and low shade at 0900h, 1200h, and 1500h on (a, b, c) the winter solstice, (d, e, f) the spring equinox, (g, h, i) the summer solstice, and (j, k, l) the fall equinox…………………………97

2.18. Relationship of percent of landscape shaded to (a) radiation, (b) air temperature, (c) wind speed, (d) percent of time wind direction is from the NE, (e) relative humidity, and (f) leaf wetness for one-day periods on solstices and equinoxes (21 December, 2016; 21 March, 2017; 21 June, 2017; 21 September, 2017) at three heights in the Discovery Tree…………………109

2.19. Relationship of percent of landscape shaded to (a) radiation, (b) air temperature, (c) wind speed, (d) percent of time wind direction is from the NE, (e) relative humidity, and (f) leaf wetness for two-week periods surrounding solstices and equinoxes (December 14-30, 2016; March 14-30, 2017; June 14-30, 2017; September 14-30, 2017) at three heights in the Discovery Tree………………………………………………………………………………………111

3.1. The location of study sites on the shaded relief map of the H.J. Andrews Forest………149

3.2. Mean daily air temperature for 1995 to 2014……………………………………………150

3.3. Relationship of frequency of daytime inversions to solar radiation at Primet…………..151

3.4. Relationship of frequency of daytime inversions to percent of landscape in high shade..152

3.5. Hourly difference in air temperature at Vanmet vs. Primet (°C) for January, April, July, and October of 2003 (a-d), 2011 (e-f), and 2014 (i-l). Positive values indicate hours with inversions. ……………………………………………………………………………………..153

3.6. Hourly wind directions at Vanmet vs. Primet (°C) for January, April, July, and October of 2003 (a-d), 2011 (e-f), and 2014 (i-l). Positive values indicate hours with inversions…….156.

3.7. The total number of hours with inversion in January, April, July, and October of 2003, 2011, and 2014……………………………………………………………………………….159

4.1. The map of study site……………………………………………………………………..179

4.2. The location of sensors on Discovery Tree……………………………………………….180

4.3. The location of one of the data loggers on Discovery Tree………………………………181

LIST OF FIGURES (Continued)

Figure Page

4.4. Histogram of light intensity at different heights of Discovery tree, Nov 2016 – April 2018. (a) 1.5 m, (b) 10 m, (c) 20 m, (d) 30 m, (e) 40 m, (f) 56 m……………………………………182

4.5. Histogram of wind speed at different heights of Discovery Tree, Nov 2016 – April 2018. (a) 1.5 m, (b) 56 m…………………………………………………………………………………183

4.6. Difference in air T (HOBO – aspirated) as a function of light intensity on the Hobo sensor for different tree heights in the Discovery Tree, Nov 2016 –April 2018……………………184

4.7. Difference in air T (HOBO – aspirated) at 56 m, as a function of light intensity on the HOBO sensor, for different wind speeds in Discovery Tree, Nov 2016- April 2018……… 185

4.8. Difference in air T (HOBO – aspirated) at 40 m, as a function of light intensity on the HOBO sensor, for different wind speeds at 56 m height in Discovery Tree, Nov 2016 – April 2018…………………………………………………………………………………………..186

4.9. Difference in air temperature at HOBO vs. aspirated sensor as a function of HOBO light intensity at 1.5 m height in Discovery Tree for wind speeds < 0.5 ms^{-1} during (a) Jan, (b) April, (c) July, and (d) October of 2017…………………………………………………………187

4.10. Difference in air temperature at HOBO vs. aspirated sensor as a function of HOBO light intensity at 56 m height in Discovery Tree for wind speeds < 0.5ms^{-1} during (a) Jan, (b) April, (c) July, and (d) October of 2017………………………………………………………….188

4.11. Difference in air T (HOBO – aspirated) at 56 m height, as a function of light intensity at the Hobo sensor, grouped by relative humidity in Discovery Tree, Nov 2016 – April 2018……189

4.12. Relative humidity vs. wind speed at 1.5 m and 56 m, Discovery Tree, Nov 2016- April 2018……………………………………………...190

LIST OF TABLES

Table Page

2.1 Sun altitude at various times of day on solstices and equinoxes at Eugene, which is 70 Km west of the Andrews Forest……………………………………52

2.2 Predicted conditions of daytime radiation, head, wind, humidity, and leaf wetness in the canopy at solstices and equinoxes………………………………53

2.3 Predicted conditions within the canopy at various times of day………………..54

2.4 Instruments deployed at the Discovery Tree, Nov 2016- present………………55

2.5 Average values of radiation (W/m^2 at Primet, 6 m) and air temperature, winds, and moisture in the Discovery Tree canopy by height (at 1.5, 30, and 50 m), during two-week periods surrounding the equinoxes and solstices of 2016 and 2017…56

2.6 Average values of radiation (Wm^{-2} at Primet) and air temperature, wind, air moisture in the Discovery Tree canopy at pre-dusk (P) (0000h to 0600h), local noon (N) (1000-1400h), and local dusk (D) (1700-2100h) on days of equinoxes and solstices of 2016 and 2017……………………………………………………………………………….57

2.7 Percent of the Andrews Forest landscape near the Discovery Tree that is illuminated and in deep shade based on terrain shading algorithm, for 9 AM, noon, and 3 PM on the equinoxes (Mar 21, Sep 21) and solstices (June 21, Dec 21)………………………58

3.1 Percent of the Andrews Forest landscape that is illuminated and in deep shade based on terrain shading algorithm, for 9 AM, noon, and 3 PM on the equinoxes (Mar 21, Sep 21) and solstices (June 21, Dec 21)……………………………………………………144

3.2 Percent of hours with various values of Vanmet-Primet air temperature difference (°C),

LIST OF TABLES (Continued)

Table Page

and with inversions (positive lapse rates). A -5.5 °C difference between Vanmet and Primet (845 m difference in elevation) is equivalent to the environmental lapse rate (-6.5°C / 1000 m)……………………………………………………………………145

3.3 Percent of hours with various wind speeds and directions by season, for valley floor site (Primet). At Primet, winds from 0 to 90 degrees are down-valley, and winds from 180 to 270 degrees are up-valley………………………………………………………………146

3.4 Percent of hours with various wind speeds and directions by season, for near-ridge site (Vanmet). At Vanmet, winds from 0 to 90 degrees are downslope, and winds from 180 to 270 degrees are upslope……………………………………………………………..147

3.5 Minimum and maximum values of mean daily air temperature at Primet and Vanmet, 1995 – 2015…………………………………………………………………………148

4.1 Instruments deployed at the Discovery Tree, Nov 2016-present………………………177

LIST OF APPENDIX FIGURES

Figure Page

A3.1 Hourly air temperature differences, Vanmet – Primet, 2011, daytime hours (radiation > 0)………………………………………………………………… 194

A3.2 Hourly air temperature differences, Vanmet – Primet, 2011, nighttime hours (radiation = 0)………………………………………………………………… 194

A3.3 Daytime hourly wind speed, Primet, 2011………………………………….195

A3.4 Daytime hourly wind direction, Primet, 2011………………………………195

A3.5 Daytime hourly wind speed, Vanmet, 2011…………………………………195

A3.6 Daytime hourly wind direction, Vanmet, 2011………………………………195

A3.7 Nighttime hourly wind speed, Primet, 2011………………………………….196

A3.8 Nighttime hourly wind direction, Primet, 2011……………………………….196

A3.9 Nighttime hourly wind speed, Vanmet, 2011………………………………….196

A3.10 Nighttime hourly wind direction, Vanmet, 2011………………………………196

A3.11 Hourly air temperature differences, Vanmet-Primet, for Jan, Apr, Jul, and Oct, 2011, daytime hours (radiation > 0)…………………………………………………………197

A3.12 Hourly air temperature differences, Vanmet-Primet, for Jan, Apr, Jul, and Oct, 2011, nighttime hours (radiation = 0)………………………………………………………197

A3.13 Daytime hourly wind speed, Primet, Jan, Apr, Jul, and Oct. 2011…………..198

A3.14 Daytime hourly wind direction, Primet, Jan, Apr, Jul, and Oct. 2011………198

A3.15 Daytime hourly wind speed, Vanmet, Jan, Apr, Jul, and Oct. 2011…………198

A3.16 Daytime hourly wind direction, Vanmet, Jan, Apr, Jul, and Oct. 2011………198

A3.17 Nighttime hourly wind speed, Primet, Jan, Apr, Jul, and Oct. 2011…………199

A3.18 Nighttime hourly wind direction, Primet, Jan, Apr, Jul, and Oct.2011………199

A3.19 Nighttime hourly wind speed, Vanmet, Jan, Apr, Jul, and Oct. 2011………199

LIST OF APPENDIX FIGURES (Continued)

Figure Page

A3.20 Nighttime hourly wind direction, Vanmet, Jan, Apr, Jul, and Oct. 2011……199

A3.21 Hourly air temperature differences, Vanmet – Primet, 2003, daytime hours (radiation > 0)……………………………………………………………200

A3.22 Hourly air temperature differences, Vanmet – Primet, 2003, nighttime hours (radiation = 0)……………………………………………………………200

A3.23 Daytime hourly wind speed, Primet, 2003……………………………………201

A3.24 Daytime hourly wind direction, Primet, 2003…………………………………201

A3.25 Daytime hourly wind speed, Vanmet, 2003……………………………………201

A3.26 Daytime hourly wind direction, Vanmet, 2003…………………………………201

A3.27 Nighttime hourly wind speed, Primet, 2003…………………………………….202

A3.28 Nighttime hourly wind direction, Primet, 2003………………………………….202

A3.29 Nighttime hourly wind speed, Vanmet, 2003……………………………………202

A3.30 Nighttime hourly wind direction, Vanmet, 2003…………………………………202

A3.31 Hourly air temperature difference, Vanmet – Primet, for Jan, Apr, Jul, and Oct, 2003, daytime hours (radiation > 0)……………………………………………..203

A3.32 Hourly air temperature difference, Vanmet – Primet, for Jan, Apr, Jul, and Oct, 2003, nighttime hours (radiation = 0)……………………………………………203

A3.33 Daytime hourly wind speed, Primet, Jan, Apr, Jul, and Oct, 2003……………..204

A3.34 Daytime hourly wind direction, Primet, Jan, Apr, Jul, and Oct, 2003………….204

A3.35 Daytime hourly wind speed, Vanmet, Jan, Apr, Jul, and Oct, 2003……………204

A3.36 Daytime hourly wind direction, Vanmet, Jan, Apr, Jul, and Oct, 2003…………204

A3.37 Nighttime hourly wind speed, Primet, Jan, Apr, Jul, and Oct, 2003……………205

A3.38 Nighttime hourly wind direction, Primet, Jan, Apr, Jul, and Oct, 2003…………205

LIST OF APPENDIX FIGURES (Continued)

Figure Page

A3.39 Nighttime hourly wind speed, Vanmet, Jan, Apr, Jul, and Oct, 2003…………205

A3.40 Nighttime hourly wind direction, Vanmet, Jan, Apr, Jul, and Oct, 2003………205

A3.41 Hourly air temperature differences, Vanmet – Primet, 2014, daytime hours (radiation > 0)…………………………………………………………………..206

A3.42 Hourly air temperature differences, Vanmet – Primet, 2014, nighttime hours (radiation = 0)…………………………………………………………………..206

A3.43 Daytime hourly wind speed, Primet, 2014………………………………………..207

A3.44 Daytime hourly wind direction, Primet, 2014…………………………………….207

A3.45 Daytime hourly wind speed, Vanmet, 2014……………………………………….207

A3.46 Daytime hourly wind direction, Vanmet, 2014……………………………………207

A3.47 Nighttime hourly wind speed, Primet, 2014……………………………………….208

A3.48 Nighttime hourly wind direction, Primet, 2014……………………………………208

A3.49 Nighttime hourly wind speed, Vanmet, 2014……………………………………….208

A3.50 Nighttime hourly wind direction, Vanmet, 2014………………………………..208

A3.51 Hourly air temperature difference, Vanmet – Primet, for Jan, Apr, Jul, and Oct, 2014, daytime hours (radiation > 0)…………………………………………..209

A3.52 Hourly air temperature difference, Vanmet – Primet, for Jan, Apr, Jul, and Oct, 2003, nighttime hours (radiation = 0)…………………………………..209

A3.53 Daytime hourly wind speed, Primet, Jan, Apr, Jul, and Oct, 2014…………….210

A3.54 Daytime hourly wind direction, Primet, Jan, Apr, Jul, and Oct, 2014…………210

A3.55 Daytime hourly wind speed, Vanmet, Jan, Apr, Jul, and Oct, 2014……………210

A3.56 Daytime hourly wind direction, Vanmet, Jan, Apr, Jul, and Oct, 2014………..210

LIST OF APPENDIX FIGURES (Continued)

Figure Page

A3.57 Nighttime hourly wind speed, Primet, Jan, Apr, Jul, and Oct, 2014…………211

A3.58 Nighttime hourly wind direction, Primet, Jan, Apr, Jul, and Oct, 2014………211

A3.59 Nighttime hourly wind speed, Vanmet, Jan, Apr, Jul, and Oct, 2014…………211

A3.60 Nighttime hourly wind direction, Vanmet, Jan, Apr, Jul, and Oct, 2014………211

A3.61_a. Reclassified hillshade map of the HJA Forest at 9:00 AM on December 21, 2016……………………………………………………………………..212

A3.61_b. Reclassified hillshade map of the HJA Forest at 12:00 PM on December 21, 2016……………………………………………………………………..213

A3.61_c. Reclassified hillshade map of the HJA Forest at 3:00 PM on December 21, 2016………………………………………………………………………214

A3.62_a. Reclassified hillshade map of the HJA Forest at 9:00 AM on June 21, 2017. …………………………………………………………………………………215

A3.62_b. Reclassified hillshade map of the HJA Forest at 12:00 PM on June 21, 2017 …………………………………………………………………………………216

A3.62_c. Reclassified hillshade map of the HJA Forest at 3:00 PM on June 21, 2017. …………………………………………………………………………………217

A3.63_a. Reclassified hillshade map of the HJA Forest at 9:00 AM on March 21, 2017. …………………………………………………………………………………218

A3.63_b. Reclassified hillshade map of the HJA Forest at 12:00 PM on March 21, 2017……………………………………………………………………219

A3.63_c. Reclassified hillshade map of the HJA Forest at 3:00 PM on March 21, 2017……………………………………………………………………220

A3.64_a. Reclassified hillshade map of the HJA Forest at 9:00 AM on September 21, 2017……………………………………………………………………..221

A3.64_b. Reclassified hillshade map of the HJA Forest at 12:00 PM on September 21, 2017……………………………………………………………………..222

A3.64_c. Reclassified hillshade map of the HJA Forest at 3:00 PM on September 21, 2017……………………………………………………………………222

CHAPTER 1
Overview of prior knowledge and motivation for the study

The topic of the PhD is empirical analyses of processes affecting drainage flows and inversions in a forested mountain landscape. Cold air drainage and inversion events are common features of mountain landscapes and have important effects on ecosystem processes, including the cycling of moisture, energy, and carbon, as well as the distribution of species. This chapter reviews the literature on causes and consequences of inversions, defines relevant terms, and identifies the gaps in knowledge addressed by this dissertation.

1.1 Consequences of cold-air drainage for ecosystem processes

Cold air drainage can be used in monitoring ecosystem metabolism in a forest mountain landscape (Pypker *et al.,* 2007). Novick *et al.,* (2016) quantified the relationship between the large scale and the local scale climate conditions including drainage flows new methods were used to study ecosystem carbon flux in a valley at the southern Appalachian mountains. The authors combined multiple datasets from climate stations and eddy covariance towers in simple models for ecosystem carbon fluxes. The results show that cold air drainage suppresses the local temperature by several degrees for several hours before and after sunset, reducing growing season respiration of above ground biomass which could increase net primary production, especially under clear, cloud-free conditions (Novick *et al.,* 2016).

In mountain landscapes, terrain complexity not only induces heterogeneity in the surface (e.g., through shading) but also affects lateral advective fluxes or local winds. Topographically-induced shading affected the thermal gradient in a subtropical forest by changing the energy distribution in different aspects. The heterogeneous distribution of energy in a forest landscape due to the topographic effect is a key factor in plant species diversity: shaded aspects support higher plant diversity whereas illuminated aspects support lower plant diversity (He *et al.,* 2017). Downslope flow and stability affected heat transfer in Douglas-fir forest canopies of Idaho, USA (Russell *et al.* 2016).

Many studies are utilizing towers to better understand heat, water, and CO_2 exchange between forest canopies and the atmosphere. Although it is difficult to characterize the complex fluxes of water, energy, and carbon in forest canopies, energy balance approaches seem to be appropriate for inferring some processes (Amiro, 1990). Despite some work (Russell *et al.* 2016), few studies have examined heat exchanges in very tall conifer canopies, especially in mountain landscapes, on seasonal timescales that can be related to ecosystem processes.

1.2. Landform effects on inversions and cold air drainage flows

Landforms play an important role in inversions. Cold air drainage flows are gravity-induced flows, i.e. they initiate due to the gravitational force. Mahrt, (1982) showed that gravity induced flows can be approximated by the relationship between buoyancy and the downslope advection of momentum. Lundquist *et al.,* (2008) developed a DEM based algorithm to identify sites prone to the formation of cold air pools.

Many studies have investigated the behavior of cold air drainage flows in complex terrain. One of the first studies found that the cold air drainage velocity is inversely related to the slope angle when the slope is uniform and extensive (Fleagle, 1950). The author showed that during the early stages of drainage flow initiation, the drainage velocity varies periodically (i.e., it oscillates) around an equilibrium value. This value is directly related to the net outgoing longwave radiation but inversely related to the slope of the ground. These oscillations are found to be the characteristic features of drainage flow which are directly related to the radiative cooling of sloping surfaces (Doran and Horst, 1981).

Topography influences the formation and breakup of inversions. Zhong *et al.,* (2001) investigated the role of westerly winds in establishing strong capping inversion and the resultant persistent cold air pool during winter on the east side of the Cascade Range, which is due to downward warming as the westerly winds descend in the lee of the Cascade Mountains.

In mountainous regions, the local temperature increase is not consistent with the temperature increase at synoptic scale predicted by global and regional models due to decoupling effect of cold pools (Daly *et al.,* 2010). Topographic factors are responsible for coupling and decoupling of surface air temperature from the free air (Holden *et al*., 2011).

To quantify the absolute and relative influence of landscape-scale topographic factors in mitigating regional temperatures and assess how these effects vary in time, Dobrowski *et al*., (2009) decomposed the variance of temperature variance into components related to the free air (synoptic = regional scale) and (physiographic = local scale) effects. They showed that 80% of the variance is due to the synoptic scale and the remaining 20% is due to the physiographic conditions.

Considerable research has examined the effects of the geometry of valleys on inversions. The cooling rate in an enclosed basin is faster than the cooling rate in a valley due to lack of down-valley flow and compensatory warming of subsidence (Clements *et al*., 2002). The minimum air temperature in closed basins (sinkholes) is highly influenced by the sky-view factor under high pressure atmospheric conditions (Whiteman *et al.,* 2004). In contrast, in moderate decoupled valleys the effect of sheltering is responsible for the rapid cooling of the air inside the valley. The cooling is due to the reduction of the down-ward turbulent heat flux and lack of mixing (Smith *et al*., 2010). Sheridan *et al.,* (2014) showed that the intensity of the cold pool (the largest negative nighttime value of [T(min) – T(mean)]) increased with valley depth up to a critical point beyond which no intensification occurred. In addition, for a given valley depth, the intensity of a cold pool is solely controlled by the horizontal wind speed near the surface.

The result of a sensitivity analysis of cold air pool evolution to valley geometry using numerical simulation showed that the cold air pool is strongest in the medium sized valley. The reason is that the downslope flow-driven cooling is more efficient in a medium sized valley compared to a large deep valley (Kiefer *et al.,* 2015).

Schmidli (2013) investigated heating processes in valleys using a Reynolds decomposition method, which decomposes the flow into mean and turbulent parts. The heating and cooling processes associated with the mean part of flow are the advection-induced cooling of upslope flow and the subsidence-induced warming of downslope flow whereas the heating and cooling processes associated with the turbulent part of the flow are warming of the mixed layer due to the sensible heat flux convergence and cooling at the top of the inversion due to the sinking of cold air (Schmidli, 2013). Carlson and Stull (1986) showed that radiative cooling from the ground and subsidence-induced warming from aloft during clear nights and under high pressure synoptic condition diminish the growth of the stable nighttime boundary layer and eventually destroy it.

1.3 Interaction of solar radiation and landforms

Inversions are influenced by the interaction of solar radiation with landforms. Some research has investigated the effects of insolation on inversions. For example, the reduced radiational cooling due to cloudiness (synoptic scale phenomenon) and humidity plus near ground turbulent mixing result in cold air drainage suppression. In addition, turbulent entrainment diminishes the established drainage flow (Barr and Orgill, 1989).

The physical mechanisms responsible for the life cycle of the thermal inversion layers in a valley are governed by seasonality. In summer, the altitude of the top of the convective boundary layer does not change whereas in winter the altitude changes within the valley (Anquetin *et al.,* 1998). Sometimes this change in the altitude is due to the warm air advection above a basin or due to the westerly wind effect. The advection of warm air strengthens an existing inversion layer by increasing the temperature deficit between the top and bottom of the boundary layer (Whiteman *et al.,* 2001). As a result, the inversion might last several days.

The effect of valley orientation on the theoretical cross-valley wind system was investigated by Gleeson (1951). The author showed that in an ideal northeast-southwest valley (in the northern hemisphere), the maximum wind speeds occur at later times in the morning and afternoon since the sun shines longer on the west slope compared to the east slope. Therefore, the winds from the east reach higher speeds during early morning. The implication of this finding is that strong persistent inversion layers are highly unlikely to form in a northeast-southwest valley.

Minder *et al.,* (2010) explored the role of landforms in inversion dynamics by investigating the spatio-temporal variability of the surface temperature lapse rate. They found that the lapse rate is a function not only of sun altitude but also of geographic position (leeward vs. windward) in a mountain landscape.

1.4. Inversions and local winds

Some work has examined relationship of cold air pooling and local winds. For example, it is found that along-slope internal wave oscillations are responsible for the sustained weak turbulence frequently observed in katabatic flows in complex terrains (Princevac *et al.,* 2008). In a seminal work, it is shown that the interaction between the drainage flow and established cold pool results in the multi directionality of wind especially within the cold pool whereas the interaction of synoptic scale flows with the drainage flow at higher elevations results in multi-directionality of wind at higher elevations in a valley (Mahrt *et al.*, 2010).

1.5. Role of vegetation in inversions

Multiple aspects of vegetation influence inversions. Gustavsson *et al.,* (1998) studied the sheltering effect of forest canopy and topographic features on the cooling rate in a valley. They showed that areas sheltered by vegetation cool at a faster rate compared to open areas during the early evening due to the reduced vertical mixing by surrounding vegetation or valley sidewalls. Unsworth *et al.*, (2010) showed that vegetation cover increases the mixing of the boundary layer. In a study of a steep forested drainage basin (WS 1 in the Andrews Forest), the authors documented that when the net radiation above the forest canopy becomes negative, a down-valley flow develops and becomes well-mixed within the canopy (relatively isothermal condition), creating a deep boundary layer during the night. Thomas (2011) argued that the forest canopy has a larger effect on wind field variability than on temperature field variability. Using an analysis of the space-time structure of the temperature and wind fields in the sub-canopy of a coast range Douglas-fir forest in a fairly complex landscape, Thomas (2011) showed that the variability in the wind fields is due to small-scale short-lived motion, whereas the variability in the temperature field is due to the larger scale long-lived motions produced by radiative cooling of the surface.

The two main warming mechanisms influencing inversion events at landform scale are subsidence (top-down) warming and the convective (bottom-up) warming (Serafin and Zardi, 2010). These mechanisms act against each other in an idealized mountain valley. While the subsidence warming is dominant in the morning, the convective warming is dominant in the early afternoon. Dorninger *et al.* (2011) examined the influence of landform scale processes on inversion events. The authors classified observed nighttime cold-air pool events into different phases: undisturbed inversion evolution, late buildups, early breakups, mixing events, and layered inversion at top, based on 230 days of 5-minute resolution temperature measurements at 1.4 to 2.2 meters from the ground. They showed that strong winds, cloud cover, and wind direction were the governing variables affecting inversions.

1.6 Key terms used in this dissertation

The following key terms are defined because they are used in the dissertation.

Cold air drainage: A thermally driven flow which initiates due to the down-slope component of buoyancy force.

Cold air pool: When the cold air drainage accumulates in topographic depressions creating a stable boundary layer inside the depression which is decoupled from the free air.

Cross-valley winds: A wind system that flow perpendicular to the along-valley axis.

Decoupled: When a part of an atmospheric boundary layer in a valley is detached from the rest of the boundary layer. In other words, when an inversion is formed inside a valley while above the valley the boundary layer is mixed.

Drainage flow: A gravity-induced flow which initiates due to the gravitational force. It is also known as down-slope flow or katabatic wind.

Gravity flow: A flow which initiates due to the force of gravity.

Inversion: When the temperature increases with height.

Nocturnal boundary layer: The layer of air adjacent to the ground which is cooled down due to the radiative cooling of the surface during night.

Nocturnal inversion: An inversion which forms during night due to the radiative cooling of the ground.

Stable condition: When an adiabatically lifted air parcel descends to its previous location.

Synoptic condition: It is related to the large scale atmospheric conditions such as the formation of high or low pressure systems and air masses with a lifespan greater than 24 hours.

Unstable condition: When an adiabatically lifted air parcel ascends.

1.7 Gaps in knowledge addressed by this dissertation

Relatively few studies have examined how vegetation in a valley floor interacts with landforms to create vertical temperature gradients in the forest canopy. The forest canopy of Douglas-fir forests can reach 80-90 m, which is a significant fraction of the total relief in a mountain landscape. Therefore, Chapter 2 examines the effect of sun angle and topographic shading on diurnal heating and cooling and the vertical profile of temperature in a forested mountain landscape.

Much of the work on landforms and inversions has been conducted in specific landforms such as sinkholes or craters. Relatively little work has been conducted in mountain landscapes considering how sun angle and azimuth, landforms and physiography interact to affect inversions. Therefore, Chapter 3 examined how sun angle and topographic shading affected inversion dynamics in a mountain landscape.

The study of the spatial and temporal dynamics of inversions depends on accurate measurement of air temperature in multiple locations. Aspirated air temperature sensors are more accurate, but they are relatively expensive. HOBO sensors have lower accuracy, but are cheaper. Solar radiation is known to heat sensors, and wind cools them. Thus, HOBO sensors could be used in a cost-effective sampling design if radiation bias could be corrected. No studies have compared HOBO sensors to aspirated sensors that are vertical mounted on old-growth trees. Therefore, Chapter 4 quantified the effect of light and wind on air temperature measurement in low-cost HOBO sensors with PVC shields mounted vertically on an old-growth tree.

LITERATURE CITED

Amiro, B.D. 1990. Comparison of turbulence statistics within three boreal forest canopies, *Boundary-Layer Meteorology*, 51 (1-2) pp: 99-121.

Anquetin, S., Guilbaud, C., Chollet, J.P. 1998. The formation and destruction of inversion layers within a deep valley, *Journal of Applied Meteorology*, 37, pp: 1547-1560.

Barr, S., and Orgill, M. M. 1989. Influence of external meteorology on nocturnal valley drainage winds, *Journal of Applied Meteorology*, 28, pp: 497-517.

Carlson, M.A., and Stull, R.B. 1986. Subsidence in the nocturnal boundary layer, *Journal of Climate and Applied Meteorology*, 25, pp: 1088- 1099.

Clements, C.B., Whiteman, C.D., and Horel, J.D. 2003. Cold-Air-Pool structure and evolution in a mountain basin: Peter Sinks, Utah, *Journal of Applied Meteorology*, 42, pp: 752- 768.

Doran, J. C., and Horst, T.W. 1981. Velocity and temperature oscillations in drainage winds, *Journal of Applied Meteorology*, 20, pp: 361-364.

Dobrowski, S. Z., Abatzoglou, J.T., Greenberg, J.A., and Schladow, S.G. 2009. How much influence does landscape-scale physiography have on air temperature in a mountain environment? *Agricultural and Forest Meteorology,* 149 (10): 1751–1758.

Daly, C., Conklin, D. R., and Unsworth, M.H. 2010. Local atmospheric decoupling in complex topography alters climate change impacts, *International Journal of Climatology*, 30 (12): 1857–1864.

Dorninger, M., Whiteman, C.D., Bica, B., Eisenbach, S., Pospichal, B., and Steinacker, R. 2011. Meteorological Events Affecting Cold-Air Pools in a Small Basin, *Journal of Applied Meteorology and Climatology,* 50 (11): 2223–2234.

Fleagle, B.R.G. 1950. A theory of air drainage, *Journal of Meteorology*, 7, pp:227-232.

Gleeson, T.A. 1951. On the theory of cross-valley winds arising from differential heating of the slopes, *Journal of Meteorology,* 8, pp: 398-405.

Gustavsson, T., Karlsson, M., Bogren, J., and Lindqvist, S. 1998. Development of temperature patterns during clear nights, *Journal of Applied Meteorology*, 37, pp: 559-571.

Holden, Z.A., Abatzoglou, J.T., Luce, C.H., and Baggett, L. S. 2011. Empirical downscaling of daily minimum air temperature at very fine resolutions in complex terrain, Agricultural and Forest Meteorology, 151, pp: 1066-1073.

He, S., Zhong, Y., Sun, Y., Su, Z., Jia, X., Hu, Y., and Zhou, Q. 2017. Topography-associated thermal gradient predicts warming effects on woody plant structural diversity in a subtropical forest, *Scientific Reports* 7, Article number: 40387.

Kiefer, M.T., and Zhong, S. 2015. The role of forest cover and valley geometry in cold-air pool evolution, *Journal of Geophysical Research: Atmospheres,* 120(17), pp: 8693-8711.

Lundquist, J.D., Pepin, N., and Rochford, C. 2008. Automated algorithm for mapping regions of cold-air pooling in complex terrain, *Journal of Geophysical Research*, 113, pp: 1-15.

Mahrt, L. 1982. Momentum balance of gravity flows, *Journal of The Atmospheric Sciences*, 39, pp: 2701-2711.

Mahrt, L., Richardson, S., Seaman, N., and Stauffer, D. 2010. Non-stationary drainage flows and motions in the cold pool, *Tellus*, 62A, pp:698-705.

Minder, J.R., Mote, P.W., and Lundquist, J.D. 2010. Surface temperature lapse rates over complex terrain: Lessons from the Cascade Mountains, *Journal of Geophysical Research*, 115, pp: 1-13.

Novick, K. A., Oishi, C.A., and Miniat, C.F. 2016. Cold air drainage flows subsidize montane valley ecosystem productivity, *Global Change Biology*, 22, pp: 4014-4027.

Pypker, T.G., Unsworth, M.H., Lamb, B., Allwine, E., Edburg, S., Sulzman, E., Mix, A.C., and Bond, B.J. 2007. Cold air drainage in a forested valley: Investigating the feasibility of monitoring ecosystem metabolism, *Agricultural and Forest Meteorology*, 145(3-4), pp: 149-166.

Princevac, M., Hunt, J.C.R., and Fernando, H.J.S. 2008. Quasi-steady katabatic winds on slope I wide valleys: Hydraulic theory and observations, *Journal of The Atmospheric Sciences,* 65, pp: 627-643.

Russell, E. S., Liu, H., Gao, Z., Lamb, B., Wagenbrenner, N. 2016. Turbulence dependence on winds and stability in a weak-wind canopy sublayer over complex terrain, *Journal of Geophysical Research: Atmospheres*, pp: 11,502-11,515,

Serafin, S. and Zardi, D. 2010. Daytime heat transfer processes related to slope flows and turbulent convection in an idealized mountain valley, *Journal of The Atmospheric Sciences*, 67, pp: 3739-3756.

Smith, S. A., Brown, A.R., Vosper, S.B., Murkin, P.A., and Veal, A.T. 2010. Observations and simulations of Cold Air Pooling in Valleys, *Boundary-Layer-Meteorology*, 134, pp: 85-108.

Schmidli, J. 2013. Daytime heat transfer processes over mountainous terrain, *Journal of The Atmospheric Sciences*, 70, pp: 4041-4066.

Sheridan, P.F., Vosper, S.B., and Brown, A.R. 2014. Characteristics of cold pools observed in narrow valleys and dependence on external conditions, *Q.J.R. Meteorol. Soc*. 140: 715-728.

Thomas, C. K. 2011. Variability of sub-canopy flow, temperature, and horizontal advection in moderately complex terrain, *Boundary-Layer-Meteorology*, 139: 61-81.

Unsworth, M. H., Bond, B. J., Mix, A. C., Pypker, T. G., and Mahrt, L. 2010. Nocturnal air drainage in forest canopies: A new way of studying physiological responses to the weather, UNPUBLISHED.

Whiteman, C. D., Zhong, S., Shaw, W. J., Hubbe, J. M., and Bian, X. 2001. Cold pools in the Columbia Basin, Weather and Forecasting, 16, pp: 432-447.

Whiteman, C. D., Pospichal, B., Eisenbach, S., Weihs, P., Clements, C. B., Steinacker, R., Radlgruber, E. M., and Dorninger, M. 2004. Inversion breakup in small Rocky mountain and Alpine basins, *Journal of Applied Meteorology*, 43, pp: 1069-1082.

Zhong, S., Whiteman, C.D., Bian, X., Shaw, W.J., Hubbe, J.M. 2001. Meteorological processes affecting the evolution of a wintertime cold air pool in the Columbia Basin. *Monthly Weather Review,* 129: 2600-2613.

CHAPTER 2

Effects of sun angle and topographic shading on vertical gradients of air temperature, wind, and humidity in an old-growth forest, Andrews Forest, Oregon

Contents

1. Introduction
2. Study site
3. Methods
4. Results
   4.1. two-week periods
      4.1.1. December 14-31, 2016
      4.1.2. March 14-31, 2017
      4.1.3. June 14-30, 2017
      4.1.4. September 14-30, 2017
   4.2. one-day periods
      4.2.1. Winter solstice
      4.2.2. Spring equinox
      4.2.3. Summer solstice
      4.2.4. Fall equinox
   4.3. Landscape shading around Discovery tree
5. Discussion
6. Conclusions
   Bibliography

ABSTRACT

The objective of this chapter is to examine the effect of different sun angles on radiation, air temperature, wind speed and direction in Discovery Tree, a 66-m tall tree located on the valley floor of a forested mountain basin, in the HJ Andrews Experimental Forest, and to relate those

patterns to processes of cold air drainage and pooling on clear, cloudless days at different times of year. The study developed a conceptual model of the energy budget of a hypothetical Douglas-fir tree in an old-growth forest stand as a function of sun angle under clear sky conditions. This conceptual model used a simple radiation budget to establish predictions about the vertical temperature profile in the canopy at various sun angles. Data from four two-week periods centered around the solstices and equinoxes of 2016 and 2017 were evaluated to test hypotheses and predictions about heat and energy exchange within the canopy and the surrounding landscape. Data on air temperature, wind speed and direction, radiation, relative humidity, and leaf wetness were analyzed from heights ranging from 1.5 to 56 m in the tree, along with data on radiation from a nearby meteorological station (Primet). In addition, the proportion of the nearby landscape that was shaded was calculated for sun angles at pre-dawn, local noon, and local dusk on the solstices and equinoxes. Predictions based on the simple radiation budget were generally consistent with observations at local noon on solstices and equinoxes. However, most observations did not match predictions during pre-dawn and dusk, because other elements of the energy budget, such as upward ground heat flux, canopy heat storage, and subsidence (advection) also play a role in controlling temperature, wind, and moisture in the forest canopy. The maximum influence of landscape shading on Discovery tree occurred when the tree is in high shade (9:00 am) whereas the minimum influence of the shading on the tree is when the tree is illuminated (3:00 pm). In general, inversions occurred more frequently during the day than at night. Drainage flow and down-valley flow may create turbulence and mixing during the night. In addition, intermittent gusts may create turbulence at canopy top and mix the boundary layer during the night. Moreover, upward soil heat flux and outgoing longwave radiation from the canopy during the night may contribute to a mixed nighttime boundary layer.

2.1. INTRODUCTION

The forest microclimate regulates many ecosystem processes. Forest canopies moderate air temperature (Oke, 1987; Hardwick *et al.* 2015). The upper parts of the forest canopy typically experience much larger variations in temperature than the mid or lower canopy (Barker, 1996). Vertical gradients of temperature within the forest canopy influence vertical patterns of biodiversity (Nakamura *et al.,* 2017), canopy epiphytes (Campbell *et al.,* 2001), and ecosystem processes such as carbon and water exchange (Novick *et al.* 2016). Many studies have examined the exchange of water and carbon between forest vegetation and the atmosphere, including CO_2 effuux (Zhao *et al*., 2018), energy distribution (He *et al.,* 2017), local atmospheric stability (Dyer, 1967), and turbulent transfer of heat, moisture, CO2, and momentum (Baldocchi and Meyers, 1988). Climate change and forest disturbance alter forest canopies, which may alter heat exchange in forest canopies and affect C and water cycling (Nakamura *et al*., 2017; Hardwick *et al.,* 2015).

The exchange of heat between the forest canopy, the atmosphere, and the ground is complex and poorly understood. Heat exchange appears to involve vertical fluxes or eddies that move heat into and out of the canopy. There are two main mechanisms of turbulent transport of scalers in forest canopies. The first is "sweep", which occurs very fast as downward moving gusts, while the second one is "ejection", which is a relatively slow upward moving current (Baldocchi and Meyers, 1988; Gao and Shaw 1989). Sweep is responsible for most of the turbulent transfer of scalers at the top and middle of the canopy, whereas ejection is responsible for transferring turbulent fluxes of scalers from sub-canopy to the mid-canopy (Gao and Shaw, 1989).

The infrequent penetration of transporting eddies into the forest can produce counter-gradient or zero-gradient fluxes (Denmead and Bradley 1985, Amiro, 1990). In addition, the stability of the nocturnal boundary layer decreases the depth of the penetration of momentum into the forest (Shaw *et al.* 1988). The stable stratification of the nighttime boundary layer decreases the transfer of heat and other scalers in the canopy because it prevents convective turbulence (free convection). Thus, most of the scaler transfer within the canopy occurs through forced convection as the strong and infrequent top-down turbulent eddies penetrate the canopy (Wharton *et al.,* 2017).

The effect of atmospheric stability on the forest canopy microclimate is debated. Some work indicates that the flux-gradients of water vapor and temperature are similar under unstable conditions whereas they are different under neutral and stable conditions, perhaps due to advection (e.g., cold air drainage) (Dyer, 1967). However, other researchers showed that water vapor and temperature gradients are similar under neutral and stable (advection-free), as well as unstable conditions (Jacovides *et al.,* 1988).

In mountain landscapes, terrain complexity not only induces heterogeneity in the surface (e.g., through shading) but also affects lateral advective fluxes or local winds. Thus, in a study in Brazil (de Araújo *et al.* 2017), more CO_2 accumulated in slope and valley bottoms than upslope areas, particularly during stable nights, and this accumulated CO_2 was "flushed" during mid-morning, when unstable or neutral conditions occur. Topographically-induced shading affected the thermal gradient in a subtropical forest by changing the energy distribution in different aspects, influencing patterns of plant species diversity (He *et al.,* 2017). Downslope flow and stability affected heat transfer in Douglas-fir forest canopies of Idaho, USA (Russell *et al.* 2016). In Douglas-fir forests of southern Washington, USA, Xu *et al.* (2018) showed that the thermal condition in the canopy is a function of canopy morphology: a dense canopy caused strong cooling but hindered vertical exchange of heat flux.

Many studies are utilizing towers to better understand heat, water, and CO_2 exchange between forest canopies and the atmosphere. Although it is difficult to characterize the complex fluxes of water, energy, and carbon in forest canopies, energy balance approaches seem to be appropriate for inferring some processes (Amiro 1990, Wharton *et al.* 2017). Despite some work (Russell *et al.* 2016, Xu *et al.* 2018), few studies have examined heat exchanges in very tall conifer canopies, especially in mountain landscapes, on seasonal timescales that can be related to ecosystem processes.

Our current understanding of the vertical gradients of microclimate variables such as radiation, wind speed, wind direction, and relative humidity within tall conifer forest canopies is limited.

Moreover, the degree in which these gradients affect vertical temperature measurements under different Sun angles and azimuths is not well understood. Thus, the objective of this chapter is to examine the effect of different sun angles on radiation, air temperature, wind speed and direction in Discovery Tree, a 66-m tall tree located on the valley floor of a forested mountain basin, and to relate those patterns to processes of cold air drainage and pooling on clear, cloudless days at different times of year. This study addresses the following questions:

1) What are the patterns of radiation, and the vertical gradients in air temperature, wind speed and direction, and relative humidity in the old-growth Discovery Tree in different seasons?

2) How are these vertical gradients affected by sun angle and day length?

3) How are these vertical gradients affected by topographic shading?

Definition of some terms used in this chapter:

Counter gradient flux: when a flux of a variable is opposite to the mean gradient of that variable.
Kurtotic distribution of wind velocity: when the wind velocity distribution has some values at both tails of the distribution.

2.2. STUDY SITE

The study site is a single old-growth tree located in a an old-growth forest stand on the valley floor of the HJA Experimental Forest in the central Cascade Range of Oregon (Figure 2.1). The Andrews Forest is a fifth-order watershed draining Lookout Creek in the western Cascades of Oregon. Elevation ranges from 410 to 1630 meters. The geology of the forest is affected by phases of volcanism separated by periods of weathering and erosion. Lower hillslopes are steep, and underlain by highly weathered breccias, while ridges are formed on lava flows. Mudflow and pyroclastic flows during early volcanic activities during late Oligocene and early Miocene (23 to 20 million years ago) formed the oldest rocks underlying lower elevation portions of the landscape, whereas volcanic activities during the late Pliocene (nearly 4 million years ago) formed the younger basaltic and andesitic ridges (Swanson and James, 1975).

The climate of the Andrews Forest is characterized by mild, wet winters and dry summers. The precipitation mostly occurs during winter in the form of rain due to prevailing warm westerly winds and low-pressure air masses from the ocean. In contrast, lack of precipitation during summer is mainly due to the establishment of high-pressure centers along the coast which bring fair weather conditions to the Andrews (Franklin and Dyrness, 1973). In addition, the polar jet stream influences the climate of the Andrews Forest. During winter, the stream of cold fronts from the northern latitudes brings cold, stormy weather to the forest, whereas in the summer when the jet stream returns to the higher latitudes, it causes the establishment of fair weather conditions (Bierlmaier and McKee, 1989).

Forests of the Andrews include old-growth forests and young plantations. Old-growth forests originated from wildfires in AD 1560 and the mid 1800s (Weisberg and Swanson 2003), are aged between 356 to 756 years (Franklin *et al*., 1981), and are dominated by Douglas fir (*Pseudotsuga menziesii*) and Western hemlock (*(Tsuga heterophylla*). Douglas-fir is the dominant tree species at the study site whereas western hemlock is the co-dominant species.

Data were obtained from a 66-meter tall Douglas-fir tree, the "Discovery Tree," which was instrumented starting on November 14, 2016. The tree is located in an old-growth Douglas-fir stand (44.216586919m N and 122.24965723m E) on an alluvial fan on a terrace of Lookout Creek. The tree is instrumented with sensors to measure air temperature, wind speed and direction, radiation, relative humidity, and leaf wetness (Figure 2.2). The sensors are mounted along the bole of the tree at 1.5 m, 10m, 20m, 30m, 40m, and 56 m above the ground, within the canopy (Figure 2.2).
Figure 2.1. Location of the Discovery Tree in the Andrews Forest
Figure 2.2. Arrangement of sensors on the Discovery Tree

2.3. METHODS

This study tested how sun angle affected the vertical gradients of air temperature, wind, and relative humidity in the canopy of the Discovery Tree. The study was guided by a conceptual model of the energy budget of a hypothetical Douglas-fir tree in an old-growth forest stand as a function of sun angle under clear sky conditions (Figure 2.3). This conceptual model uses radiation and energy budget concepts to establish predictions about the vertical temperature profile in the canopy at various sun angles.

2.3.1. Energy budget of a tree

The conceptual model is based on the energy budget of a tree. The energy balance of a tree (a hypothetical cylinder surrounding the tree) is the sum of the sensible heat flux, latent heat flux, net rate of physical heat storage, and net rate of biochemical energy storage due to photosynthesis and advection.

$Q^* = Q_H + Q_E + Q_G + \Delta Q_S + \Delta Q_P + \Delta Q_A$

Where Q^*: net energy balance of a tree (Wm^{-2})

Q_H: sensible heat flux (Wm^{-2})

Q_E: latent heat flux (Wm^{-2})

Q_G: ground heat flux (Wm^{-2})

ΔQ_S: net rate of physical heat storage (Wm^{-2})

ΔQ_P: net rate of biochemical energy storage due to photosynthesis (Wm^{-2})

ΔQ_A: advection (Wm^{-2})

The sensible heat flux is the exchange of energy in the form of heat between a substance and its surroundings without any phase change but with temperature change. For example, as the incoming solar radiation illuminates a surface, the upward sensible heat flux causes the air temperature above the surface to rise. The latent heat flux is the exchange of energy between a substance and its surroundings through phase change. During this process, the temperature of both substances do not change. For example, water undergoes a phase change from solid to liquid at 0 °C by absorbing the latent heat of melting which is 80 Cal/g. The ground heat flux is the exchange of heat between the ground surface and the layer of air above it. The flux is towards the ground during the day and away from the ground at night. The net rate of physical heat storage relates to the amount of heat which is stored in the volume of interest. In the case of an old-growth tree, this refers to the tree biomass (foliage, and trunk) and the air in a cylinder surrounding the tree. It means that, the amount of heat storage in plants is proportional to the amount of plants' biomass. The net rate of biochemical energy storage is the amount of energy stored in plants due photosynthesis. The advection term relates to all possible horizontal fluxes which might affect the energy balance of the tree (Oke, 1987).

Two terms are expected to dominate the energy balance for the top of an old-growth tree: sensible heat and advection. The sensible heat flux is large because the top of an old-growth tree receives more incoming solar radiation than the rest of the tree, producing higher turbulent heat flux convergence at the top of the tree compared to the rest of the tree. Because wind speed increases logarithmically with height, the top of an old-growth tree would be expected to experience higher daily wind speeds compared to the rest of the tree. Hence, advection would have a greater influence on the net energy balance of the top of the tree than on other parts of the tree. Under some atmospheric conditions, condensation may occur at the top of the canopy. During cold clear nights when the radiative cooling of the canopy is maximum, the air surrounding the canopy is cooled down. If the temperature of the air falls below the dew point temperature, clouds will form due to the release of latent heat (condensation). Under some atmospheric conditions, such as high pressure (anti-cyclonic) centers with high wind speeds, advection becomes the dominant term in the energy balance. On the other hand, under fair weather conditions (low wind speeds and establishment of low pressure or cyclonic centers), the advection term becomes negligible while the sensible heat flux becomes the dominant term in the energy balance. Since the atmospheric condition in which the current analysis is done is anti-cyclonic (fair weather condition) thus it is necessary to know that the influence of sensible heat flux is more important than the influence of advection in the tree energy balance.

In contrast, sensible heat and advection are expected to be relatively small terms in the energy budget at the base of an old-growth tree, while ground flux and latent heat flux are expected to dominate. The base of the tree receives the lowest amount of incoming solar radiation, and therefore the lowest turbulent heat flux convergence. However, the ground heat flux is an important term in the energy balance at the base of the tree. During the night, the upward ground heat flux warms the air layer above the soil both through conduction and convection, cooling the soil surface. During the day, the downward ground heat flux warms the soil surface through radiative and sensible heat flux convergences. In addition, the relative humidity at the base of a tree is expected to be higher than other parts of the tree. When air has high relative humidity, its temperature is close to the dew point temperature. When the air temperature drops below the dew point temperature, the air can no longer hold the water in the form of gas, and the water changes phase from gas to liquid (water droplets), releasing the latent heat of condensation (i.e. 540 Cal at 100 °C/g of water). Condensation may occur at the base of a tree, under the forest canopy, when moist air comes in direct contact with the radiatively cooled ground surface. Latent heat and water phase changes are not considered in this analysis.

2.3.2. Radiation balance of a tree

The net radiation of a tree (R_n) is a function of global solar radiation (S_t), reflection coefficient ($\boldsymbol{\rho}$), incoming longwave radiation from atmosphere (L_d), incoming longwave radiation from canopy (L_c), outgoing longwave radiation from the surface (L_u), and outgoing longwave radiation from canopy top (L_c). The unit of all these terms is Wm^{-2} except for the reflection coefficient.

$$R_n = (1- \boldsymbol{\rho})*S_t + (L_d + L_c) - (L_u + L_c)$$

Figure 2.3.

The conceptual model (Figure 2.3) predicts the vertical temperature gradient in a tree as a function of sun angle. When there is no incoming solar radiation (e.g., before dawn, Figure 2.3 a), the whole canopy is in shade and the energy budget consists of longwave exchange only. The amount of outgoing longwave radiation from the canopy top to the sky is larger than the amount of outgoing longwave radiation from the canopy to the ground. The sky view factor is at its maximum value at the top of the canopy under clear sky conditions, and determines longwave exchange. In addition, the outgoing longwave radiation from the ground is larger than the outgoing longwave radiation from the tree trunk but smaller than the outgoing longwave radiation from the canopy top to the sky. These fluxes are influenced by down-welling longwave radiation from lower parts of the canopy and the influence of sky view factor. These factors are predicted to establish an isothermal vertical temperature profile from the ground up to the canopy base. Under these conditions, the lower part of the boundary layer (from the ground to the canopy base) is fully decoupled from the rest of the vertical profile. In contrast, the upper part of the boundary layer (from the canopy base to the canopy top) is expected to deviate from the isothermal condition as a result of the imbalance between the outgoing longwave radiation from the canopy top to the clear night sky and the down-welling long-wave radiation from the canopy to the ground. Because the canopy top loses more longwave radiation to the sky compared to the lower parts of the canopy, its temperature is expected to be lower than the rest of the canopy and the ambient air. These factors are expected to create an unstable condition at canopy top, which causes an air parcel to rise adiabatically.

At maximum sun angle (Figure 2.3 b). the whole canopy is illuminated and the amount of the incoming solar radiation received by the ground is at its maximum. In addition, incoming longwave radiation to the ground exceeds outgoing longwave radiation from the ground due to the receipt of longwave radiation from the canopy. This is because the illuminated forest canopy is hotter than the ground, and this hotter canopy emits more longwave radiation than the ground, according to the Stefan-Boltzman equation, which states that the outgoing longwave radiation from a surface is linearly related to the fourth power of the surface absolute temperature. Since the amount of the incoming shortwave radiation at canopy top is higher than the amount of the outgoing longwave radiation from the canopy at local noon due to the highest position of the Sun in the sky, the temperature is expected to be higher at the top of the canopy than throughout the rest of the tree. These factors are expected to create an unstable (convective) boundary layer, causing an air parcel to ascend adiabatically.

When the sun angle is less than 90 degrees (pre-dusk, Figure 2.3 c) one side of the canopy is more illuminated than the other. The more illuminated side of the canopy has a positive radiation balance (incoming exceeds outgoing radiation), whereas the less illuminated side is more likely to have a negative radiation balance (outgoing longwave exceeds incoming shortwave). Thus, the air temperature adjacent to the more illuminated side of the canopy is higher than the air temperature in the less illuminated canopy side. This process occurs whenever one side of the canopy is shaded, which happens when the Sun altitude (angle) becomes smaller than 90 degrees (i.e., before or after the Sun passes the Zenith at local noon). The deficit between energy gain (at the illuminated side of the canopy) and energy loss (at the less illuminated side of the canopy) at two sides of the canopy creates two different conditions. While the illuminated side experiences convective currents and mixing condition, the less illuminated side might experience relatively stable condition. Therefore, an adiabatically lifted air parcel at the shaded side of the canopy tends to descend whereas an adiabatically lifted air parcel at the illuminated side of the canopy tends to ascend. The amount of outgoing longwave radiation from the ground increases as the sun angle decreases, and increases as the azimuth increases.

2.3.3. Thesis Statement

Changing sun angle and azimuth, and their interactions with landforms, affect vertical gradients of radiation, wind, and humidity in the canopy

2.3.4. Hypotheses

Solar altitude is defined as the Sun angle relative to the Earth's horizon. Solar azimuth is defined as the azimuth angle of Sun's position. Thus, both solar angle and azimuth affect how the landscape and the forest are illuminated, which in turn affects the radiation budget, local winds, and moisture exchange in the canopy. Also, radiation is received directly by the tree, and also by the landform on which the tree is located. Thus, the vertical profile of air temperature and wind in the canopy is the result of illumination both of the tree and the landforms.

H1. The Sun altitude and azimuth influence the radiation received by the tree, hence the radiation budget, vertical temperature gradient and vertical movement of air in the canopy.

Explanation of H1. Sun altitude and azimuth influence the vertical gradient of air temperature, wind speed and direction in an old-growth forest stand by regulating the amount and intensity of the incoming solar radiation received by the tree. In low Sun altitudes, the amount and intensity of incoming solar radiation is less compared to high Sun altitudes. Therefore, turbulent sensible and radiative heat fluxes are lower in low sun altitudes compared to high sun altitudes, resulting in lower air temperatures in low Sun altitudes compared to high Sun altitudes. These differences produce movement of an air parcel upward or downward in an adiabatic process (a process in which heat is not transferred). This movement is due to the balance between the upward pressure gradient force and the downward gravitational force. When these two forces are equal, the atmosphere is in hydrostatic equilibrium. This condition is common for atmosphere in general and over a vast area of landscape. In contrast, in the local atmospheric condition over a relatively small area (e.g. a narrow valley at the HJA Forest), the atmosphere deviates from the hydrostatic equilibrium. Hence, the air parcel undergoes upward or downward movement due to the positive or negative buoyancy force in a mechanism which is called convection.

H2. The Sun altitude and azimuth influence the radiation received by the landform on which the tree is located, and hence the radiation budget and horizontal movement of air, which affects the vertical gradient of air temperature and wind in the canopy.

Explanation of H2. The Sun altitude influences the diurnal patterns of longwave radiation, air temperature, wind speed and wind direction in an old-growth forest stand by regulating the amount and intensity of incoming solar radiation received by the landform where the tree is located. Sun altitude increases diurnally from local sunrise to local noon and monthly from December to June. Shaded slopes create high pressure whereas illuminated slopes create low pressure areas. Since wind blows from high pressure to the low pressure, thus wind blows from shaded slopes towards illuminated slopes due to the adiabatic heating and cooling of the opposing or adjacent surfaces. At low Sun altitudes, the amount and intensity of incoming solar radiation is less compared to high Sun altitudes. Therefore, the amount of turbulent sensible and radiative heat fluxes is lower at low compared to high sun altitudes. These two factors result in lower air temperatures at low Sun altitudes compared to high Sun altitudes. At low Sun altitudes, there is also less turbulent sensible and radiative heat flux convergence compared to high Sun altitudes. As a result, the air temperature deficit between opposing illuminated and shaded surfaces decreases. The wind strength (velocity) is proportional to the temperature deficit between the two opposing surfaces. Given that the low wind speeds occur when the temperature deficit between the opposing surfaces is small thus the lower wind speeds occur when the Sun altitude is low whereas the higher wind speeds occur when the Sun altitude is high. In addition, under clear sky conditions and in low Sun altitudes, the amount of outgoing longwave radiation is larger than the amount of incoming longwave radiation due to the radiative flux divergence from the surface, sky view factor, and also lack of cloud effect. In contrast, under clear sky condition and in high Sun altitudes, the amount of incoming longwave radiation is larger than the amount of outgoing longwave radiation due to lack of sky view factor and the influence of down-welling longwave radiation from the forest canopy.

2.3.5. Predictions

The solar angle varies according to the time of day and the azimuth or season (Table 2.1). Based on these variations, which influence the radiation balance, it is possible to predict the temperature, wind speed and direction, relative humidity, and leaf wetness expected at a site at solstices and equinoxes (Table 2.2), and at pre-dawn, local noon, and pre-dusk times of day (Table 2.3).

2.3.6. Data

Data on air temperature, wind speed and direction, relative humidity, and leaf wetness from various heights in the Discovery Tree canopy were examined for each day and two-week periods centered around each solstice and equinox from fall 2016 to summer 2017. Data on incoming and outgoing shortwave and longwave radiation from the Primet meteorological station, which is located a few hundred meters WSW of the Discovery Tree (Figure 2.1). This study used air temperature data obtained from the fan-aspirated air temperature sensors mounted at 1.5 m, 10 m, 20 m, 30 m, 40 m, and 56 m on Discovery Tree, as well as relative humidity and wind data from 1.5 and 56 m, and leaf wetness data from 1.5, 30, and 56 m (Table 2.4).

2.3.7. Analysis

For each of these periods, 15-minute data were plotted and evaluated to test hypotheses and predictions about heat and energy exchange within the canopy and the surrounding landscape. In addition, within each period, a cloudless day was selected for finer-scale analysis. For this day, the vertical profiles of light (from HOBO sensors), air temperature, wind speed and wind direction, and relative humidity were plotted hourly. Data from these 24-hr periods were evaluated to test the hypotheses and predictions about the heat and energy exchange within the canopy and also the surrounding landscape.

2.3.8. Landscape shading analysis

A DEM was obtained from 1-meter resolution LiDAR points cloud of the HJ Andrews Forest in 2008 (http://andlter.forestry.oregonstate.edu/data/spatialdata/gi01001.htm). The shaded relief models were fitted using the Hillshade function in ArcMap10.3. The solar altitude and azimuth were calculated for three times of a day: 0900h, 1200h, and 1560h, on December 21, 2016 (winter solstice), June 21, 2017 (summer solstice), March 21, 2017 (spring equinox), and September 22, 2017 (fall equinox). A total of twelve shaded relief models were created, for these three times of day on each of the four days. The resulting DN values were classified into three categories of shading: high shade (0 to 85), moderate shade (86 to 170) and low shade, or high illumination (171 to 255) by dividing the overall distributions of DN values into thirds. The values were classified using manual method in the classification algorithm. The proportion of the HJ Andrews around Discovery Tree in each shade at each time of day and time of year was calculated from the resulting shaded relief maps.

2.4. RESULTS

2.4.1. Two-week periods

This section compares the data for two-week periods surrounding each solstice and equinox to the predicted conditions based on sun angle.

2.4.1.1. December 14-31, 2016

During the two-week period surrounding the winter solstice, on average the incoming shortwave radiation was 21 Wm^{-2}. Incoming longwave radiation ranged from 256 to 348 Wm^{-2} and outgoing longwave radiation range from 298 to 308 Wm^{-2}. The diurnal range of aspirated air temperature was larger at 56 m than at 1.5m. On average the wind speed at 56 m is less than 1.5 m/s and winds are mostly from the NE (Figure 2.4, Table 2.5).

<u>Figure 2.4 (Dec. 14-30, 2016)</u>

<u>Table 2.5</u>

2.4.1.2. March 14-31, 2017

During the two-week period surrounding the spring equinox, on average the incoming shortwave radiation was 89 Wm^{-2}. Incoming longwave radiation ranged from 334 to 357 Wm^{-2} and outgoing longwave radiation range from 334 to 447 Wm^{-2}. On average the wind speed is less than 1 m/s and the dominant wind direction is the NE at 56 m height (Figure 2.7, Table 2.5).

<u>Figure 2.7 (March 14-30, 2017)</u>

2.4.1.3. June 14-30, 2017

During the two-week period surrounding the summer solstice, on average the incoming shortwave radiation was 269 Wm^{-2}. Incoming longwave radiation ranged from 356 to 400 Wm^{-2} and outgoing longwave radiation range from 456 to 580 Wm^{-2}. The diurnal range of aspirated air temperature was the same at both 10 m and 56 m heights. On average the wind speed at 56 m is 0.9 m/s and the dominant wind direction at 56 m height is the NE (Figure 2.10, Table 2.5).

Figure 2.10 (June 14-30, 2017)

2.4.1.4. September 14-30, 2017

During the two-week period surrounding the fall equinox, on average the incoming shortwave radiation was 116 Wm^{-2}. Incoming longwave radiation ranged from 285 Wm^{-2} to 407 Wm^{-2} and outgoing longwave radiation range from 367 Wm^{-2} to 540 Wm^{-2}. The diurnal range of air temperature was larger at 56 m than at 1.5m height. On average the wind speed at 56 m is 0.6 m/s and the dominant wind direction at 56 m is the NE (Figure 2.13, Table 2.5).

Figure 2.13 (September 14-30, 2017)

2.4.1.5. Comparison of predictions to results

Observations differed from predictions as follows:

Shortwave radiation was expected to be low at the winter solstice, high at the summer solstice, and moderate at the equinoxes (Table 2.2). Longwave radiation was expected to be high at the winter solstice, and low at the summer solstice (Table 2.2). However, longwave radiation did not vary much among the four periods. Observation support the prediction of shortwave radiation in solstices and equinoxes (Table 2.5).

Outgoing longwave radiation was expected to exceed incoming longwave in all four periods (Table 2.2). Observations support this prediction (Table 2.5). One of the possible explanation is the lack of clouds during these periods causing the ground to lose more longwave radiation to the sky. In addition, the location of radiation sensor at Primet could be another reason for recording higher amount of outgoing relative to incoming longwave radiation. This sensor may receive relatively little down welling long wave radiation from the upper and adjacent forest canopy.

As expected, the air temperature at 56 m was higher than the air temperature at 30 m or 1.5 m in all periods except summer (Table 2.2, D). At the summer solstice (June 14-30, 2017) air temperature at 30 m and 56 m were higher than at 1.5 m (Table 2.5).

Wind speed at 56 m was expected to be high at the winter and summer solstices but moderate at the spring and fall equinoxes (Table 2.2). Observations partially support this prediction since the highest average wind speed at the top of the tree (0.9 m/s at 56 m) occurred in the summer, and the lowest average wind speed occurred at the winter solstice (0.5 m/s at 56 m) (Table 2.5). As expected (Table 2.3), wind speeds at 56 m always exceeded wind speeds at 1.5 m (Table 2.5).

The dominant wind direction at 56 m was expected to be down-valley (the NE) during all four periods (Table 2.2). Observations support this prediction (Table 2.5). Around 66%, 44%, 48%, and 55% of the time the dominant wind direction at 56 m height is from the NE during December, March, June, and September periods respectively (Table 2.5).

2.4.2. One-day periods

2.4.2.1. Winter Solstice (December 21, 2016)

During the one-day period near the winter solstice, the maximum incoming shortwave radiation was 420Wm^{-2} (Figure 2.5 a) Incoming longwave radiation ranged from 256 to 300 Wm^{-2} and outgoing longwave radiation ranged from 300 to 305 Wm^{-2} (Figure 2.5 b) The diurnal range of aspirated air temperature was larger at 56 m than at 1.5 or 30 m (Figure 2.5 c, Table 2.6). On average the wind speed at 56 m height was less than 0.5 m/s and winds were from the NE (Figure 2.5 d, e, Table 2.6) On average wind speed at 1.5 m was 0.2 m/s winds were from the NW and NE (Figure 2.5 d, e, Table 2.6).

Figures 2.5, 2.6

Table 2.6_

At pre-dawn (6:00 AM) on the day near the winter solstice (Figure 2.6 a) air temperature at 56 m was higher than at 1.5 m. Air temperature decreased with height from 1.5 m to 20 m and then from 10 m to 40 m a relatively isothermal condition prevailed. Therefore, a released hypothetical air parcel at 1.5-meter height will ascend (upward flux) up to 20 m height due to the normal lapse rate. Relative humidity exceeded 99% at1.5 and 56 m (Figure 2.5 f, Table 2.6).

At local noon (12:00 PM) (Figure 2.6 b) air temperature at 56 m was higher than the air temperature at 1.5 m. Air temperature increased with height resulting in the formation of a stable boundary layer at the tree scale. Therefore, a released hypothetical air parcel at 1.5 m will descend (downward flux) due to the inverted lapse rate. Relative humidity exceeded 99% at1.5 and 56 m (Figure 2.5 f, Table 2.6).

At local dusk (18:00) the air temperature at 56 m was the same as at 1.5 m, but the air temperature at 30 m was slightly warmer (Figure 2.6 b, Table 2.6). Air temperature decreased from 1.5 meter to 20 meter which results in the formation of an unstable boundary layer along the lower part of the tree. Thus, a released hypothetical air parcel at 1.5-meter height will ascend (upward flux) due to the lapse rate effect. However, the temperature increased from 20 to 30 m, which results in the formation of a stable condition along the middle part of the tree. Therefore, a released hypothetical air parcel at 20 m will descend (downward flux) due to the inverted lapse rate. On the other hand, the air temperature decreased from 30 to 40 m which results in the formation of an unstable condition along the upper part of the tree. As a result, a released hypothetical air parcel at 30-meter height will ascend (upward flux) due to lapse rate effect. The air temperature was isothermal from 40 to 56 m in the tree (Figure 2.6 b). Relative humidity exceeded 99% at1.5 and 56 m (Figure 2.5 f, Table 2.6).

2.4.2.2. Spring equinox (March 21, 2017)

During the one-day period near the spring equinox (Figure 2.8 a), the maximum incoming shortwave radiation was 838 Wm^{-2}. Average incoming longwave radiation was 300 Wm^{-2} and outgoing longwave radiation was 360 Wm^{-2} (Figure 2.8 b) The diurnal range of aspirated air temperature was slightly larger at 56 m compared to 1.5 m and 30 m (Figure 2.8 c, Table 2.6). On average the wind speed at 56 m was 0.5 m/s and winds were multi-directional (Figure 2.8 d, e, Table 2.6).

Figures 2.8, 2.9

At pre-dawn dawn (6:00 AM) on the day near the spring equinox (Figure 2.9 a) the canopy top had the same temperature as the 1.5-meter sensor. Air temperature decreased slightly with height resulting the formation of a weak unstable boundary layer at the lower part of the tree. Therefore, a released hypothetical air parcel at 1.5-meter height will ascend (upward flux) due to the normal lapse rate influence. On the other hand, the air temperature increased from 20 to 56 m resulting in the formation of a relatively weak stable boundary layer (the temperature deficit between 20 m and 56 m is less than 0.5°C) at the upper part of the tree. Therefore, a released hypothetical air parcel at 20 m will descend (downward flux) due to the inverted lapse rate effect. Relative humidity exceeded 99% at1.5 and 56 m (Figure 2.8 f, Table 2.6).

At local noon (12:00 PM) air temperature is higher at 56 m than at 1.5 m (Figure 2.9 b, Table 2.6). The temperature deficit between the aspirated sensors at 1.5 m and 56 m heights is about 1°C (Table 2.6). The increase of air temperature from 1.5 to 56 m results in the formation of a stable boundary layer along the tree (Figure 2.9 b). Therefore, a released hypothetical air parcel at 1.5-meter height will descend (downward flux) due to the inverted lapse rate. Relative humidity was 99% at 1.5m and 89% at 56 m (Table 2.6).

At local dusk (18:00) air temperature at 56 m is higher than the air temperature at 1.5m (Figure 2.9 b, Table 2.6). Air temperature increases about 1°C from 1.5 to 56 m. Therefore, a stable condition forms along the tree (Figure 2.9 b). As a result, if a hypothetical air parcel is released, it will descend due to the inverted lapse. Relative humidity was 99% at 1.5m and 97% at 56 m (Table 2.6).

2.4.2.3. Summer solstice (June 21, 2017)

During the one-day period near the summer solstice the maximum incoming shortwave radiation was 1005 Wm^{-2} (Figure 2.11 a). Average incoming longwave radiation was 356 Wm^{-2} and outgoing longwave radiation was 456 Wm^{-2} (Figure 2.11 b) The diurnal range of air temperature was about 11 °C at both 1.5 and 56 m (Figure 2.11 c, Table 2.6). Average the wind speed at 56 m was 1 m/s and winds were from the NE and the SW (Figure 2.11 d, e, Table 2.6).

Figures 2.11, 2.12

At pre-dawn dawn air temperature was relatively isothermal from 10 m to 20 m (Figure 2.12 a). Thus a hypothetical air parcel at 10-meter height remains stationary due to the presence of neutral boundary layer condition. The temperature increased with height from 20 m to 40 m, leading to a stable condition at these heights. From 40 m to 56 m the boundary layer becomes mixed (isothermal) again (Figure 2.12 a). The relative humidity at 56 m height was 94% (Figure 2.11 f).

At local noon, the aspirated air temperature at 56m is slightly lower than the temperature at 10m (Figure 2.12 b, Table 2.6). Air temperature increased with height from 10 to 20 m, was isothermal from 20 m to 30 m, and decreased from 30 m to 56 m. This creates an unstable boundary layer along the upper part of the tree. As a result, a lifted hypothetical air parcel at 30 m height continues to rise due to the lower environmental lapse rate compared to the adiabatic lapse rate (temperature decreases more slowly than adiabatic lapse rate (-10°C/Km). The relative humidity was 44% at 56 m height (Figure 2.11 f).

At local dusk, the air temperature at 56 m was higher than the air temperature at 10 m (Figure 2.12 b, Table 2.6). Air temperature increased steadily from 10 m to 56 m but the rate of temperature increase from 40 m to 56 m height is greater than the rate of temperature increase in the rest of the tree. As a result, a hypothetical lifted air parcel descends due to the presence of an inverted boundary layer along the tree. The relative humidity was 40% at 56 m height (Figure 2.11 f).

2.4.2.4. Fall equinox (September 21, 2017)

During the one-day period, the maximum incoming shortwave radiation was 346 Wm^{-2} (Figure 2.14 a). Average incoming longwave radiation was 356 Wm^{-2} and outgoing longwave radiation was 440 Wm^{-2} (Figure 2.14 b). The diurnal range of aspirated air temperature was larger at 56 m compared to 1.5 m (Figure 2.14 c). On average the wind speed at 56 m height was 0.5 m/s and winds were multi-directional (Figure 2.14 d, e, Table 2.6).

Figures 2.14, 2.15

At pre-dawn the air temperature at 56 m was slightly lower than the air temperature at 10 m. The temperature decreased from 10 m to 30 m and then from 30 m to 56 m an isothermal condition prevailed (Figure 2.15 a). The relative humidity at 56 m was 99 % (Figure 2.14 f, Table 2.6).

At local noon, the air temperature was higher at 56 m than in the rest of the tree (Figure 2.15 b). Air temperature increased, indicating a stable boundary layer from 20m to 30m and from 40m to 56m heights. Air temperature was isothermal from 10-20 m, indicating neutral conditions, and decreased from 30m to 40m, indicating an unstable condition (Figure 2.15 b). Relative humidity at 56 m was 88% (Figure 2.14 f, Table 2.6).

At local dusk, the air temperature was higher at 30m than in the rest of the tree. Similar to the conditions at local noon, three stability conditions were observed along the tree. A neutral condition occurred from 10m to 20m, a stable condition occurred from 20m to 30m and also from 40m to 56m, and an unstable condition occurred from 30m to 40m (Figure 2.15 b). The relative humidity at 56 m was 98% (Figure 2.14 f, Table 2.6).

2.4.2.5. Comparison of predictions to results

Observations differed from predictions in several respects. Shortwave radiation was expected to be low at the winter solstice, high at the summer solstice, and moderate at the equinoxes (Table 2.2). Longwave radiation was expected to be high at the winter solstice, and low at the summer solstice (Table 2.2). However, longwave radiation did not vary much during the solstices and equinoxes. Observation support the prediction of shortwave radiation in solstices and equinoxes (Table 2.6).

Outgoing longwave radiation was expected to exceed incoming longwave in all four periods (Table 2.2). This prediction was supported except on December 21, 2016 when incoming slightly exceeded outgoing longwave radiation, perhaps due to the presence of clouds in the pre-dawn sky (Table 2.6).

Air temperature was expected to be higher at 56 m than at 1.5 m at local noon, but lower at pre-dawn and local dusk in all four periods (Table 2.3). The observation supports higher air temperature at 56 m compared to 1.5 height at local noon (Table 2.6). However, air temperature was the same at 56 m and 1.5 m at pre-dawn and local dusk.

Wind speed at 56 m was expected to be low at the winter solstice, moderate at the spring and fall equinoxes, and high at the summer solstice (Table 2.2). Observations partially support this prediction, especially at local noon (Table 2.6). However, the lowest wind speed al local noon occurred on September 21, 2017 and the wind speeds during spring and fall equinoxes are low.

The dominant wind direction at 56 m was expected to be down-valley (the NE) during all four periods (Table 2.2). Observations support this prediction (Table 2.6). More than 70% of the time the dominant wind direction at 56 m height is from the NE on December 21, at pre-dawn on March 21, and June 21, and at local dusk on September 21, but much less than 70% at other times (Table 2.6).

At the winter solstice at local noon the air temperature at 56 m was expected to be higher compared to 1.5 m, creating a stable condition and descending air parcels, and decrease in relative humidity with height in the tree (Table 2.3). Although air temperature was slightly higher at 56 m compared to 1.5 m, relative humidity did not change with height at local noon (Table 2.6).

At the spring equinox at local noon, the air temperature at 56 m was expected to be higher compared to 1.5 m, creating a stable condition and descending air parcels, and decrease in relative humidity with height in the tree (Table 2.3). Observations support this prediction: air temperature is higher, and relative humidity is lower, at 56 m than at 1.5 m at local noon (Table 2.6).

At the summer solstice at local noon, the air temperature at 56 m was expected to be higher compared to 1.5 m, creating a stable condition and descending air parcels, and a decrease in relative humidity with height in the tree (Table 2.3). However, observations do not support this prediction: air temperature is the same at both 1.5m and 56m (Table 2.6).

At the fall equinox at local noon, the air temperature at 56 m was expected to be higher compared to 1.5 m, creating a stable condition and descending air parcels, and a decrease in relative humidity with height in the tree (Table 2.3). Observations support this prediction: air temperature is higher, and relative humidity is lower, at 56 m than at 1.5 m at local noon (Table 2.6).

2.4.3. Landscape shading around Discovery Tree

The highest amount of landscape shading in the area around the Discovery Tree occurs at 9:00 am on the winter solstice (69% of area in high shade, 7% illuminated) (Figure 2.16, Table 2.7). However, the lowest amount of landscape shading occurs at local noon on the spring equinox (19% of area in high shade, 28% illuminated) (Figure 2.16, Table 2.7).

Figure 2.16

Table 2.7

In addition, the highest amount of landscape illumination occurs at 3:00 pm on the summer solstice (48% of the landscape illuminated). At 3:00 pm the sun altitude and azimuth were 60° and 235° respectively. On the other hand, the minimum percentage of low shade areas among the four days was 7 which occurred at 9:00 am on winter solstice. At 9:00 am the Sun altitude and azimuth were 9.7° and 137° respectively (Figure 2.16, Table 2.7).

2.4.3.1. One-day periods on solstices and equinoxes (Figure 2.18)

The percent of landscape in low shade is correlated with net radiation for winter, fall, and summer but not for spring (Fig 2.18a).

As the percent of low shade area increases (when the sun altitude increases from winter to summer) the air temperature increases too (Fig 2.18b).

As the percent of low shade area increases for spring equinox at 3 pm, Fall equinox at 3 pm, and summer solstice at 12pm, the wind speed at 56m increases too (Fig 2.18c).

The percent of landscape in low shade is not correlated with the percent of the winds from NE (Fig 2.18d).

The lowest RH at 56m occurs in summer solstice at 12pm when 47% of the landscape is in low shade whereas the highest RH occurs in the other three days. RH is not correlated with the percent of the low shade area (Fig 2.18e).

The percent of low shade area is not correlated with the leaf wetness (Fig 2.18f).

Figure 2.18

2.4.3.2. Two-week periods surrounding solstices and equinoxes (Figure 2.19)

The percent of landscape in low shade is positively correlated with net radiation (Fig 2.19a) and air temperature (Fig. 2.19b).

As the percent of landscape in low shade increases, the wind speed increases too except for fall and spring (Fig. 2.19c).

The percent of landscape in low shade is negatively correlated with the percent of time winds from NE at 56m in winter and spring. It is positively correlated in spring and fall and again negatively correlated in fall and summer (Fig. 2.19d).

The percent of landscape in low shade is negatively correlated with RH in spring, fall, and summer (Fig. 2.19e).

The percent of landscape in low shade is negatively correlated with leaf wetness in spring, fall, and summer (Fig. 2.19f).

Figure 2.19

2.5. DISCUSSION

This study used a simple energy balance to predict the vertical gradient of air temperature and vertical air movement in the forest canopy of a 66-m Douglas-fir tree on a flat surface under clear sky conditions during the equinoxes and solstices. The predictions in this study were based on a simplified energy budget, which excluded ground flux, latent heat, biochemical heat storage, and horizontal advection.

Predictions were based on principles of heat exchange and buoyancy, and were compared to observations of temperature and other variables measured in the canopy. In cases in which predictions matched observations, inferences were drawn about the role of net radiation, sensible heat and canopy storage. In cases in which predictions did not match observations, additional inferences were drawn about the roles of ground heat flux, latent heat flux and horizontal advection, based on observations of air temperature, horizontal wind speed and direction, relative humidity, and leaf wetness. Data interpretation also considered how landscape shading influenced local winds, wind speed and direction, and horizontal advection.

2.5.1 Simple predictions of the energy budget considering net radiation, sensible heat flux, and canopy storage.

In general, the predictions based on a simple radiation budget were most consistent with observations at local noon. This is because the incoming shortwave radiation is the major driving force in the energy balance (all other variables are functions of it), and incoming shortwave radiation reaches its maximum value at local noon (the highest Sun angle). In contrast, during other times of day (pre-dawn and local dusk) and also during seasons when the sun angle is low (especially winter), incoming shortwave radiation plays a lesser role in predicting the microclimate variability relative to longwave radiation from the soil and the forest canopy.

2.5.1.1. Sensible heat

Radiative heating and cooling of the forest canopy is complex since depends on leaf moisture content, surface area, leaf area, color, texture, orientation, and architecture. Under clear sky condition during the day the incoming shortwave radiation increases the release of the turbulent sensible heat flux causing the canopy temperature to rise. Then the heat is stored in the canopy due to the physical heat storage capacity of foliage. The amount of the incoming longwave radiation from the sky is negligible under this condition. In contrast, under clear sky condition during the night, the amount of incoming shortwave radiation is zero thus the turbulent sensible heat flux convergence is negligible. In addition, the amount of the incoming longwave radiation from the sky is negligible too. Therefore, the canopy skin temperature does not increase. In contrast, the amount of the outgoing longwave radiation from the canopy increases due to both the radiative cooling of the canopy surface and sky view factor.

<u>December</u>. The low shortwave inputs are due to high amounts of landscape shading in December surrounding the Discovery Tree. The observed high levels of outgoing longwave radiation may be due to the lack of clouds in the night sky which enhances the sky view factor resulting in greater radiative loss from the surface to the sky. The lower amount of radiation received by the sensor at 1.5 m compared to 56 m height is due to the combined shading effect of the upper

canopy, adjacent canopy and presence of clouds. The upper canopy shading impacts the whole lower part of the canopy uniformly whereas the adjacent canopy might cast shadow on the tree differently due to the structural variability of canopy in adjacent trees.

March. The moderate positive net radiation may reflect the presence of clouds and the resultant down-welling long-wave radiation to the ground. Relatively low average wind speeds at both 1.5 m at 56 m may be due the presence of clouds. Clouds reduce the amount of shortwave radiation received by the ground thus, the temperature deficit between the two opposing surfaces (under cloudy condition) becomes less than the temperature deficit between the two opposing surfaces under cloud-free condition. Given that wind blows from colder (high pressure) surfaces towards warmer (low pressure) surfaces, and wind speed (strength) is proportional to the temperature deficit between two opposing surfaces, thus wind speed is lower under cloudy condition compared to the cloud-free condition.

June. Due to the higher Sun angles during June 14-30 compared to the other times of the year, the daylight duration is longer compared to other times of the year. Therefore, both of the sensors receive high amounts of radiation, but the sensor at 56-meter height receives much more radiation. Hence, there is more radiative and turbulent sensible heat flux at 56 m than 1.5 m.

September. The low amount of wind speed even at 56 m height sensor is due to the obstructing effect of surrounding canopy. About 94% of times at local dusk the wind at 56 m is from the NE whereas 0% of time the wind at 56 m is from the NW. Given that the wind speed is low, these observations could explain the dominance of a slow moving air mass from the NE at local dusk with a minimum depth of 56 m.

2.5.1.2. Vertical advection (convection)

Convection is a mode of scaler transfer (heat) through gas and liquid. Since convection transfers heat in a vertical direction, it is a function of vertical temperature gradient. Under mixed (isothermal) boundary layer conditions, convection is the main heat transfer mechanism whereas under stable boundary layer (inverted lapse rate) condition, convection becomes negligible.

Convection was expected mostly during daytime due to the influence of incoming shortwave radiation during the day, and stable conditions were expected during nighttime. As a surface receives the radiation, the turbulent sensible and radiative heat fluxes release creating convective currents. These currents transfer heat from the surface to the adjacent air layer causing the air temperature to rise. However, the data shows that the convection mostly happened during nighttime and the boundary layer was stable in the afternoon. The supporting evidence was the neutral boundary layer condition along the tree during night.

Dec 21. At local dusk during the winter solstice, air temperature is the same throughout the canopy, indicating a neutral boundary layer (isothermal condition). The formation of this layer may be due to mixing from above (intrusion of air, subsidence, incoming longwave radiation from clouds), which is consistent with the relatively high observed incoming longwave radiation. It may also be due to mixing from below (convective currents due to upward soil heat flux), consistent with the relatively high outgoing longwave radiation. At local dusk in December and September, the incoming and the outgoing longwave radiation are very similar, so the released incoming and outgoing turbulent heat fluxes are equal, resulting in the formation of a thermodynamic equilibrium throughout the canopy. Subsidence also may explain the isothermal condition in the canopy observed at pre-dawn in December. Slow-moving, downslope and down-valley wind and wind speed < 0.5 m throughout the canopy are evidence of subsidence. The formation of isothermal condition along the tree is due to subsidence from canopy top and convective currents from the ground. These two mechanisms act together until a thermodynamic equilibrium is reached. At this point no heat is transferred and the system (the boundary layer surrounding Discovery tree) is in neutral (isothermal) condition. The effect of wind in mixing the air plus low amount of available energy for evaporation, and high amount of moisture causes the sensors at both heights to show the same (or very similar) relative humidity.

March 21: At local dusk, the aspirated air temperature is relatively the same throughout the canopy, due the formation of a neutral boundary layer (isothermal condition). The formation of this layer may be due to mixing both from above (intrusion of air, subsidence) and from below (convective currents due to upward soil heat flux), consistent with the relatively high outgoing longwave radiation (356 Wm^{-2}). Since both the incoming and the outgoing longwave radiation are equal, the released incoming and outgoing turbulent heat fluxes are equal resulting in the formation of a thermodynamic equilibrium throughout the canopy.

June 21: At local dusk, the observed air temperature is higher at 56 than at 10 m, which may be due to the influence of canopy heat storage. Also, at mid-day in June, air temperature data indicate that the boundary layer was isothermal between 20 and 30 m whereas it became unsTable 2.2etween 30 and 56 m. The forest canopy regulates the adjacent air temperature through both physical and biochemical heat storage. Physical heat storage is directly related to canopy biomass and foliage density whereas biochemical heat storage is very small, and is related to the photochemical reactions during photosynthesis. Since the surface of the earth experiences the longest daylight time and also receives the maximum amount of insolation in a year in the northern hemisphere at the summer solstice, thus the forest canopy reaches its maximum amount of heat storage on this day. As a result, it takes longer for the canopy to lose its heat to the clear sky through radiative cooling. Therefore, the upper canopy temperature remains relatively high even during late night hours. Although most of the tree is in a neutral condition (no vertical movement of air) the increased temperature from 40 to 56 m (due to the canopy heat storage), forms a stable local layer at the top of the canopy, resulting the downward movement of a hypothetical adiabatically lifted air parcel.

September 21: At local dusk, the observed air temperature at 10 m height is a little higher than the air temperature at 56 m height. This slight difference might be due to the release of ground heat flux. As the night progresses, the isothermal condition along the tree establishes except at 2100h. At this time the air temperature is higher at 30 m than in the rest of the tree, which might be due to the heat storage effect of the canopy. While the isothermal condition is the dominant stability condition of night time boundary layer, inversion is the dominant stability condition of afternoon boundary layer at Discovery tree scale.

An unexpected finding was the stable boundary layer condition between 20-30 m height of the tree at 1200h and 1560h in December 21, March 21, and September 21 whereas the boundary layer condition was relatively isothermal during night and early morning on all the above dates. In contrast, on June 21, 2017 the boundary layer is above 30 m at 1800h and 2100h, whereas cooling occurs above 40 m at 1200h and 1560h, causing the boundary layer to become unstable. The heat storage may be due to canopy leaf biomass, which is higher in the middle to upper part of the canopy. Thus, the temperature increases from the ground to the middle part of the canopy creating a stable boundary layer, and an adiabatically lifted air parcel tends to descend.

2.5.1.3 Ground heat flux

Shortwave and longwave radiation affect ground heat flux. During day, the incoming shortwave radiation increases the release of the turbulent sensible and radiative heat flux from the ground causing the temperature to rise. In contrast, during night, the release of the long wave radiation from the ground due to the radiative cooling effect causes the temperature to decline. The release of ground heat flux during night might increase the temperature of the lowest part of the tree.

During December at all times the air temperature at 1.5 m is higher than the air temperature at 10 m (Figure 2.6). This might be due to the ground heat flux. The effect of ground heat flux becomes more important when the soil is wet. The moisture content in the soil increases the latent heat flux causing the temperature of the adjacent air layer to rise. Because December 21, 2016 apparently was a wet day (Figure 2.4 h), thus it is conceivable that the soil was wet too. It is hypothesized that during wet seasons, when the soil moisture content is high, the air temperature at pre-dawn is higher at 1.5 m compared to the air temperature at 10 m height of the canopy, due to ground heat flux.

Upward soil heat flux also creates turbulence through convective currents. These currents mix the air and transfer the heat towards upper part of the tree. Ground heat flux may have contributed to isothermal gradients in the canopy at 0000h and 0300h on March 21 (Figure 2.9 a) and 0000h on June 21 (Figure 2.12 a).

2.5.1.4 Latent heat flux

In December, March, and September, incoming shortwave radiation is low and variable. Variable incoming shortwave radiation indicates the presence of clouds, which are associated with 99% relative humidity throughout the canopy. The presence of a mixed boundary layer facilitates circulating the air moisture content through convective currents adjacent to the ground and at the top of the canopy. Although the presence of clouds is the result of air saturation (RH=100%), they increase the relative humidity and leaf wetness in a positive feedback loop. Clouds emit longwave radiation which decreases cloud temperature but increases the temperature of the ambient air. While longwave emission and cooling increases condensation (which results in saturation and cloud formation), condensation tends to increase relative humidity and leaf wetness.

A warm air parcel holds more moisture compared to a cold air parcel. As a result, under cloudy condition, the relative humidity at the top of the canopy is always close to 100% due to the warming effect of the long wave emission from clouds. The relative humidity at 1.5 m is close to 100% as well, because the ground emits longwave radiation to the sky which decreases the ground temperature but increases the temperature of the ambient air adjacent to the ground. Therefore, saturation (RH=100%) occurs near the ground while the moisture content of the air is lower in the mid-canopy due to higher air temperature. These processes at the ground and canopy top creates a condition in which the relative humidity is 100% at the ground and canopy top while it is less than 100% at the middle part of the tree. Since this condition occurs mostly in neutral boundary layer (isothermal) condition, the vertical movement of a hypothetical air parcel is damped. Thus, the vertical distribution of moisture along the tree persists until the clouds are removed by advection or enhanced evaporation.

Latent heat exchange, measured by changes in leaf wetness, influences the skin temperature of the canopy. At dew point (the temperature in which condensation occurs) the leaf wetness is maximum and the canopy skin temperature is low due to the release of latent heat of condensation. In contrast, as the temperature increases and passes the dew point, the leaf wetness decreases until it reaches its minimum value at hottest time of day. This is mainly due to the absorption of latent heat of evaporation. As a result, the canopy skin temperature increases. Latent heat exchange also influences ground heat flux. The radiative cooling of the ground is a function of soil moisture, soil texture, and soil color. The earth emits longwave radiation mostly in the near infra-red part of the electromagnetic radiation. Water is totally non transparent (and non- reflective) to the longwave radiation whereas bare, dry soil is highly transparent (and reflective) to the longwave radiation. Thus, as the amount of soil moisture increases, the soil reflectivity in the near infrared part of the electromagnetic spectrum diminishes. This suggests that moist soil stores more energy compared to a dry bare soil and thus it should have higher temperature. However, as soil moisture increases, evapotranspiration also increases, causing the soil temperature to decrease (Small and Kurk, 2003).

2.5.2. Landscape shading

The predictions were based on a simple energy budget at a point on a presumed flat surface, and so ignored the effect of landscape shading. However, Sun altitude and azimuth interact with land forms, and aboveground vegetation to affect the spatial pattern of topography-induced shading, which in turn create local winds that influence the temperature and moisture conditions of the canopy. The landscape induced shading in a complex landscape such as the Andrews Forest creates differential surfaces of energy surplus and deficit throughout the landscape. The spatial distribution of theses energy surfaces becomes even more complex if the canopy induced shading effect is added to the landscape shading.

Wind blows from a high-pressure surface to a low-pressure surface. High-pressure surfaces are colder than the low-pressure surfaces. Cold surfaces have less energy compared to warm surfaces due to the combined effect of topography- and vegetation-induced shading. As a result, wind blows from a low-energy surface towards a high-energy surface throughout the landscape. Given that theses surfaces are distributed throughout the Andrews Forest landscape, it is hypothesized that depending on the amount of energy deficit between two opposing surfaces, diverse multidirectional local wind categories are expected to be observed.

These local winds (horizontal advection) might affect the temperature profile along the Discovery Tree. Both cold and warm advection could decrease or increase the vertical temperature gradient along the tree.

In general, it was expected to observe down valley and down slope flows when the highest percentage of the landscape surrounding the tree is in high shade. In contrast, it was expected to observe up valley and up slope flows when the highest percentage of the landscape surrounding the tree is in low shade (illuminated). It was expected to observe up-slope flows when the area surrounding the tree is in low shade (illuminated).

However, the effects of sun angle on landscape shading and local winds produced complex patterns of wind in the canopy. At many times, wind direction differed at different heights in the canopy. The percent of the wind from the NW at 1.5 m at all times is higher than the percent of the wind from the NW at 56 m height at both equinoxes and solstices. This means that the sensor at 1.5 m height is more affected by down-slope (NW) flow, whereas the sensor at 56 m is more affected by down-valley flow.

In December, the percent of the wind from the NE at 56 m is higher than the percent of the wind from the NE at 1.5 m height just during Dec 14-30, 2016. This means that the sensor at 56 m height is affected by the down-valley (NE) flow during this period. The reason could be related to the influence of synoptic forcing and the establishment of cyclonic condition. In December in the upper part of the canopy the observed condition is neutral whereas the predicted condition is unstable. One possible reason is the influence of local wind in mixing the air, as indicated by local winds of 0.5 m/s and from the NE direction at 56 m in the canopy.

During March, the percentage of the NE wind direction is the same at both sensors which might be due to the synoptic weather condition. In contrast, during June and September periods, the 1.5 m sensor receives higher percentage of the NE wind direction compared to the 56 m sensor which might be due to the shallow down-valley flow. At pre-dawn in March, the canopy is isothermal, whereas it was expected that the top of the canopy would be cooler than the lower canopy. The wind direction at both heights is from the NE and the wind speed at both heights is less than 0.5 m/s, implying a cold air pool with a minimum depth of 56 m is moving slowly down-valley. Also in March at noon, two different air movement (stability conditions) were observed for different heights in the tree: apparent downward movement from the ground to 40 m and downward movement from 40 to 56 m. One possible explanation for these patterns is the influence of cloud presence.

The multi-directionality of flow at 56 m also may be due to the influence of the surrounding canopy cover on changing the wind direction. When wind encounters a forest canopy, its direction changes due to the multiple interactions of leaf structural variability, architecture, leaf angle and orientation, canopy volume, tree species, and also leaf morphology.

In general, the landscape shading was related to radiation and temperature but was not related to the moisture and wind in forest canopy. The reason is that landscape shading is a function of radiation and topographic position. In addition, temperature is a function of radiation and topographic position (illuminated vs. shaded facets).

In contrast, landscape shading is not a function of wind and moisture in the forest canopy. Therefore, variation in wind speed/direction and amount of moisture does not have any impact on landscape shading.

2.6. CONCLUSION

The predictions of vertical gradients in temperature in the forest canopy, based on the net radiation and sensible heat exchange, were compatible with the observation mostly at local noon on solstices and equinoxes, while they were mostly inconsistent with the data during pre-dawn and dusk. The simple net radiation budget underestimates the role of upward ground heat flux, canopy heat storage, and subsidence.

Landscape shading is mainly a function of Sun altitude and azimuth. Other important environmental factors are slope, aspect, landforms, and aboveground vegetation. Landscape shading affects the Discovery Tree diurnally and seasonally. The maximum influence of landscape shading on the Discovery Tree is when the tree is in high shade (0900h) whereas the minimum influence of the shading on the tree is when the tree is in low shade (1560h) throughout the year.

The boundary layer was mixed (convective) for at least three hours per night on spring and fall equinoxes and also on the summer solstice. In contrast, the boundary layer was inverted (stable condition) at 1200h and 1560h on Dec 21, 2016; 0900h, 1200h, and 1560h on March 21, 2017; 0900h and 1800h on June 21, 2017; and 0900h, 1200h, 1300h and 1560h on September 21, 2017. In general, inversions occurred more frequently within the forest canopy during the day than at night, whereas mixing (neutral boundary layer) was more frequent at night than during the daytime. It is hypothesized that the upward soil heat flux and the outgoing longwave radiation from the canopy during the night created turbulent kinetic energy through convective currents which results in mixing the air along the tree. In addition, intermittent gusts may create turbulence at the top of the canopy, mixing the boundary layer during night. Moreover, drainage flow and down-valley flow may create turbulent flow and mixing during the night.
Daytime inversions occur because the top of the canopy receives higher intensity radiation over a longer period of time than the lower part of the canopy. Thus, its temperature increases faster than the temperature of the lower canopy. This condition creates an inverted lapse rate resulting an inversion during the day.

Additional factors not explored in this study may influence the vertical gradient of temperature in The Discovery Tree. The presence of clouds may have a significant role in the nighttime canopy energy balance. In addition, the surrounding canopy cover may influence the Discovery Tree canopy.

BIBLIOGRAPHY

Amiro, B.D., 1990. Comparison of turbulence statistics within three boreal forest t canopies. Boundary-Layer Meteorology, 51(1-2), pp.99-121.

Baldocchi, D.D., and Meyers, T.P. 1988. Turbulence Structure in a Deciduous Forest. *Boundary-Layer Meteorology*, 43(4), pp: 345-364.

Barker, M.G. 1996. Vertical profiles in a brunei rain forest: Ii. Microclimate associated with a canopy tree. *Journal of Tropical Forest Science*, 8 (4): pp. 565–519.

Bierlmaier, F. A., and McKee, A. 1989. Climatic summaries and documentation for the primary meteorological station, H.J. Andrews Experimental Forest, 1972-1984. *Gen. Tech. Rep.* PNW-GTR-242. Portland, OR: U.S. Department of Agriculture, Forest Service, Pacific Northwest Research Station. 61 p.

Campbell, J., and Coxson, D.S. 2001. Canopy Microclimate and Arboreal Lichen Loading in Subalpine Spruce – Fir Forest. *Can. J. Bot,* 79, pp: 537–555. doi:10.1139/cjb-79-5-537.

de Araújo, A.C., Kruijt, B., Nobre, A.D., Dolman, A.J., Waterloo, M.J., Moors, E.J. and de Souza, J.S., 2008. Nocturnal accumulation of CO2 underneath a tropical forest canopy along a topographical gradient. *Ecological Applications*, *18*(6), pp.1406-1419.

Denmead, O.T. and Bradley, E.F., 1985. Flux-gradient relationships in a forest canopy. In *The forest-atmosphere interaction* (pp. 421-442). Springer, Dordrecht.

Dyer, A.J. 1967. The turbulent transport of heat and water vapor in an unsTable 2.1tmosphere. *Quarterly Journal of the Royal Meteorological Society,* 93 (398), pp: 561-568.

Franklin, J.F., and Dyrness, C.T. 1973. Natural Vegetation of Oregon and Washington. USDA Forest Service General Technical Report, Pacific Northwest Forest and Range Experiment Station, No. PNW-8.

Franklin, J.F., Cromack, K., Denison, W., McKee, A., Maser, C., Sedell, J., Swanson, F., Juday, G. 1981. Ecological Characteristics of Old-Growth Douglas-Fir Forests, General Technical Report, Pacific Northwest Forest and Range Experiment Station, PNW-118.

Gao, W. and Shaw, R.H., 1989. Observation of organized structure in turbulent flow within and above a forest canopy. In *Boundary Layer Studies and Applications* (pp. 349-377). Springer, Dordrecht.

Hardwick, S.R., Toumi, R., Pfeifer, M., Turner, E.C., Nilus, R. and Ewers, R.M., 2015. The relationship between leaf area index and microclimate in tropical forest and oil palm plantation: Forest disturbance drives changes in microclimate. *Agricultural and Forest Meteorology*, *201*, pp.187-195.

He, Siyan, Zhong, Y., Sun, Y., Su, Z., Jia, X., Hu, Y., Zhou, Q. 2017. He, S., Zhong, Y., Sun, Y., Su, Z., Jia, X., Hu, Y. and Zhou, Q., 2017. Topography-associated thermal gradient predicts warming effects on woody plant structural diversity in a subtropical forest. *Scientific reports*, *7*, p.40387.Topography-Associated Thermal Gradient Predicts Warming Effects on Woody Plant Structural Diversity in a Subtropical Forest. *Nature Publishing Group*, doi:10.1038/srep40387.

Jacovides, C., Papaioannou, G., and Kerkides, P. 1988. Micro and large-scale parameters evaluation of evaporation from a lake. *Agricultural Water Management*, 13(2-4), pp: 263-272.

Nakamura, A., Kitching, R.L., Cao, M., Creedy, T.J., Fayle, T.M., Freiberg, M., Hewitt, C.N., Itioka, T., Koh, L.P., Ma, K. and Malhi, Y., 2017. Forests and their canopies: achievements and horizons in canopy science. *Trends in ecology & evolution*, *32*(6), pp.438-451.

Novick, K.A., Oishi, A.C. and Miniat, C.F., 2016. Cold air drainage flows subsidize montane valley ecosystem productivity. *Global change biology*, *22*(12), pp.4014-4027.

Oke, T.R. 1987. Boundary Layer Climates, 2nd Ed. Routledge.

Russell, E.S., Liu, H., Gao, Z., Lamb, B. and Wagenbrenner, N., 2016. Turbulence dependence on winds and stability in a weak-wind canopy sublayer over complex terrain. *Journal of Geophysical Research: Atmospheres*, *121*(19).

Shaw, R.H., Den Hartog, G. and Neumann, H.H., 1988. Influence of foliar density and thermal stability on profiles of Reynolds stress and turbulence intensity in a deciduous forest. *Boundary-Layer Meteorology*, *45*(4), pp.391-409.

Small, E.S., Kurc, S.A., 2003. Tight coupling between soil moisture and the surface radiation budget in semiarid environments: Implications for land-atmosphere interactions. *Water Resources Research*, 39(10), pp. 1-14.

Swanson, F.J., and James, M.E. 1975. Geology and Geomorphology of the H.J. Andrews Experimental Forest, Western Cascades, Oregon. *Research Paper PNW-188*, USDA Forest Service.

Weisberg, P. J., and Swanson, F. 2003. Regional synchronicity in fire regimes of western Oregon and Washington, USA. *Forest Ecology and Management*, 172 (1), pp: 17-28.

Wharton, S., Ma, S., Baldocchi, D.D., Falk, M., Newman, J.F., Osuna, J.L. and Bible, K., 2017. Influence of regional nighttime atmospheric regimes on canopy turbulence and gradients at a closed and open forest in mountain-valley terrain. *Agricultural and forest meteorology*, 237, pp.18-29.

Xu, X., Yi, C., Montagnani, L. and Kutter, E., 2018. Numerical study of the interplay between thermo-topographic slope flow and synoptic flow on canopy transport processes. *Agricultural and Forest Meteorology*, *255*, pp.3-16.

Zhao, K., Zheng, M., Fahey, T.J., Jia, Z., Ma, L. 2018. Vertical Gradients and Seasonal Variations in the Stem CO2 efflux of *Larix principis-rupprechtii* Mayr. *Agricultural and Forest Meteorology,* 262, pp: 71–80. doi:10.1016/j.agrformet. 2018.07.003.

Table 2.1. Sun altitude at various times of day on solstices and equinoxes at Eugene, which is 70 km west of the Andrews Forest. Source: https://aa.usno.navy.mil/data/docs/AltAz.php (website)

Date	Time	Sun altitude (deg)
Summer solstice	0500h	-5.1
	1300h	69.2
	2000h	11.8
Fall equinox	0600h	-11.5
	1300h	46
	1800h	11.6
Spring equinox	0620h	10.3
	1200h	43.1
	1830h	9.4
Winter solstice	0700h	-7.8
	1200h	22.6
	1700h	-1.2

Table 2.2. Predicted conditions of daytime radiation, head, wind, humidity, and leaf wetness in the canopy at solstices and equinoxes.

	Winter solstice	Spring equinox	Summer solstice	Fall equinox
Incoming shortwave radiation (W/m^2)	low	moderate	high	moderate
Incoming longwave radiation (W/m^2)	high	moderate	low	moderate
net radiation	small positive	moderate positive	large positive	moderate positive
Average temperature (°C)	low	moderate	high	moderate
Wind speed at 1.5m (m/s)	Low	Low	Low	Low
Wind speed at 50m (m/s)	high	moderate	high	moderate
Dominant wind direction at 1.5m (degrees)	Down-valley	Down-valley	Down-valley	Down-valley
Dominant wind direction at 50m (degrees)	Down-valley	Down-valley	Down-valley	Down-valley
Relative humidity (%)	high	moderate	low	moderate
Leaf wetness	high	moderate	low	moderate

Table 2.3. Predicted conditions within the canopy at various times of day.

	pre-dawn	local noon	local dusk
Air temperature deficit at 50 m vs. 1.5 m	Canopy top is cooler than 1.5 m height	Canopy top is warmer than 1.5 m height	Canopy top is cooler than 1.5 m height
Air movement at 50 m vs. 1.5 m	Vertical flux (upward); no horizontal flux	Vertical flux (downward); no horizontal flux	Vertical flux (upward); no horizontal flux
Relative humidity at 50 m vs. 1.5 m	RH is higher at 50 m compared to 1.5 m	RH is lower at 50 m compared to 1.5 m	RH is lower at 50 m compared to 1.5 m
Leaf wetness	LW is higher at 50 m compared to 1.5 m	LW is lower at 50 m compared to 1.5m	LW is lower at 50 m compared to 1.5 m

Table 2.4. Instruments deployed at the Discovery Tree, Nov 2016-present.

Instrument	Property	Description	Sensor specifications	Shield specification	Heights (m)	Dates
HOBO pendant	Air temperature	HOBO pendant (UA-001-64) temperature data logger	waterproof, one-channel logger with 10-bit resolution, range of 0 to 50 °C and accuracy +- 0.53 °C	20 cm long, 3.5 (4) inch diameter, schedule 40 PVC pipe split in half lengthwise, sensor suspended beneath	1.5, 10, 20, 30, 40, 56	11/14/16-present
Campbell Scientific 107 thermistor	Air temperature	Fan-aspirated model 107 probe	range of -40 to 60°C and accuracy of ±0.1 °C	41303-5A, 41303-5B, or RAD06 6-plate radiation shield OR fan-aspirated radiation shields (Thomas and Smoot)	10, 20, 30, 40	11/14/16-present
Rotronic HC2S3-L	Air temperature and relative humidity (RH)	HC2S3-L temperature and RH probe	capacitive sensor to measure RH and a 100 Ohm PRT to measure temperature over the range -40 degrees C to +60 degrees C with accuracy +- 0.1º C	fan-aspirated radiation shield built according to specifications in Thomas and Smoot (date) ??	1.5, 56	11/14/16-present (56 m), 11/14/16 - 5/24/17 (1.5 m)

Rotronic EE181	Air temperature and relative humidity (RH)	EE181 Temperature and RH probe	A 1000 Ohm PRT to measure air temperature over the range -40 degrees C to +60 degrees C with accuracy +-0.2ºC	41003-5, 41003-5A, or RAD 10 10-plate naturally aspirated radiation shield	1.5	6/28/17-present

Table 2.5. Average values of radiation (W/m^2 at Primet, 6 m) and air temperature, winds, and moisture in the Discovery Tree canopy by height (at 1.5, 30, and 50 m), during two-week periods surrounding the equinoxes and solstices of 2016 and 2017.

	Dec 14-30, 2016				Mar 14-30, 2017				Jun 14-30, 2017				Sep 14-30, 2017			
	1.5	30	50	6	1.5	30	50	6	1.5	30	50	6	1.5	30	50	6
Incoming shortwave				21				89				269				116
Outgoing shortwave				11				12				43				15
Incoming longwave				305				342				364				351
Outgoing longwave				308				357				418				381
Net radiation (W/m^2)				7				62				172				71
Air temperature (°C)	-1	-1	0		6	6	7		18	19	19		11	11	12	
Wind speed (m/s)	0.2		0.5		0.2		0.6		0.3		0.9		0.2		0.6	
% of time winds from NW	35		12		27		21		34		11		22		14	
% of time winds from NE	46		66		44		44		50		48		61		55	
Relative humidity (%)	99		98		99		96		72		65		--		84	
Leaf wetness (mV)	423	455	397		437	476	393		292	273	283		383	322	349	

Table 2.6. Average values of radiation (Wm^{-2} at Primet) and air temperature, wind, air moisture in the Discovery Tree canopy at pre-dusk (P) (0000h to 0600h), local noon (N) (1000-1400h), and local dusk (D) (1700-2100h) on days of equinoxes and solstices of 2016 and 2017.

	Dec 21, 2016			Mar 21, 2017			Jun 21, 2017			Sep 21, 2017		
	P	N	D	P	N	D	P	N	D	P	N	D
Incoming shortwave	-2	122	-2	-1	502	8	6	966	12	0	222	12
Outgoing shortwave	1	40	0	0	72	2	2	156	2	1	20	2
Incoming longwave	302	304	292	347	345	344	342	377	338	346	373	356
Outgoing longwave	298	304	297	350	406	365	369	493	400	349	385	362
Net radiation	1	81	-7	-4	370	-15	-22	693	-51	-5	190	3
Air temperature (°C)												
1.5 m	-1	-1	-1	7	9	9	12	23	19	6	9	9
30 m	-1	-1	0	7	10	9	12	24	19	6	9	9
50 m	-1	0	-1	7	10	9	12	23	20	6	10	9
Wind speed (m/s)												
1.5 m	0.2	0.2	0.2	0.2	0.2	0.2	0.2	0.6	0.2	0.2	0.1	0.2
50 m	0.4	0.4	0.6	0.5	0.5	0.7	0.5	1.7	0.6	0.2	0.3	0.9
% of time winds from NW												
1.5 m	68	0	53	8	13	19	4	88	47	40	88	29
50 m	0	0	0	0	6	31	0	0	24	36	18	0
% of time winds from NE												
1.5 m	32	12	47	79	19	31	88	12	24	52	6	71
50 m	72	76	94	88	6	25	100	0	65	28	18	94
Relative humidity (%)												
1.5 m	99	99	99	99	99	99	--	--	--	--	--	--
50 m	99	99	99	99	89	97	94	44	51	99	89	98
Leaf wetness (mV)												
1.5 m	301	301	312	368	403	387	266	262	262	515	501	493
30 m	294	453	300	493	443	461	265	262	261	410	371	369
50 m	289	384	280	383	307	376	330	262	261	397	271	399

Table 2.7. Percent of the Andrews Forest landscape near the Discovery Tree that is illuminated and in deep shade based on terrain shading algorithm, for 9 AM, noon, and 3 PM on the equinoxes (Mar 21, Sep 21) and solstices (June 21, Dec 21)

				Number of pixels				% of area		
Day	Local time	Solar azimuth (degrees)	Sun altitude (degrees)	High shade	Moderate shade	Low shade	Total	High shade	Moderate shade	Low shade
Winter solstice	900	137	9.7	176	59	19	254	69	23	7
	1200	177	22.5	86	89	79	254	34	35	31
	1500	219	12	112	78	64	254	44	31	25
Spring equinox	900	108	18.2	108	71	75	254	43	28	30
	1200	152	43	68	186	101	355	19	52	28
	1500	214	41	70	91	93	254	28	36	37
Summer solstice	900	35	90	84	97	74	255	33	38	29
	1200	137	64	59	76	119	254	23	30	47
	1500	235	60	66	66	123	255	26	26	48
Fall equinox	900	111	20	104	74	76	254	41	29	30
	1200	57	44	66	84	104	254	26	33	41
	1500	218	39	63	95	96	254	25	37	38

Figure 2.1. Location of the Discovery Tree in the Andrews Forest.

Figure 2.2. Arrangement of sensors on the Discovery Tree.

Figure 2.3. The conceptual model of radiation balance in an old-growth conifer tree (a) pre-dawn (no incoming solar radiation); (b) local noon (maximum sun angle); (c) local dusk (sun falling below the horizon)

Figure 2.4. The conceptual model of energy balance in an old-growth conifer tree (a) pre-dawn (no incoming solar radiation); (b) local noon (maximum sun angle); (c) local dusk (sun falling

Figure 2.5. Elements of the energy balance at Primet and the Discovery Tree, December 14-30, 2016. (a) incoming and outgoing shortwave radiation at Primet (6 m), (b) incoming and outgoing longwave radiation at Primet (6 m), (c) air temperature at 1.5, 30, and 50 m on the Discovery Tree, (d) wind speed at 1.5 m, (e) wind speed at 50 m, (f) wind direction at 1.5 m, (g) wind direction at 50 m, (h) relative humidity at 0, 30 and 50 m, (h) leaf wetness at 0, 30, and 50 m.

Figure 2.6. Elements of the energy balance at Primet and the Discovery Tree, December 21, 2016. (a) incoming and outgoing shortwave radiation at Primet (6 m), (b) incoming and outgoing longwave radiation at Primet (6 m), (c) air temperature at 1.5, 30, and 50 m on the Discovery Tree, (d) wind speed at 1.5 and 50 m, (e) wind direction at 1.5 and 50 m, (f) relative humidity at 0, 30 and 50 m, (g) leaf wetness at 0, 30, and 50 m.

Figure 2.7. Air temperature by height and time of day on the Discovery Tree on (a) afternoon and evening of December 20 and pre-dawn on December 21, 2016 (b) pre-dawn through local noon and dusk on December 21, 2016.

Figure 2.8. Elements of the energy balance at Primet and the Discovery Tree, March 14-30, 2017. (a) incoming and outgoing shortwave radiation at Primet (6 m), (b) incoming and outgoing longwave radiation at Primet (6 m), (c) air temperature at 1.5, 30, and 50 m on the Discovery Tree, (d) wind speed at 1.5 m, (e) wind speed at 50 m, (f) wind direction at 1.5 m, (g) wind direction at 50 m, (h) relative humidity at 0, 30 and 50 m, (i) leaf wetness at 0, 30, and 50 m.

Figure 2.9. Elements of the energy balance at Primet and the Discovery Tree, March 21, 2017. (a) incoming and outgoing shortwave radiation at Primet (6 m), (b) incoming and outgoing longwave radiation at Primet (6 m), (c) air temperature at 1.5, 30, and 50 m on the Discovery Tree, (d) wind speed at 1.5 and 50 m, (e) wind direction at 1.5 and 50 m, (f) relative humidity at 0, 30 and 50 m, (g) leaf wetness at 0, 30, and 50 m.

Figure 2.10. Air temperature by height and time of day on the Discovery Tree on (a) afternoon and evening of March 20 and pre-dawn on March 21, 2017 (b) pre-dawn through local noon and dusk on March 21, 2017.

Figure 2.11. Elements of the energy balance at Primet and the Discovery Tree, June 14-30, 2017. (a) incoming and outgoing shortwave radiation at Primet (6 m), (b) incoming and outgoing longwave radiation at Primet (6 m), (c) air temperature at 1.5, 30, and 50 m on the Discovery Tree, (d) wind speed at 1.5 m, (e) wind speed at 50 m, (f) wind direction at 1.5 m, (g) wind direction at 50 m, (h) relative humidity at 0, 30 and 50 m, (h) leaf wetness at 0, 30, and 50 m.

Figure 2.12. Elements of the energy balance at Primet and the Discovery Tree, June 21, 2017. (a) incoming and outgoing shortwave radiation at Primet (6 m), (b) incoming and outgoing longwave radiation at Primet (6 m), (c) air temperature at 1.5, 30, and 50 m on the Discovery Tree, (d) wind speed at 1.5 and 50 m, (e) wind direction at 1.5 and 50 m, (f) relative humidity at 0, 30 and 50 m, (g) leaf wetness at 0, 30, and 50 m.

Figure 2.13. Air temperature by height and time of day on the Discovery Tree on (a) afternoon and evening of June 20 and pre-dawn on June 21, 2017 (b) pre-dawn through local noon and dusk on June 21, 2017.

Figure 2.14. Elements of the energy balance at Primet and the Discovery Tree, September 14-30, 2017. (a) incoming and outgoing shortwave radiation at Primet (6 m), (b) incoming and outgoing longwave radiation at Primet (6 m), (c) air temperature at 1.5, 30, and 50 m on the Discovery Tree, (d) wind speed at 1.5 m, (e) wind speed at 50 m, (f) wind direction at 1.5 m, (g) wind direction at 50 m, (h) relative humidity at 0, 30 and 50 m, (h) leaf wetness at 0, 30, and 50 m.

Figure 2.15. Elements of the energy balance at Primet and the Discovery Tree, September 21, 2017. (a) incoming and outgoing shortwave radiation at Primet (6 m), (b) incoming and outgoing longwave radiation at Primet (6 m), (c) air temperature at 1.5, 30, and 50 m on the Discovery Tree, (d) wind speed at 1.5 and 50 m, (e) wind direction at 1.5 and 50 m, (f) relative humidity at 0, 30 and 50 m, (g) leaf wetness at 0, 30, and 50 m.

Figure 2.16. Air temperature by height and time of day on the Discovery Tree on (a) afternoon and evening of September 20 and pre-dawn on September 21, 2017 (b) pre-dawn through local noon and dusk on September 21, 2017.

Figure 2.17. Proportion of the landscape surrounding the Discovery Tree that is in high, moderate and low shade at 0900h, 1200h, and 1500h on (a, b, c) the winter solstice, (d, e, f) the spring equinox, (g, h, i) the summer solstice, and (j, k, l) the fall equinox.

Figure 2.18. Relationship of percent of landscape shaded to (a) radiation, (b) air temperature, (c) wind speed, (d) percent of time wind direction is from the NE, (e) relative humidity, and (f) leaf wetness for one-day periods on solstices and equinoxes (21 December, 2016; 21 March, 2017; 21 June, 2017; 21 September, 2017) at three heights in the Discovery Tree.

Figure 2.19. Relationship of percent of landscape shaded to (a) radiation, (b) air temperature, (c) wind speed, (d) percent of time wind direction is from the NE, (e) relative humidity, and (f) leaf wetness for two-week periods surrounding solstices and equinoxes (December 14-30, 2016; March 14-30, 2017; June 14-30, 2017; September 14-30, 2017) at three heights in the Discovery Tree.

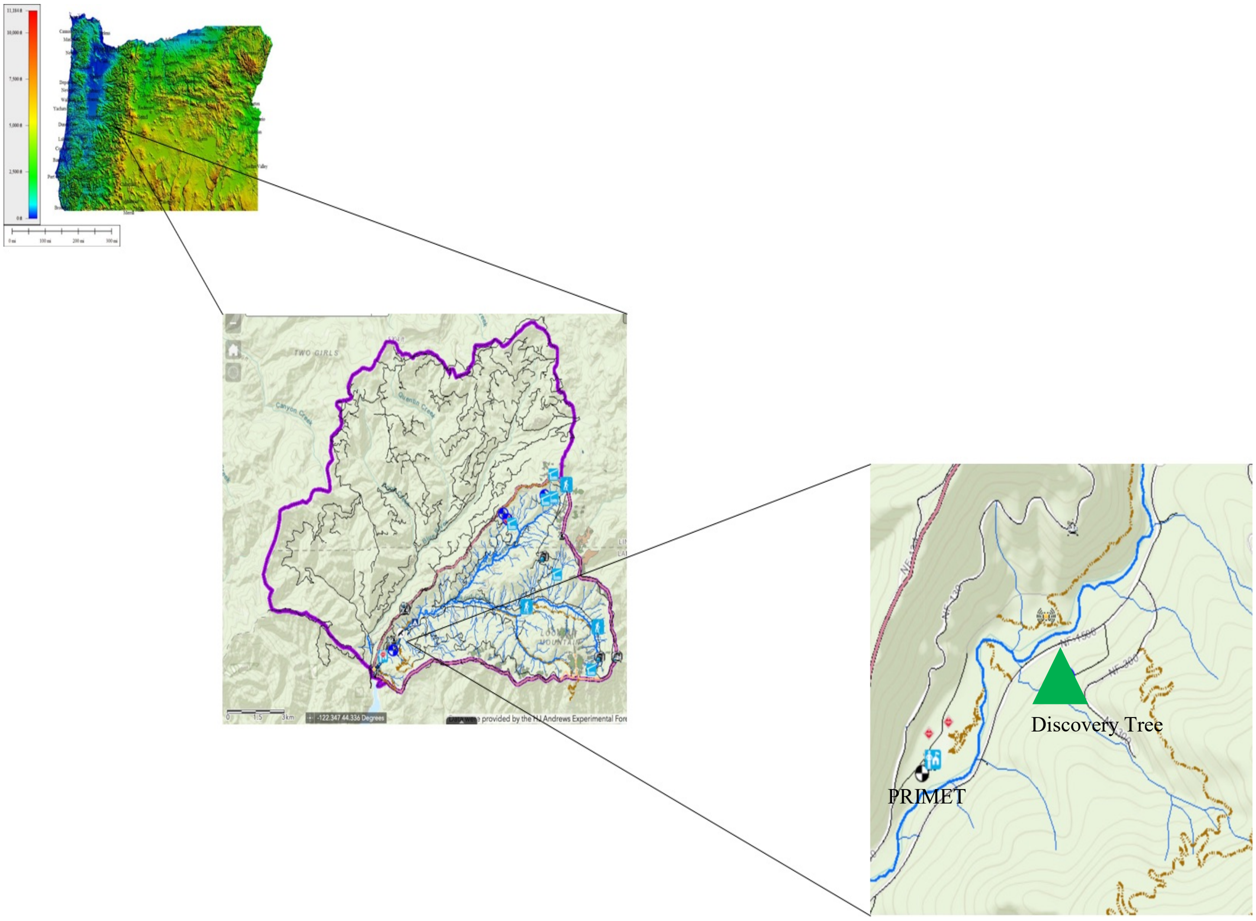

Figure 2.1

Figure 2.2

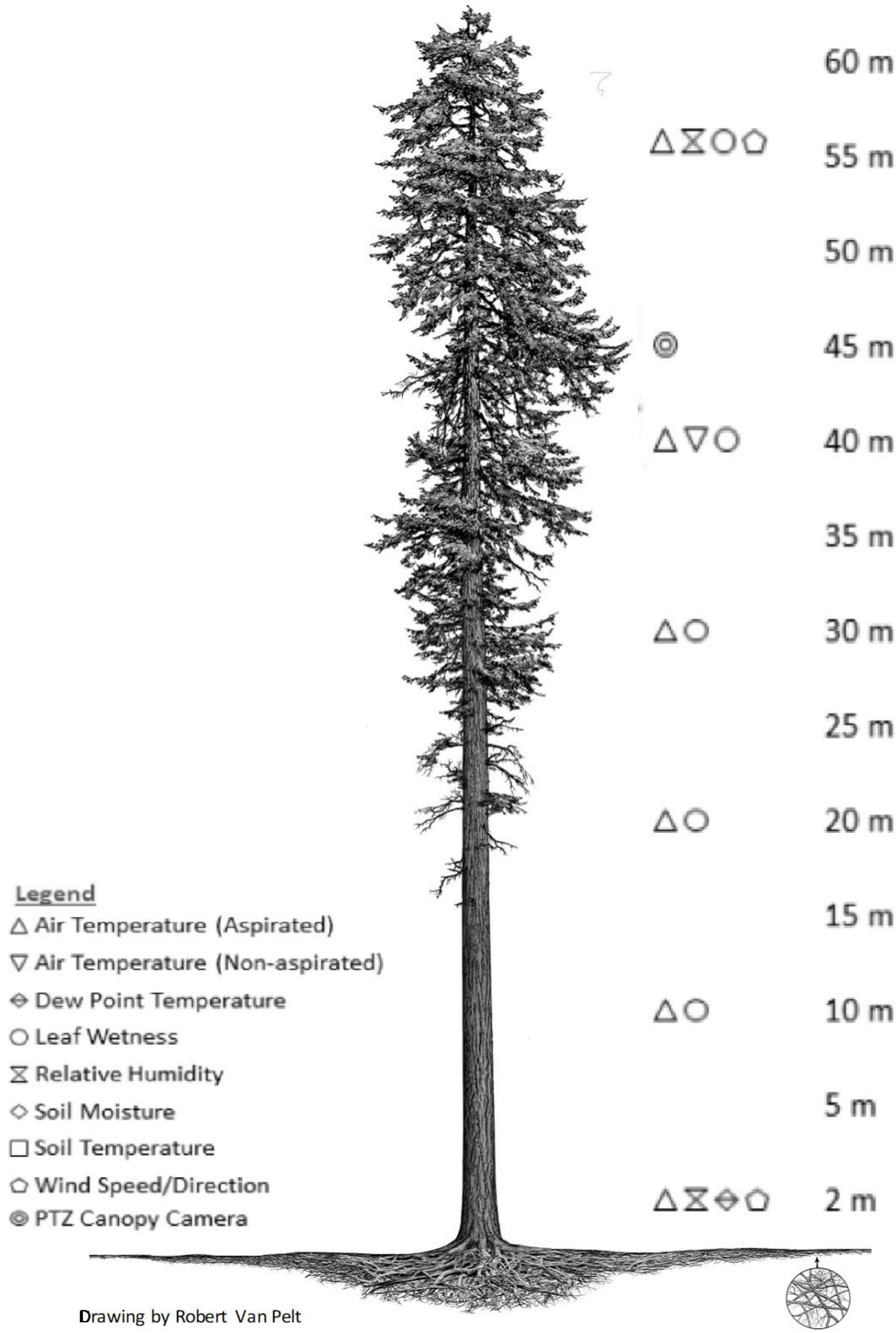
60 m
△⧖○⬠ 55 m
50 m
◎ 45 m
△▽○ 40 m
35 m
△○ 30 m
25 m
△○ 20 m
15 m
△○ 10 m
5 m
△⧖⬖⬠ 2 m
Legend
△ Air Temperature (Aspirated)
▽ Air Temperature (Non-aspirated)
⬖ Dew Point Temperature
○ Leaf Wetness
⧖ Relative Humidity
◇ Soil Moisture
□ Soil Temperature
⬠ Wind Speed/Direction
◎ PTZ Canopy Camera
Drawing by Robert Van Pelt

Figure 2.3
(a)

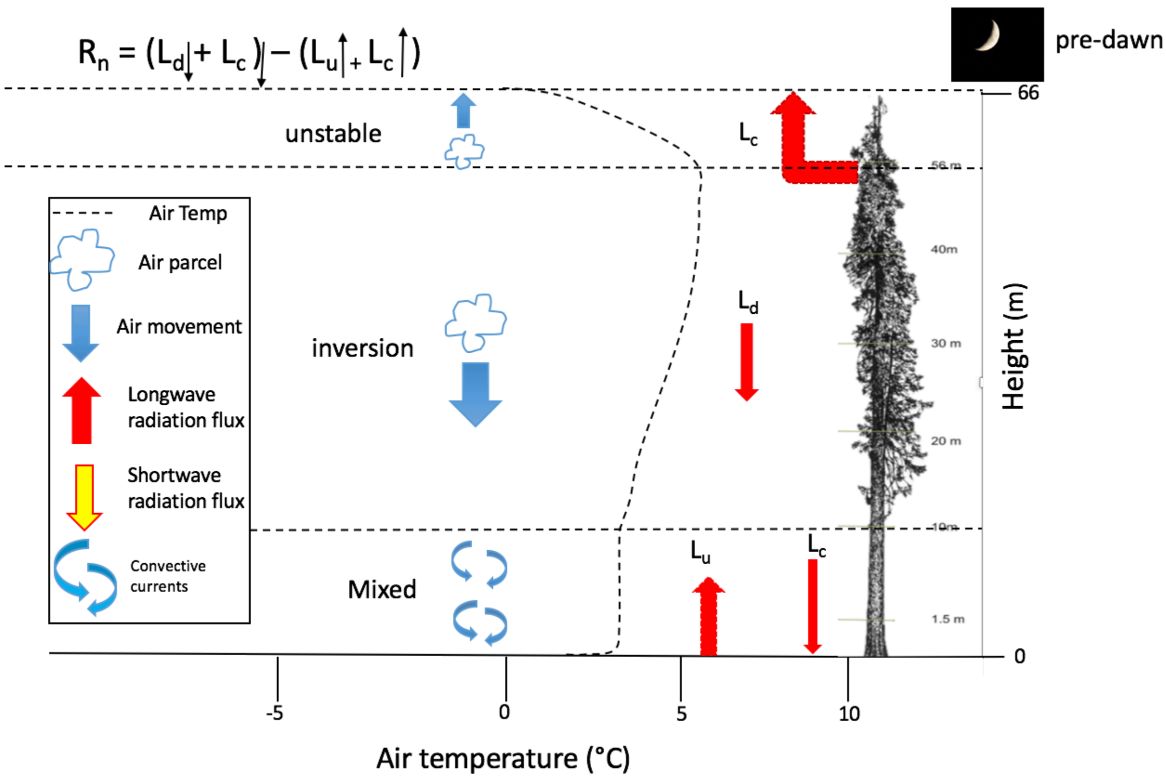

$R_n = (L_d\downarrow + L_c\downarrow) - (L_u\uparrow + L_c\uparrow)$
pre-dawn
unstable
inversion
Mixed
Air Temp
Air parcel
Air movement
Longwave radiation flux
Shortwave radiation flux
Convective currents
L_c
L_d
L_u
L_c
66
56 m
40m
30 m
20 m
10m
1.5 m
0
Height (m)
-5
0
5
10
Air temperature (°C)

Figure 2.3, cont'd.
(b)

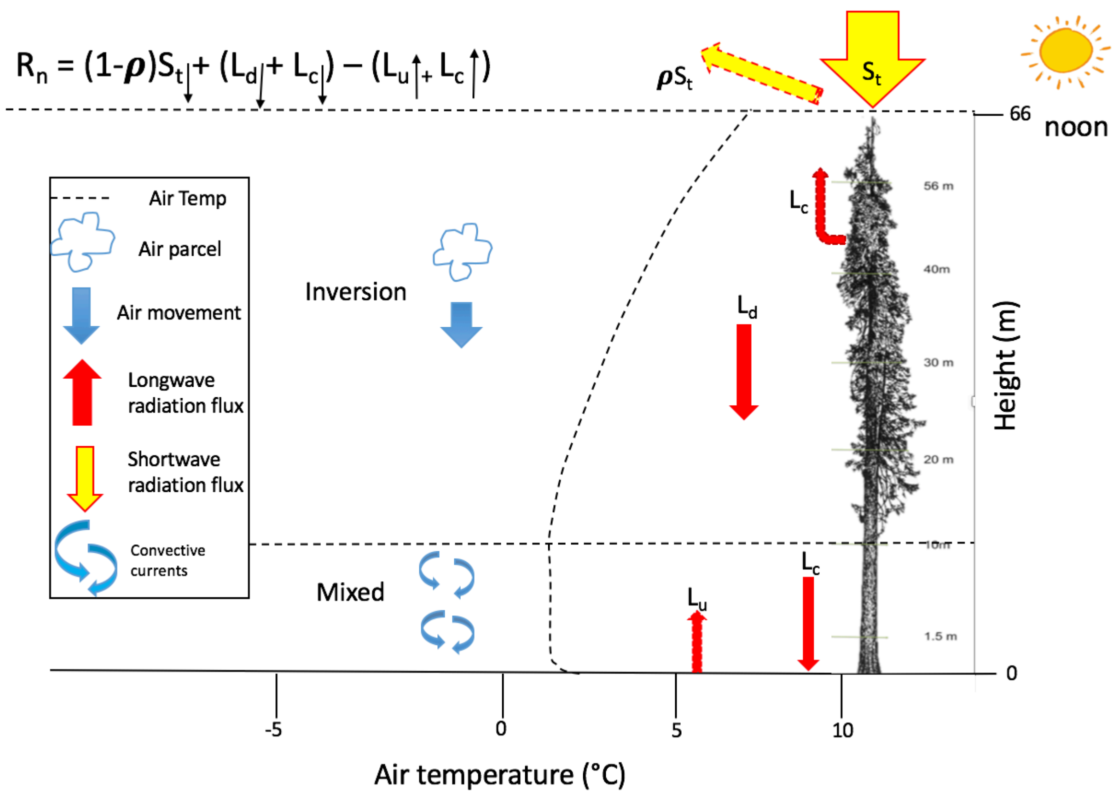

Figure 2.3, cont'd.
(c)

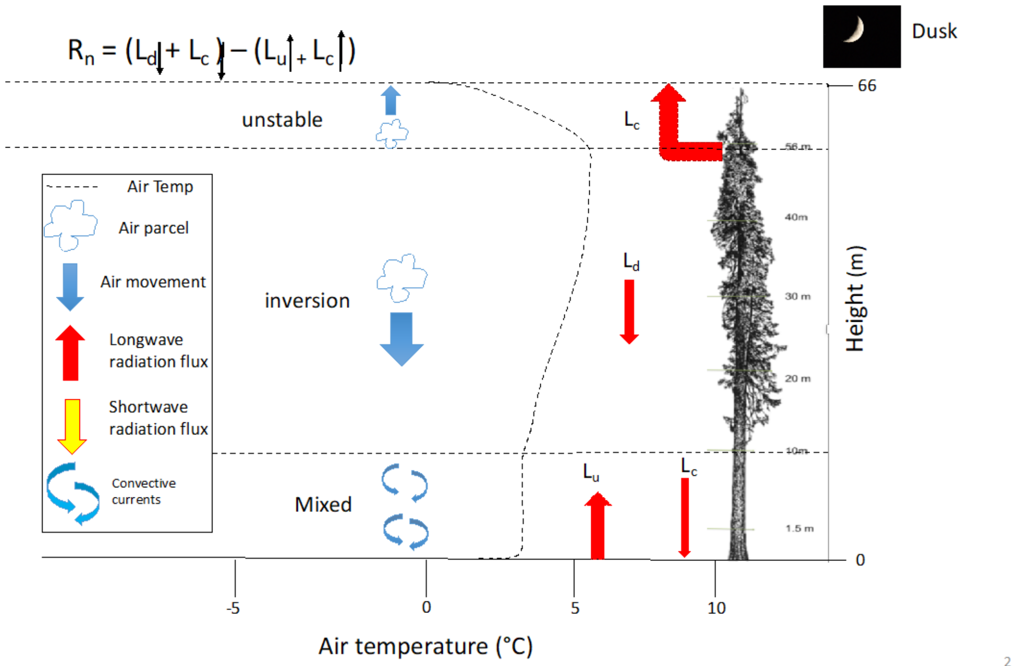

Figure 2.4
(a)

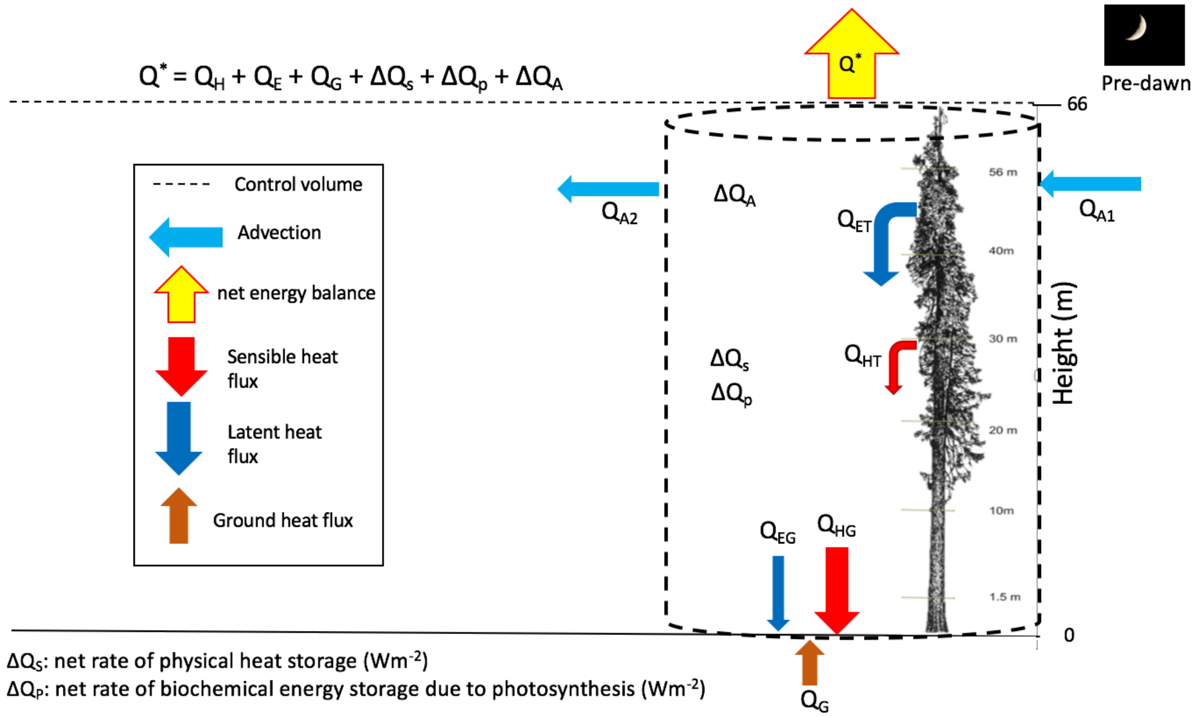

$Q^* = Q_H + Q_E + Q_G + \Delta Q_s + \Delta Q_p + \Delta Q_A$
Q^*
Pre-dawn
66
0
Height (m)
56 m
40m
30 m
20 m
10m
1.5 m
Control volume
Advection
net energy balance
Sensible heat flux
Latent heat flux
Ground heat flux
Q_{A2}
Q_{A1}
ΔQ_A
Q_{ET}
ΔQ_s
ΔQ_p
Q_{HT}
Q_{EG}
Q_{HG}
Q_G
ΔQ_S: net rate of physical heat storage (Wm^{-2})
ΔQ_P: net rate of biochemical energy storage due to photosynthesis (Wm^{-2})

Figure 2.4, cont'd.
(b)

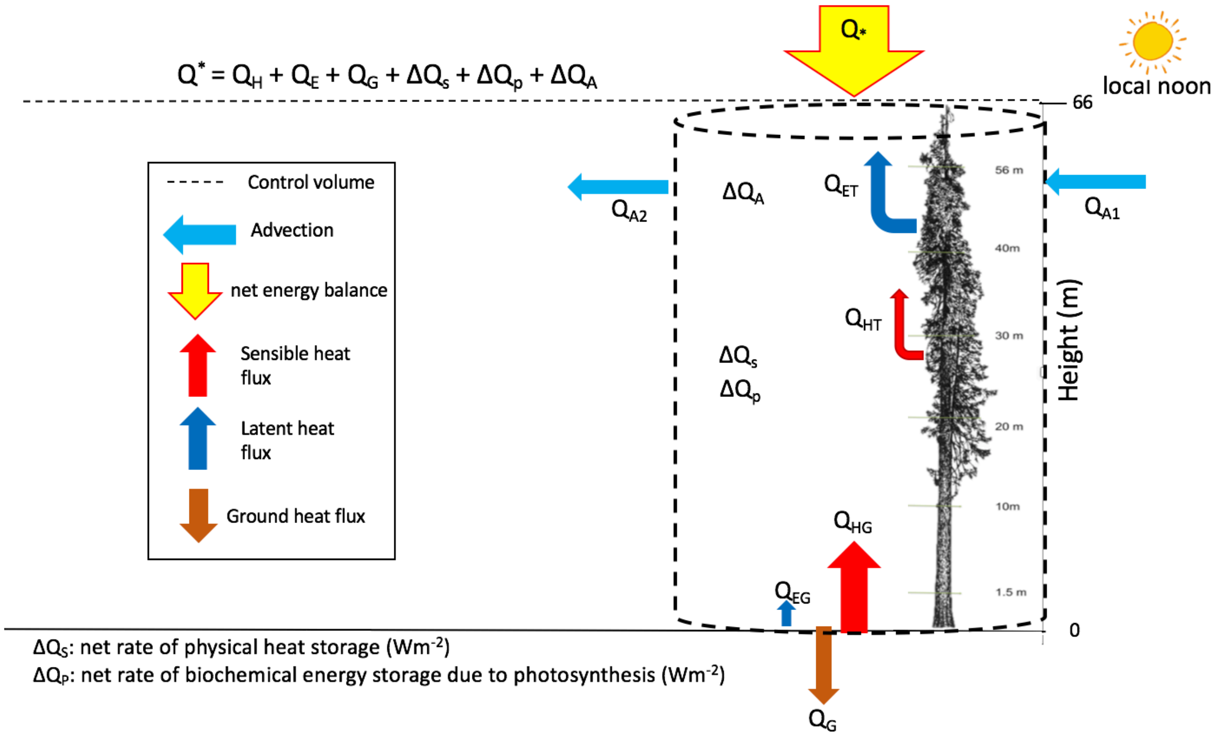

Figure 2.4, cont'd.
(c)

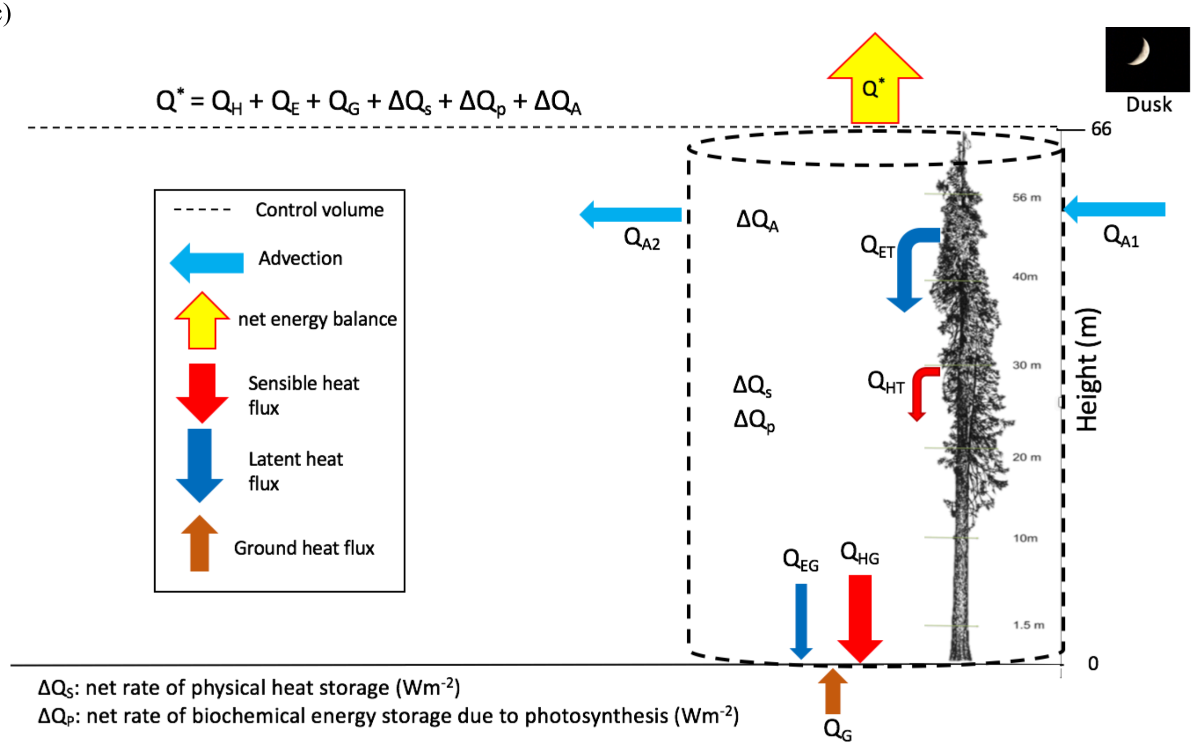

Figure 2.5

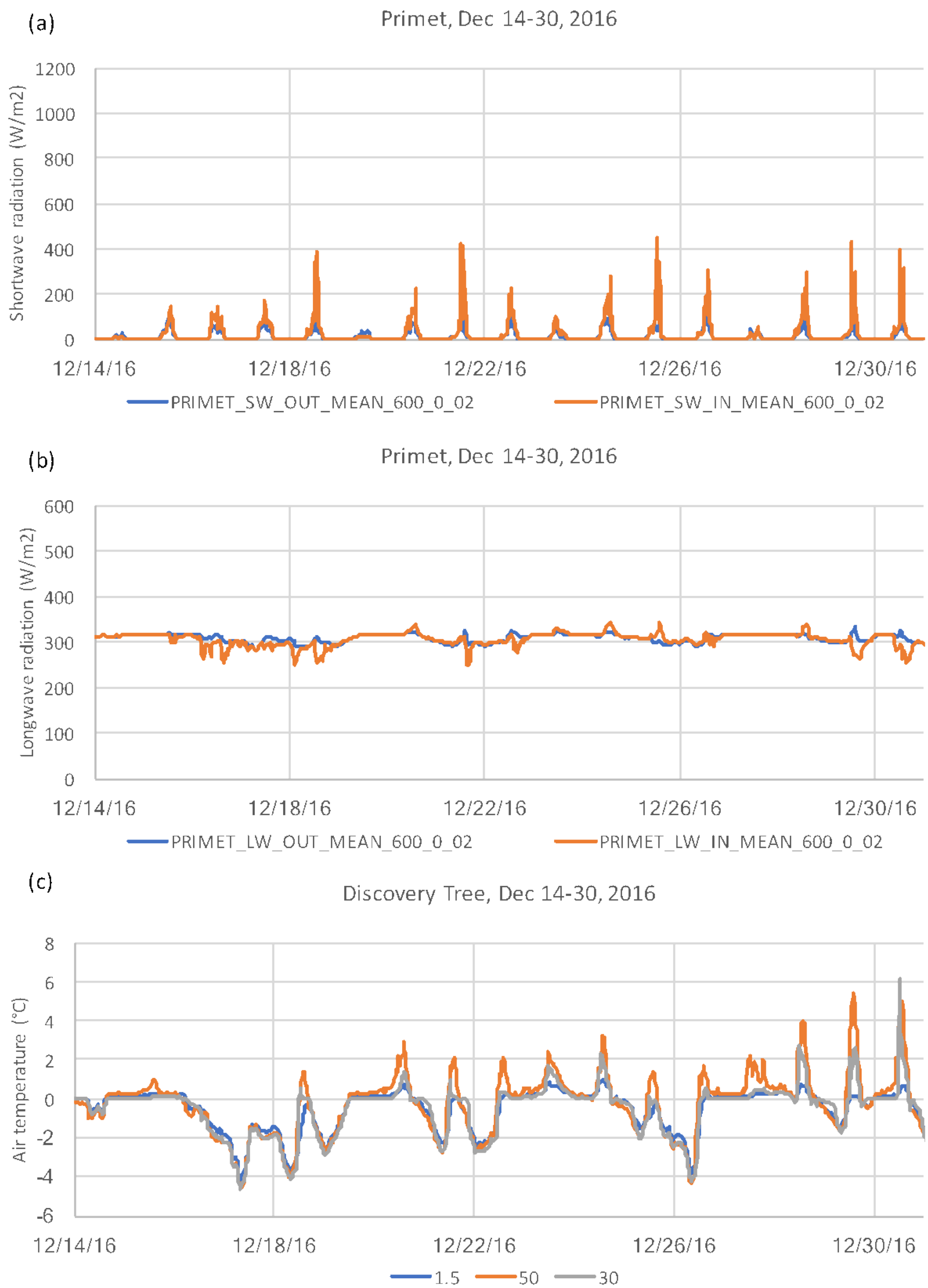
(a)
Primet, Dec 14-30, 2016
Shortwave radiation (W/m2)
0
200
400
600
800
1000
1200
12/14/16
12/18/16
12/22/16
12/26/16
12/30/16
PRIMET_SW_OUT_MEAN_600_0_02
PRIMET_SW_IN_MEAN_600_0_02
(b)
Primet, Dec 14-30, 2016
Longwave radiation (W/m2)
0
100
200
300
400
500
600
12/14/16
12/18/16
12/22/16
12/26/16
12/30/16
PRIMET_LW_OUT_MEAN_600_0_02
PRIMET_LW_IN_MEAN_600_0_02
(c)
Discovery Tree, Dec 14-30, 2016
Air temperature (°C)
-6
-4
-2
0
2
4
6
8
12/14/16
12/18/16
12/22/16
12/26/16
12/30/16
1.5
50
30

Figure 2.5, Cont'd.

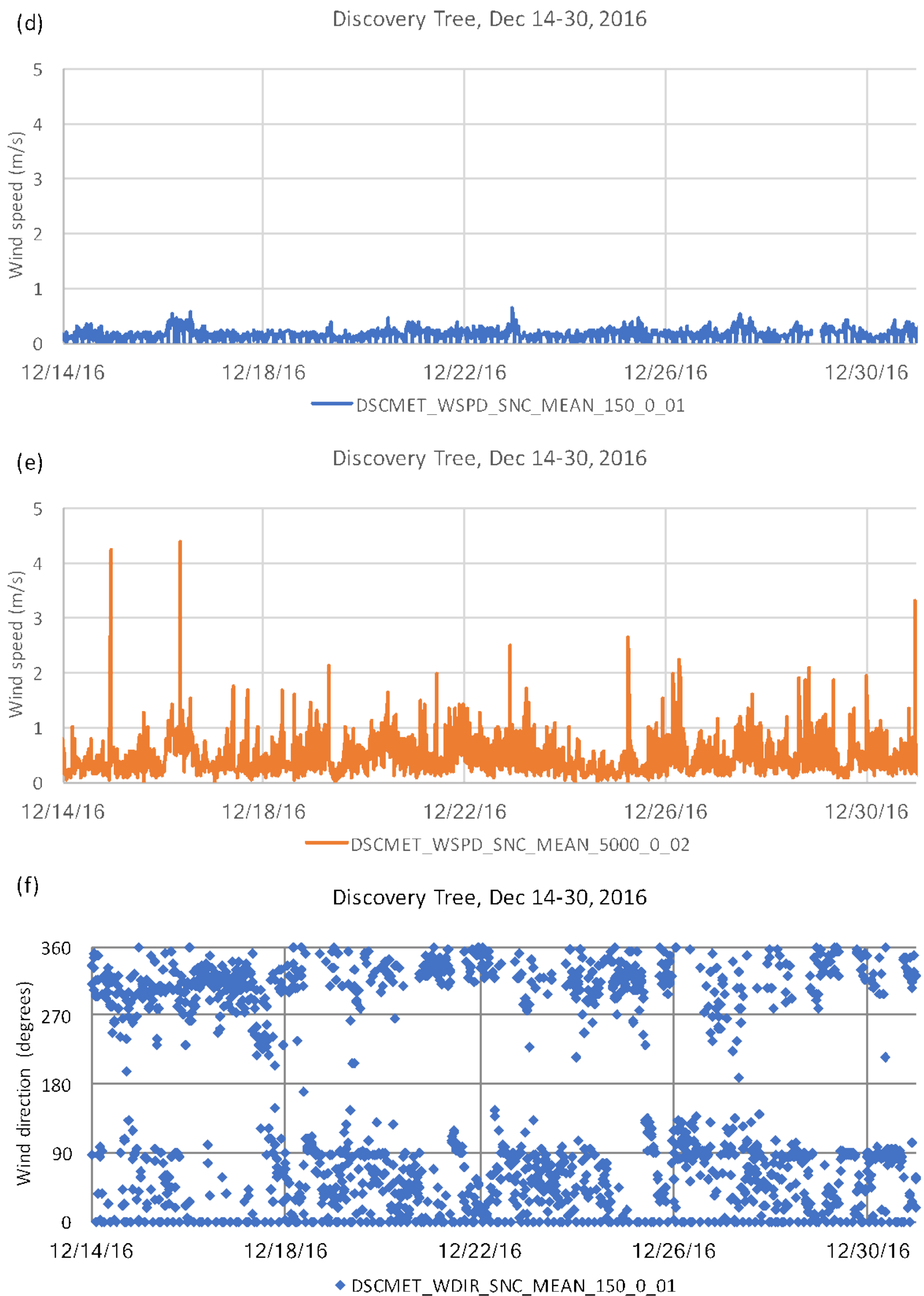

Figure 2.5, cont'd.

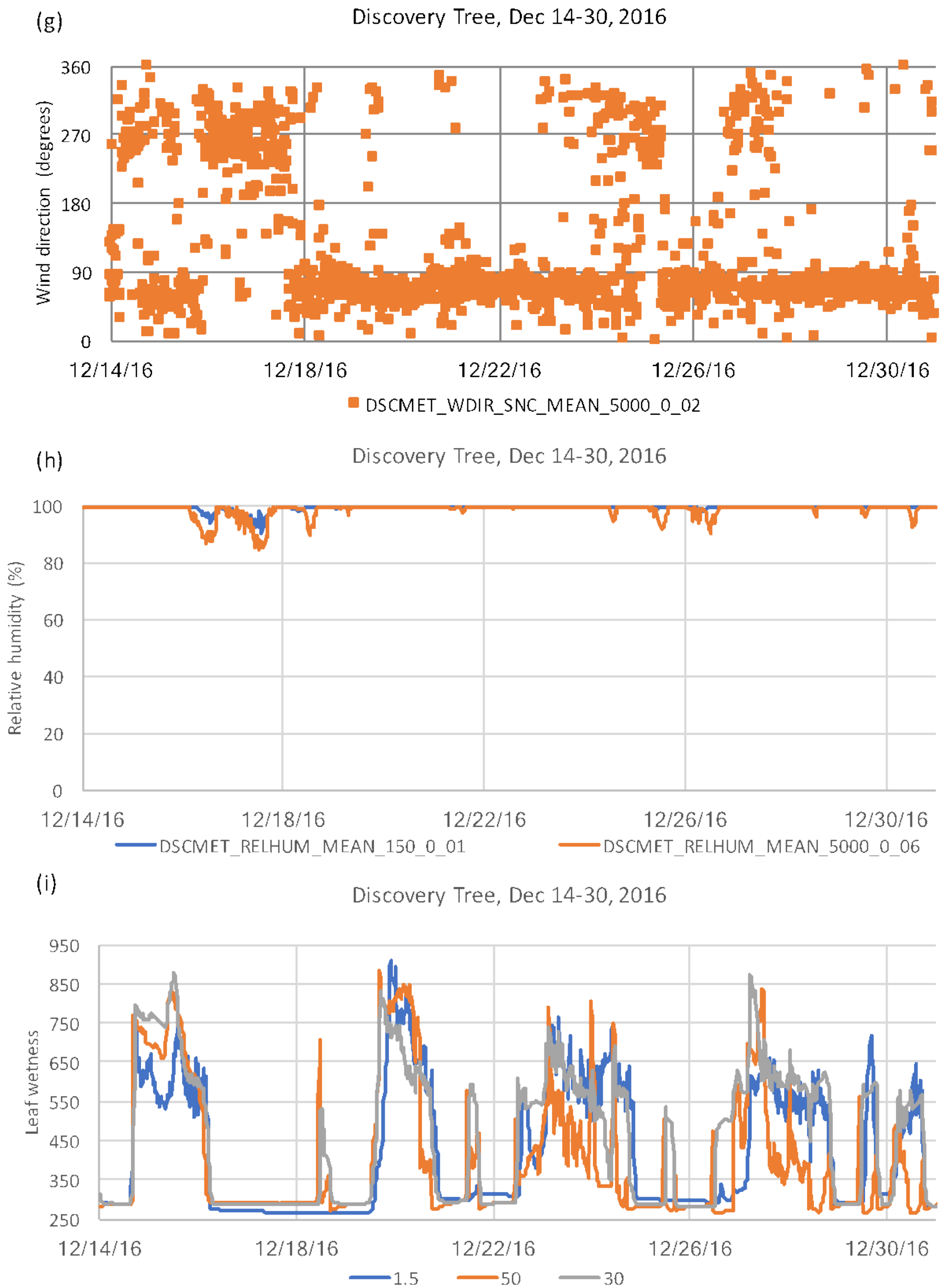

Figure 2.6

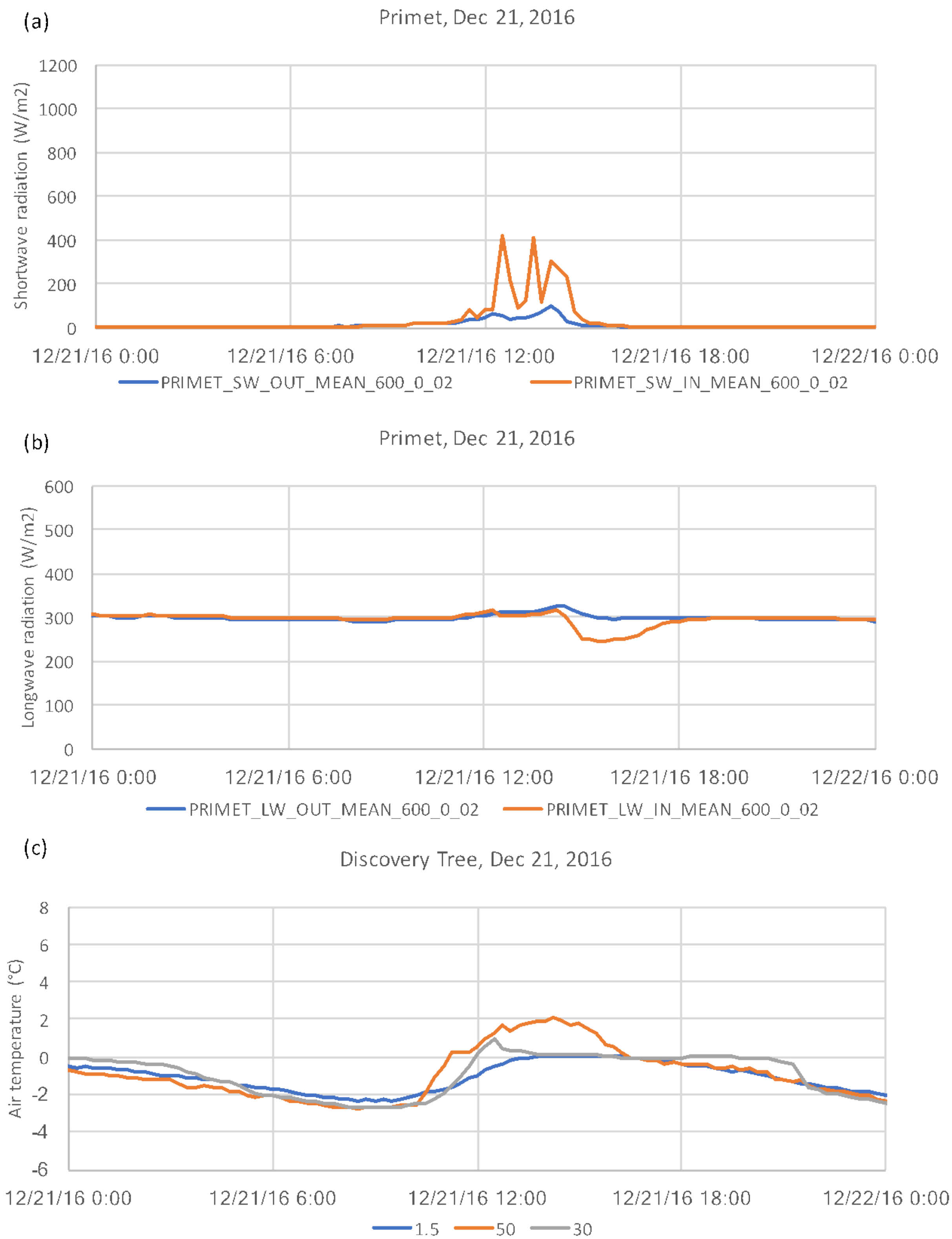

(a)
Primet, Dec 21, 2016
Shortwave radiation (W/m2)
1200
1000
800
600
400
200
0
12/21/16 0:00
12/21/16 6:00
12/21/16 12:00
12/21/16 18:00
12/22/16 0:00
PRIMET_SW_OUT_MEAN_600_0_02
PRIMET_SW_IN_MEAN_600_0_02
(b)
Primet, Dec 21, 2016
Longwave radiation (W/m2)
600
500
400
300
200
100
0
12/21/16 0:00
12/21/16 6:00
12/21/16 12:00
12/21/16 18:00
12/22/16 0:00
PRIMET_LW_OUT_MEAN_600_0_02
PRIMET_LW_IN_MEAN_600_0_02
(c)
Discovery Tree, Dec 21, 2016
Air temperature (°C)
8
6
4
2
0
-2
-4
-6
12/21/16 0:00
12/21/16 6:00
12/21/16 12:00
12/21/16 18:00
12/22/16 0:00
1.5
50
30

Figure 2.6, cont'd.

(d)

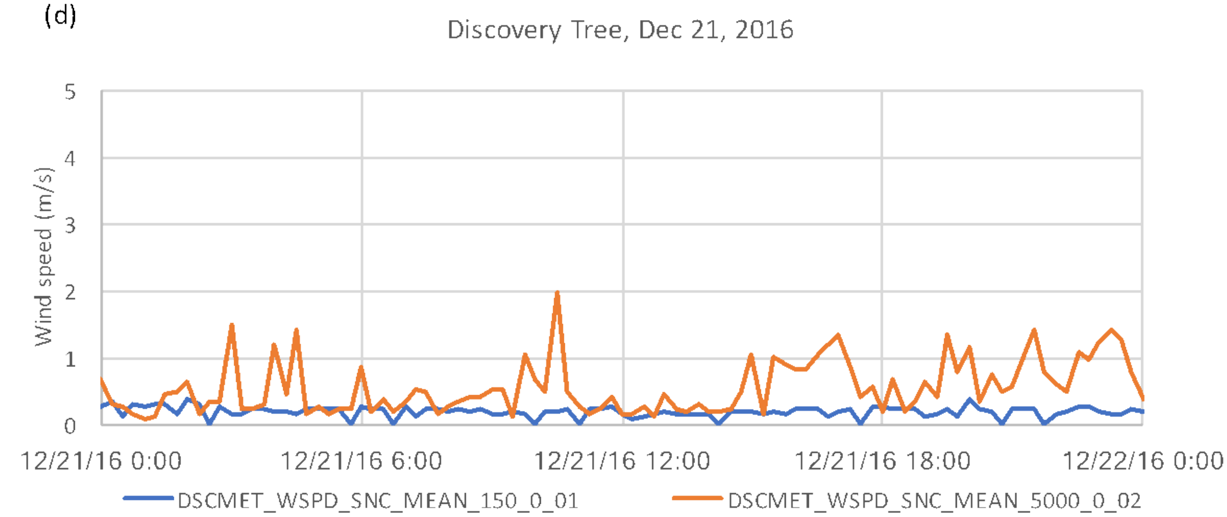

(e)

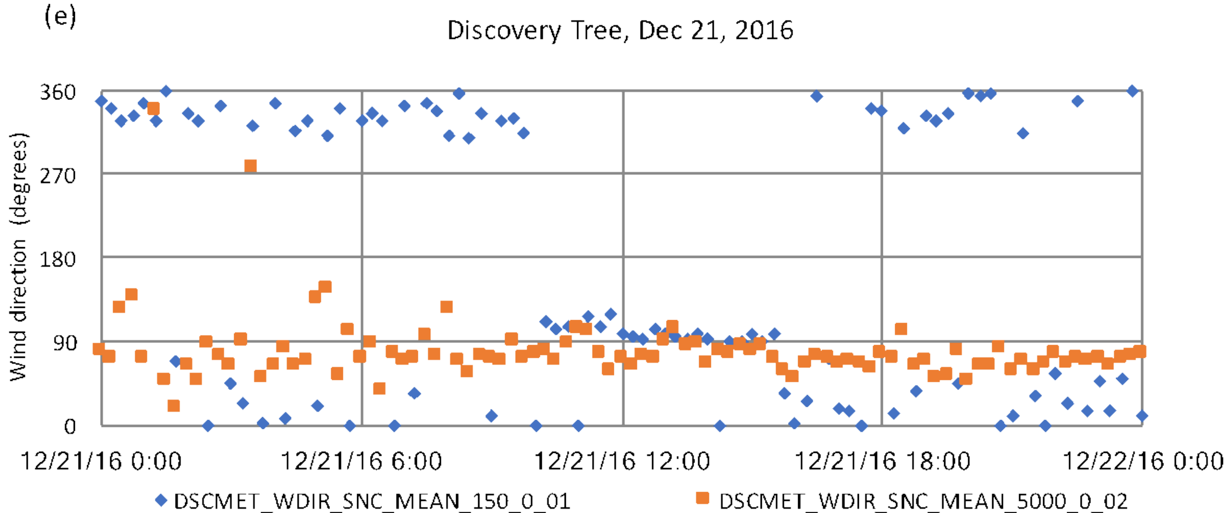

Figure 2.6, cont'd.

(f)

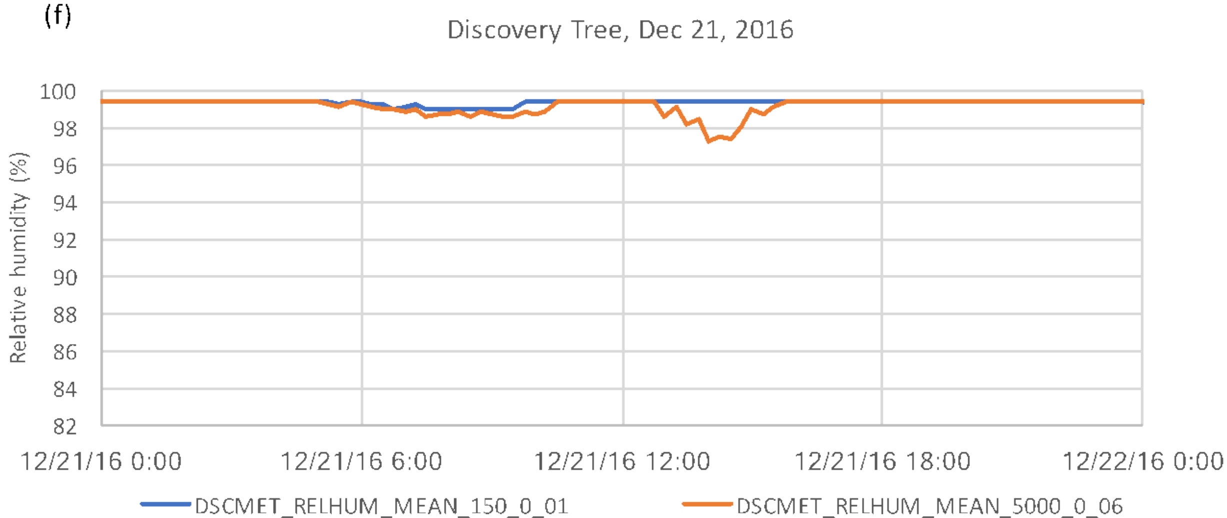

(g)

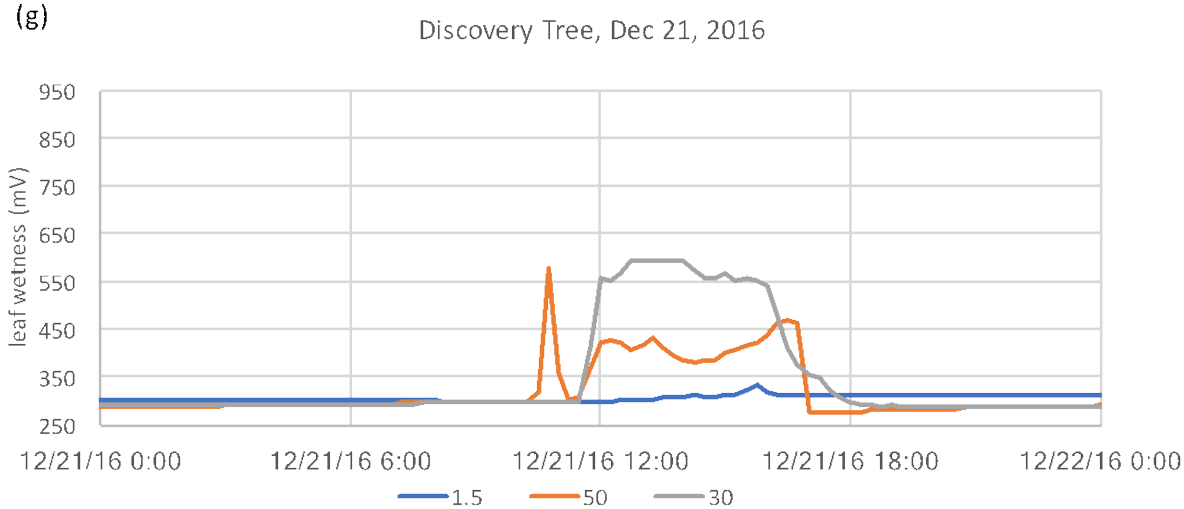

Figure 2.7

(a)

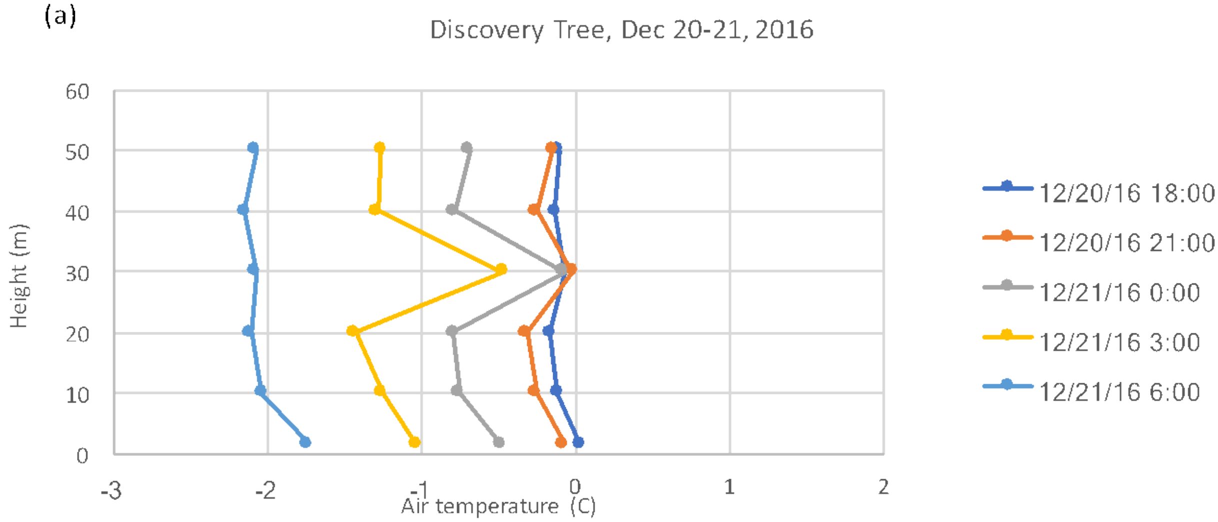
Discovery Tree, Dec 20-21, 2016
Height (m)
Air temperature (C)
12/20/16 18:00
12/20/16 21:00
12/21/16 0:00
12/21/16 3:00
12/21/16 6:00

(b)

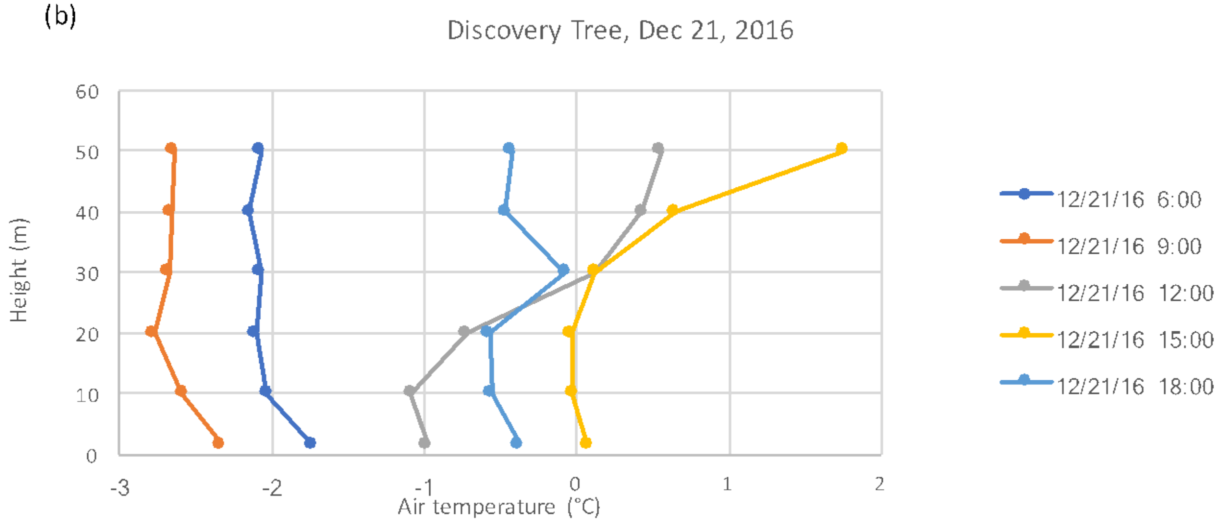
Discovery Tree, Dec 21, 2016
Height (m)
Air temperature (°C)
12/21/16 6:00
12/21/16 9:00
12/21/16 12:00
12/21/16 15:00
12/21/16 18:00

Figure 2.8

(a)

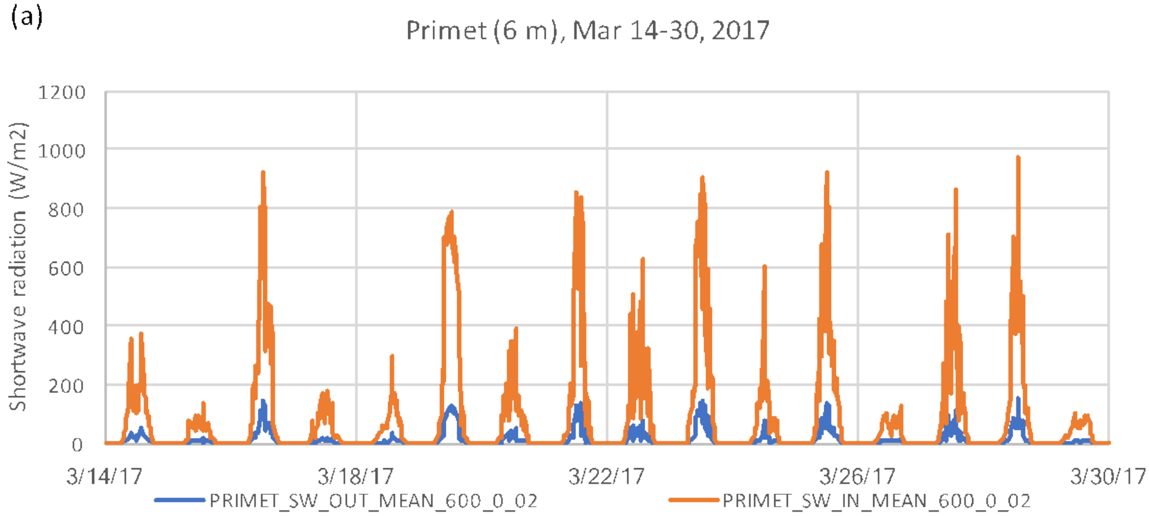

(b)

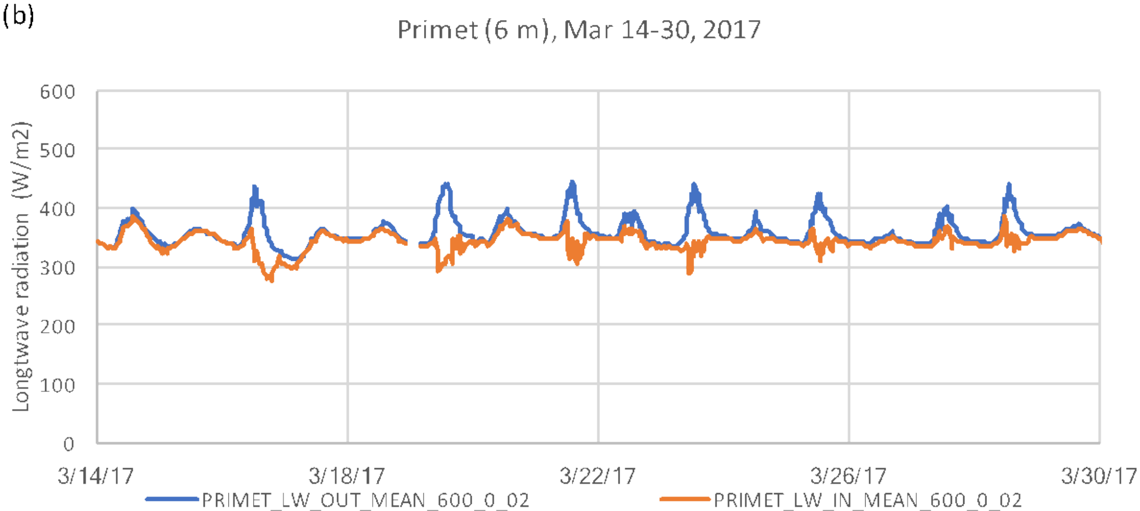

(c)

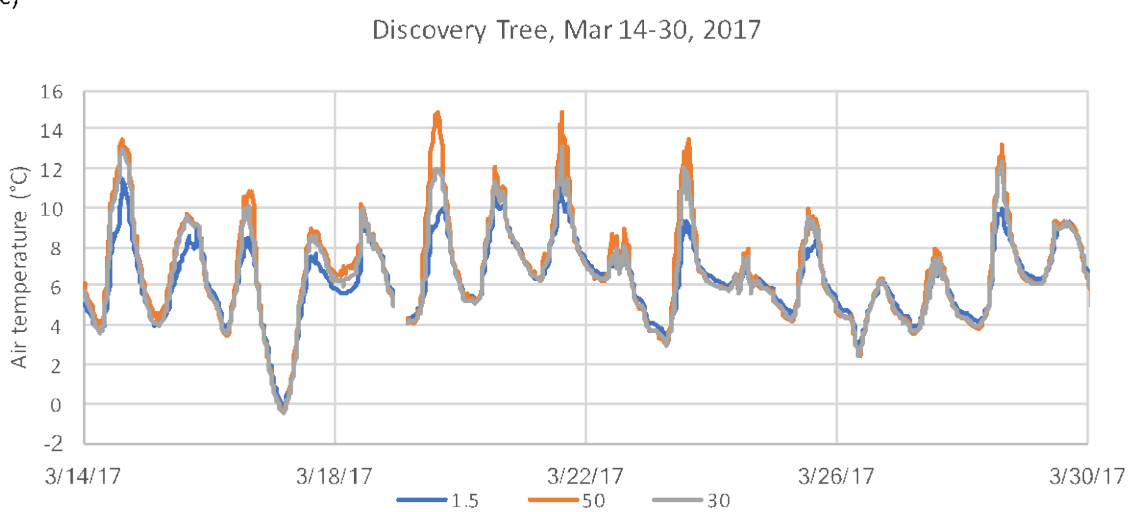

Figure 2.8, cont'd.

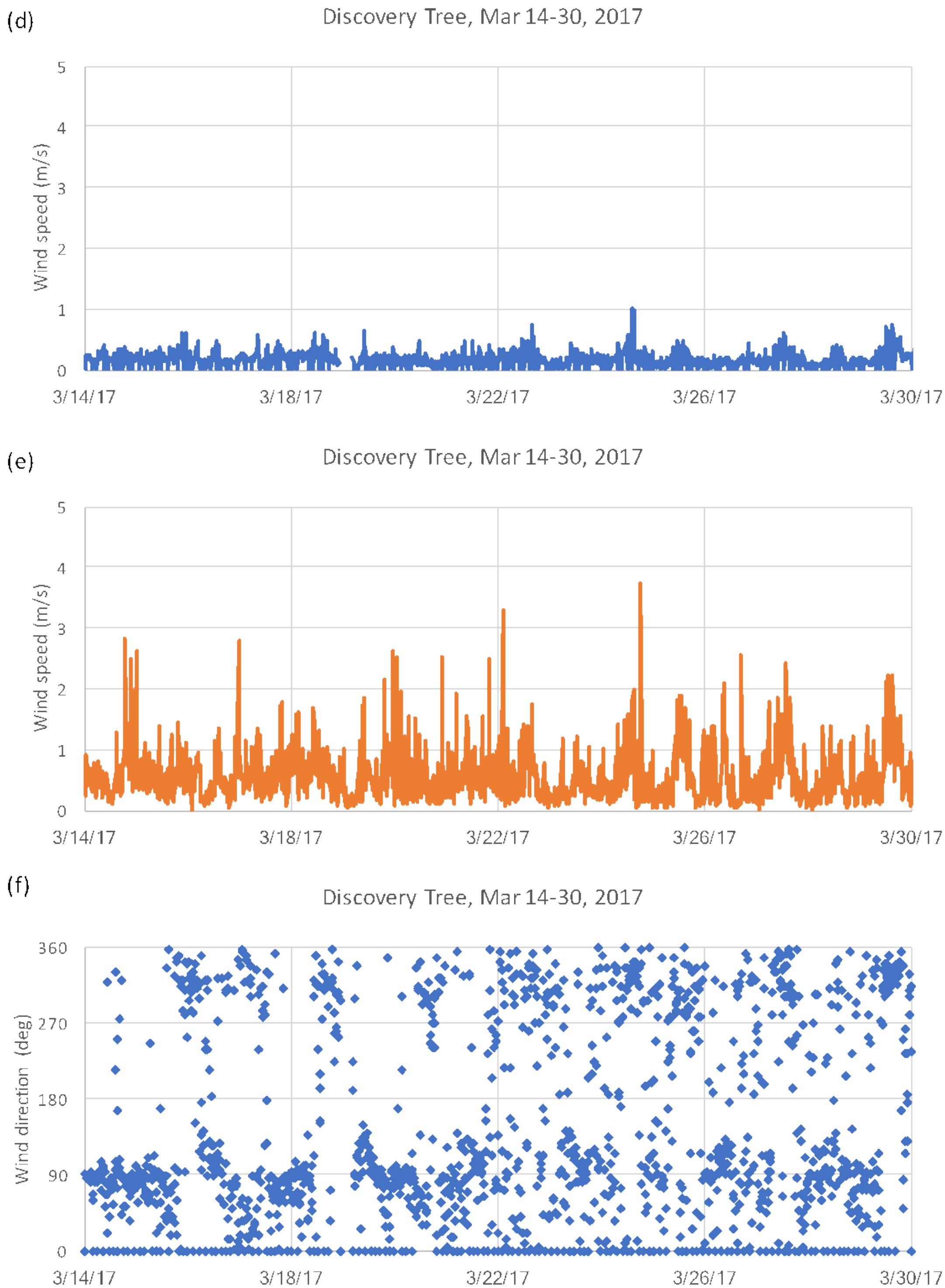

Figure 2.8, Cont'd.

(g)

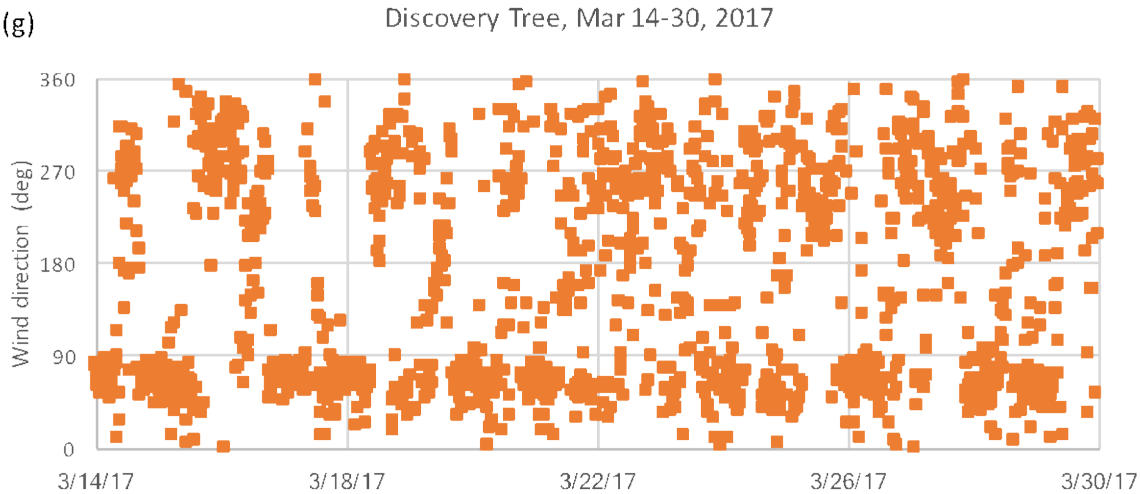

(h)

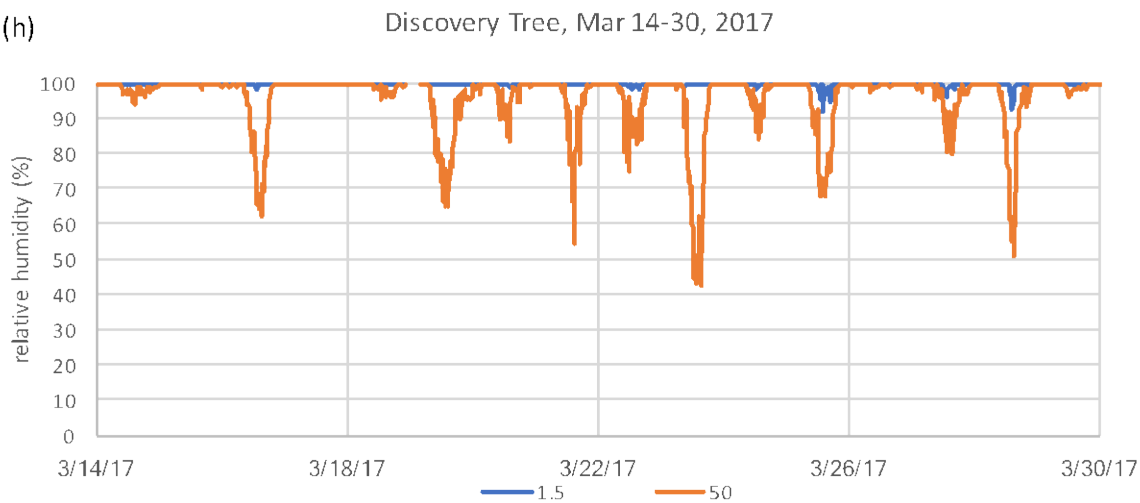

(i)

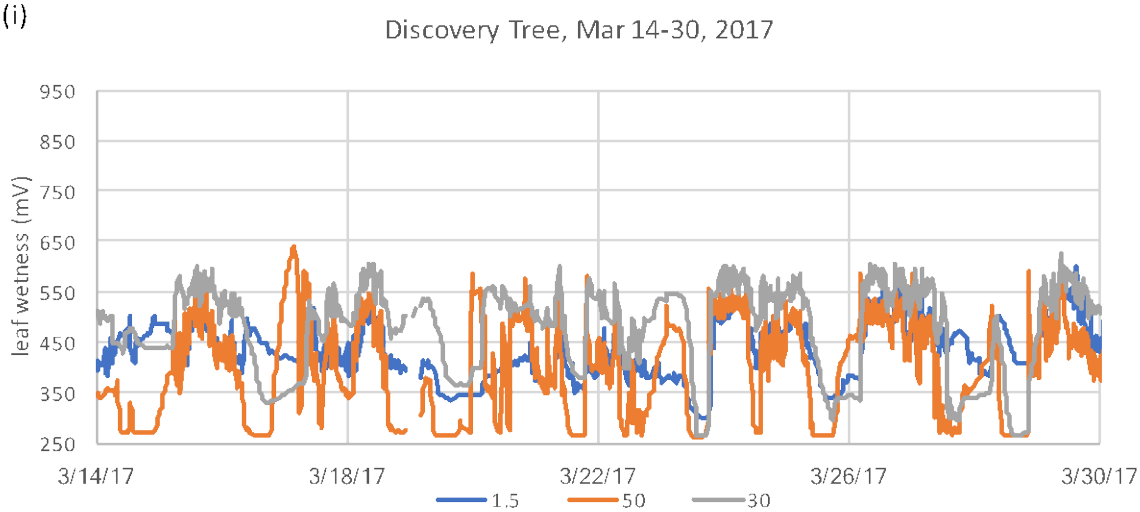

Figure 2.9

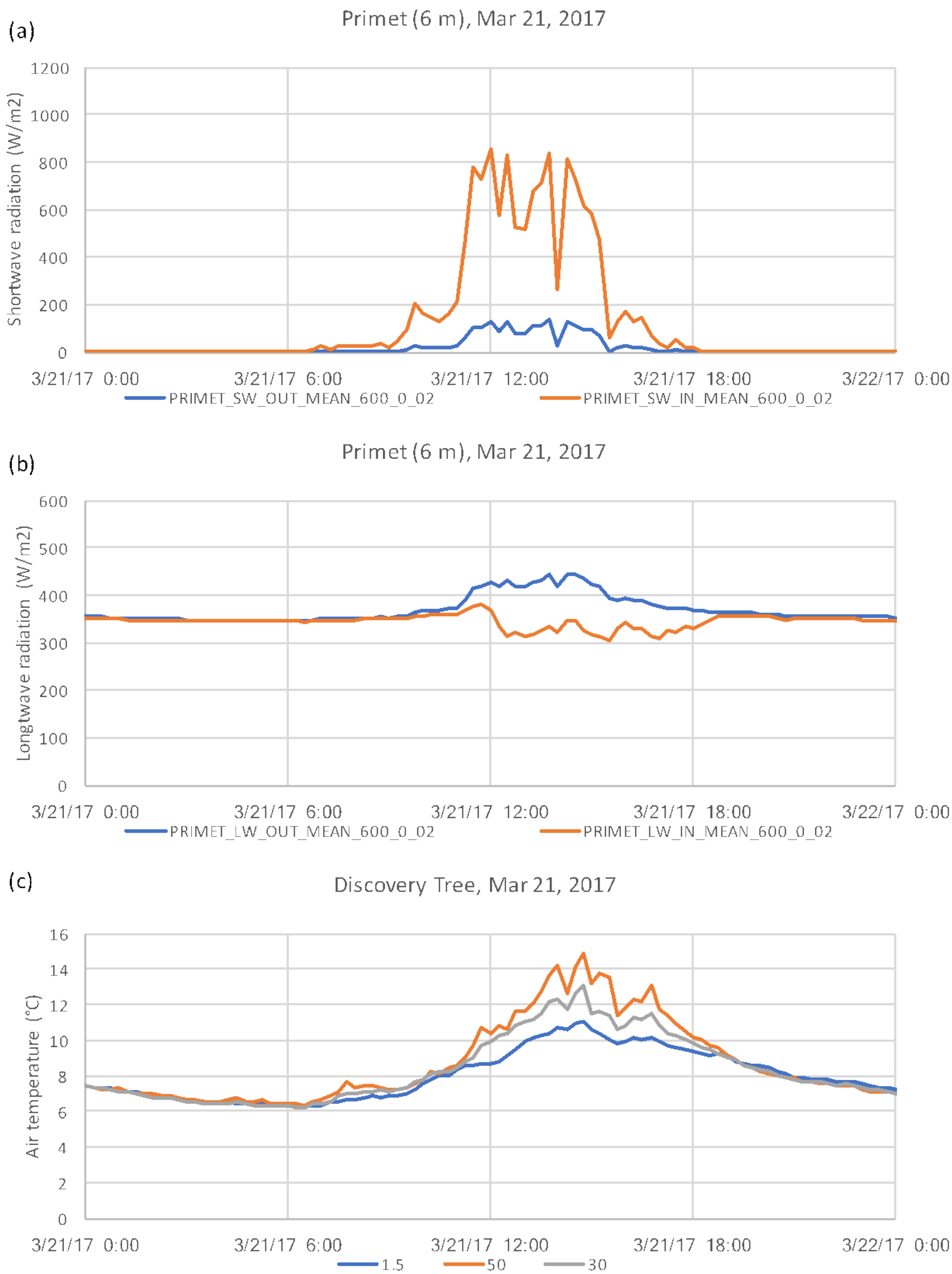
(a)
Primet (6 m), Mar 21, 2017
Shortwave radiation (W/m2)
1200
1000
800
600
400
200
0
3/21/17 0:00
3/21/17 6:00
3/21/17 12:00
3/21/17 18:00
3/22/17 0:00
PRIMET_SW_OUT_MEAN_600_0_02
PRIMET_SW_IN_MEAN_600_0_02
(b)
Primet (6 m), Mar 21, 2017
Longtwave radiation (W/m2)
600
500
400
300
200
100
0
3/21/17 0:00
3/21/17 6:00
3/21/17 12:00
3/21/17 18:00
3/22/17 0:00
PRIMET_LW_OUT_MEAN_600_0_02
PRIMET_LW_IN_MEAN_600_0_02
(c)
Discovery Tree, Mar 21, 2017
Air temperature (°C)
16
14
12
10
8
6
4
2
0
3/21/17 0:00
3/21/17 6:00
3/21/17 12:00
3/21/17 18:00
3/22/17 0:00
1.5
50
30

Figure 2.9, Cont'd.

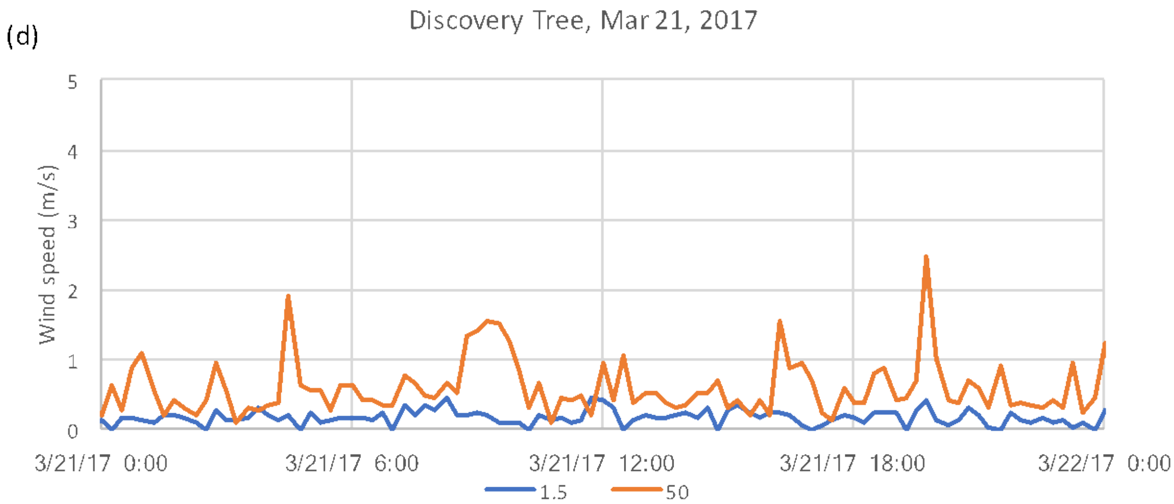

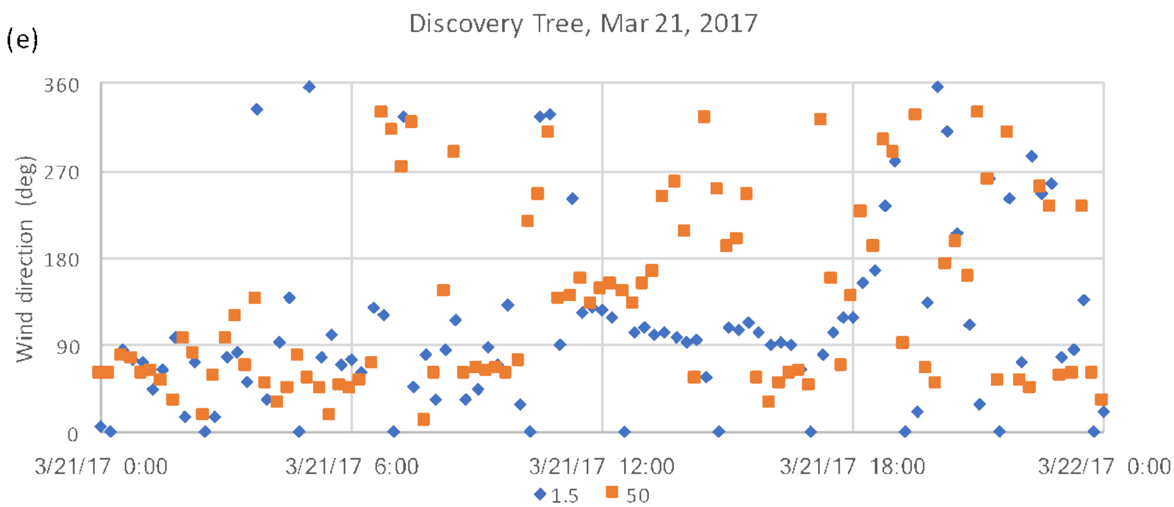

Figure 2.9, cont'd.

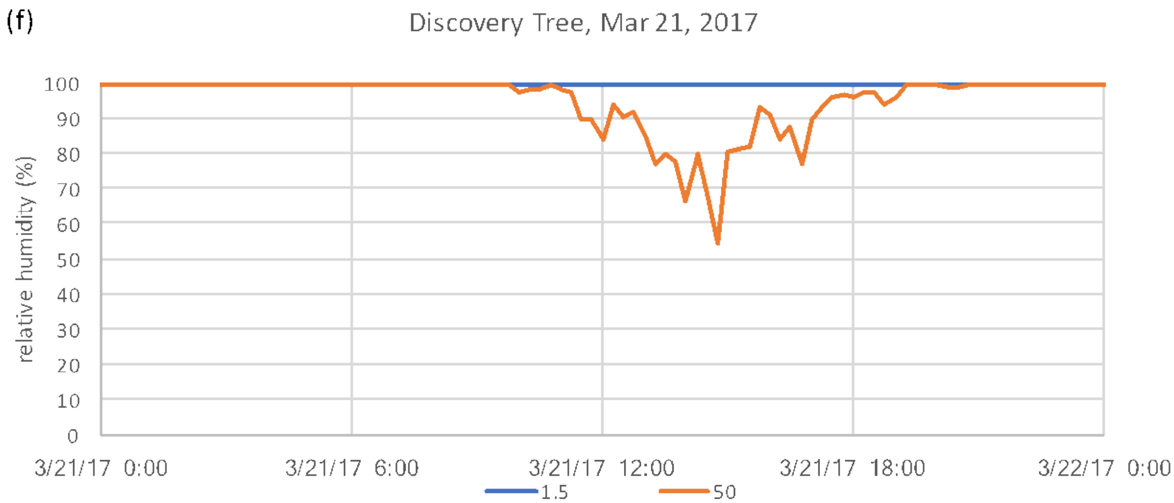

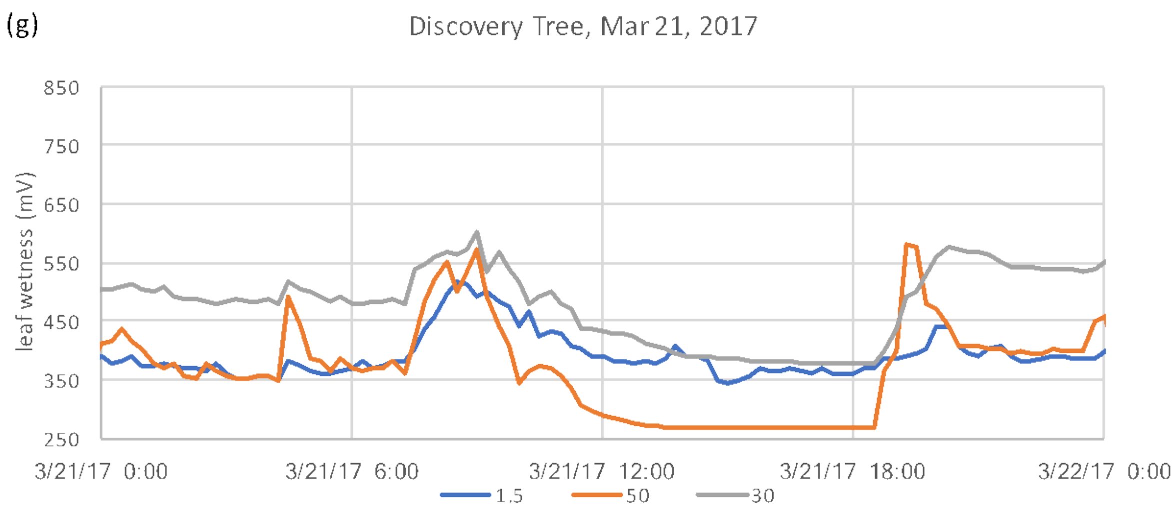

Figure 2.10

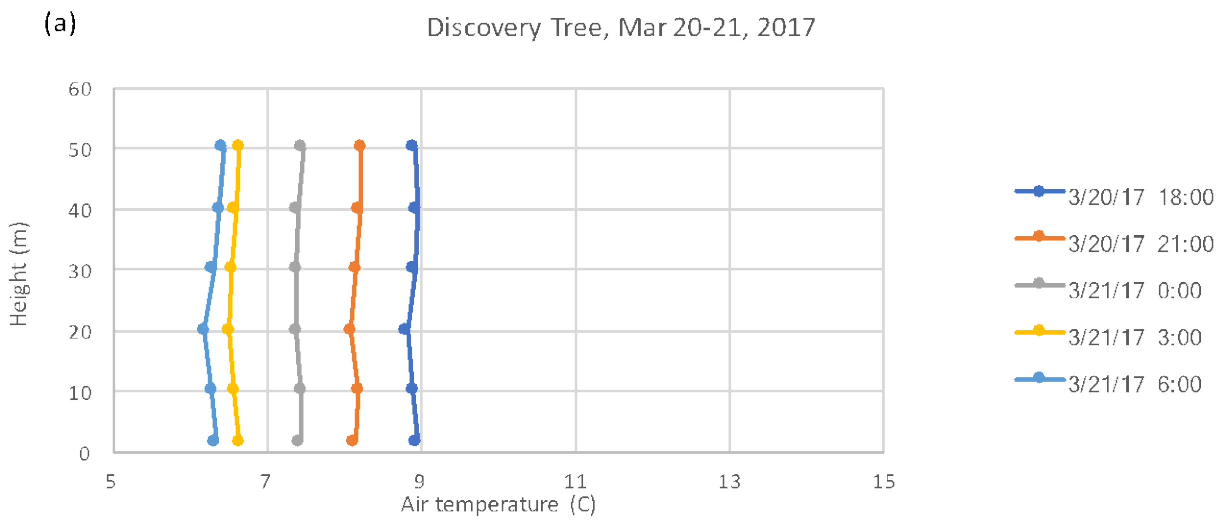
(a)
Discovery Tree, Mar 20-21, 2017
Height (m)
Air temperature (C)
3/20/17 18:00
3/20/17 21:00
3/21/17 0:00
3/21/17 3:00
3/21/17 6:00

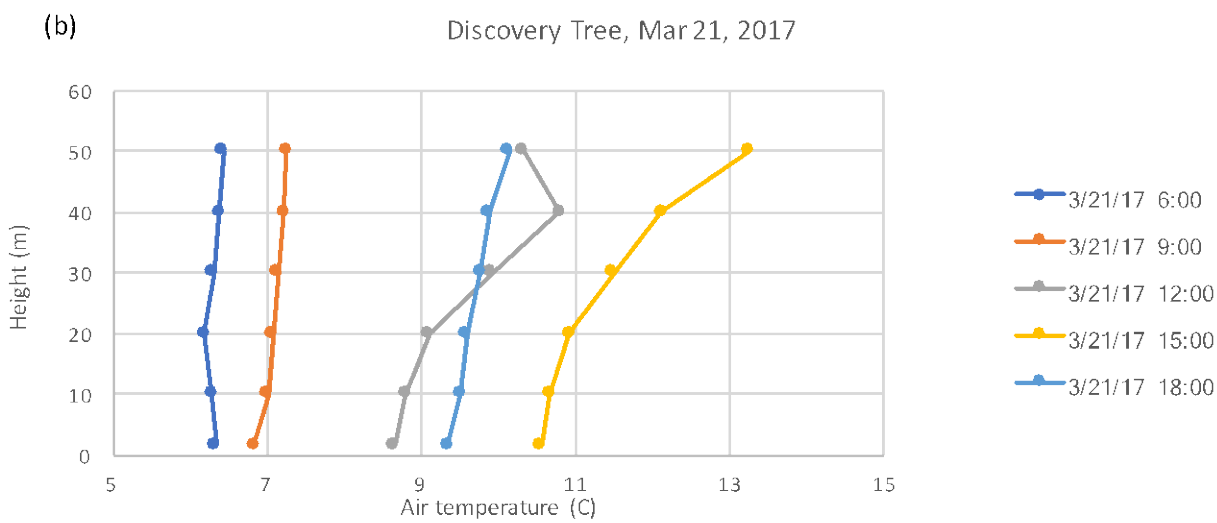
(b)
Discovery Tree, Mar 21, 2017
Height (m)
Air temperature (C)
3/21/17 6:00
3/21/17 9:00
3/21/17 12:00
3/21/17 15:00
3/21/17 18:00

Figure 2.11

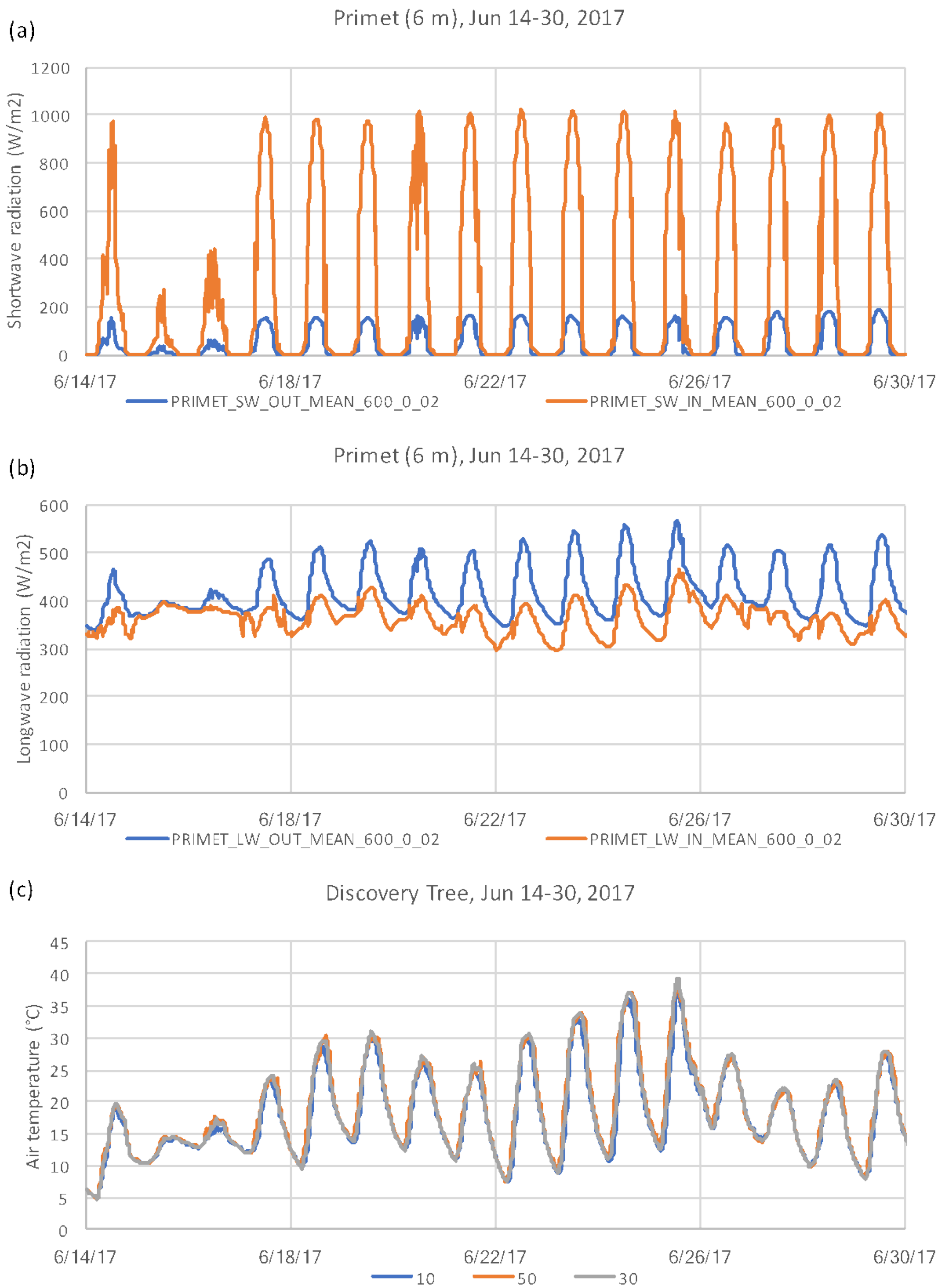
(a)
Primet (6 m), Jun 14-30, 2017
Shortwave radiation (W/m2)
0
200
400
600
800
1000
1200
6/14/17
6/18/17
6/22/17
6/26/17
6/30/17
PRIMET_SW_OUT_MEAN_600_0_02
PRIMET_SW_IN_MEAN_600_0_02
(b)
Primet (6 m), Jun 14-30, 2017
Longwave radiation (W/m2)
0
100
200
300
400
500
600
6/14/17
6/18/17
6/22/17
6/26/17
6/30/17
PRIMET_LW_OUT_MEAN_600_0_02
PRIMET_LW_IN_MEAN_600_0_02
(c)
Discovery Tree, Jun 14-30, 2017
Air temperature (°C)
0
5
10
15
20
25
30
35
40
45
6/14/17
6/18/17
6/22/17
6/26/17
6/30/17
10
50
30

Figure 2.11, cont'd.

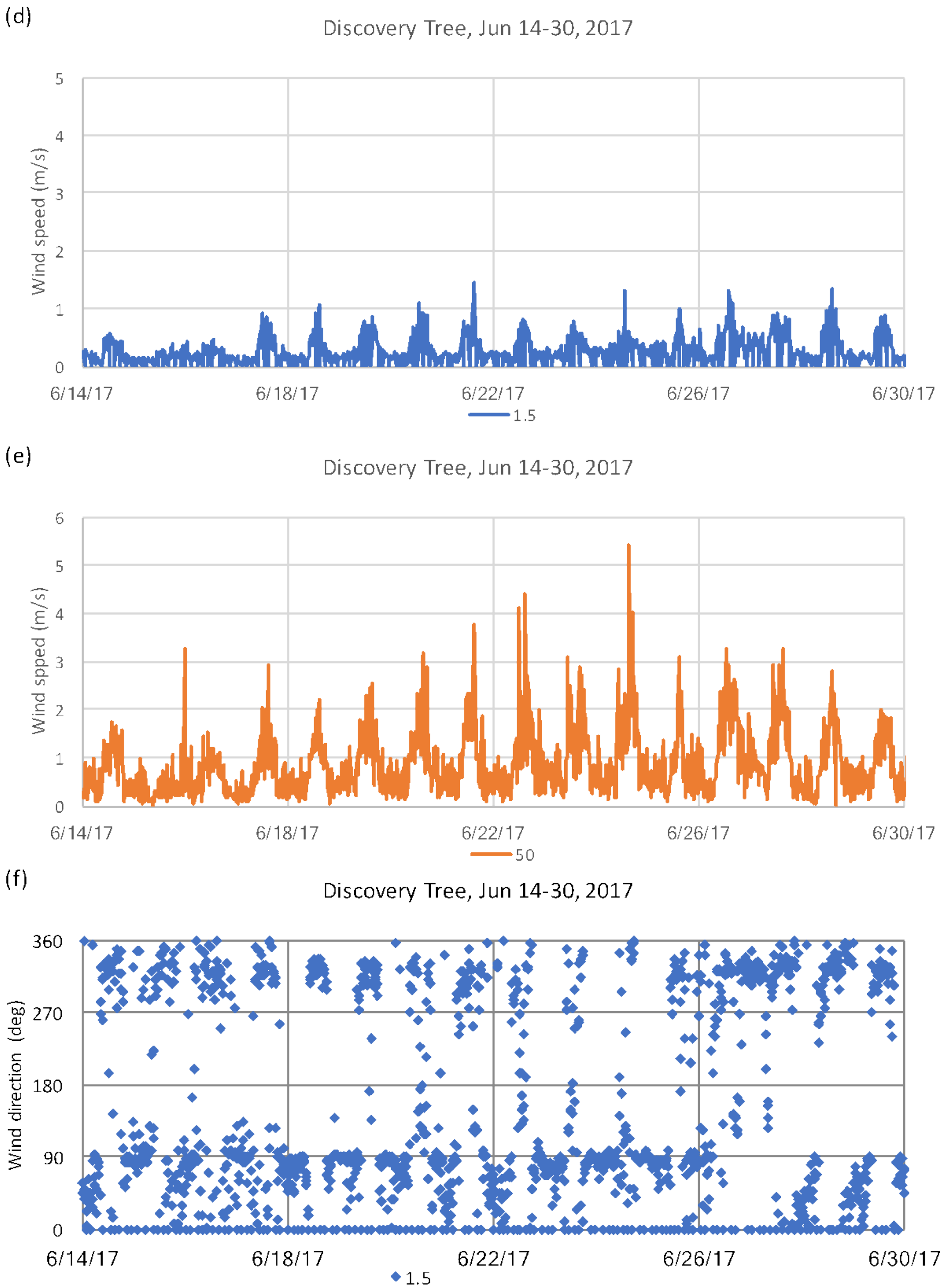

Figure 2.11, cont'd.

(g)

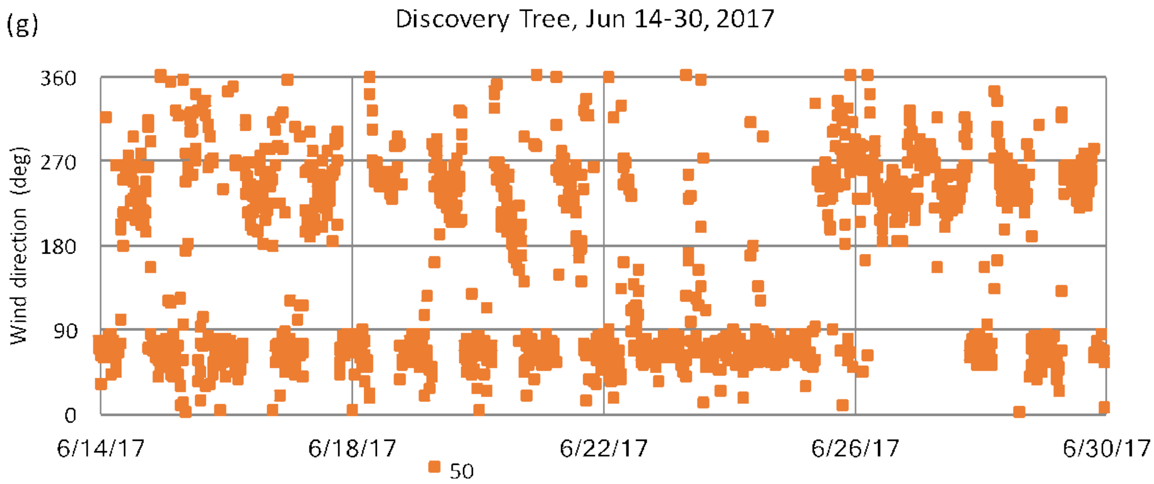

(h)

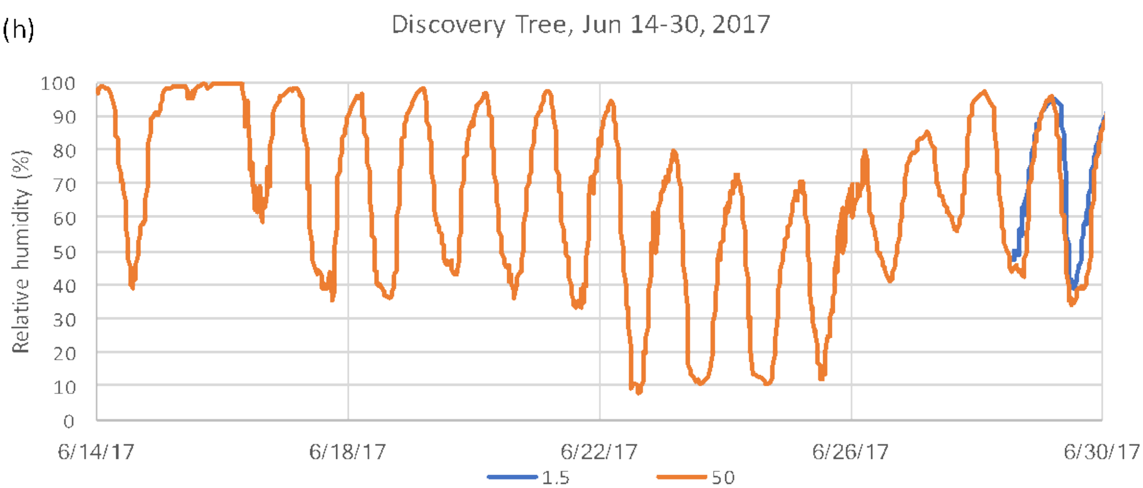

(i)

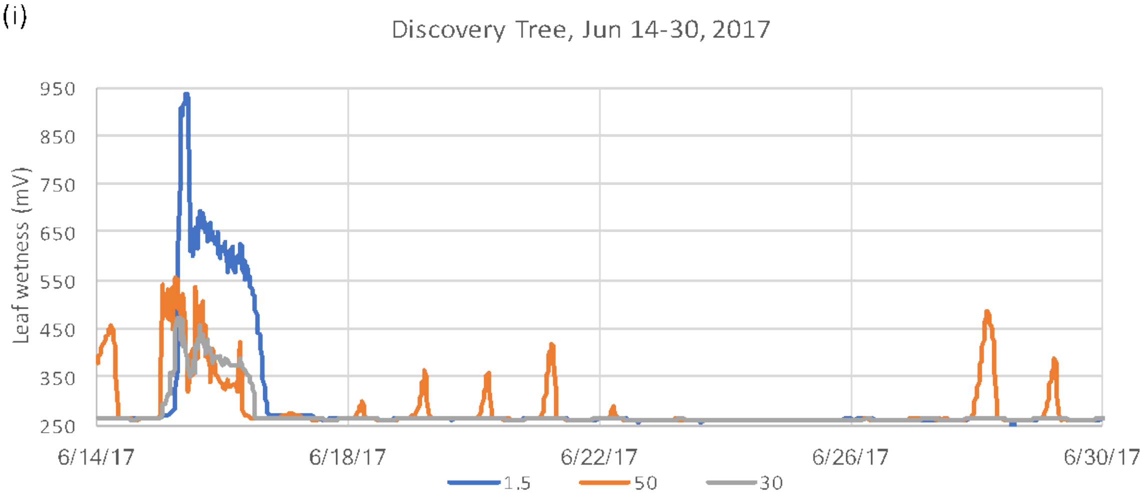

Figure 2.12

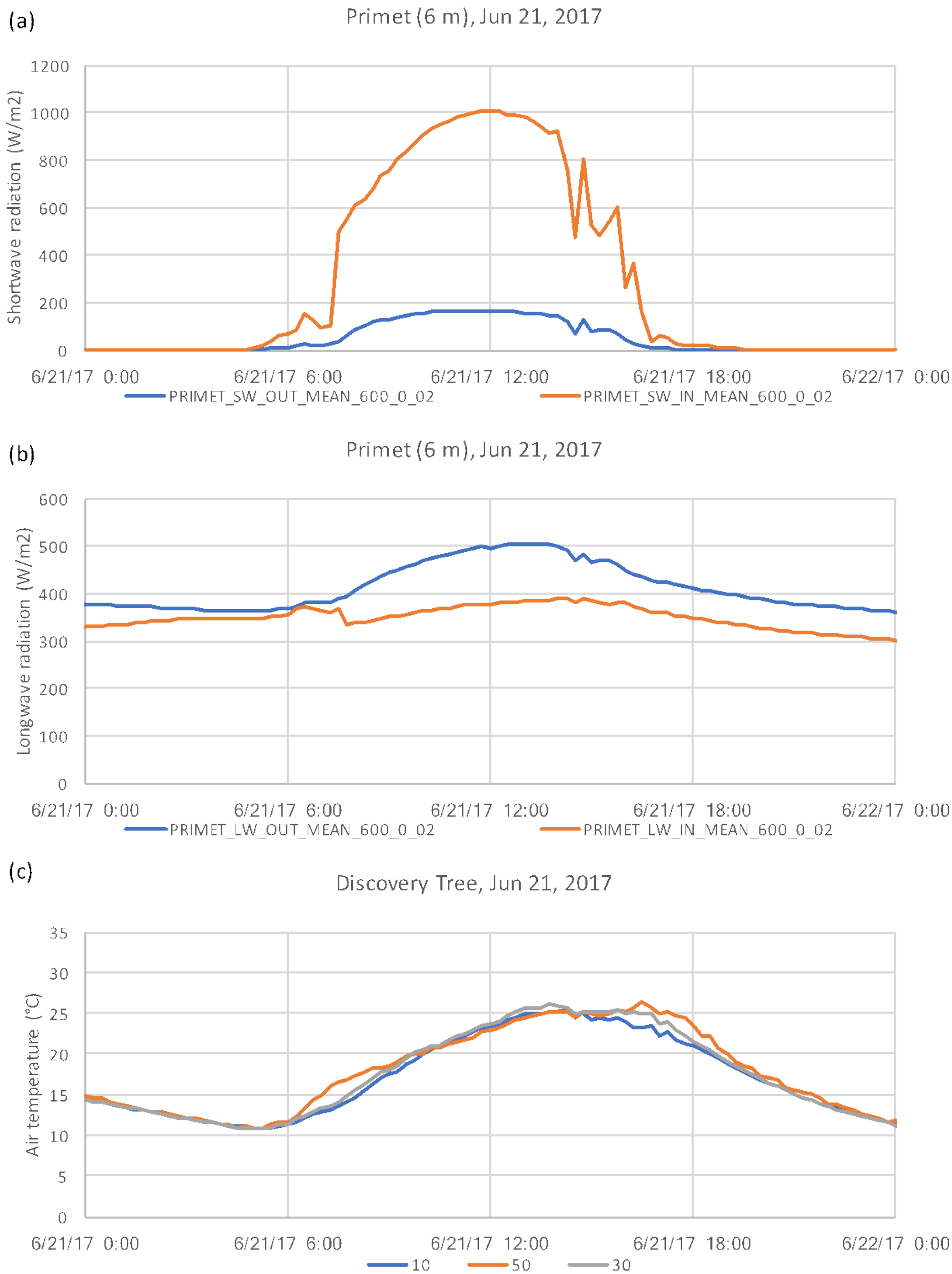
(a)
Primet (6 m), Jun 21, 2017
Shortwave radiation (W/m2)
1200
1000
800
600
400
200
0
6/21/17 0:00
6/21/17 6:00
6/21/17 12:00
6/21/17 18:00
6/22/17 0:00
PRIMET_SW_OUT_MEAN_600_0_02
PRIMET_SW_IN_MEAN_600_0_02
(b)
Primet (6 m), Jun 21, 2017
Longwave radiation (W/m2)
600
500
400
300
200
100
0
6/21/17 0:00
6/21/17 6:00
6/21/17 12:00
6/21/17 18:00
6/22/17 0:00
PRIMET_LW_OUT_MEAN_600_0_02
PRIMET_LW_IN_MEAN_600_0_02
(c)
Discovery Tree, Jun 21, 2017
Air temperature (°C)
35
30
25
20
15
10
5
0
6/21/17 0:00
6/21/17 6:00
6/21/17 12:00
6/21/17 18:00
6/22/17 0:00
10
50
30

Figure 2.12, cont'd.

(d)

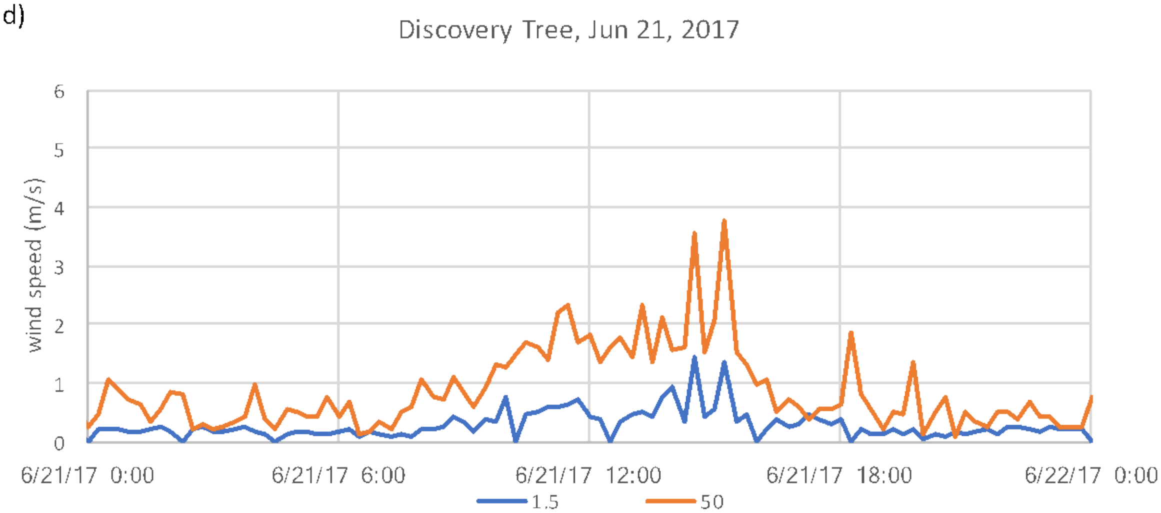

(e)

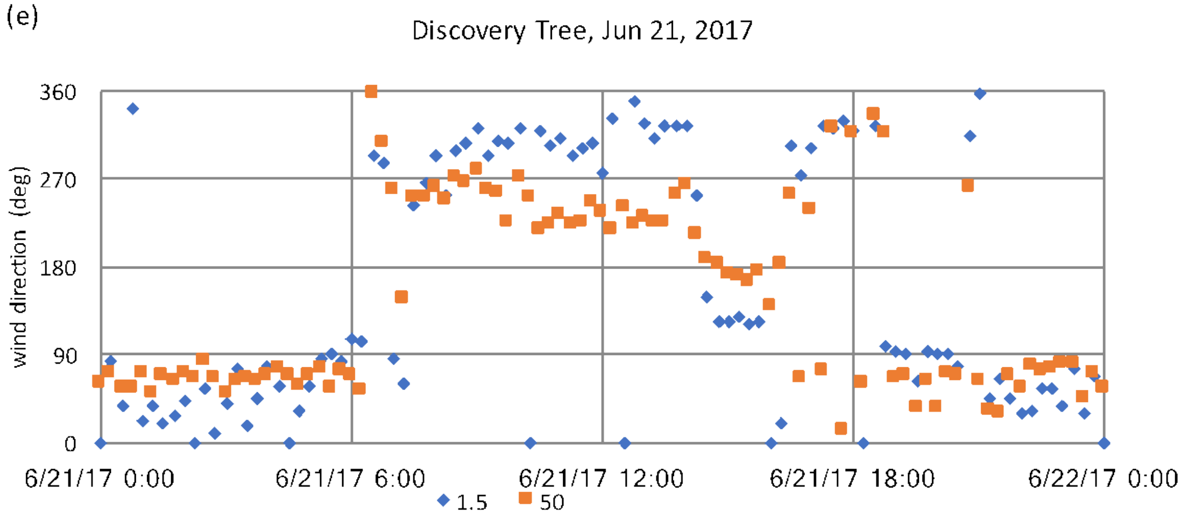

Figure 2.12, cont'd.

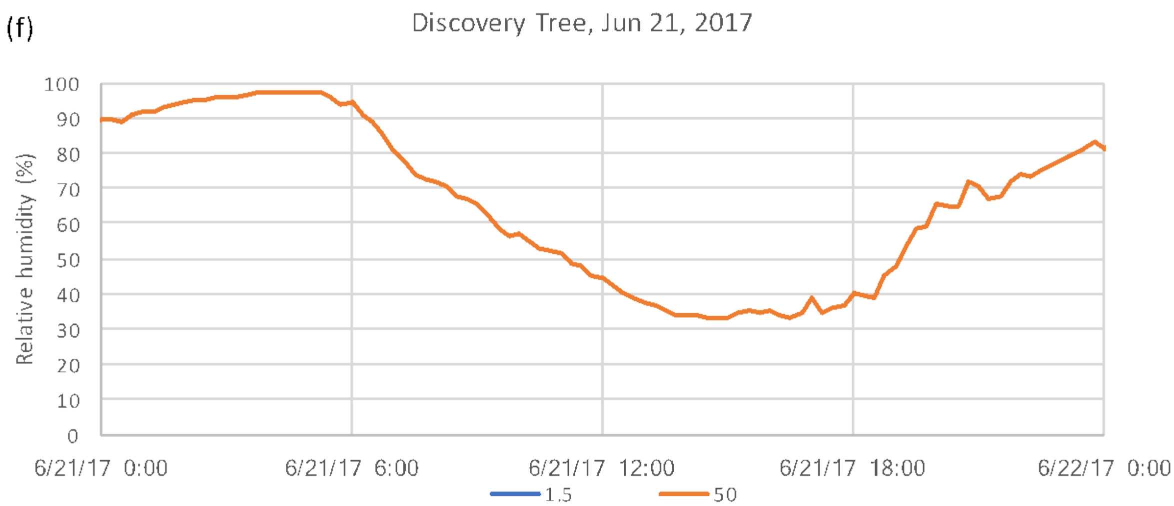

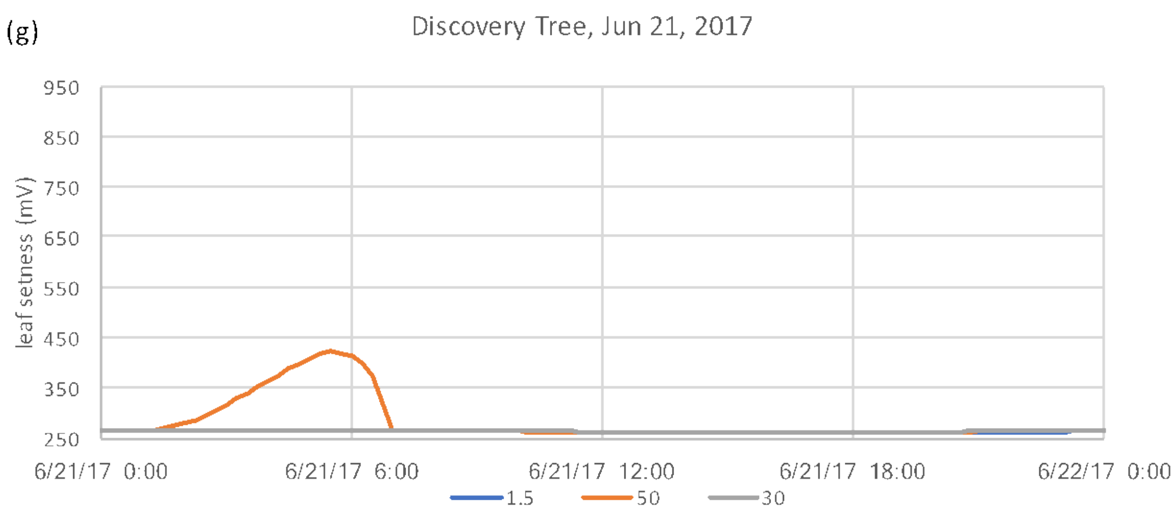

Figure 2.13

(a)

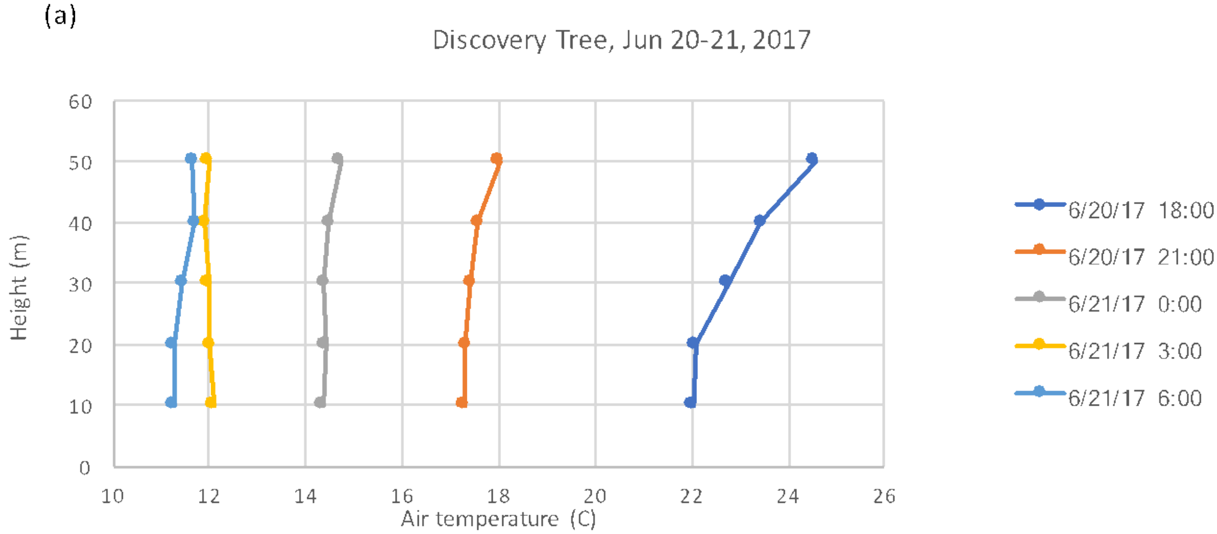

(b)

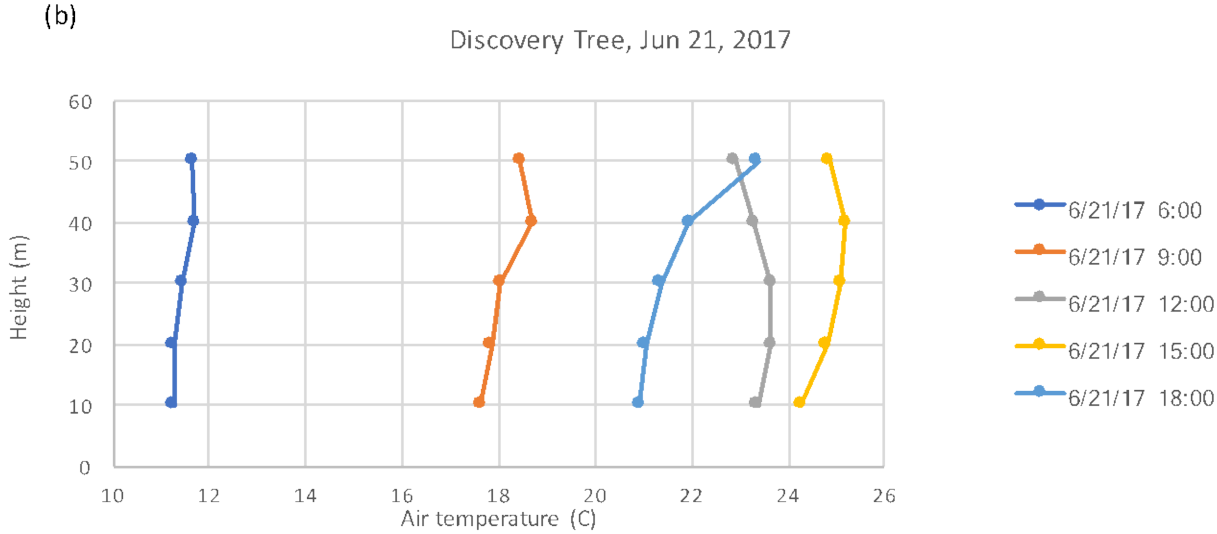

Figure 2.14

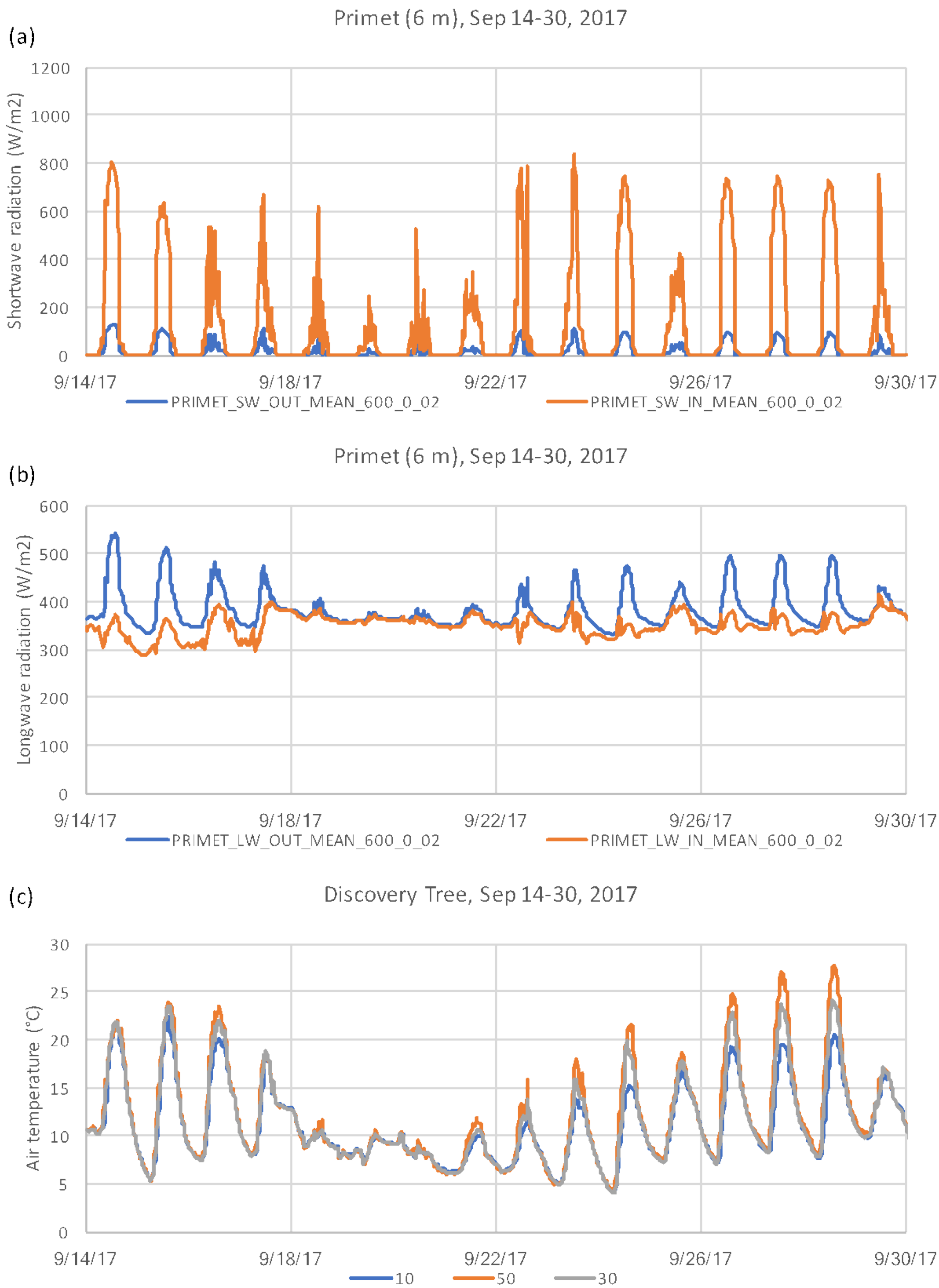
(a)
Primet (6 m), Sep 14-30, 2017
Shortwave radiation (W/m2)
1200
1000
800
600
400
200
0
9/14/17
9/18/17
9/22/17
9/26/17
9/30/17
PRIMET_SW_OUT_MEAN_600_0_02
PRIMET_SW_IN_MEAN_600_0_02
(b)
Primet (6 m), Sep 14-30, 2017
Longwave radiation (W/m2)
600
500
400
300
200
100
0
9/14/17
9/18/17
9/22/17
9/26/17
9/30/17
PRIMET_LW_OUT_MEAN_600_0_02
PRIMET_LW_IN_MEAN_600_0_02
(c)
Discovery Tree, Sep 14-30, 2017
Air temperature (°C)
30
25
20
15
10
5
0
9/14/17
9/18/17
9/22/17
9/26/17
9/30/17
10
50
30

Figure 2.14, cont'd.

(d)

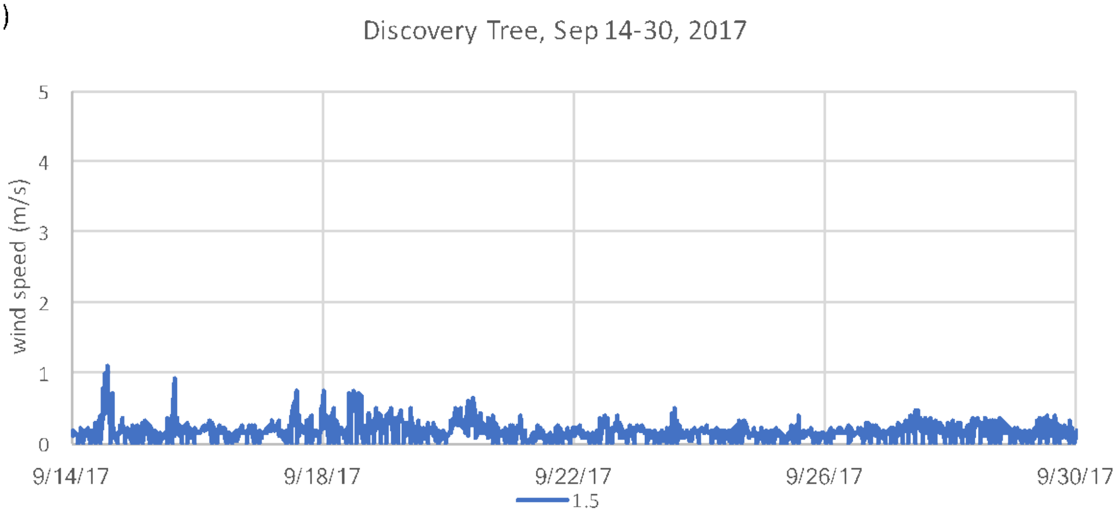

(e)

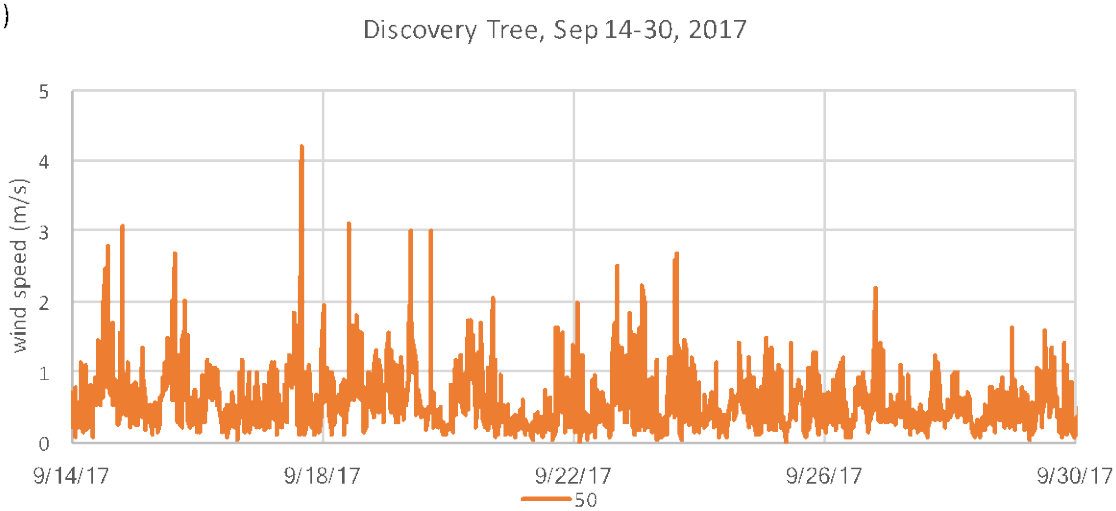

(f)

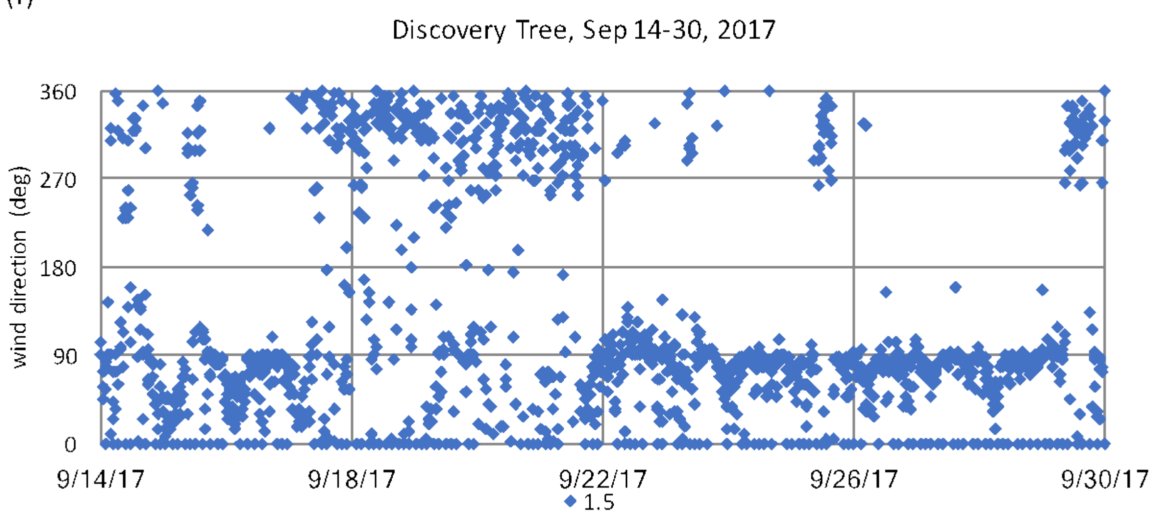

Figure 2.14, cont'd.

(g)

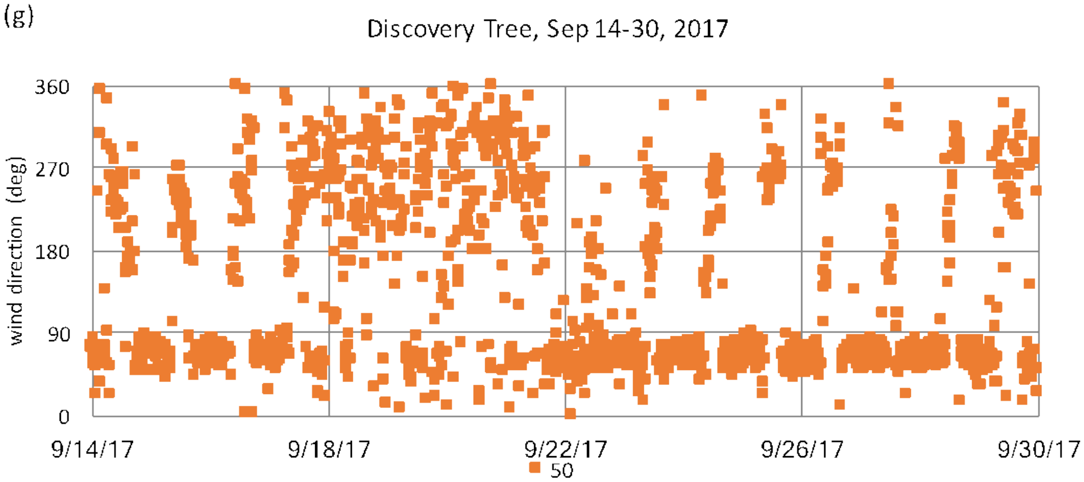

(h)

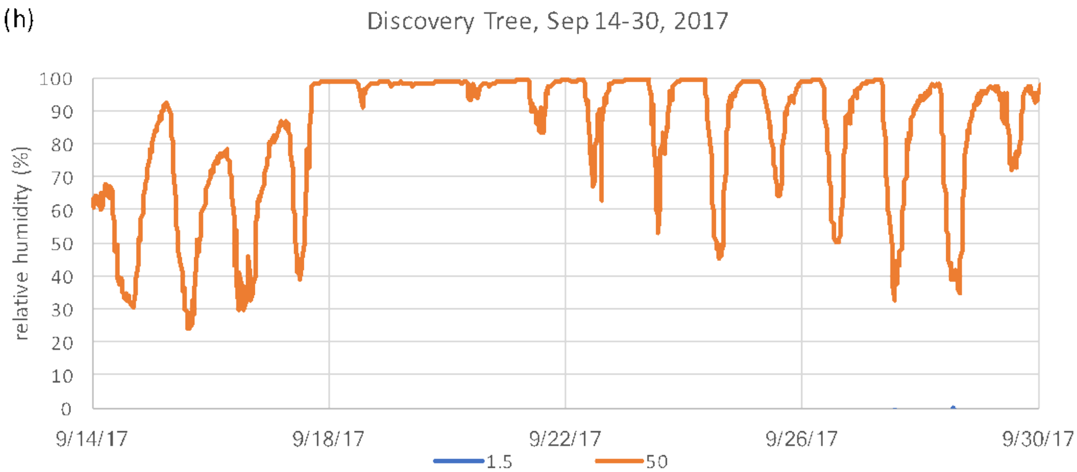

(i)

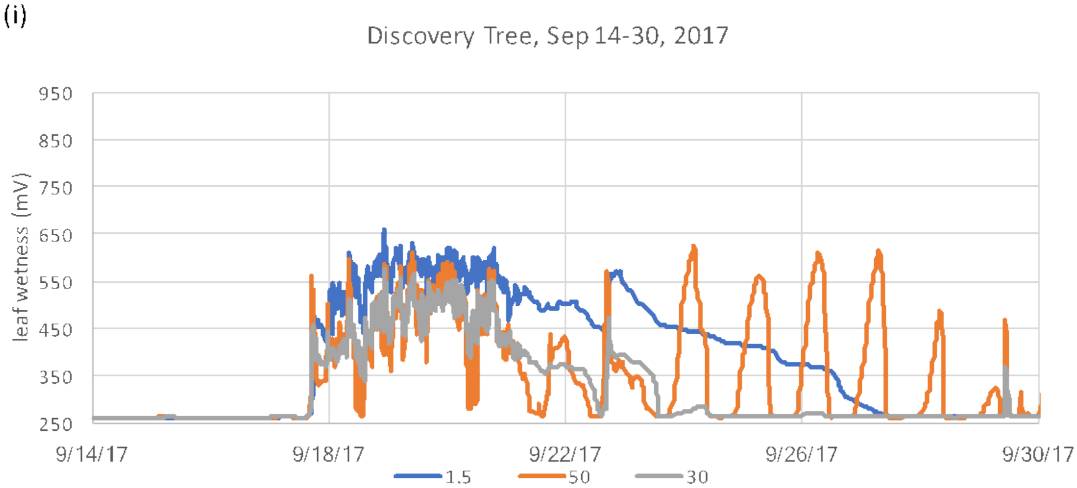

Figure 2.15

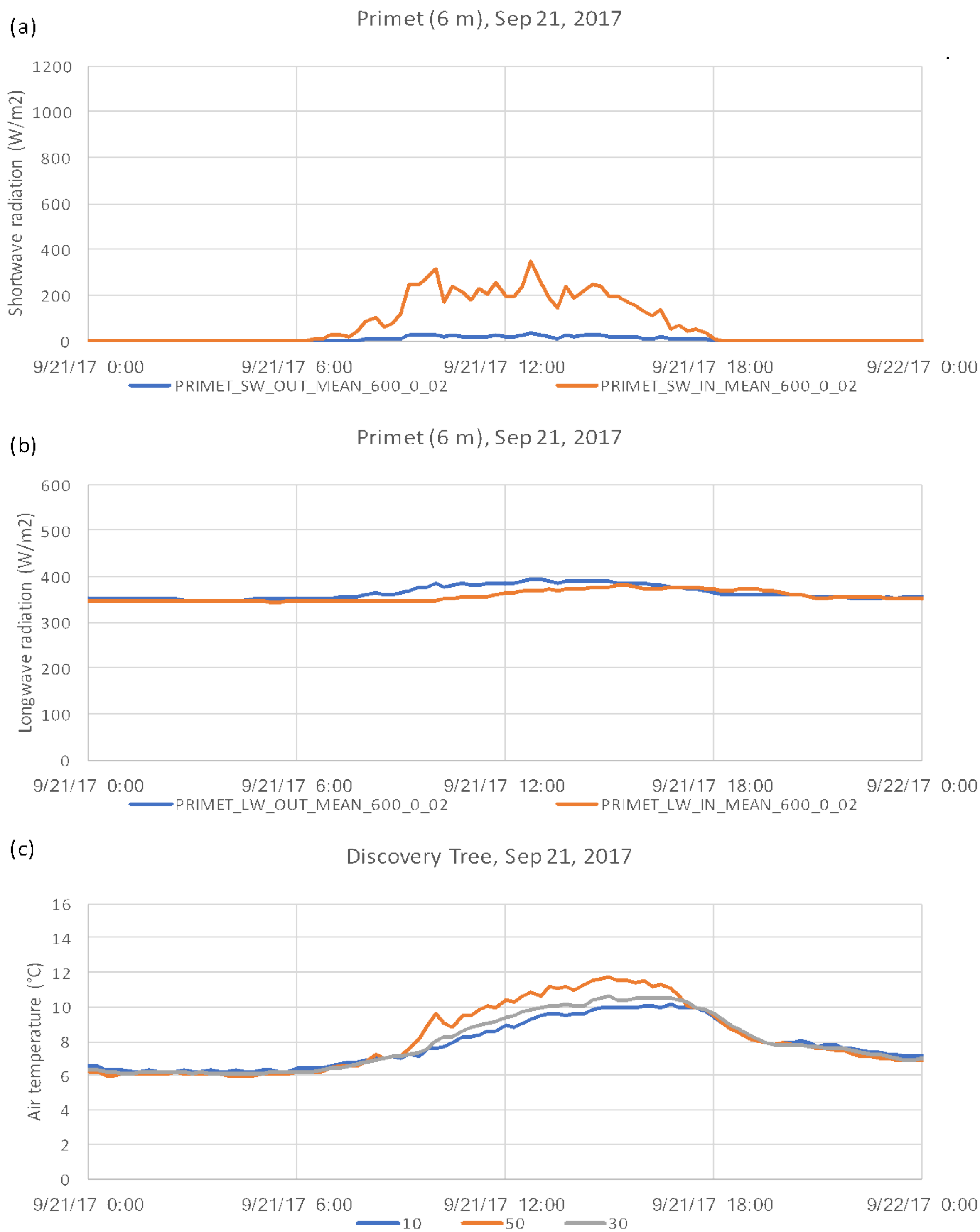
(a)
Primet (6 m), Sep 21, 2017
Shortwave radiation (W/m2)
1200
1000
800
600
400
200
0
9/21/17 0:00
9/21/17 6:00
9/21/17 12:00
9/21/17 18:00
9/22/17 0:00
PRIMET_SW_OUT_MEAN_600_0_02
PRIMET_SW_IN_MEAN_600_0_02
(b)
Primet (6 m), Sep 21, 2017
Longwave radiation (W/m2)
600
500
400
300
200
100
0
9/21/17 0:00
9/21/17 6:00
9/21/17 12:00
9/21/17 18:00
9/22/17 0:00
PRIMET_LW_OUT_MEAN_600_0_02
PRIMET_LW_IN_MEAN_600_0_02
(c)
Discovery Tree, Sep 21, 2017
Air temperature (°C)
16
14
12
10
8
6
4
2
0
9/21/17 0:00
9/21/17 6:00
9/21/17 12:00
9/21/17 18:00
9/22/17 0:00
10
50
30

Figure 2.15, Cont'd.

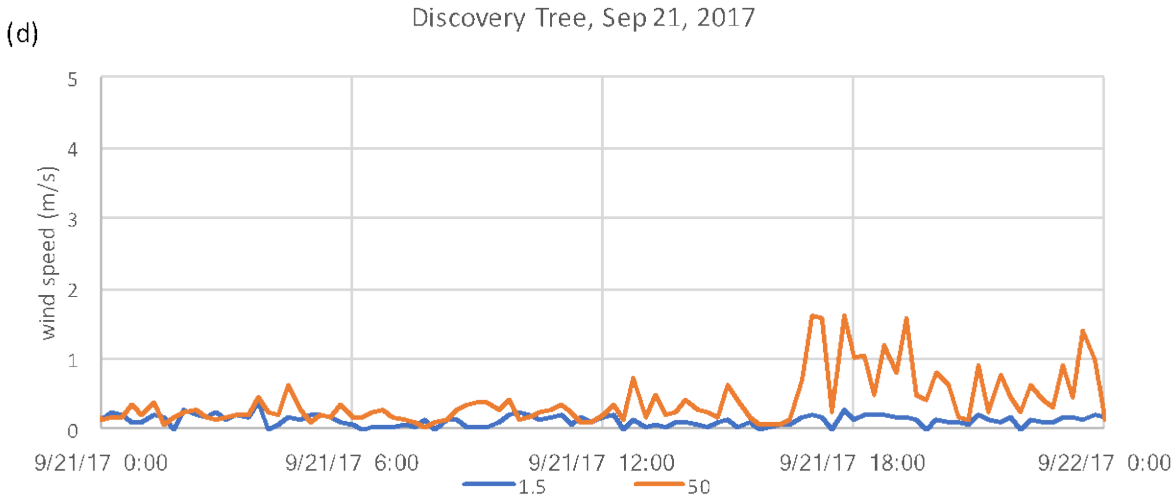

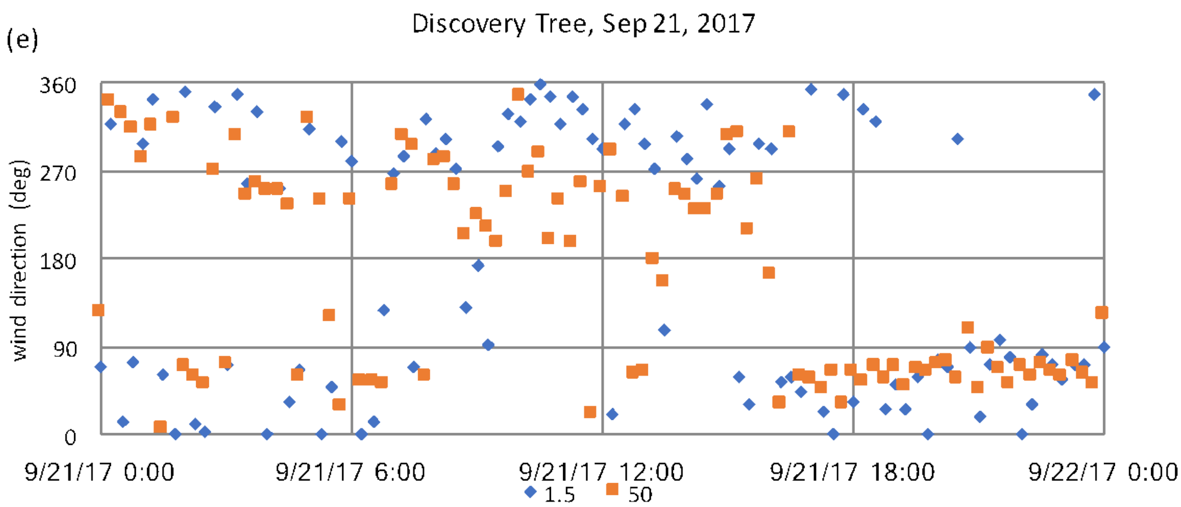

Figure 2.15, cont'd.

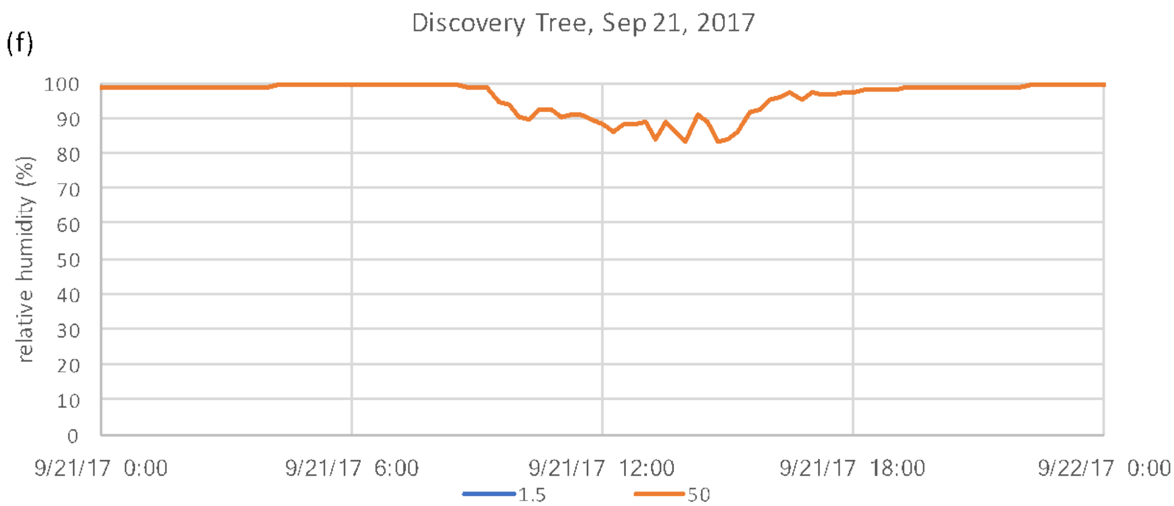

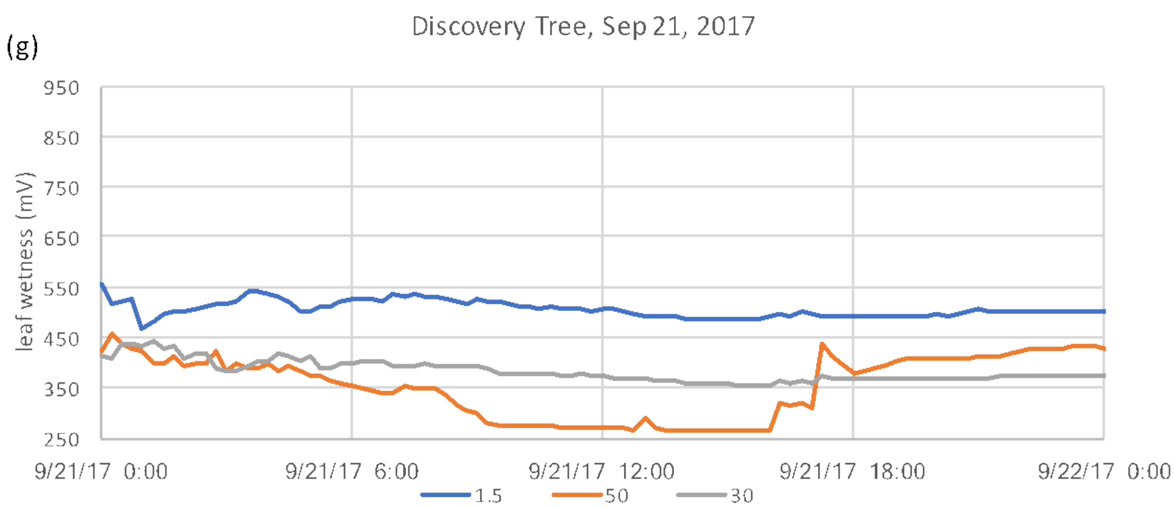

Figure 2.16

(a)

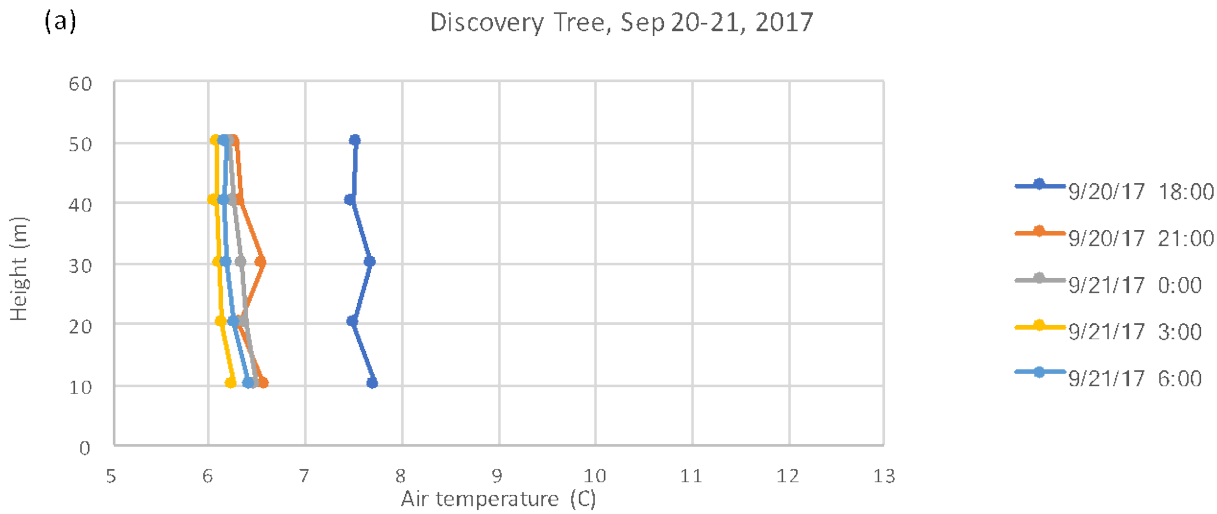

(b)

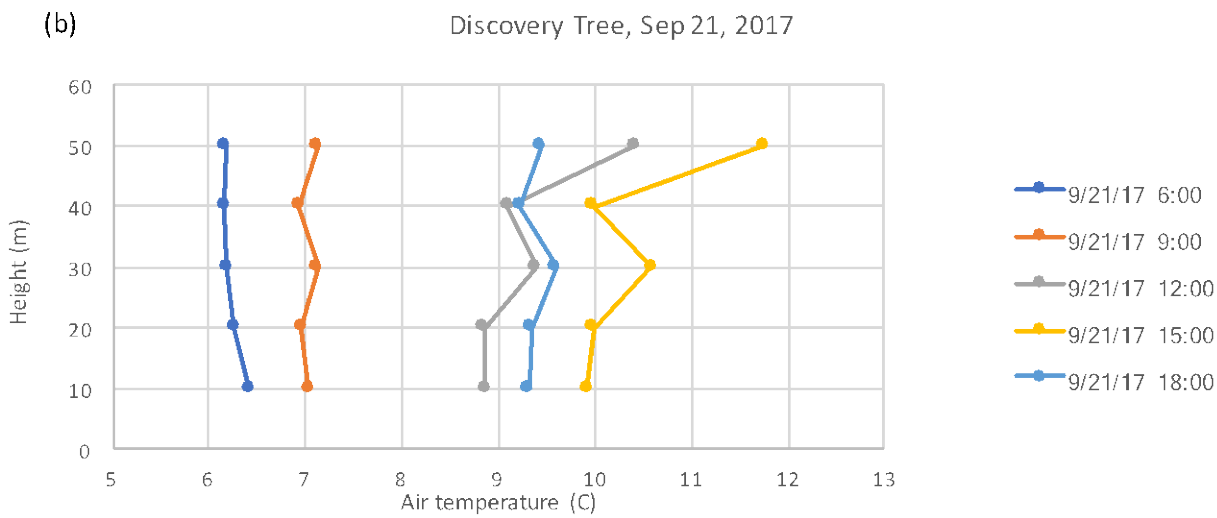

Figure 2.17 (a)

The shading map of the Discovery tree's surrounding area at 9:00 AM on December 21, 2016

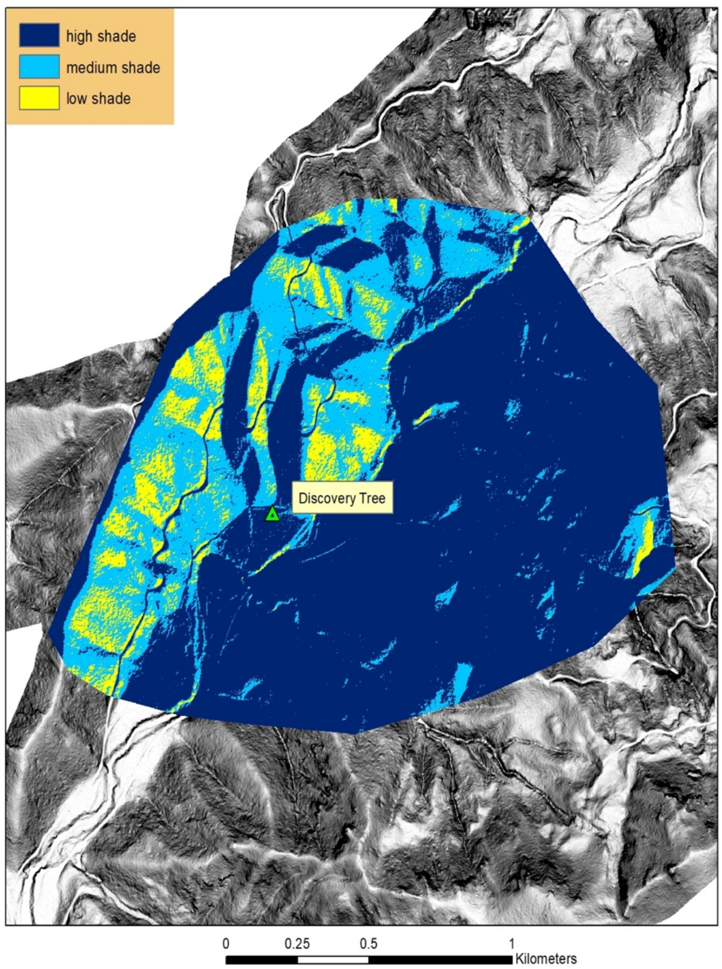

N

Data source:
1- meter DEM of the HJA Forest created from the LiDAR point clouds acquired on August 10th and 11th 2008 by Watershed Sciences, Inc.
Coordinate: NAD-1983-UTM-zone-10N
Datum: D-North-American-1983

Figure 2.17 (b)

The shading map of the Discovery tree's surrounding area at 12:00 PM on December 21, 2016

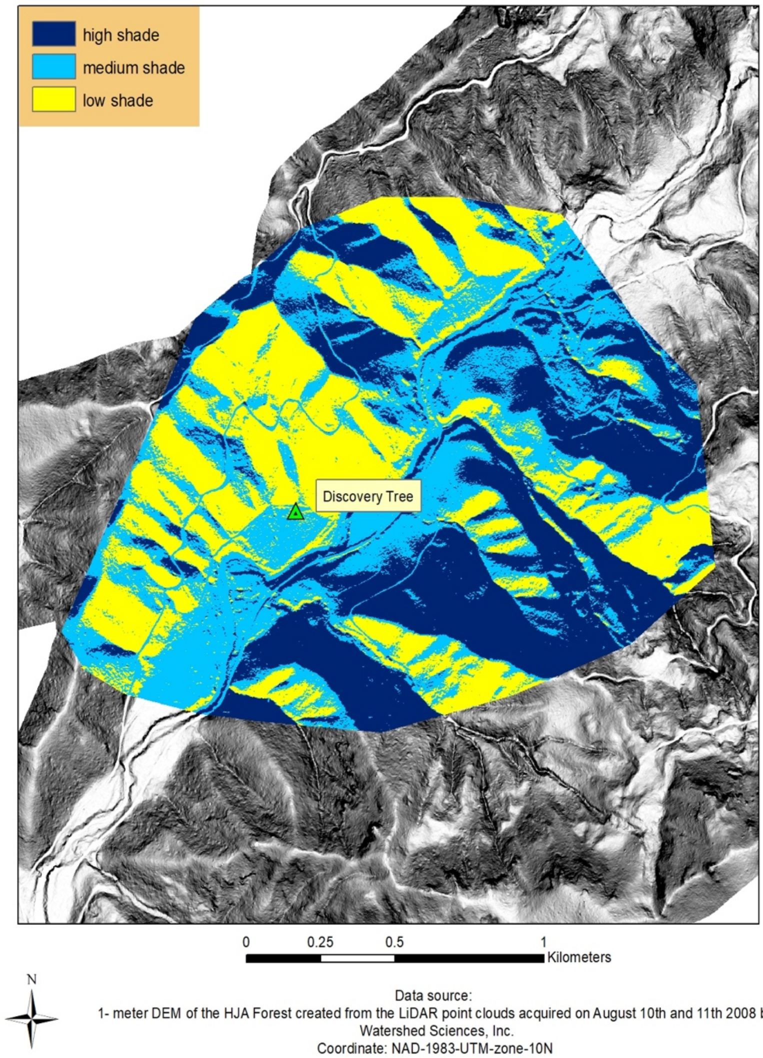

Data source:
1- meter DEM of the HJA Forest created from the LiDAR point clouds acquired on August 10th and 11th 2008 by Watershed Sciences, Inc.
Coordinate: NAD-1983-UTM-zone-10N
Datum: D-North-American-1983

Figure 2.17 (c)

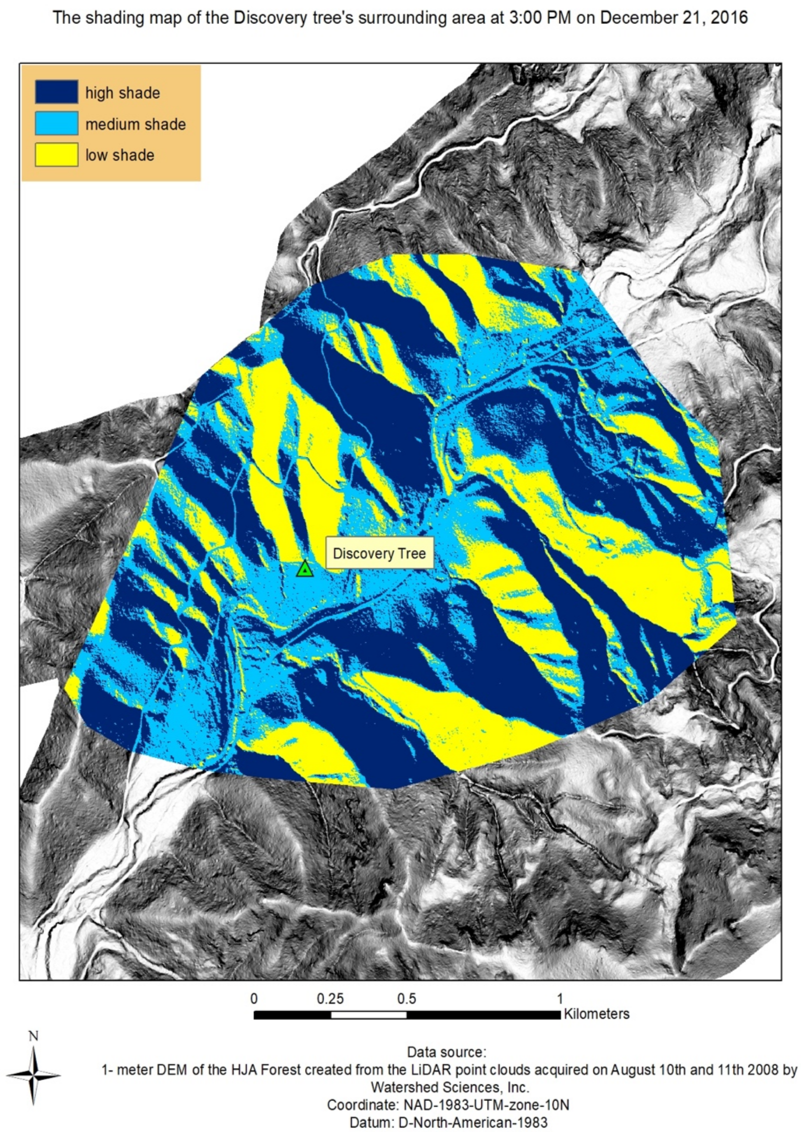
The shading map of the Discovery tree's surrounding area at 3:00 PM on December 21, 2016
high shade
medium shade
low shade
Discovery Tree
0
0.25
0.5
1
Kilometers
N
Data source:
1- meter DEM of the HJA Forest created from the LiDAR point clouds acquired on August 10th and 11th 2008 by Watershed Sciences, Inc.
Coordinate: NAD-1983-UTM-zone-10N
Datum: D-North-American-1983

Figure 2.17 (d)

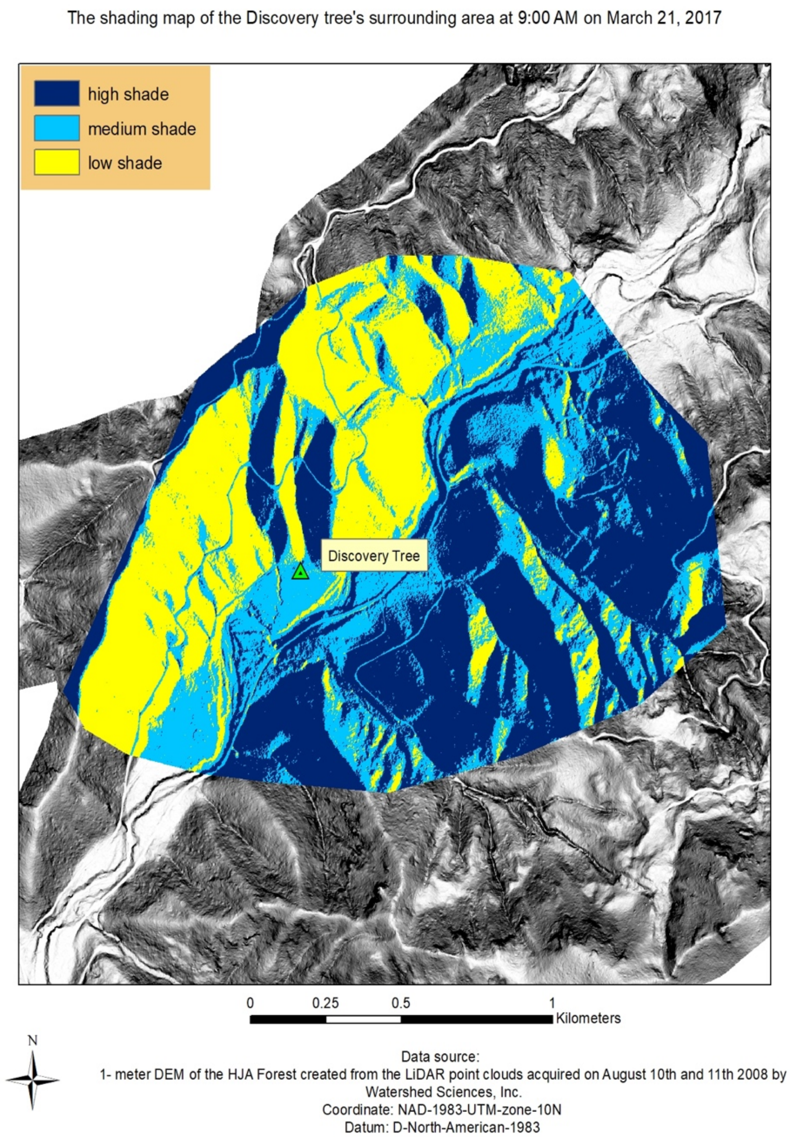
The shading map of the Discovery tree's surrounding area at 9:00 AM on March 21, 2017
high shade
medium shade
low shade
Discovery Tree
0
0.25
0.5
1
Kilometers
N
Data source:
1- meter DEM of the HJA Forest created from the LiDAR point clouds acquired on August 10th and 11th 2008 by Watershed Sciences, Inc.
Coordinate: NAD-1983-UTM-zone-10N
Datum: D-North-American-1983

Figure 2.17 (e)

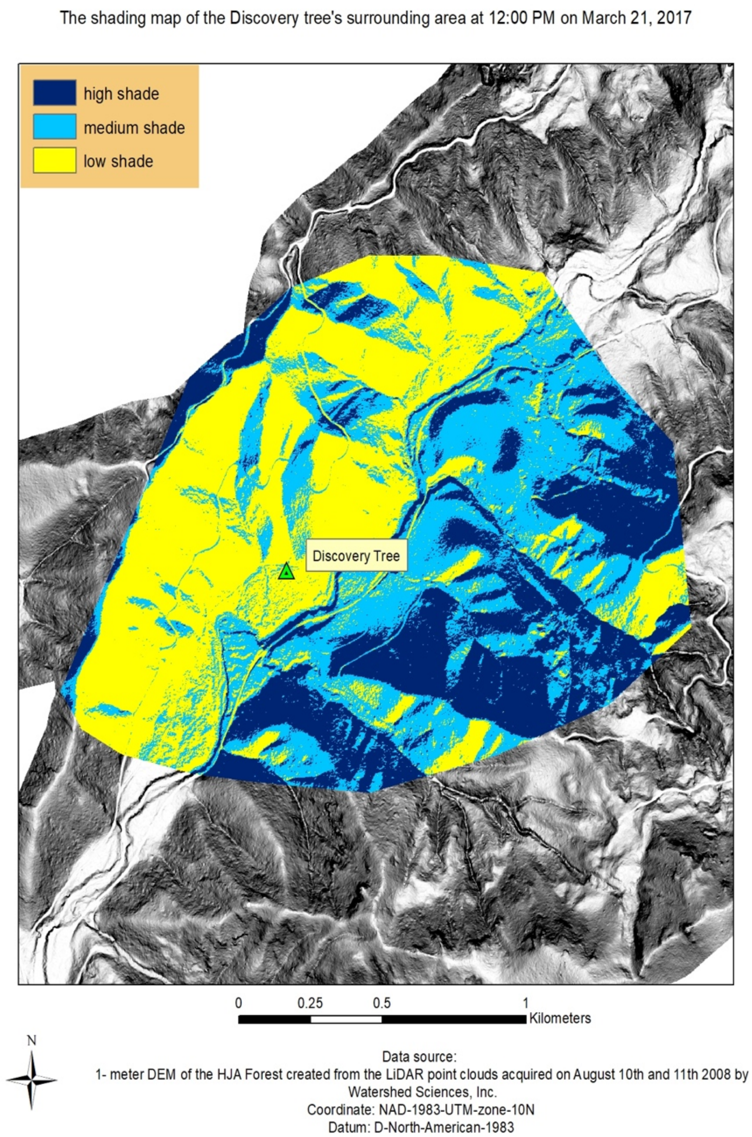
The shading map of the Discovery tree's surrounding area at 12:00 PM on March 21, 2017
high shade
medium shade
low shade
Discovery Tree
0
0.25
0.5
1
Kilometers
N
Data source:
1- meter DEM of the HJA Forest created from the LiDAR point clouds acquired on August 10th and 11th 2008 by Watershed Sciences, Inc.
Coordinate: NAD-1983-UTM-zone-10N
Datum: D-North-American-1983

Figure 2.17 (f)

The shading map of the Discovery tree's surrounding area at 3:00 PM on March 21, 2017

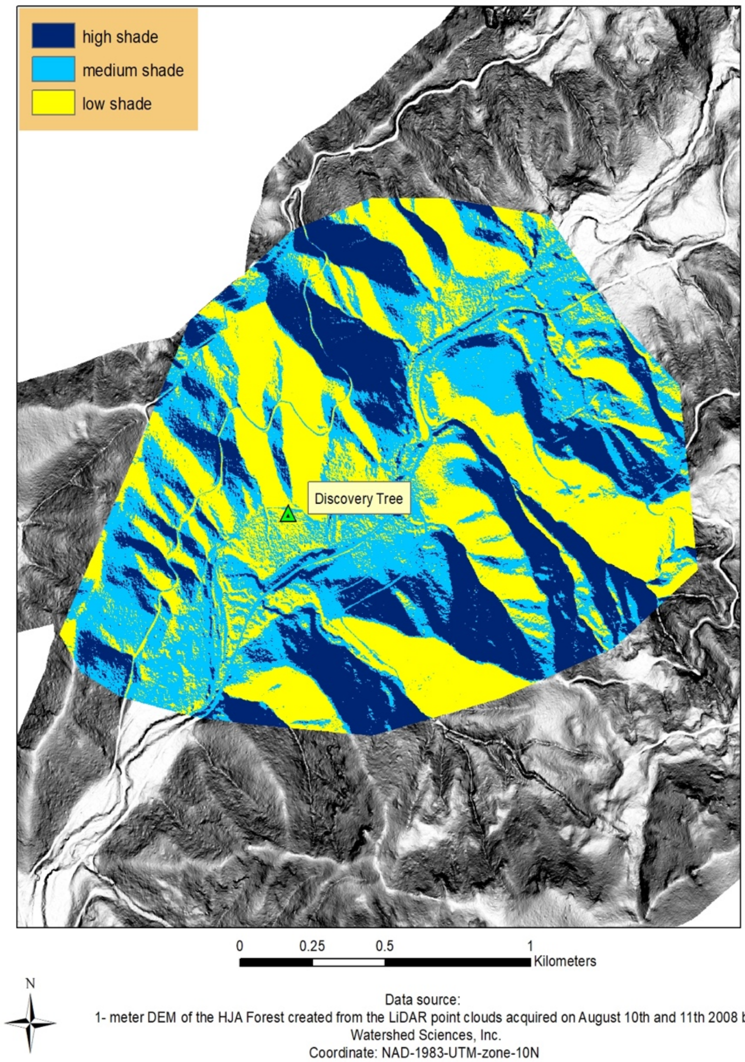

Data source:
1- meter DEM of the HJA Forest created from the LiDAR point clouds acquired on August 10th and 11th 2008 by Watershed Sciences, Inc.
Coordinate: NAD-1983-UTM-zone-10N
Datum: D-North-American-1983

Figure 2.17 (g)

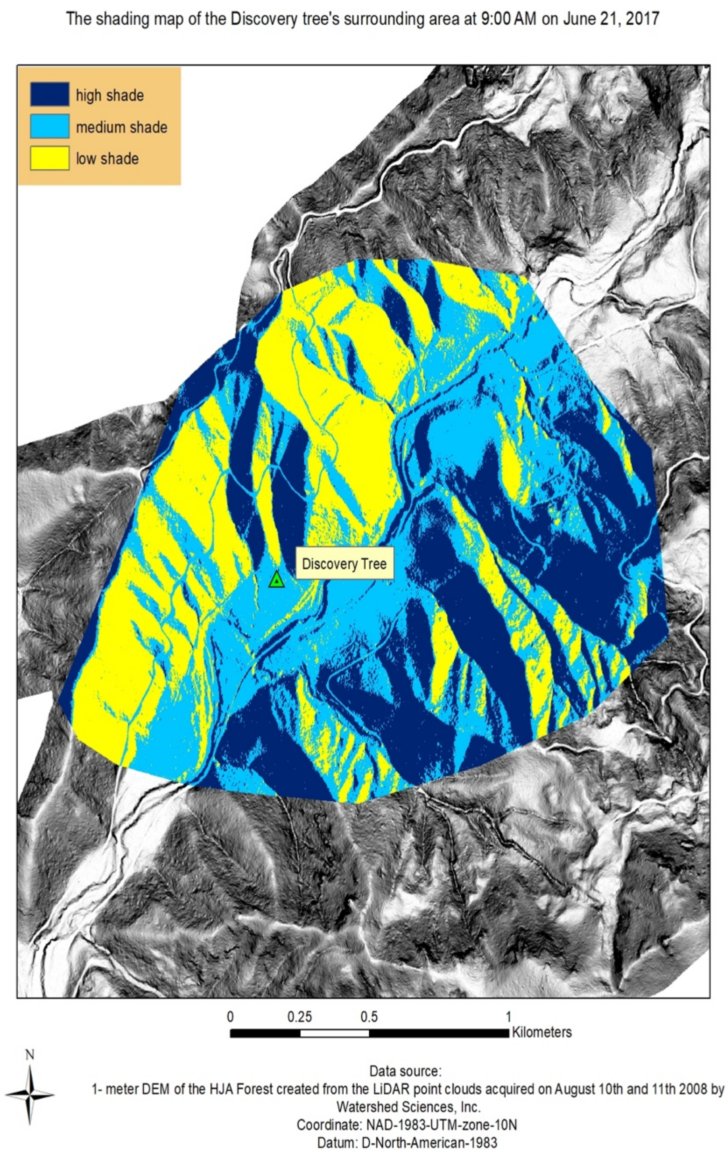
The shading map of the Discovery tree's surrounding area at 9:00 AM on June 21, 2017
high shade
medium shade
low shade
Discovery Tree
0
0.25
0.5
1
Kilometers
N
Data source:
1- meter DEM of the HJA Forest created from the LiDAR point clouds acquired on August 10th and 11th 2008 by Watershed Sciences, Inc.
Coordinate: NAD-1983-UTM-zone-10N
Datum: D-North-American-1983

Figure 2.17 (h)

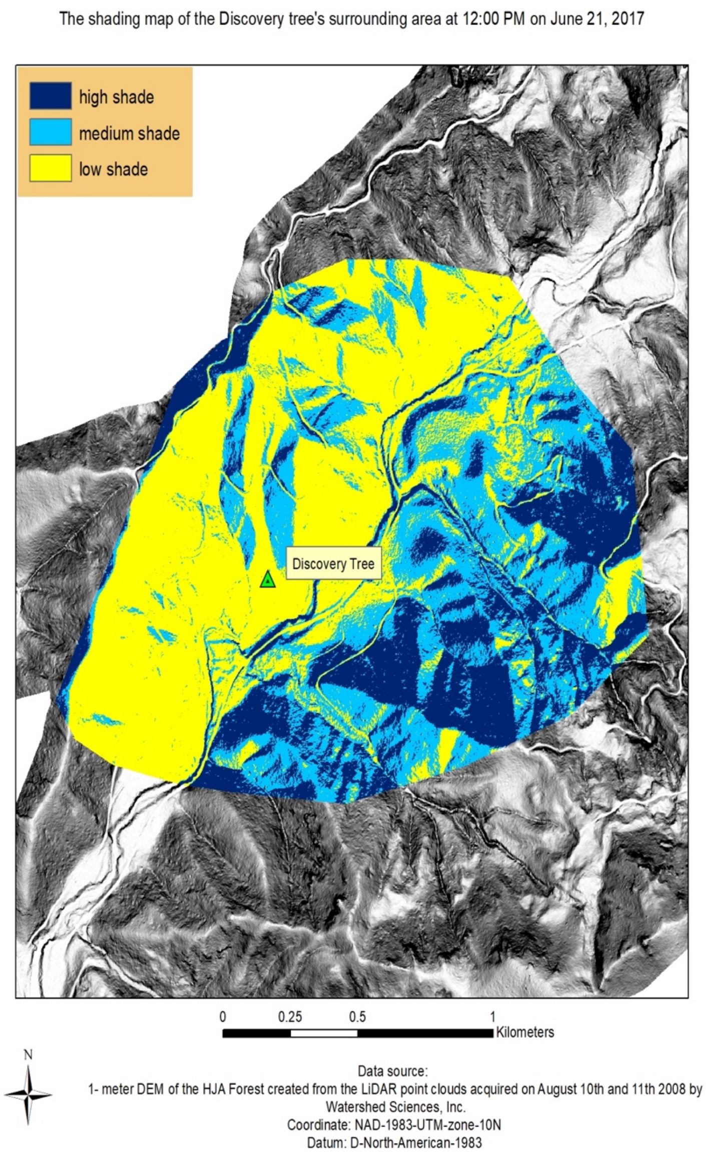
The shading map of the Discovery tree's surrounding area at 12:00 PM on June 21, 2017
high shade
medium shade
low shade
Discovery Tree
0
0.25
0.5
1
Kilometers
N
Data source:
1- meter DEM of the HJA Forest created from the LiDAR point clouds acquired on August 10th and 11th 2008 by Watershed Sciences, Inc.
Coordinate: NAD-1983-UTM-zone-10N
Datum: D-North-American-1983

Figure 2.17 (i)

The shading map of the Discovery tree's surrounding area at 3:00 PM on June 21, 2017

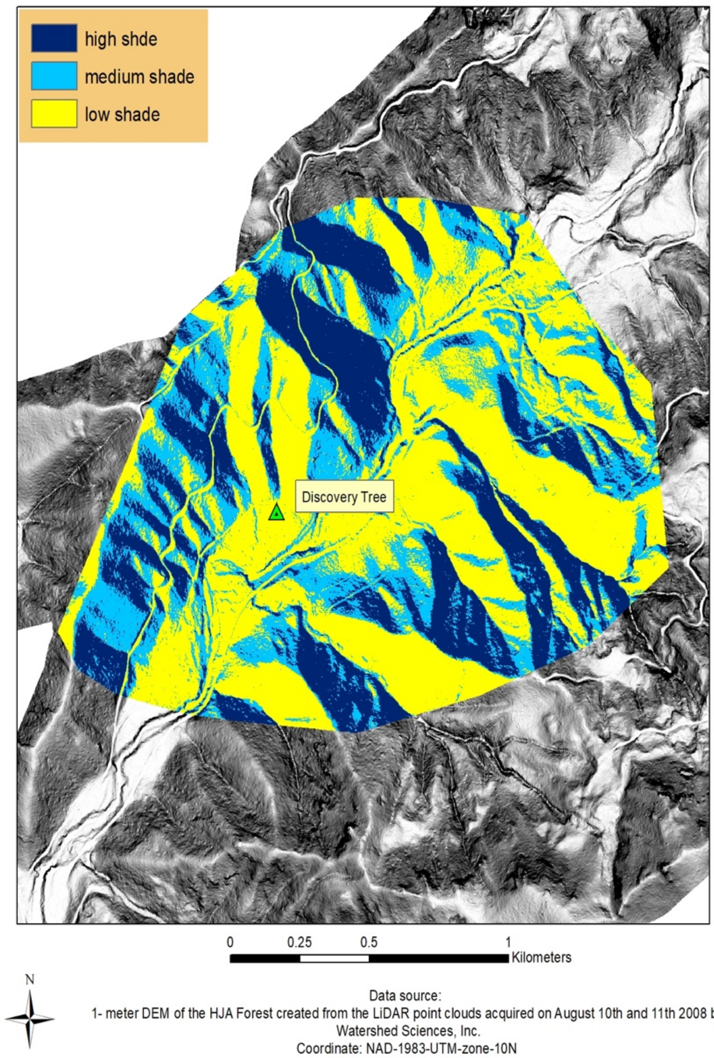

Data source:
1- meter DEM of the HJA Forest created from the LiDAR point clouds acquired on August 10th and 11th 2008 by Watershed Sciences, Inc.
Coordinate: NAD-1983-UTM-zone-10N
Datum: D-North-American-1983

Figure 2.17 (j)

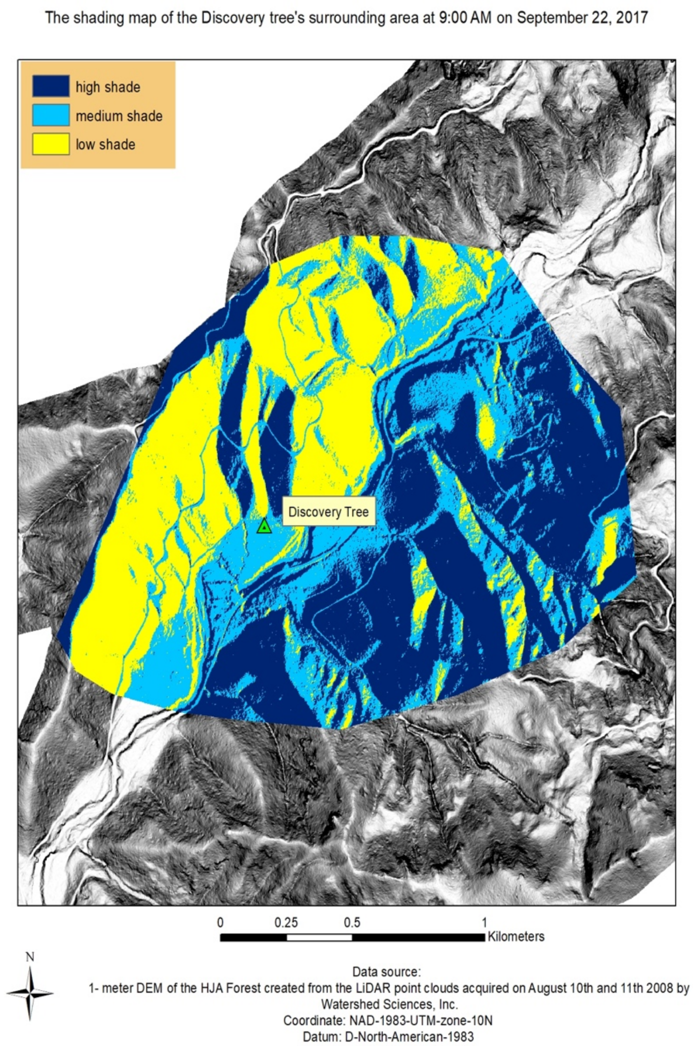
The shading map of the Discovery tree's surrounding area at 9:00 AM on September 22, 2017
high shade
medium shade
low shade
Discovery Tree
0
0.25
0.5
1
Kilometers
N
Data source:
1- meter DEM of the HJA Forest created from the LiDAR point clouds acquired on August 10th and 11th 2008 by Watershed Sciences, Inc.
Coordinate: NAD-1983-UTM-zone-10N
Datum: D-North-American-1983

Figure 2.17 (k)

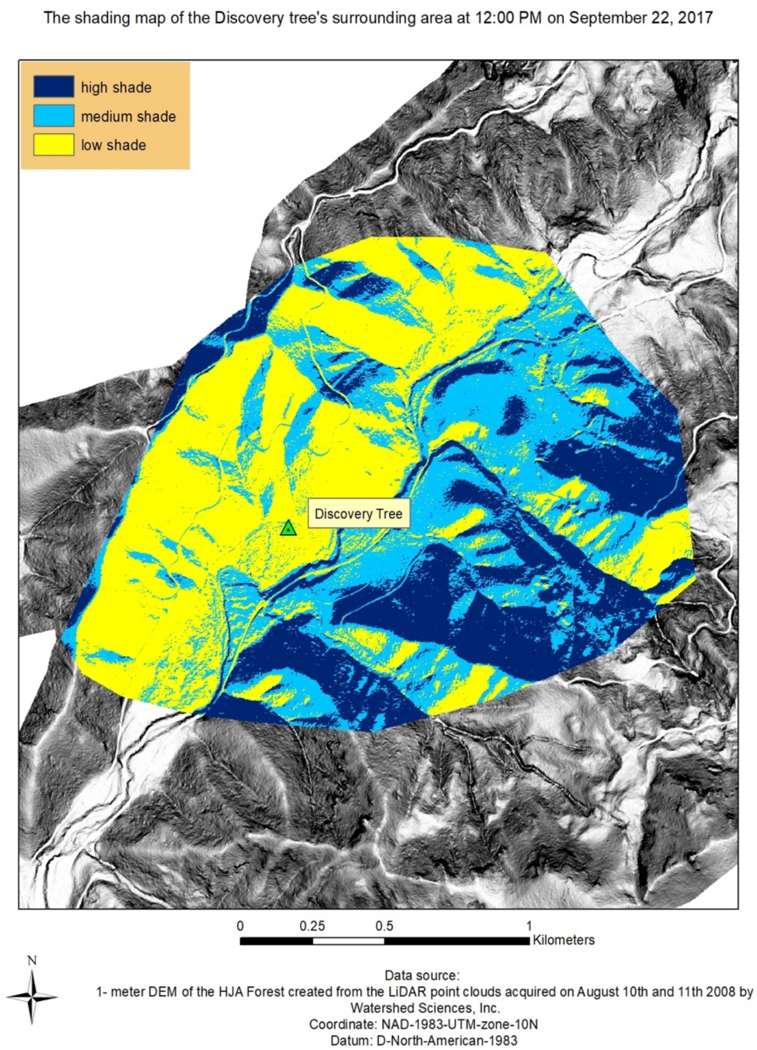
The shading map of the Discovery tree's surrounding area at 12:00 PM on September 22, 2017
high shade
medium shade
low shade
Discovery Tree
0
0.25
0.5
1
Kilometers
N
Data source:
1- meter DEM of the HJA Forest created from the LiDAR point clouds acquired on August 10th and 11th 2008 by Watershed Sciences, Inc.
Coordinate: NAD-1983-UTM-zone-10N
Datum: D-North-American-1983

Figure 2.17 (l)

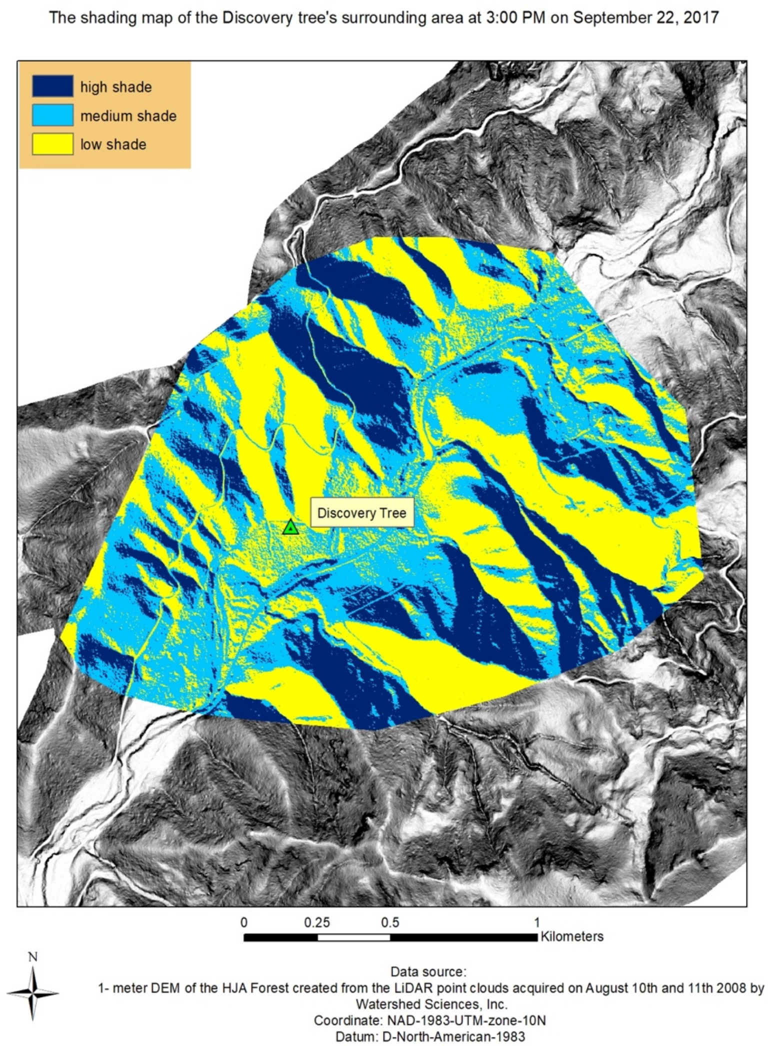
The shading map of the Discovery tree's surrounding area at 3:00 PM on September 22, 2017
high shade
medium shade
low shade
Discovery Tree
0
0.25
0.5
1
Kilometers
N
Data source:
1- meter DEM of the HJA Forest created from the LiDAR point clouds acquired on August 10th and 11th 2008 by Watershed Sciences, Inc.
Coordinate: NAD-1983-UTM-zone-10N
Datum: D-North-American-1983

Figure 2.18

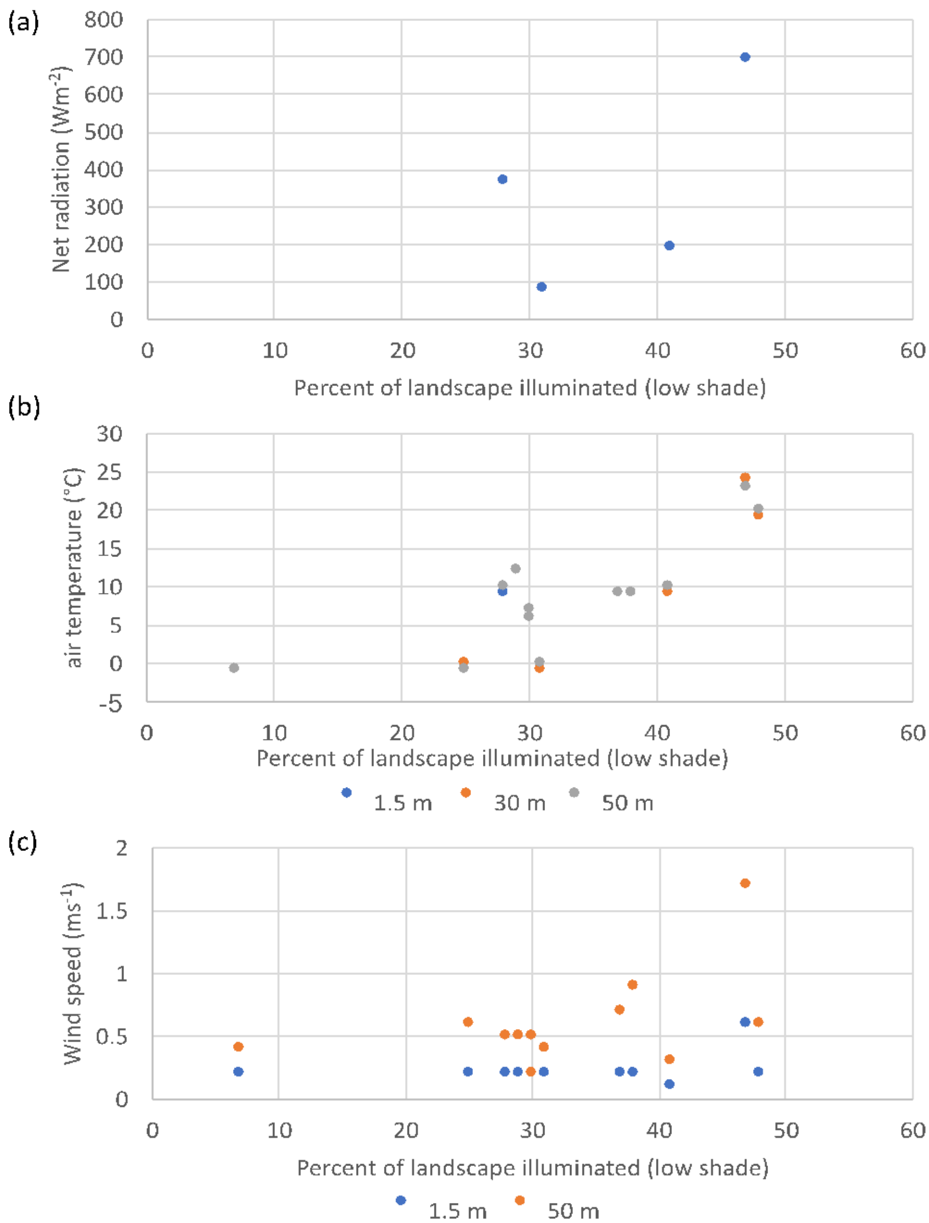
(a)
Net radiation (Wm-2)
800
700
600
500
400
300
200
100
0
0
10
20
30
40
50
60
Percent of landscape illuminated (low shade)
(b)
air temperature (°C)
30
25
20
15
10
5
0
-5
0
10
20
30
40
50
60
Percent of landscape illuminated (low shade)
1.5 m
30 m
50 m
(c)
Wind speed (ms-1)
2
1.5
1
0.5
0
0
10
20
30
40
50
60
Percent of landscape illuminated (low shade)
1.5 m
50 m

Figure 2.18, Cont'd.

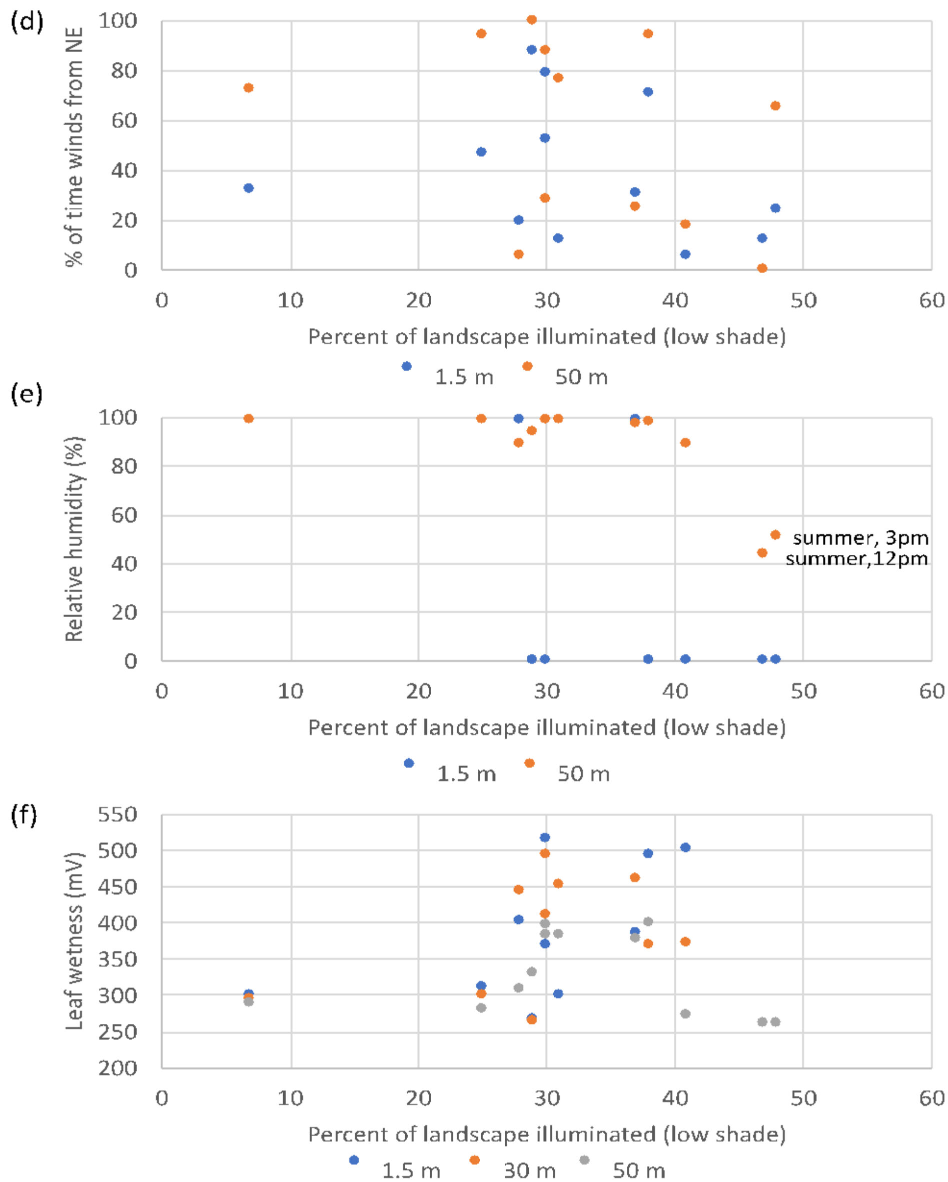

Figure 2.19

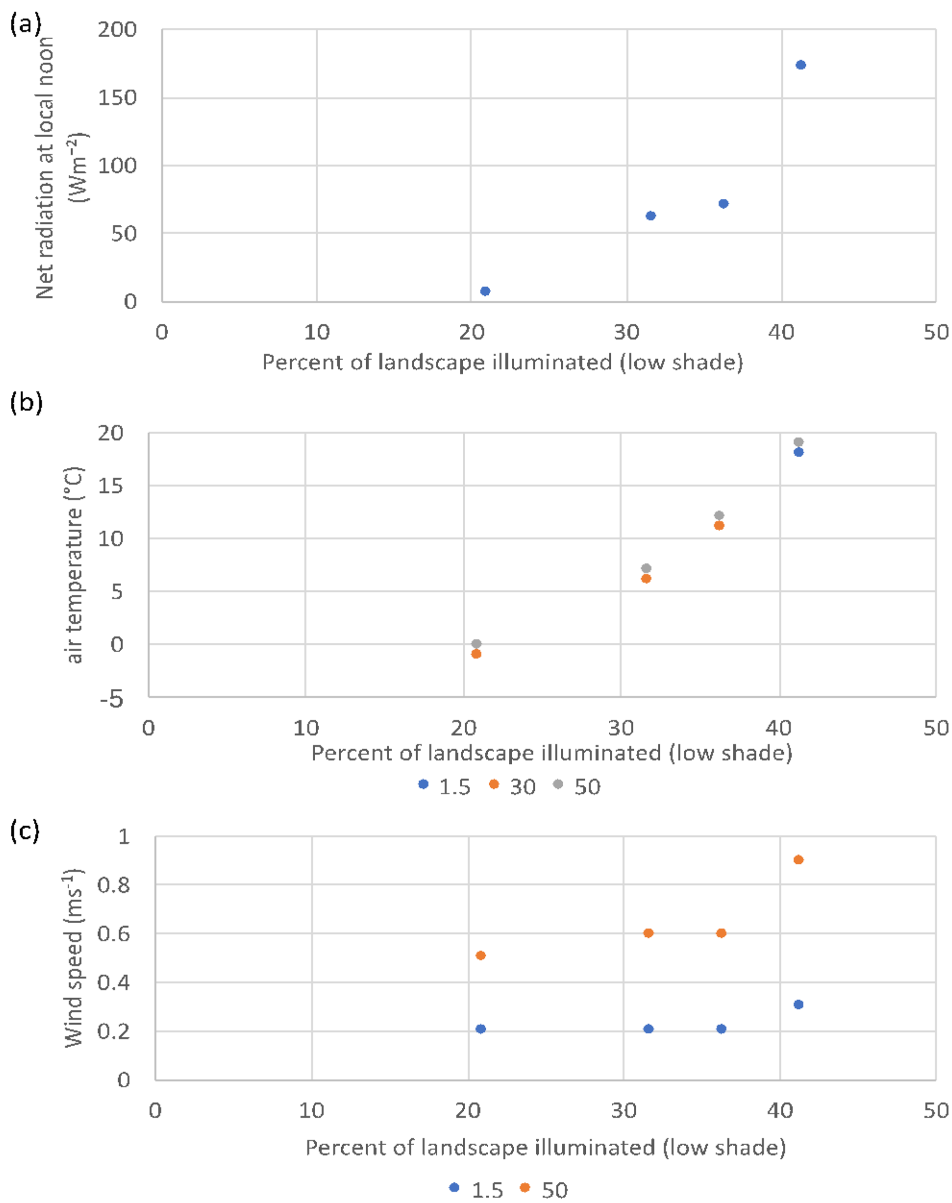
(a)
Net radiation at local noon (Wm-2)
200
150
100
50
0
0
10
20
30
40
50
Percent of landscape illuminated (low shade)
(b)
air temperature (°C)
20
15
10
5
0
-5
0
10
20
30
40
50
Percent of landscape illuminated (low shade)
1.5
30
50
(c)
Wind speed (ms-1)
1
0.8
0.6
0.4
0.2
0
0
10
20
30
40
50
Percent of landscape illuminated (low shade)
1.5
50

Figure 2.19, Cont'd.

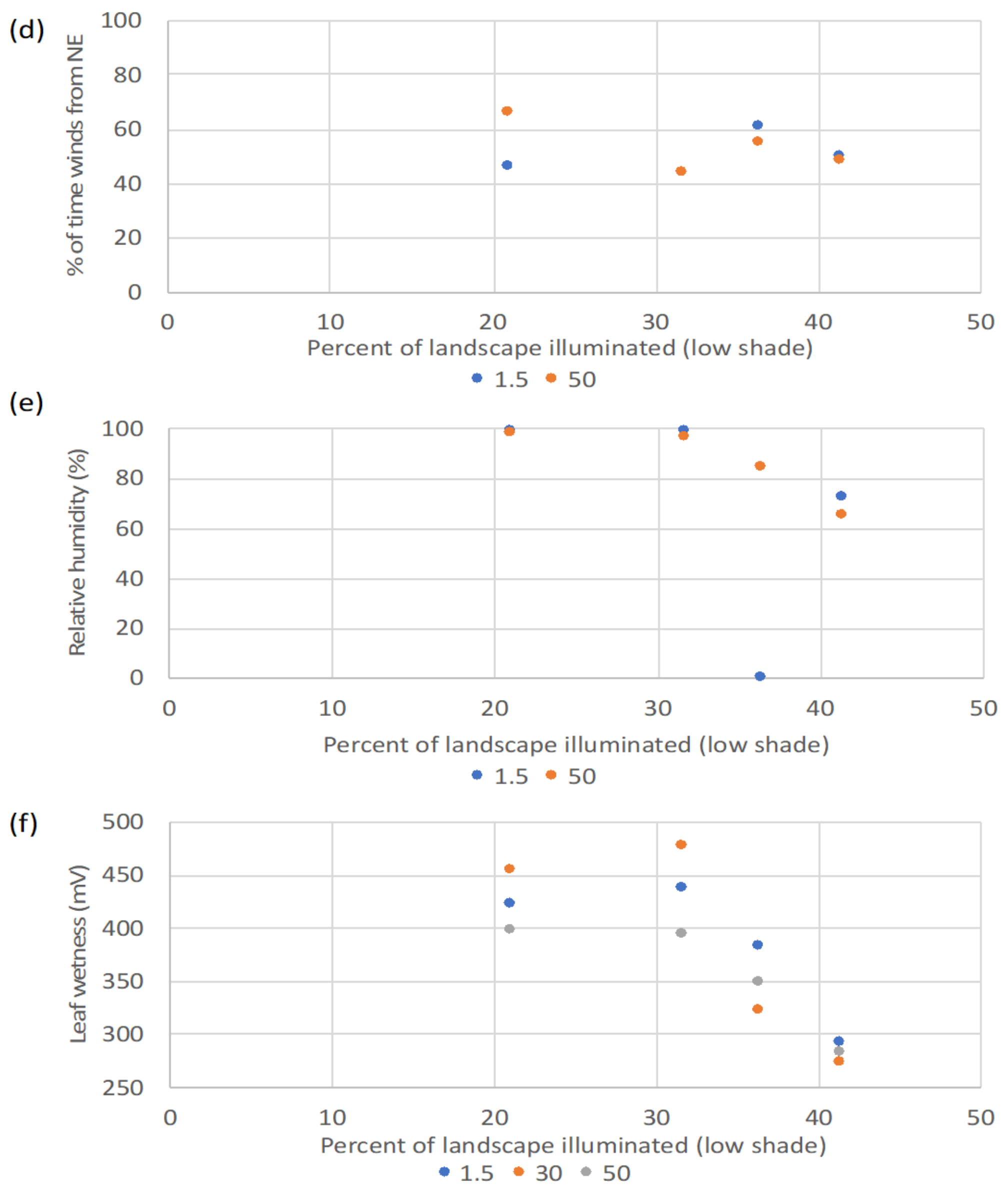

CHAPTER 3

The Influence of seasonal and daily topographic shading and weather variability on inversions in a forested mountain watershed, H.J. Andrews Forest, Oregon

ABSTRACT

The objective of this study was to investigate how solar illumination affects topography-induced shading, local winds, and the frequency of inversions (when the temperature increases with height) in a forested mountain landscape. The study site is the H.J. Andrews Experimental Forest in the western Cascades, Oregon. It was expected that the frequency of stable conditions, i.e. when the lapse rate is more positive than the environmental lapse rate, and the strength of inversions would be greatest when the landscape is most illuminated, and vice-versa. The study used digital elevation data as well as hourly data from a low elevation (PRIMET) and a high elevation (VANMET) meteorological station in the Andrews Forest during months near the solstices and equinoxes (October, January, April, and July) of 2003, 2011, and 2014. Landscape shading is greatest at 0900 hours on all four dates, and least at 1200 at the winter solstice and at 1500 h at the summer solstice and the spring and fall equinoxes. The highest frequency of stable conditions and the strongest inversions occurred in January of 2003, 2011, and 2014. The frequency of inversions was negatively related to solar radiation and positively related to the proportion of the landscape in high shade. Overall, the interaction of sun angle with landscape shading strongly influenced the strength and persistence of inversions in this forested mountain landscape.

Key words: inversion, complex terrain, seasonal variability, landscape shading

3.1. INTRODUCTION

The objective of this study is to investigate how solar illumination affects topographic shading, local winds, and the frequency of inversions in a forested mountain landscape. The study takes advantage of the topography of the Andrews Forest (east-west trending mountain valley) to examine how topography-induced shading is related to long-term weather observations in a valley versus a near-ridge location.

3.1.1. Mechanisms of atmospheric heat exchange that cause inversions

A temperature inversion is the result of the formation of stable cold air in a topographic depression, which results in a positive lapse rate, such that air temperature increases with elevation. The physical mechanisms responsible for formation and dissipation of an inversion include turbulent sensible and radiative heat flux convergence/divergence, advection, and latent heat exchange.

Sensible heat flux is defined as the exchange of energy in the form of heat between a substance and its surroundings that results in temperature change. Radiative heat transfer is one form of sensible heat flux. Radiative heat transfer is defined as the exchange of heat through radiation. Radiative cooling is a mechanism by which a surface loses heat by emitting long wave radiation to the sky. In contrast, radiative heating is a mechanism by which a surface gains heat by receiving incoming shortwave radiation and downward longwave radiation from the sky. The underlying physical law of radiative heating and cooling is described by the Stephan-Boltzman equation (Arya, 2001). This equation states that the thermal energy radiated by a blackbody radiator per second per unit area is proportional to the deficit of the fourth power of the absolute temperature of the radiative surface and the fourth power of the absolute temperature of the ambient air.

$B = e*\partial*A\ (T^4 - Tc^4)$

where

B: the radiated thermal energy per second per unit area (Wm^{-2})

e: emissivity

∂: Stefan-Boltzmann constant, $5.6703 * 10^{-8}\ Wm^{-2}\ K^{-1}$

A: the area of the radiative surface

T: absolute temperature of the radiative surface (K)

Tc: absolute temperature of the ambient air (K)

Energy is provided to a valley atmosphere through surface sensible heat flux (Whiteman and McKee, 1982). When this energy is equal or greater than the required energy for breaking up the cold air pool the inversion breaks up, assuming that there is no energy leakage from the valley.

Leaukauf *et al*., (2015) showed that surface sensible heat flux amplitude increases linearly with solar forcing (incoming shortwave radiation). Their simulation results showed that the selected range of solar forcing required to break up an inversion ranged from 150 W m^{-2} to 850 W m^{-2}. This range is consistent with a range of sensible heat flux amplitudes of 5 to 450 W m^{-2} observed in an experimental study by Rotach and Zardi (2007).

Radiative cooling affects the formation of inversions by decreasing the temperature of the radiated surface and its adjacent layer of air. This mechanism results in sinking of the coldest air to the valley bottom creating an inverted lapse rate, or an inversion. In contrast, radiative heating affects the dissipation of inversions by increasing the convective currents from below due to the release of the turbulent sensible heat flux from the surface. These currents break up the inversion from below. In a shaded landscape, radiative heating may also influence inversions by heating the air or surfaces that are at high elevation and/or illuminated, thus raising the temperature of the air at these high elevation locations relative to the valleys or landforms that are shaded.

Convection is defined as a heat transfer mechanism in which heat is transferred through the movement of molecules in liquid or gas. There are two types of convection: natural and forced convection. Natural convection occurs when the motion is caused by density variation while forced convection occurs when the motion is caused by an outside force such as a pump. The governing equation of convective heat transfer from a surface area is as follows.

$Q^\circ = h*A*\Delta T$

where

Q°: rate of heat transfer (Wm^{-2})

h: convective heat transfer coefficient ($Wm^{-2}K^{-1}$)

A: surface area for heat transfer (m^2)

ΔT: temperature difference (K)

Convective cooling and heating are mechanisms similar to adiabatic cooling and heating. In both mechanisms, cooling and heating occur due to the pressure difference between two locations in a boundary layer. As a warm air parcel ascends, it expands, its density decreases, and it cools adiabatically. In contrast, as a cool air parcel descends, it contracts and its density increases, and thus it warms adiabatically. Convective cooling occurs when the boundary layer is unstable (no inversion) whereas convective heating occurs when the boundary layer is stable.

Advective heating is a mechanism by which the heat is transported laterally due to some external force to a colder area, whereas advective cooling is a mechanism by which a cold air is transported laterally due to some force to a warmer area. The force might be due to the influence of a synoptic scale forcing or the pressure deficit between shaded and illuminated landforms. The underlying physical law in advection is different than convection. In advection, an external force such as a front is needed to transfer the heat whereas in convection, the heat is transferred due to temperature differences.

$$U.\nabla Q = Ux\,{}^{\partial}/_{\partial Qx} + Uy\,{}^{\partial}/_{\partial Qy} + Uz\,{}^{\partial}/_{\partial Qz}$$

where

U = (Ux, Uy, Uz) = velocity field

$\nabla Q := \left(\frac{\partial Q}{\partial x}, \frac{\partial Q}{\partial y}, \frac{\partial Q}{\partial z}\right)$ = gradient of heat (thermal energy) field

Advective cooling decreases the strength of an established inversion layer by decreasing the temperature deficit between the top and the bottom of the inversion layer. This process eventually results in breaking down the inversion. In contrast, advective heating increases the strength of an established inversion by increasing the temperature deficit between the top and the bottom of an inversion layer. This process could result in multi-day inversion events.

Along-valley and cross-valley winds are forms of advective heat exchange. Along-valley winds blow parallel to the valley axis from higher to lower elevations as mountain winds (drainage flow) during calm nights and from lower to higher elevations as valley winds during daytime. Cross-valley winds blow perpendicular to the valley axis from the less heated sidewall towards the more heated sidewall. Both along-valley and cross-valley winds are thermally driven flows. Anabatic refers to winds blowing upslope or up-valley, whereas katabatic refers to winds blowing downslope or down-valley.

Latent heat exchange is a mechanism in which energy is gained or lost during a change of phase while the temperature remains unchanged. Cooling occurs through the release of evaporative latent heat whereas warming occurs through the absorption of condensation latent heat. During the phase change of one gram of liquid water to one gram of water vapor, 540 calories of latent heat are absorbed whereas during the phase change of one gram of water vapor to one gram of liquid water, 540 calories of latent heat are released.

3.1.2. Factors that produce and disperse temperature inversions

The formation of valley inversions is an important process in forested mountain landscapes. Several empirical studies have examined how topographic shading and weather conditions influence this process.

3.1.2.1. Synoptic factors (anticyclonic, cyclonic, and zonal flow)

Dobrowski *et al* (2009) examined the absolute and relative influences of landscape-scale topographic factors in mitigating regional temperatures. The temperature variance was decomposed into components related to the free-air (synoptic = regional scale) and physiographic (local scale) effects. The results showed that 80 % of the variance was due to the synoptic scale and the remaining 20 % was due to local (landscape) scale effects. In addition, they noted that the effect of physiographic (landform) variables changes seasonally and is controlled by physiography. Thus, during well-mixed periods a simple elevation-based lapse rate can be used to estimate temperature, while during unstable periods (fair weather conditions) physiographic factors are much more important for estimating temperature (Dobrowski *et al.* 2009).

3.1.2.2. Weather: warm fronts, cold fronts, precipitation, and wind

Lu and Zhong (2013) showed that synoptic forcing and radiative cooling combine to affect persistent cold air pooling events. Synoptic forcing (regional winds) increases the velocity of drainage (down-valley) flow due to the accumulating effect of the wind speeds. By examining the influence of warm and cold air advection in formation and dissipation of three persistent cold air pooling events in Salt Lake Valley, Utah during 12-15 December 2012, Lu and Zhong (2013) showed that the inversion events were formed mainly by the combined effect of synoptic subsidence and advection of warm air from above and radiative flux divergence (radiative cooling) in the valley under anti-cyclonic (clear sky) conditions. In contrast, the inversion events were dissipated by the combined effect of warm advection from southerly winds and the synoptic-scale cold advection from above. The intrusion of cold air at top of the valley weakened the inversion by decreasing the temperature deficit between the valley bottom and top (Lu and Zhong 2013).

3.1.2.3. Topographic shading and cold air drainage and pooling

Matzinger *et al.* (2003) compared the surface radiation budget between days with fair weather conditions versus overcast days in the Riviera Valley in southern Switzerland from August to October 1999. They argued that the difference between the incoming longwave radiation between the valley-floor and slope sites is larger during days with no cloud cover compared to overcast days because the valley side walls have higher temperature and emit more longwave radiation compared to the valley-floor during the day. In addition, the authors found that topographic shading has an important role in spatio-temporal variation of radiation in a valley when the solar altitude (the angle of the Sun relative to the Earth's horizon) changes diurnally. They documented a decrease in the downward longwave radiation and an increase in the net radiation with increasing elevation in this mountain valley (Matzinger *et al*. 2003).

Colette *et al*. (2003) simulated the breakup of inversions in several idealized valleys of varying shape, ranging from very steep to very wide, using the Advanced Regional Prediction System (ARPS). They showed that the effect of topographic shading in an idealized valley is very significant especially during very early morning hours, because landscape shading delays the onset of upslope flows, which in turn delays the breakup of the inversion. They argue that the effect of topographic shading is more important in steep valleys. Thus, terrain shading effects have been shown to influence the timing of inversion layer breakup and slope wind systems in idealized valleys (Colette *et al.* 2003).

Hoch and Whiteman (2009) examined the different effects of topography (terrain exposure, terrain shading, and terrain reflection) on the surface radiation budget in and around Arizona's Meteor Crater at three sites on the crater floor, mid slope, and crater rim on four clear days during 19-22 October 2006. The rim site received larger direct but smaller diffuse radiation, whereas the crater floor site received smaller direct but larger diffuse radiation. The authors attribute this difference to the reflection of shortwave radiation on the elevated terrain of the crater sidewalls. In addition, shading affected the receipt of direct solar radiation by delaying local sunrise and advancing local sunset. Sites on the lower western and eastern sidewalls of the crater were affected by shading more than the sites on steep locations or on the crater rim. Moreover, the crater walls as well as high elevation landforms surrounding the crater also reflect diffuse radiation, which affects the balance of shortwave radiation in the crater. Thus, when the crater floor was fully illuminated, diffuse shortwave radiation reflected from illuminated crater sidewalls caused diffuse radiation to be higher at the crater floor than at the sloping site or the crater rim.

The emission of longwave radiation from the sidewalls during nights affected the life cycle of inversion events in the crater. The radiative cooling of the sidewalls caused the initiation of drainage flow and its subsequent accumulation in the crater floor. This process was followed by the advection of warmer air aloft due to mass conservation law (continuity equation). As a result, the sidewalls became warmer compared to their surroundings and started to emit longwave radiation due to radiative cooling. This process produced cold air which drained to form cold air pools. On the other hand, the accumulated cold air pool at the floor caused the outgoing longwave radiation to decline based on the Stefan-Boltzman's law (Hoch and Whiteman, 2009).

3.1.2.4. Relative importance of synoptic vs. topographic factors

Pepin *et al.* (2012) investigated the effect of "decoupling" of local air from synoptic air using historical climate data in the Central and Western parts of the U.S. from 1948 to 2006. Decoupling is defined as the boundary layer condition in which the local weather is not affected by the synoptic weather condition. The authors developed and applied topographic, coupling, and fair weather indexes to explain patterns in the weather data. Both synoptic weather patterns (at the regional scale) as well as local topography affected decoupling. The surface marine layer on the west coast of the U.S. (a regional scale phenomenon) affected decoupling especially during summer, as did the jet stream (Pepin *et al.,* 2012). In contrast, Daly *et al.,* (2010) found that although topography was less important than synoptic forcing (cyclonic condition) in the formation of cold air pooling during winter, this effect reverses during summer when the anti-cyclonic condition prevails.

Kiefer *et al.* (2015) examined the influence of valley geometry and canopy density on the evolution of cold air pooling using numerical simulation. They considered alternative configurations of canopy density ranging from bare ground to dense canopy, as well as alternative valley geometry ranging from a small, narrow valley to a medium valley. They showed that the cold air pool is the strongest in the medium sized valley, and the minimum potential temperature was 15K warmer under a dense canopy compared to bare ground (Kiefer *et al.* 2015).

3.1.3. Gaps in knowledge

Relatively few studies have addressed the role of landform illumination on the frequency of inversions in mountain landscapes. In other words, there is a lack of knowledge on how landforms interact with solar illumination to produce inversions. This study proposes that, for any landscape, there should be a threshold value of solar illumination angle, such that solar illumination angles below this threshold contribute to the formation of inversions, whereas angles above this threshold contribute to the dissipation of inversions.

3.1.4. Study objectives and research questions

The objective of this study is to estimate the frequency of temperature inversions observed under clear-sky conditions for various times of year in a mountain landscape, and to test how topographic shading and winds influence the formation and breakup of temperature inversions. This study takes advantage of long-term meteorological data at low and high elevations in a forested mountain valley at the HJ Andrews Forest in western Oregon.

Research questions:

1. How does landscape illumination vary by season and time of day throughout the year?
2. How are landscape illumination and associated wind speeds and directions at various times of year related to the observed frequency of inversions?

3.2. STUDY SITE

Established in 1948, the Andrews Forest is a 64 km^2 experimental site in the western Cascades Range of Oregon (Lat: 44° 3′ 37" N; Long: 122° 5′ 30" W) and a long-term ecological research (LTER) site supported by NSF. The Andrews Forest is steep, westward draining mountain valley of Lookout Creek, a 5th-order river basin characterized by complex topography, including V-shaped and U-shaped valleys, alluvial fans, fluvial terraces, hillslopes, and vegetated floodplains (Figure 3.1). Elevation ranges from 410 m to over 1600 m above sea level. The higher elevations are located in the NE and some parts of the south whereas the lower elevations are located in the NW and west part of the forest. Landforms at higher elevations of the east part of the forest show evidence of glaciation, while large mass movements have affected much of the east and central portions of the Forest. The east-west alignment of the Lookout Creek valley and the variety of landforms such as deep narrow valleys, ridges, hills, and some mass movement patterns create a complex landscape in which the solar altitude and landform interact to creates high spatial and temporal variability of illumination.

The climate of the Andrews Forest varies seasonally as a result of global circulation patterns. Energy and moisture are transported globally through three types of circulation cells: Hadley, Ferrel, and polar. Hadley cells are responsible for circulating heat and moisture from the equator to 30° latitudes, whereas Ferrel and polar cells are responsible for circulating heat and moisture from 30° to 60° and 60° to the poles, respectively. The Andrews Forest is located at mid latitude, and it is affected by Ferrel cell circulation, which produces prevailing westerly winds that bring warm air from the SW to the Andrews. Since warm air has lower pressure compared to cold air, it rises, causing an unstable boundary layer condition (cyclonic). Given that the westerlies are stronger in winter compared to summer, therefore, the cyclonic condition is stronger in winter compared to summer, causing frequent unstable atmospheric condition (low pressure) over the

Andrews forest. This condition brings high amount of moist air and precipitation to the forest. In addition, maritime polar air masses (mP) affect the Pacific Northwest throughout the year. Maritime polar air masses cause heavy rain and cool air on the windward of a mountain range, but transform to continental polar air mass (cP) as they move to the leeward of a mountain range, producing dry, cold air and heavy snow. In contrast, in summer, when the strength of the westerlies is diminished and the polar jet stream migrates further to the north, anti-cyclonic conditions (high pressure systems) bring fair weather to the Andrews Forest (Christopherson, 2012). Average annual precipitation at the Andrews Forest is approximately 2500 mm, and most of this precipitation occurs between November and March. At higher elevation the precipitation is in the form of snow, while at the lower elevations rain is the dominant form of precipitation.

Vegetation is forest, dominated by Douglas fir (*Pseudotsuga menziesii*) and western hemlock *(Tsuga heterophylla)* at low elevation and noble fir (*Abies Procera*) and Pacific silver fir (*Abies amabilis)* at high elevation.

Topographic shading is affected by various landforms of the Andrews Forest including mountain ridges, deep incised valleys, small to medium sized hills, glaciated U-shaped valleys, and different mass wasting types such as landslides, debris flow, slump, and creep (Figure 3.1). Topographic shading is divided into shaded relief and cast shadow. Shaded relief is the self-shadowing of an object at a given location and is due to slope and aspect relative to sun angle, whereas cast shadow is due to the shadow created by the topographic feature (Olson and Rupper, 2018). Therefore, when the solar angle is low (during early morning and late afternoon) the cast shadow effect becomes very pronounced. At high elevation in the Andrews Forest (such as VANMET) when the solar angle is low, the site is affected by shaded relief but when the solar angle is high, the site is not affected by shaded relief or shadow cast. In contrast, at low elevation in the Andrews Forest (such as PRIMET) the site is affected by shadow cast due to its topographic location. The E-W trending valley, and the many narrow incised tributaries of Lookout Creek in the Andrews Forest are strongly affected by shaded relief. The interaction of incoming shortwave radiation with these landforms creates a complex pattern of illuminated versus shaded surfaces across the landscape. Because illuminated surfaces receive more sensible heat flux compared to shaded surfaces, their temperature is higher. These patterns of energy surplus and energy deficit are expected to produce complex patterns of air temperature and winds in the Andrews Forest. The interaction of the above processes with the spatial pattern of net energy across the landscape makes the Andrews Forest a suitable site for studying the dynamics of cold air drainage and pooling during different times of year.

3.3. METHODS

The study used hourly data from a low elevation (PRIMET) and a high elevation (VANMET) meteorological stations in the Andrews Forest in October, January, April, and July of 2003, 2011, and 2014. The study goal was to test hypotheses about factors associated with air temperature inversions at different times of day and different seasons.

3.3.1. Thesis statement

Inversions in a forested mountain landscape depend upon solar altitude and horizontal solar azimuth, a measure of day length, because topographic shading affects radiative heating and cooling of the surface, which in turn affect convective and advective heat exchanges.

3.3.2. Hypotheses and predictions

H1: The solar altitude (and day length) interacts with mountain landforms to produce terrain shading, which leads to spatial variation in net radiation. Positive radiation balances produce heating in illuminated areas, while negative radiation balances produce cooling in shaded areas.

Prediction 1: Air temperature is expected to be higher in locations with greater illumination (i.e., mountain ridges, equator-facing slopes) compared to shaded areas (i.e., mountain valleys, polar-facing slopes). Hence, inversions (higher air temperature at high vs. low elevation) are expected to occur during the daytime at low solar altitudes (or short day lengths), because much of the landscape is shaded.

H2: (a) The differential heating of and cooling of illuminated and shaded areas produces spatial variation in air pressure, creating local winds (10 to 20 km scale) that blow from shaded (cool, high pressure) to unshaded (warm, low pressure) areas. These processes produce cold air drainage originating from shaded (unlit) areas, and upslope (up-valley) winds from illuminated areas of the mountain landscape.

Prediction 2: Hence, when synoptic (upper-elevation) wind speeds are low, wind directions are expected to be up-slope and up-valley during the daytime.

H2: (b) When the mountain landscape is not illuminated, and synoptic wind (a category of wind which spans a few hundred to a few thousand kilometers and have a short life span) speeds are low, the net negative radiation balance produces cooling and descending air, which interacts with topography to flow downslope, producing cold air drainage.

Prediction 3: Wind speeds are expected to be relatively low and wind directions are expected to be downslope or down-valley at night, resulting in more inversions at night than daytime.

H2: (c) When synoptic wind speed is high, convective processes overwhelm the effects of differential illumination and radiation balances on heat exchange, breaking up inversions or preventing their formation.

Prediction 4: When synoptic (upper elevation) wind speeds are high, low elevation wind speeds and wind directions are expected to be variable and unrelated to landforms.

3.3.3. Data

A DEM was obtained from 1-meter resolution LiDAR points cloud of the HJ Andrews Forest in 2008 (http://andlter.forestry.oregonstate.edu/data/spatialdata/gi01001.htm). Shaded relief models were fitted using the Hillshade function in ArcMap10.3. Solar altitude and azimuth were calculated for three times of a day: 0900h, 1200h, and 1500h, on December 21, 2016 (winter solstice), June 21, 2017 (summer solstice), March 21, 2017 (spring equinox), and September 22, 2017 (fall equinox). A total of twelve shaded relief models were created, for these three times of day on each of the four days. The resulting DN values were classified into three categories of shading: high shade (0 to 85), moderate shade (86 to 170) and low shade, or high illumination (171 to 255) by dividing the overall distributions of DN values into thirds. The values were classified using manual method in the classification algorithm. The proportion of the HJ Andrews that was in each shade category at each time of day and time of year was calculated from the resulting shaded relief maps (Table 3.1).

Data on air temperature, radiation, wind speed, and wind direction were obtained from http://andlter.forestry.oregonstate.edu/data/abstract.aspx?dbcode=MS001. The study used data from two meteorological stations, PRIMET and VANMET. Primet is located at 450 meters above sea level on a fluvial terrace while Vanmet is located at 1250 meters above sea level close to a ridge.

The study used data from 2003, 2011, and 2014 because 2011 and 2014 were the coldest and the warmest years from 1995 to 2014, and 2003 was the second warmest year in this period in Oregon (Figure 3.2). Mean daily mean air temperature data from 1995 to 2014 showed different hottest and coolest years at Primet compared to Vanmet (Table 3.5). Thus, the warmest and the coldest years were selected based on the NOAA data (Figure 3.2).

Hourly air temperature, radiation, wind speed and direction data in 2003, 2011, and 2014 were obtained from different probes at PRIMET and Vanmet. In 2011, all the above weather variables were obtained from probe 6 at 3.5-meter height at both Primet and Vanmet whereas in 2003, the variables were obtained from probe 1 at 3.5-meter height at both stations. In 2014, hourly air temperature at Primet was obtained from probe 7 at height of 450 cm whereas the hourly air temperature at Vanmet was obtained from probe 8 at height of 350 cm. Radiation data were obtained from probe 1 at height of 100 cm at Primet whereas it was obtained from probe 1 at height of 860 cm at Vanmet. The wind speed and direction were obtained from probe 2 (Sonic anemometer) at the height of 1000 cm at both Primet and Vanmet. Data from different probes were used because no single probe had complete data over the course of the three years.

3.3.4. Analyses

Inversions were defined from the mean hourly air temperature at Vanmet minus Primet. These air temperature differences can be converted to lapse rates (°C/1000 m) using the conversion factor 1000/845 (the elevation difference between the two stations is 845 m). Positive values mean the temperature increases with height whereas negative values mean the temperature decreases with height. The former means the boundary layer is inverted (stable conditions) while the latter means the boundary layer is convective (unstable conditions).

Hourly air temperature differences were calculated for each year (2003, 2011, and 2014) as a whole, and for four months (April, July, October, and January) which represent different seasons (spring, summer, fall, winter) and corresponding solar altitudes (equinoxes and solstices).

Hourly air temperature differences were separated into “day” and “night” using a conditional statement in Excel which grouped air temperature deficits based on whether the radiation was zero (night) or otherwise (day).

Distributions (histograms) were created showing the proportion of hours that were associated with specific air temperature differences between VANMET and PRIMET, subdivided by night and day, by season (winter and summer, spring and fall), and by year. Bin values ranged from -10° C to + 10° C based on the assumption that this range of temperature values captures most of the temperature differentials between Primet and Vanmet. These distributions were compared to assess the effect of night vs. day, time of day (sun angle), season (sun angle), and year, on the air temperature difference (VANMET – PRIMET), and on wind speed and direction at VANMET and PRIMET.

3.4. RESULTS

3.4.1. Landscape illumination

Table 3.1

Figures A3.61 to A3.64.

Shading of the landscape varies with solar altitude. The greatest amount of shading occurs at the winter solstice, whereas the greatest amount of illumination occurs at the summer solstice (Table 3.1, Figures A3.61 to A3.64). The percent of the landscape in high shade is greatest at 0900 hours on all four dates. However, the percent of the landscape in low shade (illuminated) is highest at 1200 at the winter solstice, but highest at 1500 h at the summer solstice and the spring and fall equinoxes (Table 3.1, Figures A3.61 to A3.64).

3.4.2. Daytime lapse rates

Table 3.2

Figures A3.1, A3.11 (2011)

Figures A3.21, A3.31 (2003)

Figures A3.41, A3.51 (2014)

Hourly air temperature differences during the daytime for the entire year ranged from -9°C to more than 10°C for 2003, -10°C to more than 10°C for 2011, and -8°C to more than 10°C for 2014 (Figures A3.1, A3.21, A3.41). The lapse rate was equal to or higher than the environmental lapse rate, indicating unstable conditions, during the following percentages of hours for those years: 22 % for 2003, 20 % for 2011, and 13 % for 2014 (Table 3.2). Temperature inversions (stable conditions, lapse rate > 0) occurred on >20% of daytime hours (Table 3.2, Figures A3.1, A3.21, A3.41).

The frequency of stable and unstable conditions during the daytime varied by season (Table 3.2). The strongest daytime inversions (most stable conditions, lapse rate > 5.5°C) occurred in January (Table 3.2, Figures A3.11, A3.31, A3.51). The highest frequency of daytime inversions occurred in January (>40% of hours), and the lowest occurred in April (<12%, Table 3.2, Figures A3.11, A3.31, A3.51). The highest frequency daytime unstable conditions (lapse rate equal to or more negative than the environmental lapse rate) was in April (25 to 31% of hours), and the lowest was in January (<1% of hours) (Table 3.2).

3.4.3. Nighttime lapse rates

Table 3.2

Figures A3.2, A3.12 (2011)

Figures A3.22, A3.32 (2003)

Figures A3.42, A3.52 (2014)

Hourly air temperature differences during the nighttime for the entire year ranged from -8°C to more than 10°C for 2003, -7°C to more than 10°C for 2011, and -7°C to more than 10°C for 2014 (Figures A3.2, A3.22, A3.42). The lapse rate was equal to or higher than the environmental lapse rate, indicating unstable conditions, during the following percentages of hours for those years: 66 % for 2003, 71 % for 2011, and 70 % for 2014 (Table 3.2). Temperature inversions (stable conditions, lapse rate > 0) occurred in more than 26% of nighttime hours (Table 3.2, Figures A3.2, A3.22, A3.42).

The frequency of stable and unstable conditions during the nighttime varied by season (Table 3.2). The strongest nighttime inversions (most stable conditions, lapse rate > 5.5°C) occurred in January (Table 3.2, Figures A3.12, A3.32, A3.52). The highest frequency of nighttime inversions occurred in January (>49% of hours), and the lowest occurred in April (<16%, Table 3.2, Figures A3.12, A3.32, A3.52). The highest frequency nighttime unstable conditions (lapse rate equal to or more negative than the environmental lapse rate) was in July (1 to 6% of hours), and the lowest was in January (<2% of hours) (Table 3.2, Figures A3.12, A3.32, A3.52).

3.4.4. Wind speeds and directions, valley floor site (Primet)

Table 3.3

Figures A3.3, A3.4, A3.7, A3.8, A3.13, A3.14, A3.17, A3.18 (2011)

Figures A3.23, A3.24, A3.27, A3.28, A3.33, A3.34, A3.37, A3.38 (2003)

Figures A3.43, A3.44, A3.47, A3.48, A3.53, A3.54, A3.57, A3.58 (2014)

Daytime average wind speeds at Primet varied from 0.8 m s^{-1} in 2003 and 2014 to 1.1 m s^{-1} in 2011 (Figure A3.3, A3.23, and A3.43). Wind speed was zero for 26 % of hours in 2003, 31% of hours in 2011, and 0 % of hours in 2014. Wind speed exceeded 2 m s^{-1} for 7 % of daytime hours in 2003, 1% in 2011, and 0 % in 2014 (Table 3.3, Figure A3.3, A3.23, and A3.43).

Daytime wind speeds at Primet varied by season and among years (Table 3.3). The highest average daytime hourly wind speeds at Primet occurred in January of 2003 and 2014, and April of 2014 (Table 3.3, Figure A3.13, A3.33, and A3.53). The lowest average daytime hourly wind speeds occurred in January in 2011, followed by October in 2011, April in 2011, and July in 2003. The highest average daytime hourly wind speeds occurred in January in 2003, July in 2011, and January in 2014 (Table 3.3, Figure A3.13, A3.33, and A3.53).

Daytime wind directions at Primet were dominated by winds from the southwest (up-valley). The wind direction was from the SW (up-valley, 180° to 270°) for 31 % of daytime hours in 2003, 43 % in 2011, and 40 % in 2014 (Table 3.3, Figure A3.4, A3.24, A3.44).

Daytime wind directions at Primet varied by season and among years. Daytime wind directions were dominated (i.e., more than one-third of hours) by winds from the southwest (up-valley, 180° to 270°) in January and July of 2003; April, July, and October of 2011; and January, July, and October of 2014 (Table 3.3, Figure A3.14, A3.34, and A3.54). Daytime wind directions were dominated (i.e., more than one-third of hours) by winds from the northeast (down-valley, 0° to 90°) in October of 2003 (Table 3.3, Figure A3.14, A3.34, and A3.54).

Nighttime average wind speeds at Primet were less than 0.4 m s^{-1} in 2003 and less than 0.8 m s^{-1} in 2011 and 2014. (Table 3.3, Figure A3.7, A3.27, and A3.47). Wind speed was zero for 65% of nighttime hours in 2003, 78% in 2011, and 0 % in 2014 and <0.5 m s^{-1} for 65 % of nighttime hours in 2003, 0 % in 2011, and 0 % in 2014. Wind speed exceeded 2 m s^{-1} for 7% of daytime hours in 2003, 1% in 2011, and 0% in 2014 (Table 3.3, Figure A3.7, A3.27, and A3.47).

Nighttime wind speeds at Primet did not vary by season and among years (Table 3). Average nighttime hourly wind speeds at Primet did not differ by month in 2003, 2011, and 2014 (Table 3.3, Figure A3.17, A3.37, and A3.57).

Nighttime wind directions at Primet were dominated by winds from the northeast. The wind direction was from the NE (0° to 90°) for 16 % of nighttime hours in 2003, 8 % in 2011, and 42 % in 2014 (Table 3.3, Figure A3.8, A3.28, A3.48).

Nighttime wind directions at Primet varied by season and among years. Wind directions were dominated by winds from the north (cross-valley or down-valley, 315° to 45°) in January, April, July and October of 2014, but nighttime winds were practically undetectable in 2003 and 2011 (Table 3.3, Figure A3.18, A3.38, and A3.58).

3.4.5. Wind speeds and directions, near ridge site (Vanmet)

Table 3. 4
Figures A3.5, A3.6, A3.9, A3.10, A3.15, A3.16, A3.19, A3.20 (2011)
Figures A3.25, A3.26, A3.29, A3.30, A3.35, A3.36, A3.39, A3.40 (2003)
Figures A3.45, A3.46, A3.49, A3.50, A3.55, A3.56, A3.59, A3.60 (2014)

Daytime wind speeds at Vanmet varied from 0 to more than 3.75 m s^{-1} in 2003, 0 to 2.5 m s^{-1} in 2011, and 0 to more than 3.75 m s^{-1} in 2014 (Figure A3.5, A3.25, and A3.45). Average daytime wind speeds at Vanmet were 1.8 m s^{-1} in 2003, 1.4 m s^{-1} in 2011, and 1.6 m s^{-1} in 2014 (Table 3.3). Wind speed was zero for 0 % of hours in 2003, 1% of hours in 2011, and 0 % of hours in 2014. Wind speed exceeded 2 m/s for 27 % of daytime hours in 2003, 4 % in 2011, and 10 % in 2014 (Table 3.4, Figure A3.5, A3.25, and A3.45).

Daytime wind speeds at Vanmet varied by season and among years (Table 3.4). The highest daytime hourly wind speeds at Vanmet occurred in January and July of 2003, July and October of 2011, and April of 2014 (Figure A3.15, A3.35, A3.55). The lowest daytime hourly wind speeds occurred in April of 2003, January of 2011, and July of 2014. Wind speed was zero for 2% of hours in April of 2003, 5 % of hours in April of 2011, and 0 % of hours in January of 2014 (Table 3.4, Figure A3.15, A3.35, A3.55).

Daytime wind directions at Vanmet were dominated by winds from the southwest. The wind direction was from the SW (180° to 270°) for 22 % of daytime hours in 2003, 73 % in 2011, and 68 % in 2014 (Table 3.4, Figure A3.6, A3.26, A3.46).

Daytime wind directions at Vanmet did not vary by season or among years. Wind directions were dominated by winds from the southwest (up-slope, 180° to 270°) in January, April, July and October of 2003, 2011 and 2014 (Table 3.4, Figure A3.16, A3.36, and A3.56).

Nighttime wind speeds at Vanmet varied from 0 to 2.75 m s^{-1} in 2003, 0 to >3.75 m s^{-1} in 2011, and 0 to >3.75 m s^{-1} 2014 (Figure A3.9, A3.29, and A3.49). Average nighttime wind speed at Vanmet was 1.7 m s^{-1} in 2003, 1.4 m s^{-1} in 2011, and 1.6 m s^{-1} in 2014 (Table 3.4). Wind speed was zero for 1% of nighttime hours in 2003, 2% of hours in 2011, and 0 % of hours in 2014. Wind speed exceeded 2 m/s for 23% of nighttime hours in 2003, 5% in 2011, and 12% in 2014 (Table 3.4, Figure A3.9, A3.29, and A3.49).

Nighttime wind speeds at Vanmet varied by season and among years (Table 3.4). The highest nighttime hourly wind speeds at Vanmet occurred in January and July of 2003, January of 2011, and January of 2014 (Table 3.4, Figure A3.19, A3.39, and A3.59). The lowest daytime hourly wind speeds occurred in October in 2003, July in 2011, and July in 2014 (Table 3.4).

Nighttime wind directions at Vanmet were dominated (greater than one-third of hours) by winds from the SW (up-slope, 180 to 270°) and NE (downslope, 0 to 90°). The wind direction was from the NE (0° to 90°) for 23 % of nighttime hours in 2003, 37 % in 2011, and 47 % in 2014 (Table 3.4, Figure A3.10, A3.30, A3.50).

Nighttime wind directions at Vanmet varied by season and among years. Wind directions were dominated by winds from the northeast (down-slope, 0 to 90°) in January of 2003; July of 2011; and January, July and October of 2014 (Table 3.4, Figure A3.20, A3.40, and A3.60). Wind directions were dominated by winds from the southwest (up-slope, 180 to 270°) in January, April, and July of 2003; January, April, and October of 2011; and January, April, July, and October of 2014 (Table 3.4, Figure A3.20, A3.40, and A3.60).

The results show that the total number of hours with inversion in 2003, 2011, and 2014 were 919, 666, and 997 respectively. In 2003, on average 341 hours (37%) of inversion occurred in January, 32 hours (3%) in April, 239 hours (26%) in July, and 307 hours (33%) in October. During January, the inversion events were mostly persistent (lasted more than 24 hours), in April diurnal and occurred during night, in July diurnal and occurred during night and morning, and in October diurnal and multi-day.

In 2011, on average 417 hours (63%) of inversion occurred in January, 20 hours (3%) in April, 87 hours (13%) in July, and 142 hours (21%) in October. During January, the inversion events were mostly persistent (lasted more than 24 hours), in April diurnal and occurred during night, in July diurnal and occurred during night and early morning, and in October diurnal and multi-day.

In 2014, on average 489 hours (49%) of inversion occurred in January, 90 hours (9%) in April, 164 hours (16%) in July, and 254 hours (25%) in October. During January, the inversion events were mostly persistent (lasted more than 24 hours), in April diurnal and occurred during night and early morning, in July diurnal and occurred during night and early morning, and in October mostly multi-day.

January and April had the largest and the smallest numbers of hours with inversion in all three years. The smallest and the largest numbers of hours with inversion occurred in April 2011 and January 2014 respectively (Figure 3.5).

During inversion in January, the wind direction at Primet was from the NE in 2003 and 2011 and from the N and the NE in 2014 whereas at Vanmet the wind direction was from the NE and SW in 2003, the W and SW in 2011, and N, S, and SW in 2014 (Figures 3.5, 3.6).

During inversion in April, the wind direction at Primet was multi-directional in all three years whereas the wind direction at Vanmet was SW in 2003, and multi-directional in 2011 and 2014 (Figures 3.5, 3.6).

During inversion in July, the wind direction at Primet was from the N and the SW in 2003, NE, and SW in 2011, and the N and the SW in 2014 whereas at Vanmet the wind direction was from N, NW, and SW in 2003, NE and SW in 2011, N and SW in 2014 (Figures 3.5, 3.6).
During inversion in October, the wind direction at Primet was from the NE in 2003, multi-directional in 2011, N, NE and SE in 2014 whereas at Vanmet the wind direction was from the NE, NW, and SW in 2003, multi-directional in 2011, the N and SW in 2014 (Figures 3.5, 3.6).
The wind direction at Primet during non-inversion hours in 2014 was multi-directional in January, E, SE, S, W, and SW in April, SW to N in July, and multi-directional in October (Figure 3.5, 3.6).
In general, the result show that the wind direction co-vary with inversion at both Primet and Vanmet in January and April of 2003, 2011, and 2014. In January the wind direction at Primet and Vanmet was NE and SW respectively. In contrast, in April, the wind direction at both Primet and Vanmet was multi-directional.

3.5. DISCUSSION

Solar altitude and azimuth change daily and monthly, resulting in the receipt of different amounts of incoming solar radiation by the Earth's surface in different times of day and different seasons. The receipt of incoming solar radiation by the Earth's surface is a function of solar altitude, solar horizontal azimuth, topography (slope, aspect, elevation), and atmospheric conditions (presence of clouds). Positive radiation balances produce heating in illuminated areas, while negative radiation balances produce cooling in shaded areas. Observed air temperature, wind speed and wind direction in shaded areas differ from those in illuminated areas. In mountain landscapes the land surface receives highly variable amounts of solar radiation due to the influence of topographic-induced shading. Therefore, high spatial variability is expected in observed air temperature, wind speed and wind direction.

Because soil moisture availability is a function of soil temperature, the low temperature shaded surfaces should have more moisture compared to the high temperature illuminated surfaces. This is important in understanding some of the hydro-ecological and hydro-meteorological processes that occur on forest soil (under forest canopy). Since the distribution of fauna and flora on the forest soil is a function of soil moisture, shaded surfaces may support higher diversity of fauna and flora compared to the illuminated surfaces when the soil is dry during summer. The reason is that soil moisture is a limiting factor and becomes more important when the soil is dry. Since the soil is dry during summer due to higher soil temperature, thus the importance of moisture content of shaded surfaces in the spatial distribution of fauna and flora becomes more important compared to the moisture content of shaded surfaces in winter when the soil is wet.

Topographic shading in the Andrews Forest is greatest when the sun altitude is low in early morning. This is mainly due to the location of high ridges on the east of the forest which cast shadow on the lower elevation sites (Table 3.1). Colette *et al. (*2003) argued that the effect of topographic shading in an idealized valley is especially significant during early morning hours since landscape shading delays the onset of upslope flows, which in turn delays the breakup of nighttime inversions. Hoch and Whiteman (2009) argued that topographic shading affects the receipt of direct solar radiation by delaying local sunrise and advancing local sunset. In the Andrews Forest, this effect is more common in Primet (in the valley) than at Vanmet (near a ridge).

3.5.1. Solar illumination and inversions

Based on H1, this study predicted (Prediction 1) that air temperature would be higher in locations with greater illumination (i.e., mountain ridges, equator-facing slopes) compared to shaded areas (i.e., mountain valleys, polar-facing slopes).

Inversions (higher air temperature at high vs. low elevation) were expected to be observed during the daytime at low solar altitudes (or short day lengths), because much of the landscape is shaded. This study found that during periods of low solar altitudes (or short day lengths), stable conditions (inversions) were more frequent than unstable conditions. Daytime inversions or stable conditions were most frequent in January, followed by April and October, and least frequent in July (Table 3.2). The percent of daytime hours with positive lapse rate is negatively related to the amount of incoming solar radiation in all three years (Figure 3.3). This finding supports the idea that there is a threshold of incoming solar radiation that breaks the inversion.

The data suggests that at the threshold value of 242 Wm^-2, more than 98% of the daytime hours in April are inversion free. In contrast to what was expected, for radiation values larger than the threshold, the percent of daytime hours with inversion increased (in July). A possible explanation is that during July, Vanmet receives more radiation than Primet. In addition, the duration and intensity of radiation received at Vanmet is higher that the duration and intensity of radiation received at Primet. Therefore, the average daytime air temperature at Vanmet is higher than the average daytime air temperature at Primet. This condition creates a daytime stable boundary layer over the forest (between Primet and Vanmet). In addition, the warm advection from the surrounding ridges might increase the temperature deficit between Vanmet and Primet causing the already formed inversion layer to be stronger.

Moreover, the frequency of inversions was positively related to the proportion of the landscape in high shade except for April (Figure 3.4). In other words, as the percent of landscape in high shade increases the percent of hours with inversion increases for July, October, and January but not for April. One possible explanation for observing this trend in April is the influence of synoptic scale processes such as storm which break inversion.

.

There are fewer daytime inversions in April than July, despite lower incoming solar radiation, perhaps because the air is relatively well mixed during April as indicated by the higher proportion of days with unstable conditions in April compared to January (Table 3.2). Both inversion and mixed conditions occurred in April and October (Table 3.2, Figure 3.3, Figure 3.4). Both daytime and nighttime boundary layer stability was considerably higher near the fall equinox (October) compared to the Spring equinox (April) (Table 3.2, Figure 3.3, Figure 3.4). One of the possible explanation for observing this kind of pattern could be the influence of the large scale synoptic forcing on the Andrews Forest. Storms during fall, winter and spring produce warm advection of air which creates strong inversion events by increasing the air temperature deficit between the Vanmet and Primet and also the westerly winds that bring warm air from the SW towards the Cascade Mountains. Another possible explanation for observing this pattern could be related to the production of turbulent kinetic energy (TKE) during nights which creates mixing in the nighttime boundary layer. The turbulent kinetic energy is produced on the sloping terrain due to the vertical buoyancy fluxes. This happens when the ratio of the along-slope to the slope normal of kinematic heat flux is greater than the cotangent of slope angle (Oldroyd *et al.,* 2016). When this happens, the down-valley movement of flow starts.

During periods of no incoming solar radiation (nighttime) stable conditions (inversions) were more frequent than unstable conditions (lapse rates > 0) (Table 3.2). Downvalley flow or zero wind speed occurred on more than 75 % of nighttime hours at Primet, and 23% to 47% of hours at Vanmet in the three years (Table 3.3, Table 3.4). Downvalley flow initiate when the pressure deficit between valley and surrounding ridges becomes negative. In other words, when the high pressure forms over ridge and low pressure forms over valley. Downslope flow initiate when the slope surface cools down radiatively. As a result, the thin layer of the air above the slope surface becomes cooler (high pressure) than the layer of air above it (low pressure). Thus the along-slope component of buoyancy force causes the flow to slide over the slope.

It was expected to observe more frequent downvalley flow at Primet compared to Vanmet due to the lower topographic location of Primet compared to Vanmet. As the cold downvalley and downslope flow collect at Primet, a cold pool forms which becomes deeper with time. After a few hours, the cold pool is decoupled from the upper boundary layer.

3.5.2. Solar illumination and local winds

Based on H2, this study predicted (Prediction 2) that when synoptic wind speeds are low, wind directions would be up-slope and up-valley during the daytime. This study found that on average when wind speeds were low at Vanmet, wind directions were predominantly up-slope and up-valley during the daytime (Table 3.3). In addition, this study predicted (Prediction 3) that wind speeds are expected to be relatively low and wind directions are expected to be downslope or down-valley at night. Relative to Prediction 3, this study found that on average at night, wind speeds were lower than during the daytime, and nighttime wind directions were predominantly down-slope and down-valley (Table 3.3, Table 3.4).

At both Primet and Vanmet, daytime wind directions are more frequently up-valley or upslope than down-valley or downslope, whereas nighttime wind directions are more frequently down-valley or downslope. The anemometer was unable to detect the direction of winds lower than 0.5 m s^{-1} until 2014, when the sonic anemometers were installed. The daytime upvalley and the nighttime downvalley flows are mainly driven by large pressure deficit between the valley and the surrounding ridges whereas the daytime upslope and the nighttime downslope flows are mainly driven by pressure deficits between opposing slopes.

The interaction of solar radiation with the H.J. Andrews's complex topography creates an uneven distribution of the illuminated (warmer or lower pressure) surfaces versus shaded (colder or higher pressure) surfaces across the landscape. As a result, depending on the location and orientation of these surfaces, local (zonal) winds are expected throughout the landscape. These localized winds interact with the along valley and along slope flows which might be responsible for observing multi-directionality of wind at Primet.

In addition, depending upon the time of year, the hierarchical influence of the synoptic wind at regional scale on the local scale wind (mainly the along valley wind in the Andrews Forest) and the micro-scale wind (mainly the along slope wind at Primet and Vanmet) either increases the wind speed and multi-directionality of wind at Primet or decreases the wind speed and multi-directionality of wind at Primet.

During winter when the cyclonic condition is dominant, the hierarchical influence of the synoptic wind on the Primet's wind field (velocity and direction) is stronger compared to summer when the anti-cyclonic condition prevails. Therefore, higher wind speeds and less flow directionality are expected at Primet during winter but lower wind speeds and higher flow directionality are expected at Primet during summer.

Based on H2 new, this study predicted (Prediction 4) when synoptic (upper elevation) wind speeds are high, low elevation wind speeds and wind directions are expected to be variable and unrelated to landforms. Relative to prediction 4, this study found that during periods of high wind speeds at Vanmet, wind directions were predominantly upslope or up-valley, which coincides with the direction of prevailing winds (Table 3.4). However, during these same periods, wind speeds were low and variable at Primet (Table 3.3). This finding is consistent with Pepin *et al*., (2011), who showed that the wind conditions at ridge sites in the western United States are coupled with the free atmosphere (synoptic) condition and less affected by the near surface condition.

The wind showed multi-directionality at both sites during days and nights in 2003, 2011, and 2014 (Tables 3.3 and 3.4) but it was more pronounced at Primet during the day. One possible explanation is that since Primet microclimate is decoupled from the synoptic condition, thus the wind direction is less affected by the dominant wind direction at synoptic scale. In contrast, the wind direction at Primet is more affected by local site conditions such as microtopography, small land forms, and surrounding forest canopy. These site conditions affect the wind direction through their influence on the spatial pattern of illuminated versus shaded surfaces at Primet during the day.

Another possible explanation for the multi-directionality of wind at Primet is that forest canopy and local landforms cause the flow to become more turbulent due to their impact on wind speed and the wind direction. Temperature and wind fields have oscillatory behavior in katabatic winds which can be accompanied by surges (pulses) as well (Fleagle, 1950, Doran and Horst, 1981, and Van Gorsel *et al*., 2003). This oscillatory behavior might be responsible for the multi-directionality of flow. This kind of pattern is observed in the wind direction histograms at Primet and Vanmet in all the three years_ 2003, 2011, and 2014_ during January, April, July, and October. The reason is believed to be the internal gravity waves which can suppress or enhance oscillatory behavior of wind field in katabtic winds (Van Gorsel, 2003).

Another possible explanation for the multi-directionality of the nighttime wind field could be related to cold air drainage disruption by some transient modes. These modes are believed to be responsible for the vertical mixing (turbulence) in the nighttime boundary layer on sloping terrain (Mahrt, 2014). Turbulent kinetic energy might be responsible for the multi-directionality of flow observed at Primet during nights in 2003, 2011, and 2014. Because downslope flow produces turbulent kinetic energy on sloping terrain even under stable boundary layer conditions (Oldroyd *et al.* 2016), thus the observed multi-directionality of wind at both Primet and Vanmet during nighttime could be related to the turbulent kinetic energy production.

The reason why inversion duration is different in the four months is due to the interaction between synoptic forcing and local scale topographic factors. In January, the synoptic forcing has more influence on inversion duration than the local scale topographic factors whereas in April, the topographic factors have more influence on inversion duration than synoptic forcing. The result show that the wind direction co-vary with inversion at both Primet and Vanmet in January and April of 2003, 2011, and 2014. In January the wind direction at Primet and Vanmet was NE and SW respectively. In contrast, in April, the wind direction at both Primet and Vanmet was multi-directional. The main reason for observing this contrasting pattern in wind direction in January versus April is the prevailing effect of the large scale synoptic wind systems on along-valley flows. In January the dominant wind direction at Primet is NE which is a cold gravity-induced flow from higher topography whereas at Vanmet, the dominant wind direction is SW which is due to the influence of Westerly winds which bring relatively warm air to the Cascades. These large scale atmospheric flows outweigh the smaller scale wind patterns at the HJA landscape resulting two distinct wind directions at Primet and Vanmet in January. In contrast, in April, the wind direction at both Primet and Vanmet is multi-direction due to lack of large scale prevailing wind patterns and also other topographic factors such as local advection, zonal flows, convection, and ground heat flux.

In general, multi-day inversion events mostly occurred in January whereas diurnal inversion events were more frequent in April, July, and October of 2003, 2011, and 2014.

The main reasons for observing multi-day inversion events in January are related to the amount of net radiation and also synoptic forcing. The net radiation reaches its lowest values during January compared to other months of a year due to the lowest sun altitude values in January compared to other months of a year. Therefore, the diurnal inversion events are not broken due to the weak radiation forcing. As a result, the inversion events might last for multiple days under calm weather conditions.

Under the influence of synoptic forcing in January, the westerly winds bring warm weather to the Cascades and the HJA Forest. This process strengthens the already established diurnal inversion events at the forest by increasing the temperature deficit between Primet and Vanmet (The air temperature at Vanmet increases since it is coupled with the free atmosphere whereas the air temperature at Primet does not change since it is de-coupled from the free atmosphere). As a result, the inversion events might last for multiple days.

3.6. CONCLUSIONS

This study investigated the relationship between solar illumination, atmospheric inversion, and local wind. The study showed that solar altitude and topographic shading explained most of the observed frequency of stable atmospheric conditions and wind speeds and directions. At other times, synoptic winds associated with regional air masses overwhelmed the effects of local topographic shading on air temperature, wind speed, and wind direction, preventing the formation of inversions. This study has important implications for understanding how solar illumination affects topographic shading, local winds, and the frequency of inversions in a forested mountain landscape.

BIBLIOGRAPHY

Arya, P.S. 2001. “Introduction to Micrometeorology.” *second Edition,* Academic Press.
Christopherson, R. W. 2012. “Geosystems.” *Eight Edition*, Prentice Hall.

Colette, Augustin, Fotini Katopodes Chow, and Robert L Street. 2003. “A Numerical Study of Inversion-Layer Breakup and the Effects of Topographic Shading in Idealized Valleys.” *Journal of Applied Meteorology* 42 (9): 1255–72. doi:10.1175/1520-0450(2003)042<1255:ANSOIB>2.0.CO;2.

Daly, Christopher, David R Conklin, and Michael H. Unsworth. 2010. “Short Communication Local Atmospheric Decoupling in Complex Topography Alters Climate Change Impacts” 1864 (September 2009): 1857–64. doi:10.1002/joc.2007.

Daly, Christopher, David R. Conklin, and Michael H. Unsworth. 2010. “Local Atmospheric Decoupling in Complex Topography Alters Climate Change Impacts.” *International Journal of Climatology* 30 (12): 1857–64. doi:10.1002/joc.2007.

Dobrowski, Solomon Z., John T. Abatzoglou, Jonathan A. Greenberg, and S. G. Schladow. 2009. “How Much Influence Does Landscape-Scale Physiography Have on Air Temperature in a Mountain Environment?” *Agricultural and Forest Meteorology* 149 (10): 1751–58. doi:10.1016/j.agrformet.2009.06.006.

Doran, J. C., and T. W. Horst. 1981. “Doran and Horst, 1981.Pdf.” *Journal of Applied Meteorology*.

Fleagle, Robert. 1950. “Fleagle, 1950_ Theory of Drainage.Pdf.” *Journal of Meteorology* 7.

Gorsel, Eva Van, Roland Vogt, Andreas Christen, and Mathias W Rotach. n.d. “Low Frequency Temperature and Velocity Oscillations in Katabatic Winds” 2: 2–5.

Hoch, Sebastian W., and C. David Whiteman. 2010. "Topographic Effects on the Surface Radiation Balance in and around Arizona's Meteor Crater." *Journal of Applied Meteorology and Climatology* 49 (6): 1114–28. doi:10.1175/2010JAMC2353.1.

Kiefer, Michael T., and Shiyuan Zhong. 2015. "The Role of Forest Cover and Valley Geometry in Cold-Air Pool Evolution." *Journal of Geophysical Research: Atmospheres* 120 (17): 8693–8711. doi:10.1002/2014JD022998.

Leukauf, Daniel, Alexander Gohm, Mathias W. Rotach, and Johannes S. Wagner. 2015. "The Impact of the Temperature Inversion Breakup on the Exchange of Heat and Mass in an Idealized Valley: Sensitivity to the Radiative Forcing." *Journal of Applied Meteorology and Climatology* 54 (11): 2199–2216. doi:10.1175/JAMC-D-15-0091.1.

Lu, Wei, and Shiyuan Zhong. 2014. "Journal of Geophysical Research : Atmospheres." *Journal of Geophysical Research: Atmospheres* 119: 1733–52. doi:10.1002/2013JD020410.Received.

Mahrt, Larry. 1982. "Momentum Balance of Gravity Flows." *Journal of Atmospheric Sciences* 39.

Mahrt, Larry. 2014. "Transient Cold Air Drainage down a Shallow Valley." *Journal of Atmospheric Sciences*.

Matzinger, N., M. Andretta, E. Van Gorsel, R. Vogt, A. Ohmura, and M. W. Rotach. 2003. "Surface Radiation Budget in an Alpine Valley." *Quarterly Journal of the Royal Meteorological Society* 129 (588 PART B): 877–95. doi:10.1256/qj.02.44.

Oldroyd, Holly J, Eric R Pardyjak, Chad W Higgins, and Marc B Parlange. 2016. "Buoyant Turbulent Kinetic Energy Production in Steep-Slope Katabatic Flow." *Boundary-Layer Meteorology* 161 (3). Springer Netherlands: 405–16. doi:10.1007/s10546-016-0184-3.

Olson, M.H., Rupper, S.B. 2018. "Impacts of topographic shading on direct solar radiation for valley glaciers in complex topography." *The Cryosphere Discussion*. doi.org/10.5194/tc-

2018-64.

Pepin, N. C., C. Daly, and J. Lundquist. 2011. “The Influence of Surface versus Free-Air Decoupling on Temperature Trend Patterns in the Western United States.” *Journal of Geophysical Research Atmospheres* 116 (10): 1–16. doi:10.1029/2010JD014769.

Rotach, Mathias W, and Dino Zardi. 2007. “On the Boundary-Layer Structure over Highly Complex Terrain : Key Findings from MAP.” *Quarterly Journal of the Royal Meteorological Society* 948 (133): 937–48. doi:10.1002/qj.

Whiteman, David, and Thomas McKee. 1982. “Whiteman, D, 1982_ Valley Inversion_ part 2_Thermodynamics.Pdf.” *Journal of Applied Meteorology*.

Table 3.1. Percent of the Andrews Forest landscape that is illuminated and in deep shade based on terrain shading algorithm, for 9 AM, noon, and 3 PM on the equinoxes (Mar 21, Sep 21) and solstices (June 21, Dec 21)

				Number of pixels				% of area		
Day	Local time	Solar azimuth (degrees)	Sun altitude (degrees)	High shade	Moderate shade	Low shade	Total	High shade	Moderate shade	Low shade
Winter solstice	900	137	9.7	5275	1572	182	7029	75	22	3
	1200	177	22.5	3253	2768	1008	7029	46	39	14
	1500	219	12	4355	2293	381	7029	62	33	5
Spring equinox	900	108	18.2	4596	1951	482	7029	65	28	7
	1200	152	43	1349	2812	2869	7030	19	40	41
	1500	214	41	1181	2488	3361	7030	17	35	48
Summer solstice	900	35	90	2287	3219	1522	7028	33	46	22
	1200	137	64	56	1731	5243	7030	1	25	75
	1500	235	60	84	1483	5462	7029	1	21	78
Fall equinox	900	111	20	4311	2141	5778	12230	35	18	47
	1200	57	44	1239	2738	3052	7029	18	39	43
	1500	218	39	1305	2628	3097	7030	19	37	44

Table 3.2. Percent of hours with various values of Vanmet-Primet air temperature difference (°C), and with inversions (positive lapse rates). A -5.5 °C difference between Vanmet and Primet (845 m difference in elevation) is equivalent to the environmental lapse rate (-6.5°C / 1000 m)..

	Day						Night					
	<-5.5	-5.5 to 0	>0 to 5.5	>5.5	total	>0	<-5.5	-5.5 to 0	>0 to 5.5	>5.5	total	>0
Year												
2003	22	58	14	7	100	21	2	66	24	8	100	32
2011	20	58	14	7	100	21	3	71	18	8	100	26
2014	13	66	14	7	100	21	3	70	20	8	100	28
January												
2003	1	58	18	23	100	41	1	50	27	22	100	49
2011	0	40	45	15	100	60	2	46	51	1	100	53
2014	0	33	27	40	100	67	0	33	27	40	100	67
April												
2003	25	71	4	0	100	4	1	93	5	0	100	6
2011	30	67	2	0	100	2	3	95	3	0	100	3
2014	31	58	9	1	100	11	3	82	15	0	100	16
July												
2003	26	51	18	5	100	23	6	44	45	6	100	50
2011	26	62	11	1	100	12	2	53	36	9	100	45
2014	3	78	18	1	100	20	0	74	26	0	100	26
October												
2003	13	55	20	12	100	33	3	48	39	10	100	50
2011	7	72	14	7	100	21	0	83	13	4	100	17
2014	1	66	20	13	100	33	1	63	26	11	100	37

Table 3.3. Percent of hours with various wind speeds and directions by season, for valley floor site (Primet). At Primet, winds from 0 to 90 degrees are down-valley, and winds from 180 to 270 degrees are up-valley.

	Daytime wind speed (m/s)					Daytime wind direction			Nighttime wind speed (m/s)					Nighttime wind direction		
	0.001 to 0.5	0.5 to 1	1 to 2	>2	mean	none	down	up	0.001 to 0.5	0.5 to 1	1 to 2	>2	mean	none	down	up
Year																
2003	49	23	21	7	0.8	26	11	31	65	32	3	0	0.4	65	16	5
2011	0	57	42	1	1.1	31	12	43	0	90	10	0	0.8	78	8	9
2014	24	50	26	0	0.8	0	26	40	0	94	6	0	0.8	0	42	14
January																
2003	33	17	37	13	1.2	16	9	64	98	3	0	0	0.3	76	22	0
2011	98	3	0	0	0.3	57	26	13	98	2	0	0	0.3	80	15	2
2014	15	18	65	3	1.2	0	13	74	0	90	10	0	0.8	0	50	12
April																
2003	46	26	22	6	0.8	26	17	47	94	5	1	0	0.3	77	8	14
2011	62	25	13	0	0.5	19	7	55	93	6	1	0	0.3	68	3	23
2014	0	50	50	0	1.1	0	35	26	0	98	2	0	0.8	0	33	19
July																
2003	64	26	10	1	0.5	38	30	24	91	3	6	0	0.3	80	6	10
2011	49	13	36	3	0.8	22	3	64	98	2	0	0	0.3	94	0	5
2014	6	70	25	0	0.9	0	23	43	0	97	3	0	0.8	0	27	5
October																
2003	54	22	18	6	0.8	26	75	0	86	10	4	0	0.3	51	30	10
2011	74	24	2	0	0.4	42	7	34	98	2	0	0	0.3	87	2	7
2014	0	85	15	0	0.9	0	18	56	0	96	4	0	0.8	0	48	10

Table 3.4. Percent of hours with various wind speeds and directions by season, for near-ridge site (Vanmet). At Vanmet, winds from 0 to 90 degrees are downslope, and winds from 180 to 270 degrees are upslope.

	Daytime wind speed (m/s)					Daytime wind direction			Nighttime wind speed (m/s)					Nighttime wind direction		
	0.001 to 0.5	0.5 to 1	1 to 2	>2	mean	none	down	up	0.001 to 0.5	0.5 to 1	1 to 2	>2	mean	none	down	up
Year																
2003	5	9	59	27	1.8	0	6	22	3	21	54	23	1.7	1	23	6
2011	3	22	72	4	1.4	1	14	73	4	22	68	5	1.4	2	37	36
2014	2	6	82	10	1.6	0	16	68	3	6	79	12	1.6	0	47	34
January																
2003	1	13	56	31	1.9	0	4	28	9	9	66	16	1.6	0	40	25
2011	29	35	29	7	1.0	0	17	63	1	18	72	9	1.5	6	32	35
2014	0	22	67	11	1.5	0	17	59	4	1	81	15	1.7	0	54	33
April																
2003	3	10	69	17	1.6	0	3	21	0	22	72	6	1.4	0	31	52
2011	20	29	48	3	1.1	0	12	79	8	21	70	2	1.3	0	26	60
2014	0	5	82	13	1.7	0	14	52	0	10	81	9	1.6	0	38	49
July																
2003	0	13	53	34	1.9	0	8	16	7	10	66	17	1.6	0	31	50
2011	10	32	57	1	1.2	0	9	29	0	39	61	0	1.2	0	41	15
2014	0	20	76	4	1.4	0	15	75	0	44	56	0	1.2	0	74	6
October																
2003	5	6	61	28	1.8	0	3	22	4	19	77	0	1.3	0	31	27
2011	4	39	55	2	1.2	0	10	72	2	30	66	2	1.3	0	31	43
2014	0	4	88	8	1.6	0	22	59	0	2	89	10	1.6	0	45	34

Table 3.5. Minimum and maximum values of mean daily air temperature at Primet and Vanmet, 1995 - 2015

Site	Date	Minimum (°C)	Date	Maximum (°C)
Primet	12/08/2013	-11	7/29/2009	26.4
Vanmet	12/20/1998	-16	8/16/2008	27.6

Figure 3.1. The location of study sites on the shaded relief map of the H.J. Andrews Forest.

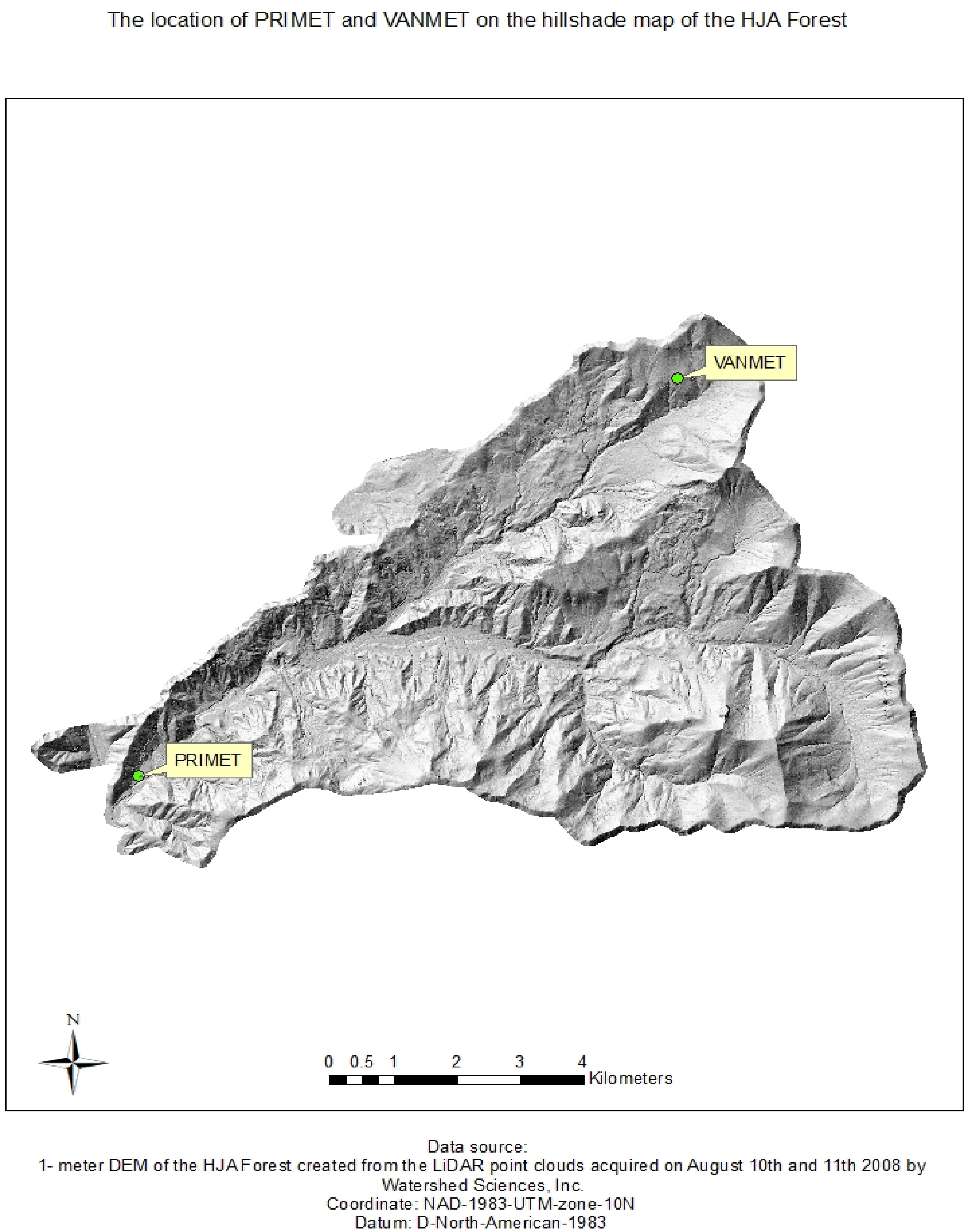

Figure 3.2. Mean daily air temperature for 1995 to 2014. Source: (NOAA).

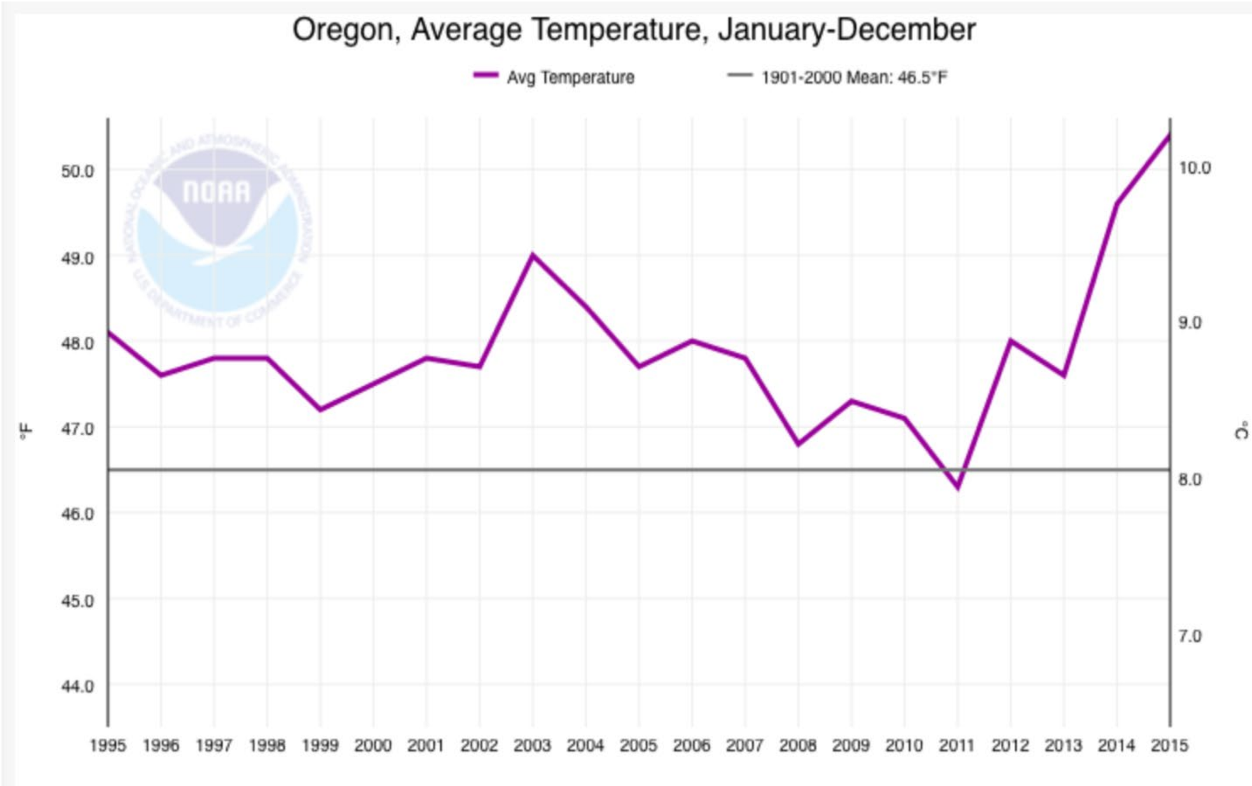

Figure 3.3. Relationship of frequency of daytime inversions to solar radiation at Primet.

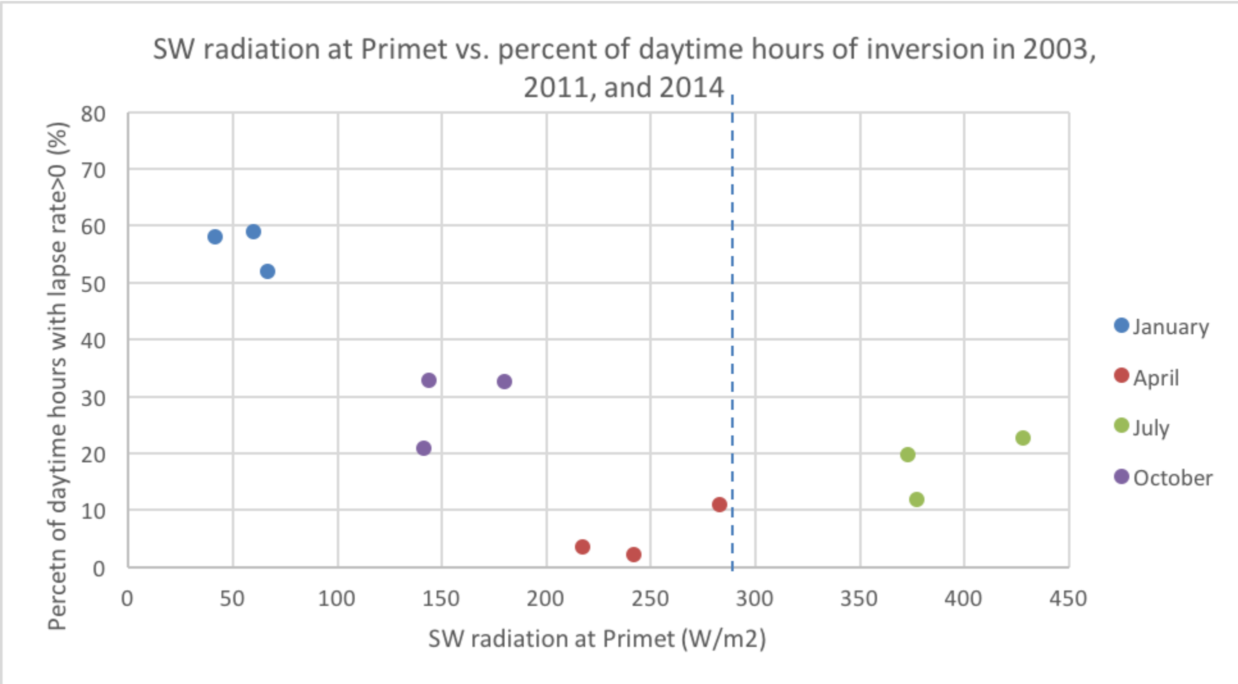

Figure 3.4. Relationship of frequency of daytime inversions to percent of landscape in high shade.

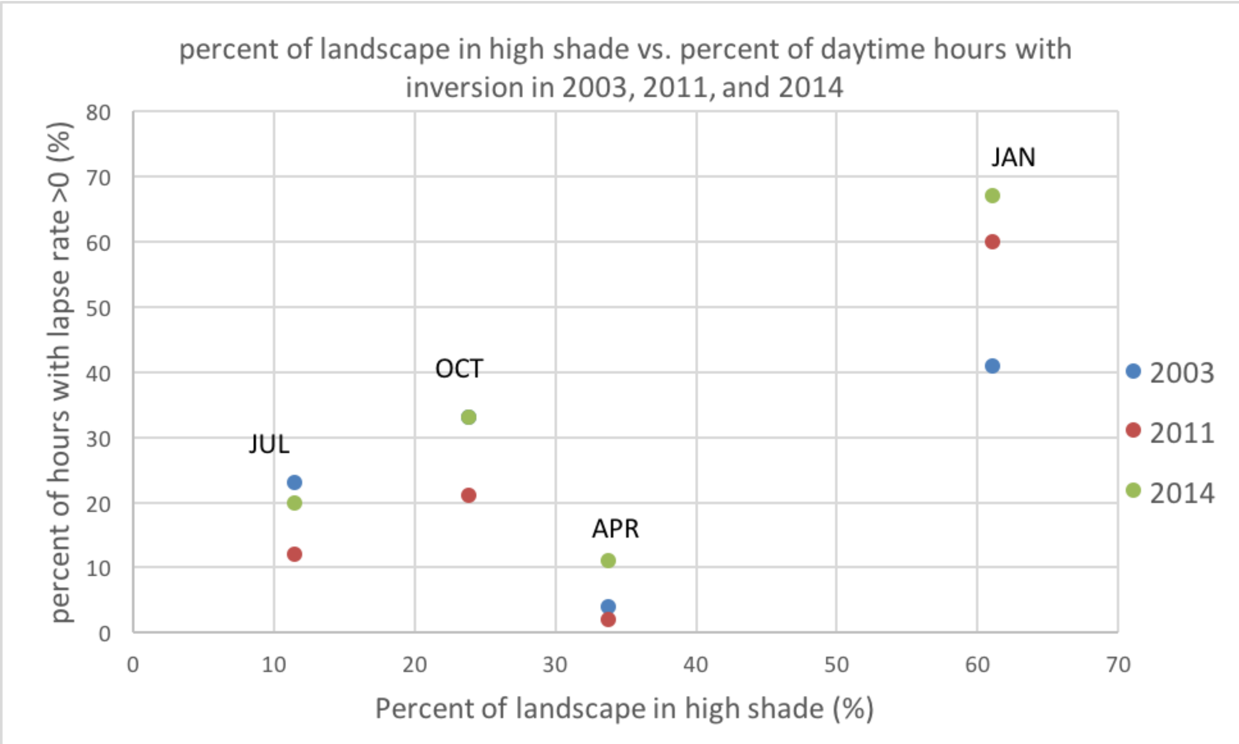

Figure 3.5. Hourly difference in air temperature at Vanmet vs. Primet (°C) for January, April, July and October of 2003 (a-d), 2011 (e-f), and 2014 (i-l). Positive values indicate hours with inversions.

Figure 3.5, Cont'd.

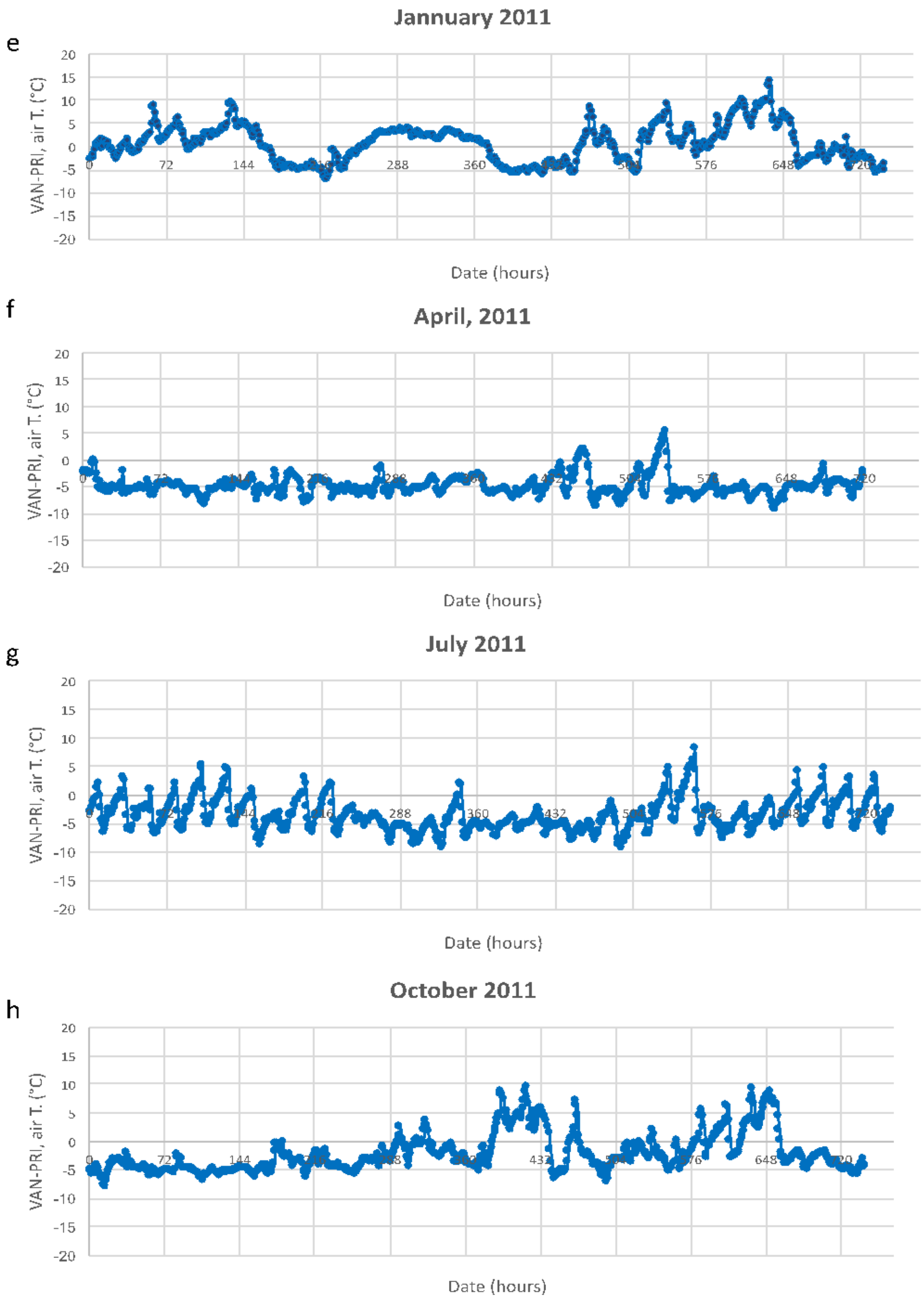

Figure 3.5, Cont'd.

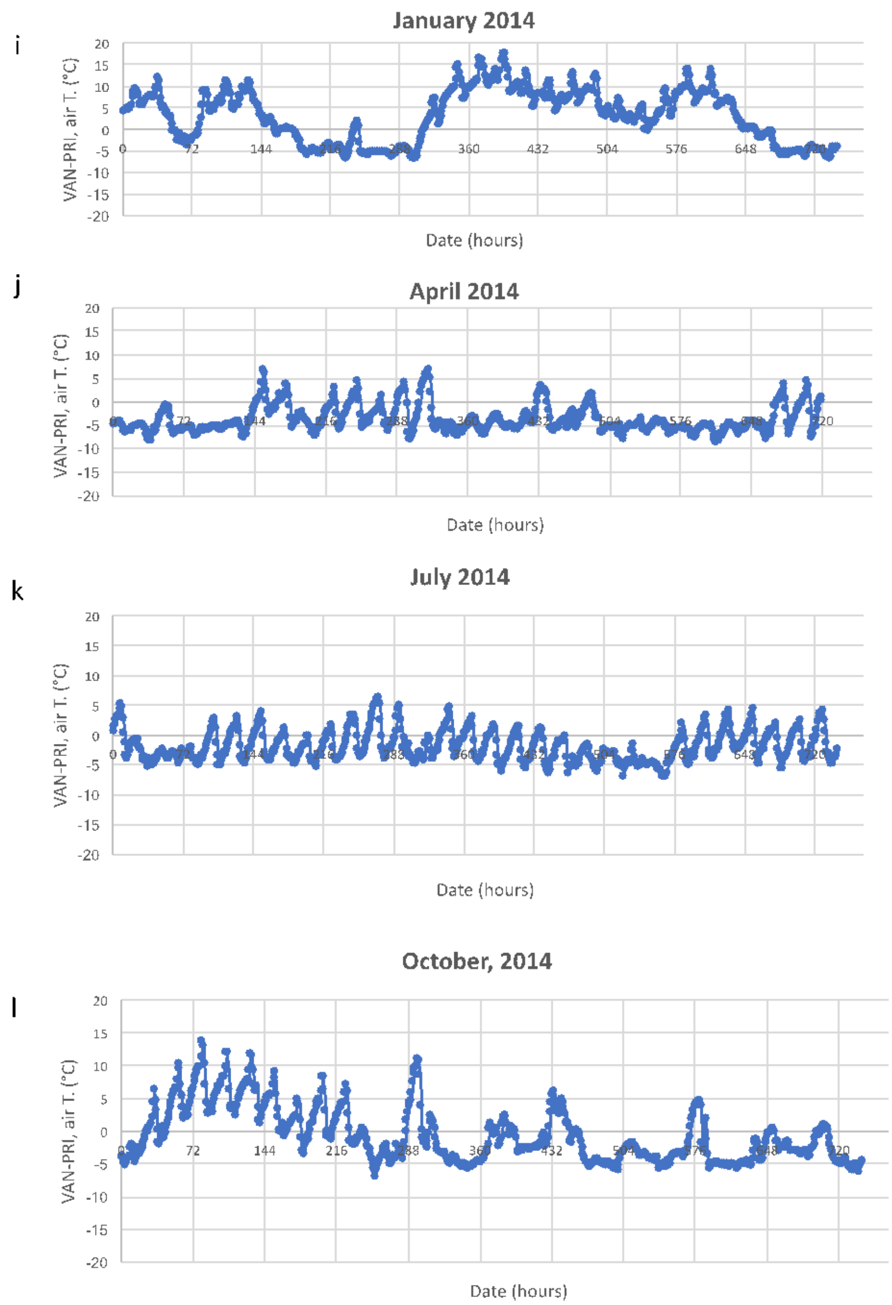

Figure 3.6. Hourly wind directions at Vanmet vs. Primet (°C) for January, April, July and October of 2003 (a-d), 2011 (e-f), and 2014 (i-l). Positive values indicate hours with inversions.

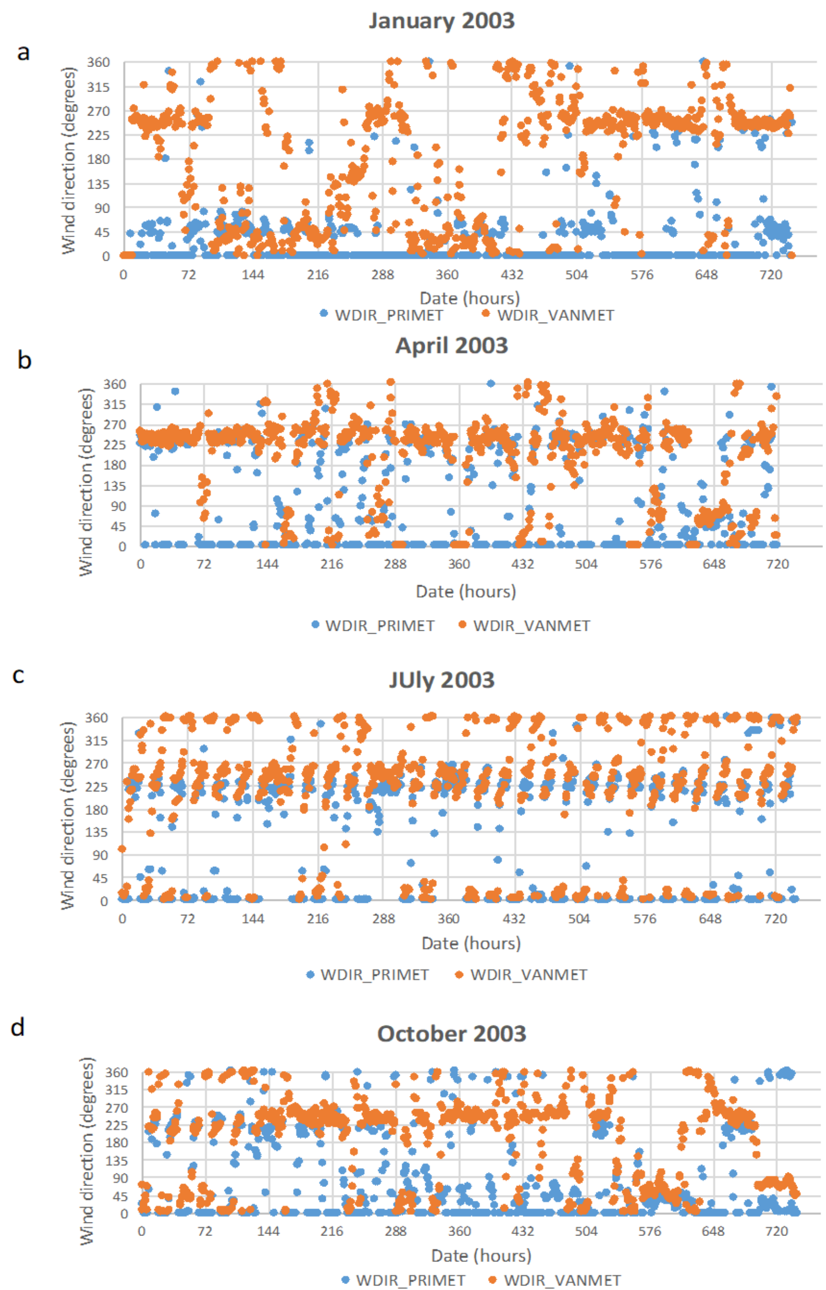

Figure 3.6, cont'd.

e

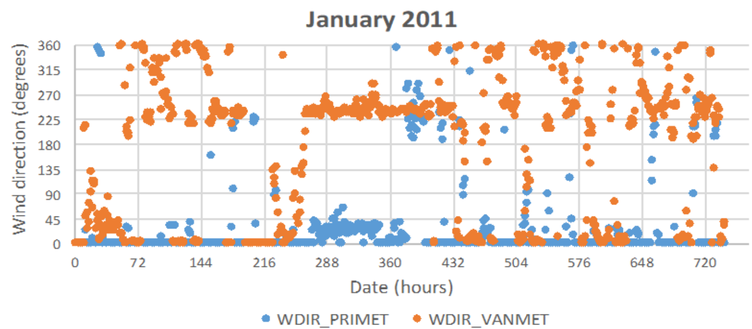

f

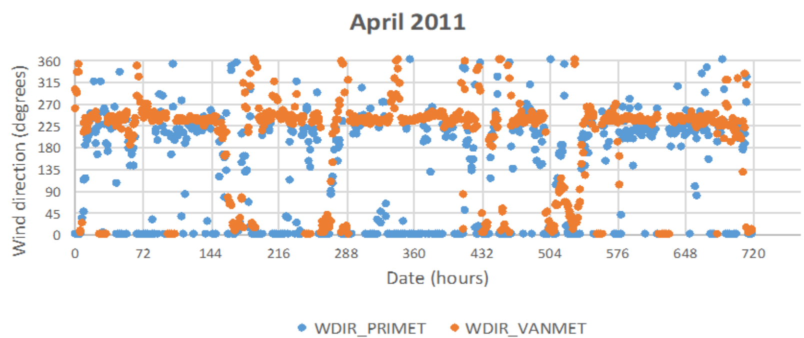

g

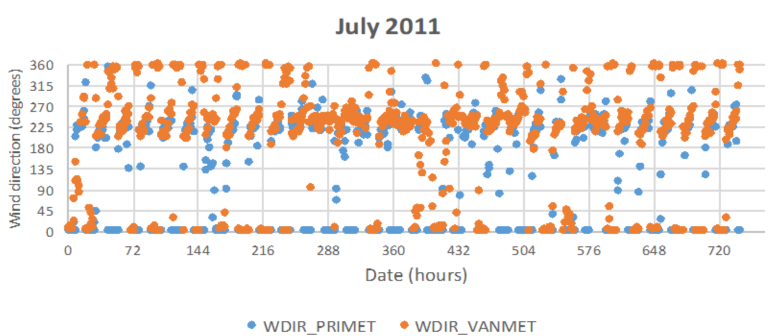

h

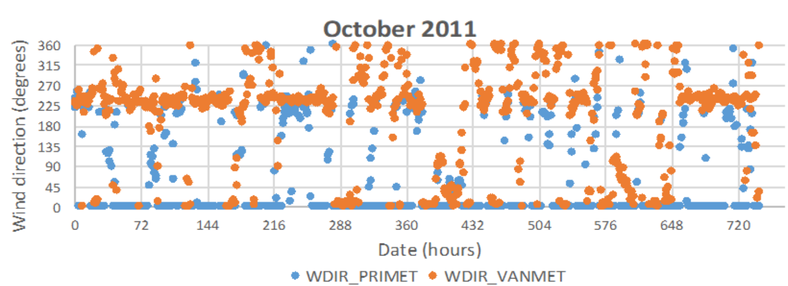

Figure 3.6, cont'd.

i
j
k
l

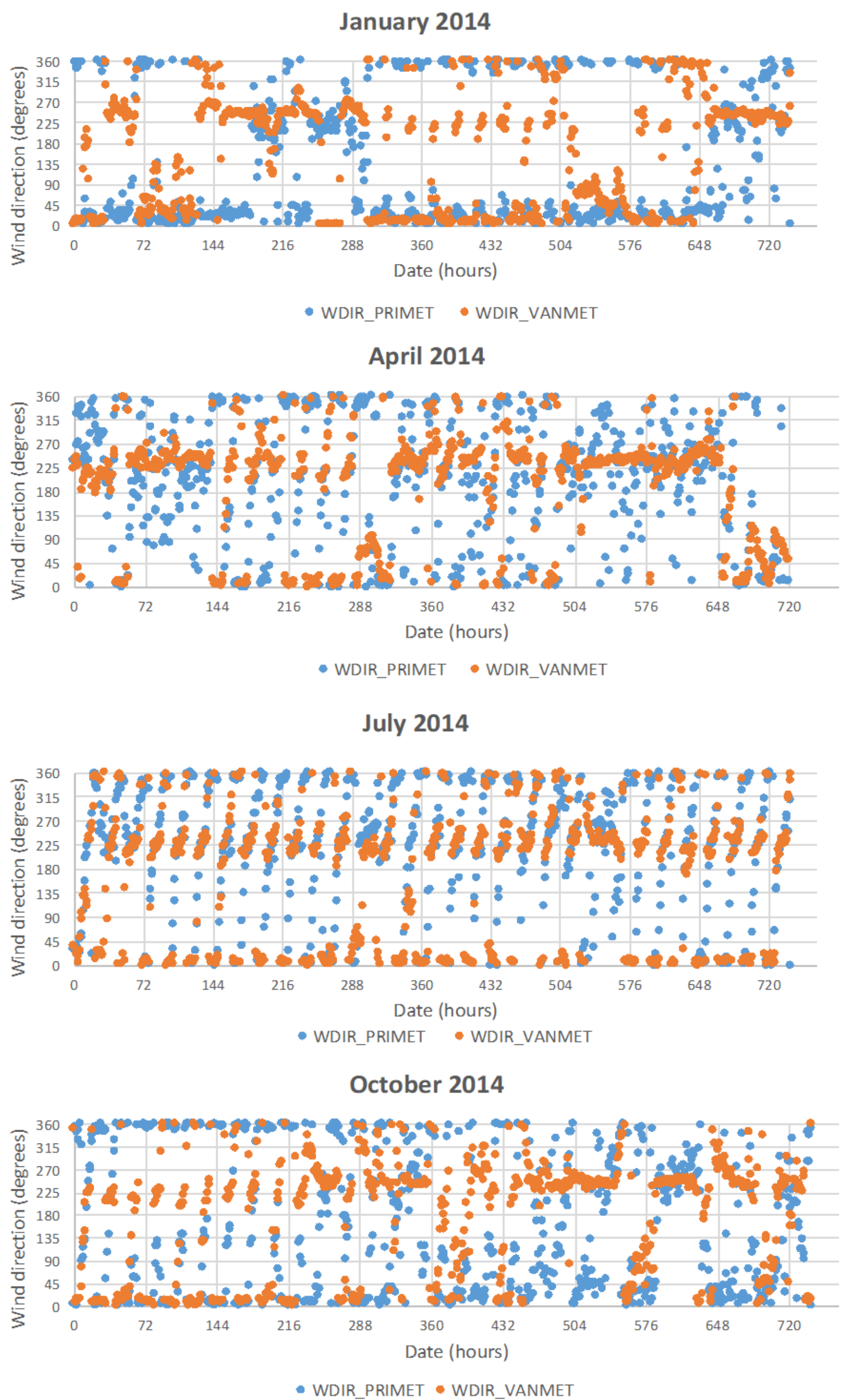

Figure 3.7. The total number of hours with inversion in January, April, July, and October of 2003, 2011, and 2014

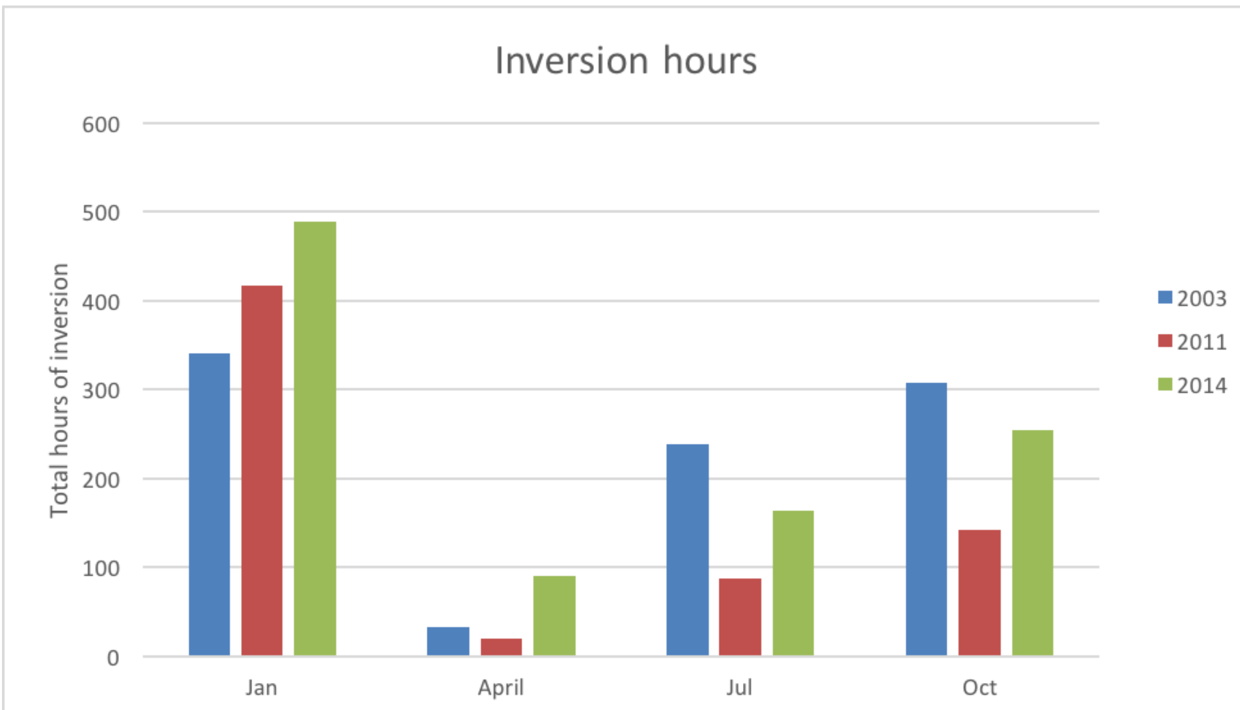

CHAPTER 4

The effect of light, wind, humidity, and sensor type on the measurement of air temperature in Discovery Tree, Andrews Forest, Oregon

ABSTRACT

This chapter examined the effect of light, wind, and humidity, and sensor type on the measurement of air temperature in the Discovery Tree, Andrews Forest, Oregon. The temperature difference between HOBO and aspirated sensors was significantly related to the HOBO light intensity at 40m and 56 m height in the tree. These relationships indicate that at 30 m and above, an increase of 1000 lux is associated with an increase of 0.10 to 0.18 °C in the temperature difference between the HOBO sensor and the aspirated one. At these heights, and at wind speeds < 1 m/s, an increase of 1000 lux is associated with an increase of 0.17 °C in the temperature difference between the HOBO sensor and the aspirated sensor, whereas at wind speed ≥ 1 m/s, an increase of 1000 lux is associated with an increase of only 0.1°C (at 56 m) or 0.13°C (at 40 m) in the temperature difference between the HOBO sensor and the aspirated sensor. These relationships can be used to correct HOBO sensor measurements in locations lacking aspirated sensors.

4.1 INTRODUCTION

One of the main systematic errors associated with temperature measurement is the influence of radiative forcing on the temperature sensor-shield system (Nakamura and Mahrt, 2005). The principal theory to calculate and minimize the effect is the same for both naturally and forced ventilated systems. Both the temperature probe and radiation shield exchange energy with their surroundings through radiation and convection. The energy exchange via conduction is very small due to the low thermal conductivity of plastic which is a typical material of a radiation shield (Thomas and Smoot, 2012). The energy balance of such a system is the sum of received shortwave radiation (SW), exchanged longwave radiation (LW) and the convective sensible heat transfer between the system and its surroundings (H) (Nakamura and Mahrt, 2005). The energy balance of the system can be written as

$$SW + LW + H = 0 \qquad [1]$$

Net radiation (Rn) is

$$Rn = SW + LW \qquad [2]$$

This simplifies to

$$Rn + H = 0 \qquad [3]$$

The received incoming shortwave radiation is the dominant term in the energy balance of a temperature probe-shield system. The influence of the longwave radiation exchange between the system and the ambient air on the system's energy balance is very small (less than 0.1°C increase in the system temperature) especially during daytime (Anderson and Baumgartner, 1998; Mauder *et al.,* 2008). Therefore, the exchanged longwave radiation effect is ignored in the system's heat budget formula. Thus, the heat budget of such a system can be written as

$$\propto *R*A = L + S \qquad [4]$$

where

∝: absorption coefficient

R: shortwave flux density

A: the area normal to the incident solar radiation

L: heat transfer term for the forced convection

S: heat transfer term for the natural convection

The product of the left hand side terms is called the radiative heating term. The shortwave flux density can be written as (Mauder *et al.,* 2008):

$$R = \frac{SW}{rd+(1-rd)sin\emptyset}$$

[5]

where

R: Shortwave flux density (Wm^{-2})

SW: shortwave radiation normal to the surface of radiation shield (Wm^{-2})

Ø: Sun elevation angle (degrees)

rd: constant ratio of the diffuse radiation to the total downward radiation (rd = 0.1)

The value of 0.1 is justified under clear sky and not under a cloudy sky. Under the presence of clouds the amount of diffuse radiation surpasses the amount of direct radiation resulting in a value of rd larger than 0.1.

There are two types of temperature sensor shield systems: naturally aspirated and fan aspirated. Naturally aspirated sensors are low cost, rugged, and suitable for measuring temperature in remote locations. Fan-aspirated sensors are less rugged and more expensive due to the use of electricity to run the fan. The radiation-induced temperature error is significant in naturally ventilated sensors and may reach 2-8 K under wind speeds <= 1m/s and radiative forcing >=800 Wm^{-2}) (Tanner *et al.* 1996; Anderson and Baumgartner 1998; Lin *et al.* 2001; Nakamura and Mahrt 2005; Mauder *et al.* 2008). Thus many studies have investigated how to minimize this error in recording temperature measurements.
An early study of sensor-shield systems examined how different types of coating materials (chrome plating, polished aluminum, and white paint) affected the absorption of solar and thermal radiation. The study showed that while a clear coating on polished aluminum is the best type of coating for shielding from thermal radiation, it is not suitable for use in solar radiation shields (Fuchs and Tanner, 1965).

In another study of the design of a new class of sensor-shield systems, a guideline was developed to minimize the heating errors associated with multiplate shields. These aspirated multiplate radiation shields are able to operate in a dual mode: active vs passive. Under low wind speed conditions, the active mode is activated and turns on the fan, whereas under a high wind speed condition the passive mode is activated and the fan turns off automatically. The authors used different methods such as ray tracing analysis, wind tunnel experiments, field testing and numerical flow simulations. The result showed that the radiative heating error decreased from 2°C to 1.2°C. Nighttime low wind speed errors also decreased from 1.6°C to 0.3°C (Richardson and Brock, 1999).

In an attempt to minimize the radiation-induced error in naturally ventilated HOBO temperature sensors, Nakamura and Mahrt (2005) proposed an empirical correction model. The model is a ratio between net radiation and the product of the wind speed, air density, specific heat capacity of the air at constant pressure, and air temperature. The result showed that the radiative error becomes large during daytime and under low wind speed and strong radiation forcing whereas it reduces as the wind speed increases due to ventilating the sensor-shield system (Nakamura and Mahrt, 2005).

In a similar study but under different site conditions, a naturally ventilated temperature sensor was compared with a forced ventilated (fan-aspirated) sensor on the Antarctic Plateau from the end of 2009 to the mid 2010. The result showed that the naturally ventilated sensor had a radiation-induced warming error, which occasionally reached more than 10° C, especially under weak wind conditions. The authors argued that to minimize the bias one option would be to keep only the observations which are recorded under wind speeds larger than a threshold, which they suggested should be 4m/s (Genthon *et al.*, 2011).

Mauder *et al.* (2008) attempted to minimize radiation-induced error in naturally ventilated HOBO sensors in a spatial network of 25 sensors over an area of 3.5 by 3.5 km of farmland in SW Ottawa, Ontario, Canada from 17 May to 20 June, 2007. The authors showed that, in addition to wind speed and radiation, the surface area of the HOBO shield (a cube shape) that is normal to the Sun should be considered in developing any correction to account for temperature errors. The results showed that the root mean square error of the HOBO temperature measurements was reduced from 0.49°C to 0.15°C after applying the correction (Mauder *et al.,* 2008).

To reduce the uncertainty in temperature measurements and associated spatiotemporal gradients in micrometeorological networks, a study was conducted to design a double-walled aspirated radiation shield. The result showed that the aspirated sensor had a minor impact on the spatiotemporal gradient of air temperature under weak wind speeds and stable boundary layer condition (Thomas and Smoot, 2012).

According to the aforementioned studies, the naturally ventilated (non-aspirated) temperature sensor-shield systems are subject to radiation induced heating error, especially under low wind conditions. These studies examined the temperature error placed near the ground surface in open, un-vegetated systems. Therefore, it is not known how these factors influence the vertical pattern of the radiation-induced heating error in an old-growth forest stand in the Western Cascades, Oregon.

The purpose of this analysis was to understand the effects of light intensity and wind speed on HOBO and aspirated air temperature measurements. The study took advantage of a year of 15-minute data collected at various heights in the canopy of a 66-m tall Douglas-fir tree (Discovery Tree) in the Andrews Forest, western Oregon. Specifically, this study examined how temperature readings from HOBO sensors under a simple PVC cover differ from readings from Campbell 107 thermistors located in fan-aspirated radiation shields. This study addressed how light, wind speed, and relative humidity influence the temperature measured at the HOBO sensors compared to the aspirated sensors. The specific objective of this study was to propose a set of correction factors which could be applied to data collected from other trees instrumented only with HOBO sensors.

4.2. STUDY SITE

The study site is a 66-meter tall Douglas-fir tree located in the H.J. Andrews Experimental Forest in the central Cascade Range of Oregon (Figure 4.1). The tree is located on a relatively flat valley floor in an old-growth Douglas-fir stand (UTM coordinates of 44.216586919m N and 122.24965723m E).

The tree is instrumented with sensors to measure air temperature, wind speed and direction, radiation, relative humidity, and leaf wetness (Figure 4.2). The sensors are mounted along the bole of the tree at 1.5 m, 10m, 20m, 30m,40m, and 56 m above the ground, within the canopy (Figure 4.3).

The climate of the Andrews Forest is characterized by mild, wet winters and dry summers. Precipitation mostly occurs during fall and winter in the form of rain due to the establishment of low-pressure centers from the ocean and also the combining effect of warm westerly winds. In contrast, lack of precipitation during summer is mainly due to the establishment of high-pressure centers along the coast which bring fair weather conditions to the Andrews (Franklin and Dyrness, 1973). In addition, the polar jet stream influences the climate of the Andrews Forest. During winter, the stream of cold fronts from the northern latitudes (60 degrees) to the lower latitudes bring cold, stormy weather to the forest, whereas in the summer when the jet stream returns to the higher latitudes (60 degrees), it causes the establishment of fair weather conditions (Bierlmaier and McKee, 1989).

The Andrews Forest is a watershed draining Lookout Creek in the western Cascades of Oregon. Elevation ranges from 400 to 1600 meters. The geology of the forest is affected by phases of volcanism separated by periods of weathering and erosion. Early volcanic activities during late Oligocene and early Miocene (23 to 20 million years ago) formed the oldest rocks consisting of mudflows, pyroclastic flows, and fine-grained lake deposits, whereas late volcanic activities during the late Pliocene (nearly 4 million years ago) formed the youngest rocks which consist of basalt and andesite (Swanson and James, 1975).

The forest stand around Discovery tree is an old-growth forest which originated from wildfires in AD 1500 and the mid 1800s (Weisberg and Swanson, 2003), are aged between 350 to 750 years (Franklin *et al*., 1981), and are dominated by Douglas fir (*Pseudotsuga menziesii*) and Western hemlock (*(Tsuga heterophylla*). Douglas-fir is the dominant tree species at the study site and western hemlock is the co-dominant species.

Figure 4.1. The map of study site.

Figure 4.2. The location of sensors on Discovery Tree

Figure 4.3. The location of one of the data loggers on Discovery Tree

4.2.1. Configurations of temperature sensors on Discovery Tree

Discovery Tree is instrumented with several types of temperature sensors (Table 4.1). This study contrasted the behavior of HOBO pendants with PVC shields to other temperature probes that are fan-aspirated. The HOBO sensors were suspended below partial radiation shields made from 4-inch schedule 40 PVC pipe split in half and cut to 20cm length. These shields are inexpensive and require no power, which makes them practical for large-scale deployments at remote locations. The fan-aspirated radiation shields are built according to specifications in Thomas and Smoot, 2012. The primary function of a fan in aspirated sensors is to increase the cooling of sensor probe inside the solar radiation shield by drawing the air from below and ejecting it from the top of the shield. The paired sensors are mounted on next to each other on the north side of the Discovery tree at 1.5 m, 10m, 20m, 30m, 40m, and 56 m above the ground (Figures 4.2 and 4.3).

HOBO sensors with PVC shields have been used to measure forest understory microclimates at the Andrews Forest (Frey *et al*. 2016; Ward, 2018), and to observe vertical gradients in microclimate at remote sites spanning the elevation gradient at the Andrews (Frey, unpublished). The tradeoff with this low-cost, low-maintenance measurement system is an expected bias in air temperature measurements that is positively related to solar radiation. The HOBO and fan aspirated sensors are different at least in two ways. The HOBO sensors do not have a fan while the fan aspirated sensors do. In addition, both sensors are different in terms of probe types.

4.2.2. Data

This study examined data on air temperature, light intensity from the HOBO sensors, and air temperature, light intensity, relative humidity, and wind speed from the aspirated sensors. Data were recorded at 15-minute resolution from 11/14/2016 to 3/31/2018 at various tree heights.

4.3. METHODS

4.3.1. Assessing the effects of light on air temperature measurements

The difference between the temperature measured at each HOBO sensor and the matching aspirated sensor (HOBO – aspirated) was plotted against the HOBO light intensity, for sensors at each height in the canopy. Linear models were fitted to the data and the resulting models were used to characterize the effect of light on temperature differences between HOBO and aspirated sensors.

4.3.2. Assessing the effects of wind and light on air temperature measurements

To examine the influence of wind speed on measured temperature deficits between the HOBO and aspirated sensors, the measured HOBO light intensities at different heights of Discovery Tree were grouped into two wind speed categories: < 1 m/s, and >= 1m/s. Linear models were fitted to the data and the resulting models were used to characterize the effect of light and wind speed on temperature differences between HOBO and aspirated sensors.

4.4. RESULTS

4.4.1 Vertical distribution of light intensity as a function of height (Figure 4.4)

Light intensity is low at 1.5 m: 100 % of light intensity measurements over the year (Nov 2016 to April 2018) were < 5 lux. Light intensity was highest at 56 m: 2% of light intensity measurements over the year (Nov 2016 to Nov 2017) were > 15 lux.

Figure 4.4. Histogram of light intensity at different heights of Discovery tree, Nov 2016 – April 2018. (a) 1.5 m, (b) 10 m, (c) 20 m, (d) 30 m, (e) 40 m, (f) 56 m.

4.4.2. Vertical distribution of wind speed as a function of height (Figure 4.5)

Wind speed is low at 1.5 m: 99.5 % of wind speed measurements over the year (Nov 2016 to Apr 2018) were < 2 m/s. Wind speed was highest at 56 m: 3 % of wind speed measurements over the year (Nov 2016 to April 2018) were > 3 m/s.

Figure 4.5. Histogram of wind speed at different heights of Discovery Tree, Nov 2016 – April 2018. (a) 1.5 m, (b) 56 m.

4.4.3. Temperature difference as a function of light intensity (Figure 4.6)

The temperature difference between HOBO and aspirated sensors is not significantly related to the HOBO light intensity at 1.5 m ($R^2 = 0.0005$), 10 m ($R^2 = 0.03$), or 20 m ($R^2 = 0.05$). Linear models are weakly significantly positive at 30m ($R^2 = 0.20$), and strongly significantly positive at 40m ($R^2 = 0.76$) and 50m ($R^2 = 0.63$). The slopes of these relationships indicate that at 30 m and above, an increase of 1000 lux is associated with an increase of 0.10 to 0.15 °C in the temperature difference between the HOBO sensor and the aspirated sensor.

Figure 4.6. Difference in air T (HOBO – DSCMET [aspirated]) as a function of light intensity on the Hobo sensor, for different tree heights in the Discovery Tree, Nov 2016-April 2018.

4.4.4. Temperature difference as a function of wind speed (Figures 4.7, 4.8, 4.9a, 4.10a)

At 56 m height in the tree, the temperature difference between HOBO and aspirated sensors is strongly positively related to HOBO light intensity at wind speeds < 1 m/s ($R^2 = 0.82$) and at wind speeds > 1 m/s ($R^2 = 0.83$). The slopes of these relationships indicate that at wind speeds < 1 m/s, an increase of 1000 lux is associated with an increase of 0.17 °C in the temperature difference between the HOBO sensor and the aspirated sensor, whereas at wind speed > = 1 m/s, an increase of 1000 lux is associated with an increase of only 0.1°C in the temperature difference between the HOBO sensor and the aspirated sensor. In other words, the radiation-induced temperature error is lower when the wind speed is high compared to when it is low.

The relationship between HOBO and aspirated air temperature difference to HOBO light intensity when the wind speeds are less than 0.5 m/s is very different at 1.5 m compared to 56 m. In general, the effect of light intensity on temperature difference between HOBO and aspirated sensor is larger at 56m compared to 1.5m. In addition, this effect is stronger at both heights in January compared to other months. It means that the slopes of regression models at both heights are larger than the slopes of other models in other times of year. Therefore, when the wind speed is less than 0.5 m/s an increase of 1000 lux in light intensity causes a larger temperature difference between HOBO and aspirated sensor compared to other times of year (Figures 4.9a, 4.10a).

At 40 m height in the tree, the temperature difference between HOBO and aspirated sensors is strongly positively related to HOBO light intensity at wind speeds < 1 m/s ($R^2 = 0.76$), but only weakly related to light intensity at wind speeds > 1 m/s ($R^2 = 0.38$) (Figure 4.8a). The slopes of these relationships indicate that at wind speed < 1 m/s, an increase of 1000 lux is associated with an increase of 0.17 °C in the temperature difference between the HOBO sensor and the aspirated sensor, whereas at wind speed > = 1 m/s, an increase of 1000 lux is associated with an increase of only 0.13°C in the temperature difference between the HOBO sensor and the aspirated sensor. As above, this means that the radiation-induced temperature error is lower when the wind speed is high compared to when it is low.

Figure 4.7 (a,b). Difference in air T (HOBO – aspirated) at 56 m, as a function of light intensity on the HOBO sensor, for different wind speeds in Discovery Tree, Nov 2016 – April 2018.

Figure 4.8 (a.b). Difference in air T (HOBO – aspirated) at 40 m, as a function of light intensity on the HOBO sensor, for different wind speeds at 56 m height in Discovery Tree, Nov 2016 – April 2018.

Figure 4.9. Difference in air temperature at HOBO vs. aspirated sensor as a function of HOBO light intensity at 1.5 m height in Discovery Tree for wind speeds < 0.5 m s^{-1} during (a) Jan, (b) April, (c) July, and (d) October of 2017.

Figure 4.10. Difference in air temperature at HOBO vs. aspirated sensor as a function of HOBO light intensity at 56 m height in Discovery Tree for wind speeds < 0.5 m s^{-1} during (a) Jan, (b) April, (c) July, and (d) October of 2017.

4.4.5. Temperature difference as a function of relative humidity (Figure 4.11)

At 56 m height in the tree, the temperature difference between the HOBO and aspirated sensors is strongly positively related to the HOBO light intensity for relative humidity values greater than 80% but less than 100 % (R^2 = 0.84) (Figure 4.11a). The slope of this relationship indicates that an increase of 1000 lux is associated with an increase of 0.18 °C in the temperature difference between the HOBO sensor and the aspirated one. In contrast, the temperature difference between the HOBO and aspirated sensors is weakly correlated with the HOBO light intensity for relative humidity values less than or equal 80% (R^2 = 0.36) (Figure 4.11 b). The slope of this relationship indicates that an increase of 1000 lux is associated with an increase of 0.12 °C in the temperature difference between the HOBO sensor and the aspirated one.

Figure 4.11. Difference in air T (HOBO –aspirated) at 56 m height, as a function of light intensity at the Hobo sensor, grouped by relative humidity in Discovery Tree, Nov 2016 – April 2018.

4.4.6. Wind speed and relative humidity

Wind speed at 1.5 m is not related to relative humidity. In other words, as wind speed increases at 1.5 m, relative humidity does not change (Figure 4.12 a). At 56 m, wind speed is negatively correlated to relative humidity. In other words, as wind speed increases at 56 m, relative humidity decreases (Figure 4.12 b).

Figure 4.12. Relative humidity vs. wind speed at 1.5 m and 56 m, Discovery Tree, Nov 2016-April 2018.

4.5. DISCUSSION

This analysis confirms other studies showing that light has a linear effect on the difference of air temperature measurement between an un-aspirated and an aspirated temperature sensor. As light hits a surface, the radiative and turbulent sensible heat flux convergence causes the temperature of the surface to rise. At higher wind speeds the effect of radiation-induced heating is decreased due to the increased mixing of the air surrounding the sensor.

This study showed that light and wind affect temperature measurements at HOBO compared to the aspirated sensors, and relative humidity is correlated to air temperature differences. On average, the light induced temperature increase at the HOBO compared to the aspirated sensors was about 0.14°C per 1000 Lux at 50-meter height. Given that the HOBO light levels increase with tree height thus, the HOBO air temperature measurements increase with height in the tree. Thus, the HOBO sensors at higher elevations are more affected by the light-induced effects on measured temperature.

Wind affects the measured temperature at the HOBO sensors compared to the aspirated sensors. The largest difference between the measured temperature of the HOBO sensor and the aspirated sensor is associated with low wind speed, and the difference decreases as the wind speed increases. The impact of light is greater when the wind speed is lower than 1m/s. When the wind speed is above 1m/s, light increases the measured temperature at the HOBO compared to the aspirated sensors by about 0.1° C per 1000 Lux.
When the wind speed is less than 0.5 m/s, light increases the measured temperature at HOBO compared to aspirated sensor at 1.5m and 56m in January 2017 by 0.2 ºC per 1000 Lux. The reason is that under low wind speed conditions the temperature deficit (error) between HOBO and aspirated sensor increases due to lack of mixing whereas under high wind speed conditions the temperature deficit between HOBO and aspirated sensor decreases due to mixing.
Wind speed increases with height in the tree. When the wind speed is above 1m/s, the wind speed at 56-meter height is less affected by the light-induced effect on measured temperature.

In terms of relative humidity, at values less than or equal 80 %, the effect of light on the measured temperature at HOBO compared to aspirated sensors is weak. On the other hand, at the values larger than 80 %, light increases the temperature at the HOBO sensors compared to the aspirated ones by about 0.18°C per 1000 Lux. In other words, the radiation-induced temperature error is larger for relative humidity values greater than 80% compared to relative humidity values less than or equal 80%. Relative humidity would not be expected to directly influence the radiation balance (as explained in the introduction). In addition, wind speed and relative humidity are not correlated at 1.5 m but negatively correlated at 50 m height of Discovery tree (Figure 10). In general, and under clear sky condition as wind speed and relative humidity are inversely correlated. In other words, as wind speed increases, the relative humidity decreases. This is mainly due to the increased rate of evaporation in windy condition.

The dominant heat transfer mechanism responsible for temperature increase at both HOBO and aspirated sensors is radiative transfer followed by convection. As the light hits the shields of the HOBO and aspirated sensors, the temperature of the shield increases. This heat then radiates to the sensor suspended below it. The heated shield also heats the air below the shield and around the sensor through convection.

The material and thickness of the radiation shield influences how solar radiation affects the sensor. If the radiation shield is made of thick PVC material, conduction will be negligible due to the very low thermal conductivity of plastic polymer. Thus, radiation shields are made of plastic polymer to diminish the effect of conduction-induced temperature increase on temperature sensors.

Convection is not much affected by the type and color of the sensor shields. Convection occurs either naturally as free convection or due to some force (using a fan) as forced convection. The type of convection at the HOBO sensors is free convection which occurs due to the buoyancy effect. In contrast, forced convection at the aspirated sensors is due to the effect of fan in mixing the air around the sensor.

This study confirmed that the aspirated sensor is more suitable for measuring the ambient air temperature because the air around the aspirated sensor is more representative of the natural condition of air in the old-growth forest canopy, compared to the air around the unaspirated sensor. On the other hand, the HOBO sensors are more cost effective compared to the aspirated sensors.

The relationships identified in this could be applied to correct air temperature measured at sites that are instrumented with only HOBO sensors. The first set of corrections applys when the HOBO light intensities and temperatures are available, but wind speeds are not available.

The best-fitting equations could be used to correct HOBO temperature measurements obtained from sites which lack measurements of aspirated air temperature or wind speed.

40 m $Y = 0.1496\,X + 0.1787$

50 m $Y = 0.1455\,X + 0.1515$

where Y = (HOBO – Aspirated) air temperature (°C) at 40 or 50 m, X = HOBO light intensity (thousands of Lux). When Y is subtracted from the HOBO air temperature measurement this yields the estimated value that would have been measured by an aspirated sensor.

A second set of equations could be used to correct HOBO temperature measurements obtained from sites which lack measurements of aspirated air temperature, but have measurements of wind speed:

wind speed < 1 m/s $Y = 0.1721\,X + 0.1272$

wind speed >= 1 m/s $Y = 0.1089\,X + 0.1831$

The correction factors obtained from models based on measurements at the Discovery Tree may enable more accurate measurements to be made using HOBO sensors at less accessible sites in the Andrews Forest.

The correction factors should be used with caution to correct HOBO sensor measurements at 1.5-meter heights. Measurements at these sensors may be affected by upward soil heat flux and reflection of shortwave radiation from snow below the sensor. These factors were not considered in the relationships calculated here.

BIBLIOGRAPHY

Anderson, S., and Baumgartner, M.F. 1998. Radiative Heating Errors in Naturally Ventilated Air Temperature Measurements Made from Buoys. *Journal of Atmospheric and Oceanic Technology,* 15, pp: 157-173.

Bierlmaier, F.A., and McKee, A. 1989. Climatic Summaries and Documentation for the Primry Meteorological Station, H.J. Andrews Experimental Forest, 1972 to 1984. USDA, Pacific Northwest Research Station, *General Technical Report, PNW-GTR-242*.

Fuchs, M., and Tanner, C.B. 1965. Radiation Shields for Air Temperature Thermometers. *Journal of Applied Meteorology,*4, pp: 544-547.

Franklin, J., F., and Dyrness, C., T. 1973. *Natural Vegetation of Oregon and Washington*. General Technical Report, No. PNW-8. Pacific Northwest Forest and Range Experiment Station.

Franklin, J. F., Cromack, K., Denison, W., McKee, A., Maser, C., Sedell, J., Swanson, F., Juday, G. 1981. *Ecological Characteristics of Old-Growth Douglas-Fir Forests*. General Technical Report, No. PNW-118. Pacific Northwest Forest and Range Experiment Station.

Genthon, C., Six, D., Favier, V., Lazzara, M., and Keller, L. 2011. Atmospheric Temperature Measurement Biases on the Antarctic Plateau. *Journal of Atmospheric and Oceanic Technology*, 28, pp: 1598-1605.

Lin, X., Hubbard, K. G., Walter-Shea, E. A. 2001. Radiation Loading Model for Evaluating Air Temperature Errors with A Non-Aspirated Radiation Shield. *Transactions of The ASAE*, 44(5), pp: 1299-1306.

Mauder, M., Desjardins, R.L., Gao, Z., and Haarlem, R. V. 2008. Errors of Naturally Ventilated Air Temperature Measurements in a Spatial Observation Network. *Journal of Atmospheric and Oceanic Technology*, 25, pp: 2145-2151.

Nakamura, R., and Mahrt, L. 2005. Air temperature measurement errors in naturally ventilated radiation shields. *Journal of Atmospheric and Oceanic Technology,* 22, pp:1046–1058.

Richardson, S. J., Brock, F.V., Semmer, S. R., Jirak, C. 1999. Minimizing Errors Associated with Multiplate Radiation Shields. *Journal of Atmospheric and Oceanic Technology*, 16, pp: 1862-1872.

Swanson, F. J., and James, M. E. 1975. Geology and Geomorphology of the H.J. Andrews Experimental Forest, Western Cascades, Oregon. *USDA Forest Service, Research Paper PNW-188.*

Tanner, B. D., Swiatek, E., and Maughan, C. 1996. Field comparisons of naturally ventilated and aspirated radiation shields for weather station air temperature measurements. Preprints, *22d Conf. on Agricultural and Forest Meteorology,* Atlanta, GA, Amer. Meteor. Soc., pp: 227–230.

Thomas, C. K., and Smoot, A. R. 2012. An Effective, Economic, Aspirated Radiation Shield for Air Temperature Observations and Its Spatial Gradients. *Journal of Atmospheric and Oceanic Technology*, 30, pp: 526-537.

Weisberg, P. J., and Swanson, F. J. 2003. Regional synchronicity in fire regions of western Oregon and Washington, USA. *Forest Ecology and Management*, 172, pp: 17-28.

Table 4.1. Instruments deployed at the Discovery Tree, Nov 2016-present.

Instrument	Property	Description	Sensor specifications	Shield specification	Heights (m)	Dates
HOBO pendant	Air temperature	HOBO pendant (UA-001-64) temperature data logger	waterproof, one-channel logger with 10-bit resolution, range of 0 to 50 °C and accuracy +- 0.53 °C	20 cm long, 3.5 (4) inch diameter, schedule 40 PVC pipe split in half lengthwise, sensor suspended beneath	1.5, 10, 20, 30, 40, 56	11/14/16-present
Campbell Scientific 107 thermistor	Air temperature	Fan-aspirated model 107 probe	range of -40 to 60°C and accuracy of ±0.1 °C	41303-5A, 41303-5B, or RAD06 6-plate radiation shield OR fan-aspirated radiation shields (Thomas and Smoot)	10, 20, 30, 40	11/14/16-present
Rotronic HC2S3-L	Air temperature and relative humidity (RH)	HC2S3-L temperature and RH probe	capacitive sensor to measure RH and a 100 Ohm PRT to measure temperature over the range -40	fan-aspirated radiation shield built according to specifications in Thomas and Smoot (date) ??	1.5, 56	11/14/16-present (56 m), 11/14/16 - 5/24/17

			degrees C to +60 degrees C with accuracy +- 0.1 ºC			(1.5 m)
Rotronic EE181	Air temperature and relative humidity(RH)	EE181 Temperature and RH probe	A 1000 Ohm PRT to measures air temperature over the range -40 degrees C to +60 degrees C with accuracy +-0.2ºC	41003-5, 41003-5A, or RAD 10 10-plate naturally aspirated radiation shield	1.5	6/28/17-present

Figure 4.1

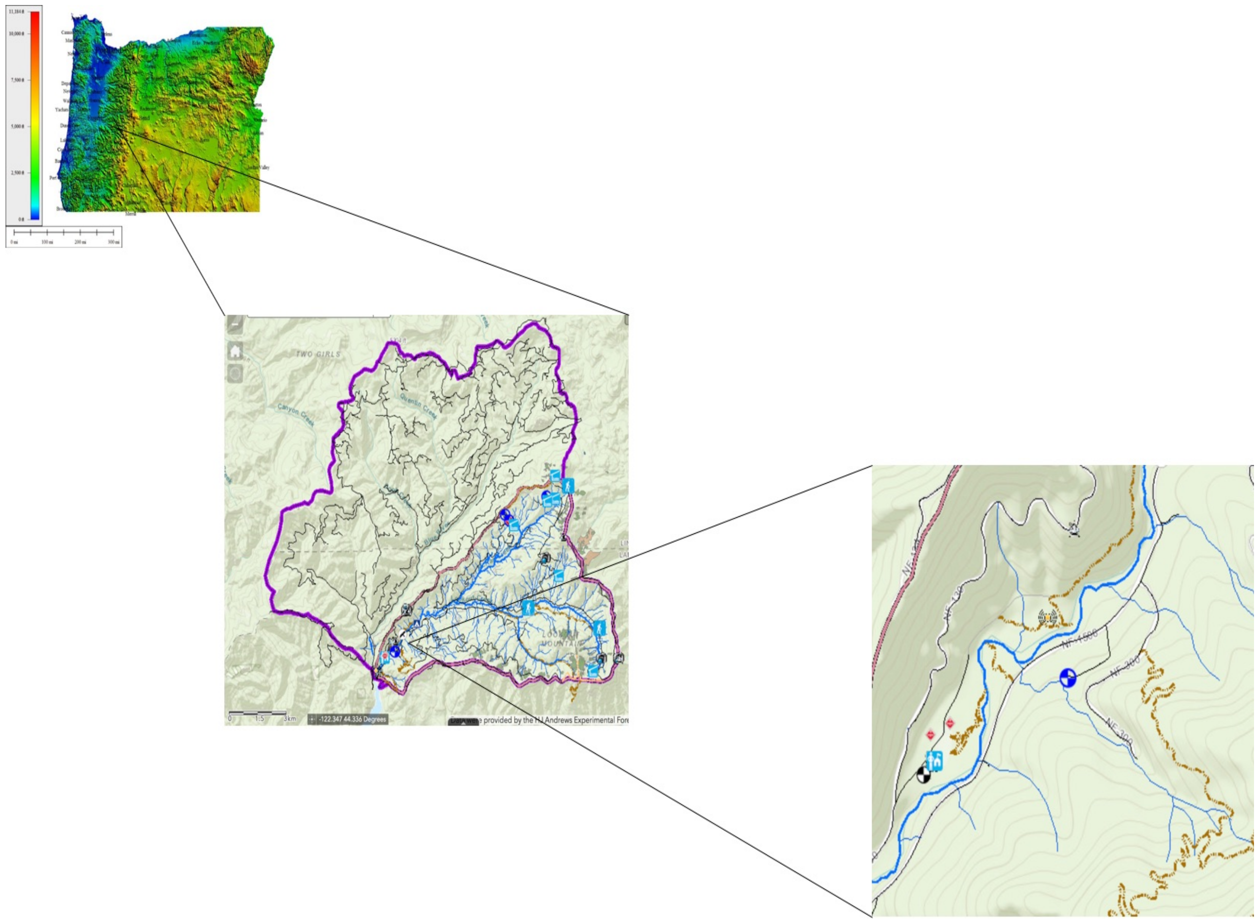
TWO GIRLS
NF-1506
NF-300
provided by the HJ Andrews Experimental Fore
-122.347 44.336 Degrees

Figure 4.2

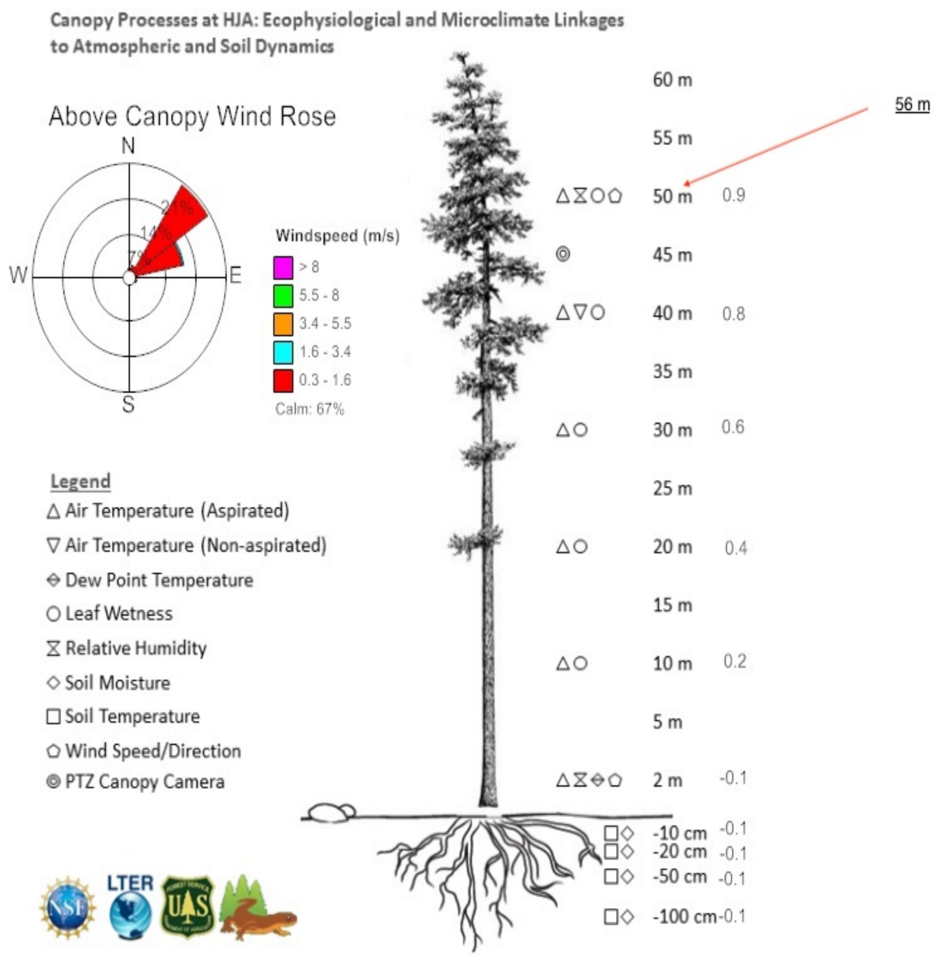
Canopy Processes at HJA: Ecophysiological and Microclimate Linkages to Atmospheric and Soil Dynamics
Above Canopy Wind Rose
N
E
S
W
Windspeed (m/s)
> 8
5.5 - 8
3.4 - 5.5
1.6 - 3.4
0.3 - 1.6
Calm: 67%
Legend
△ Air Temperature (Aspirated)
▽ Air Temperature (Non-aspirated)
Dew Point Temperature
○ Leaf Wetness
Relative Humidity
◇ Soil Moisture
□ Soil Temperature
Wind Speed/Direction
PTZ Canopy Camera
LTER
60 m
56 m
55 m
50 m 0.9
45 m
40 m 0.8
35 m
30 m 0.6
25 m
20 m 0.4
15 m
10 m 0.2
5 m
2 m -0.1
-10 cm -0.1
-20 cm -0.1
-50 cm -0.1
-100 cm -0.1

Figure 4.3

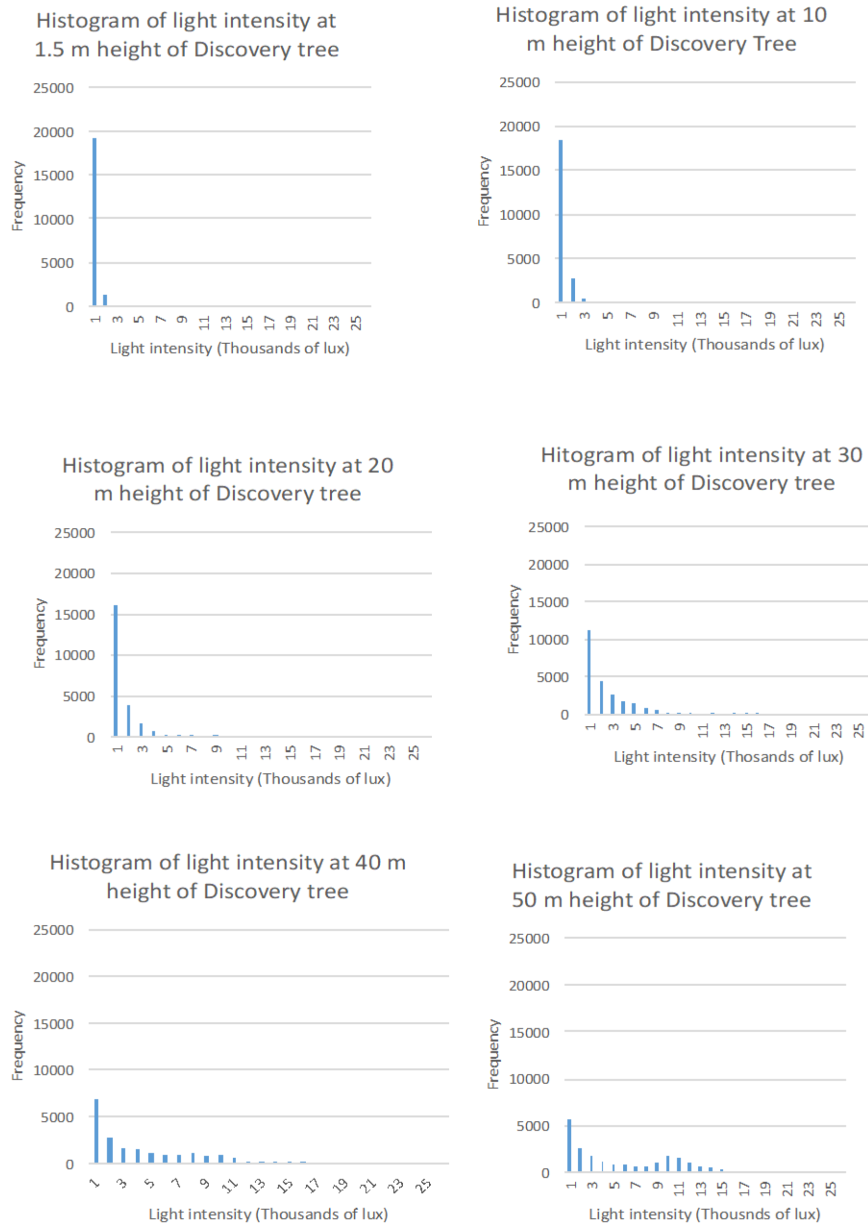
a
Histogram of light intensity at 1.5 m height of Discovery tree
Frequency
Light intensity (Thousands of lux)
b
Histogram of light intensity at 10 m height of Discovery Tree
Frequency
Light intensity (Thousands of lux)
c
Histogram of light intensity at 20 m height of Discovery tree
Frequency
Light intensity (Thousands of lux)
d
Hitogram of light intensity at 30 m height of Discovery tree
Frequency
Light intensity (Thosands of lux)
e
Histogram of light intensity at 40 m height of Discovery tree
Frequency
Light intensity (Thousands of lux)
f
Histogram of light intensity at 50 m height of Discovery tree
Frequency
Light intensity (Thousnds of lux)

Figure 4.4

Figure 4.5

a

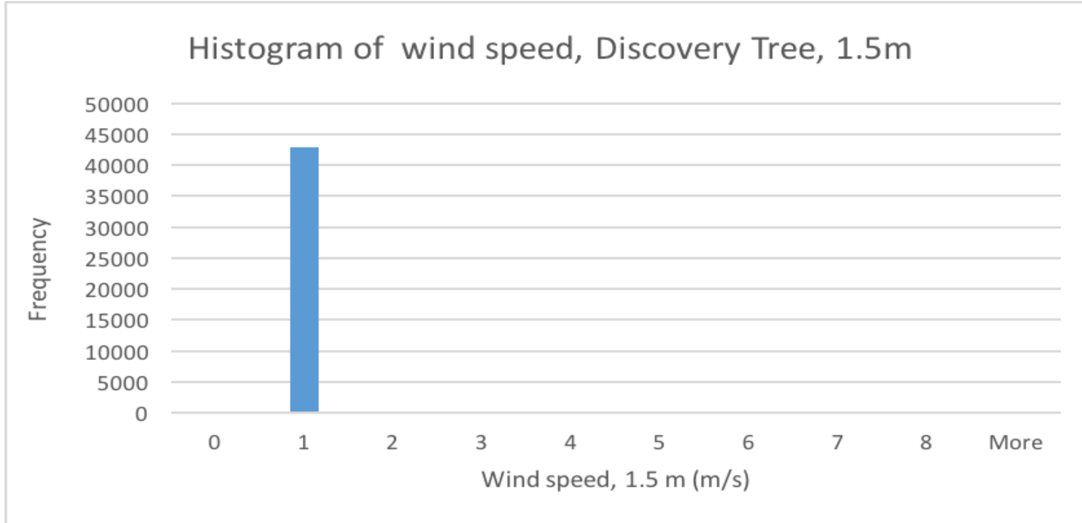
Histogram of wind speed, Discovery Tree, 1.5m
50000
45000
40000
35000
30000
25000
20000
15000
10000
5000
0
Frequency
0
1
2
3
4
5
6
7
8
More
Wind speed, 1.5 m (m/s)

b

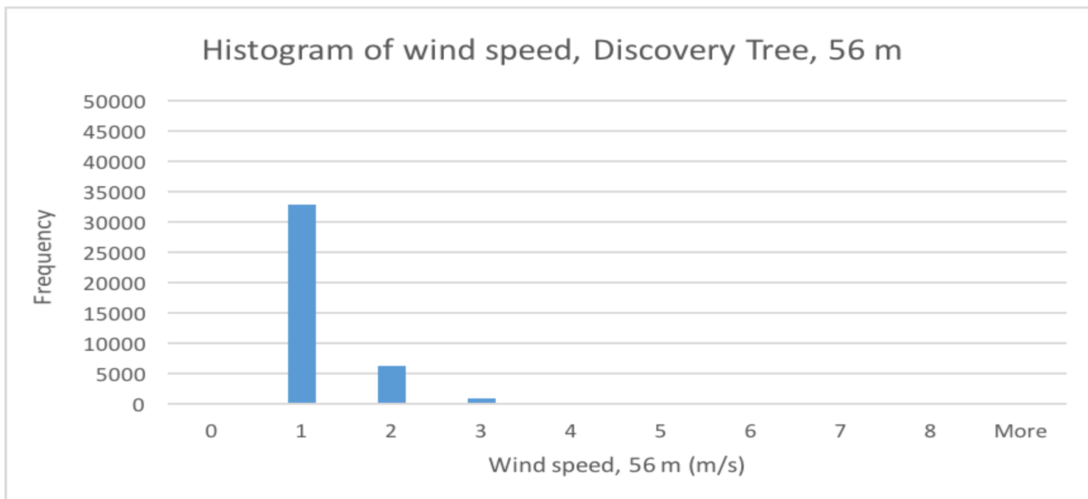
Histogram of wind speed, Discovery Tree, 56 m
50000
45000
40000
35000
30000
25000
20000
15000
10000
5000
0
Frequency
0
1
2
3
4
5
6
7
8
More
Wind speed, 56 m (m/s)

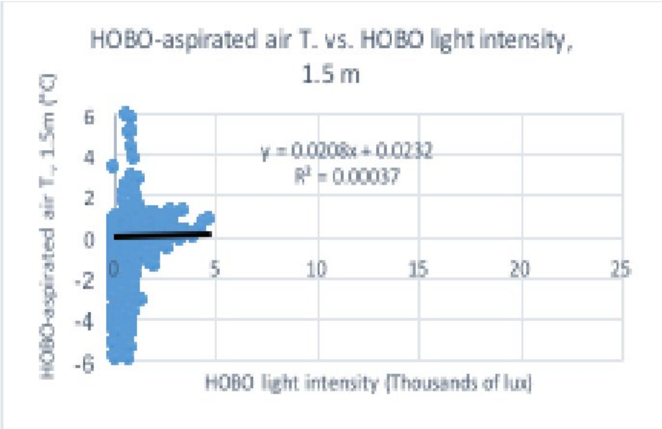

a

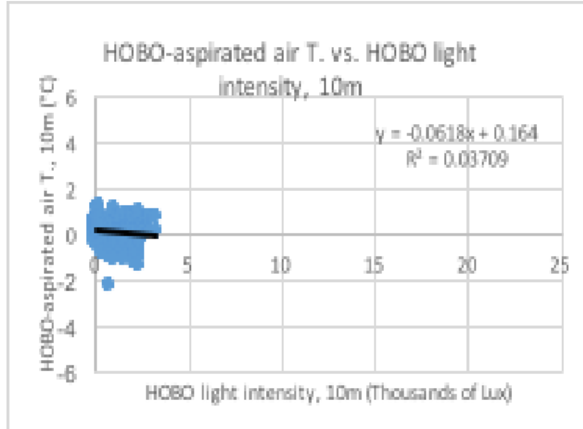

b

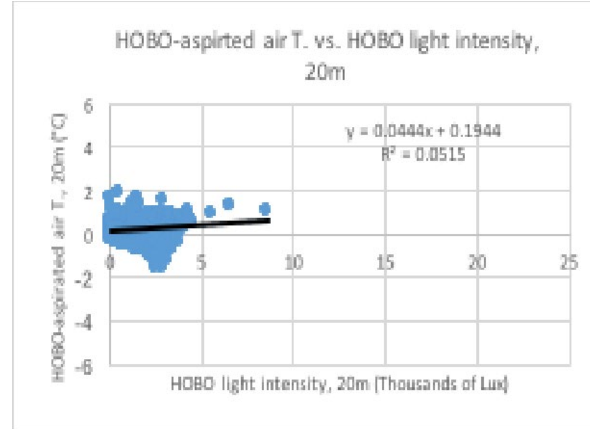

c

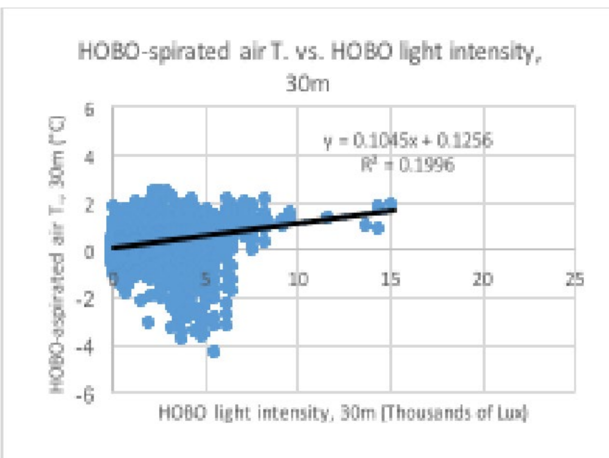

d

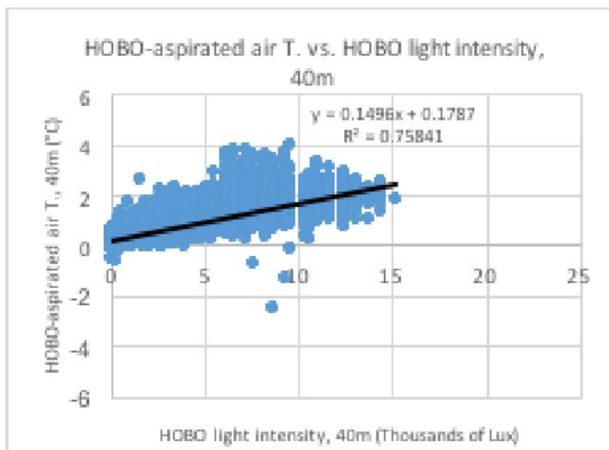

e

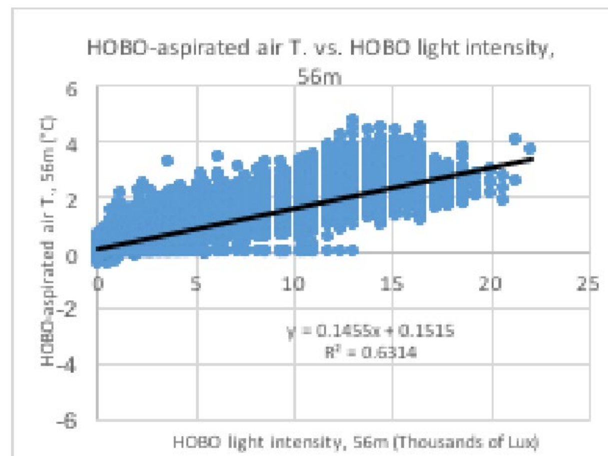

f

Figure 4.6

Figure 4.7a

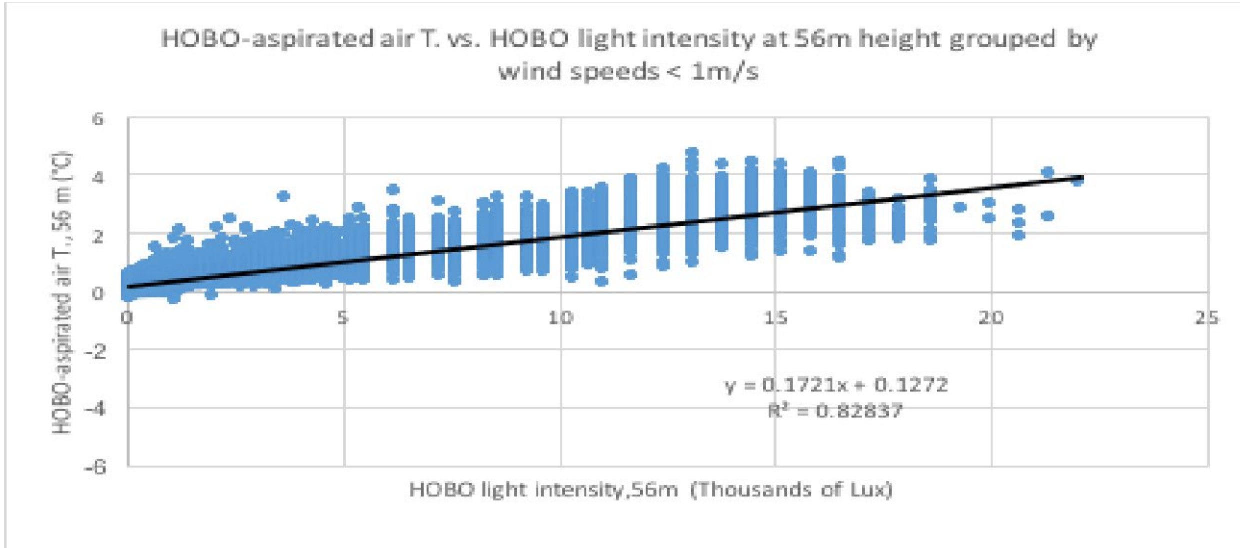

Figure 4.7b

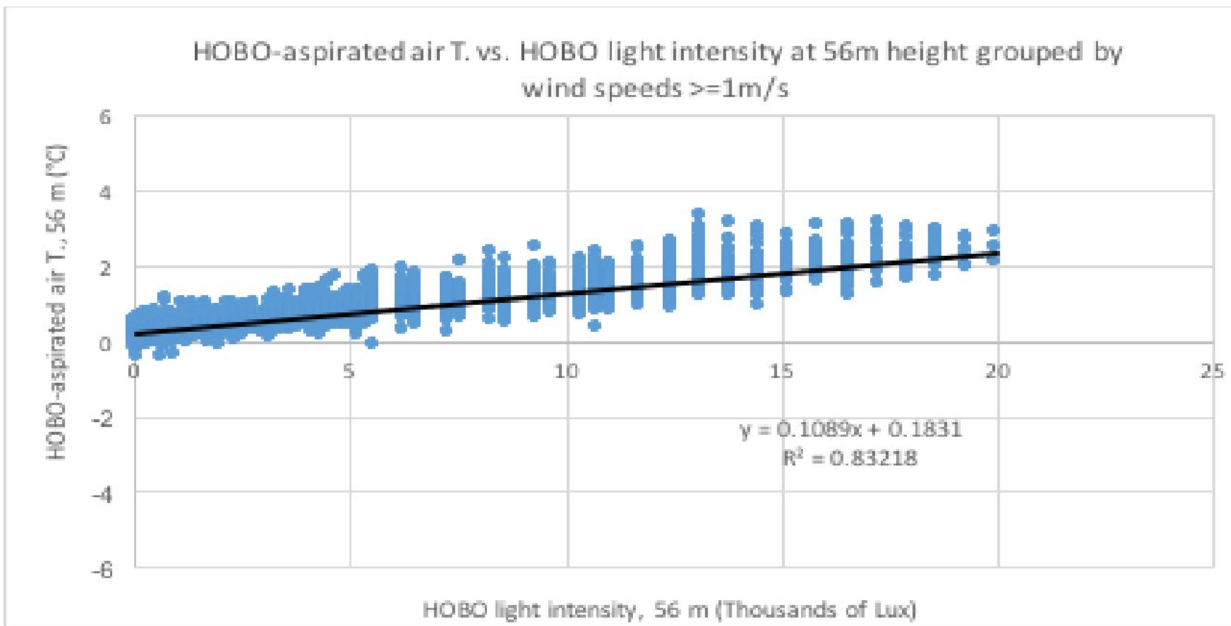

Figure 4.8a

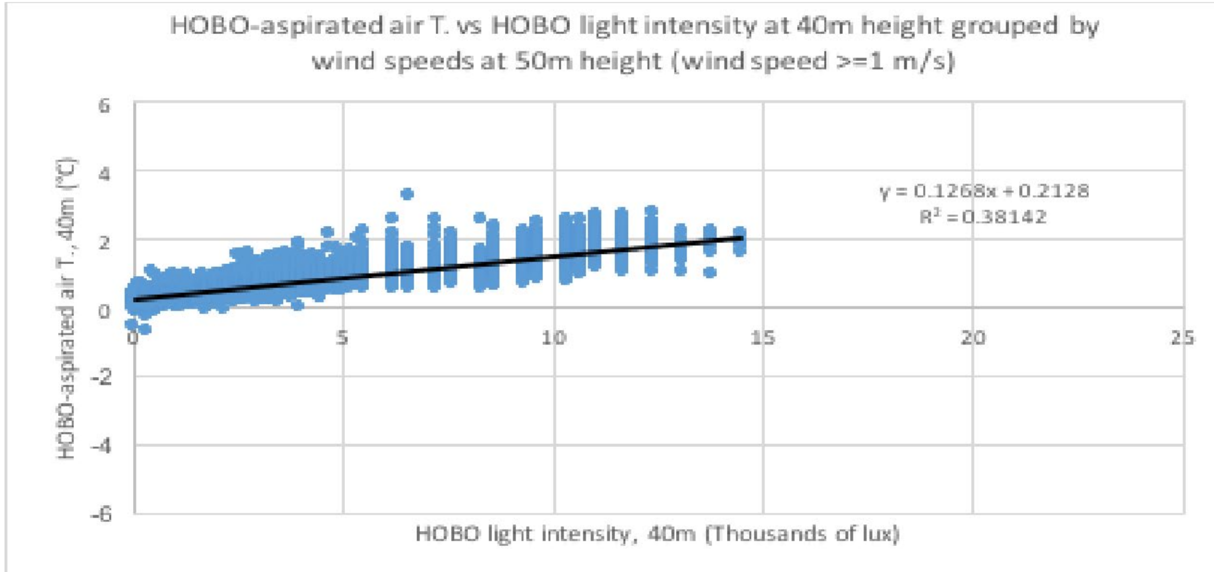

Figure 4.8b

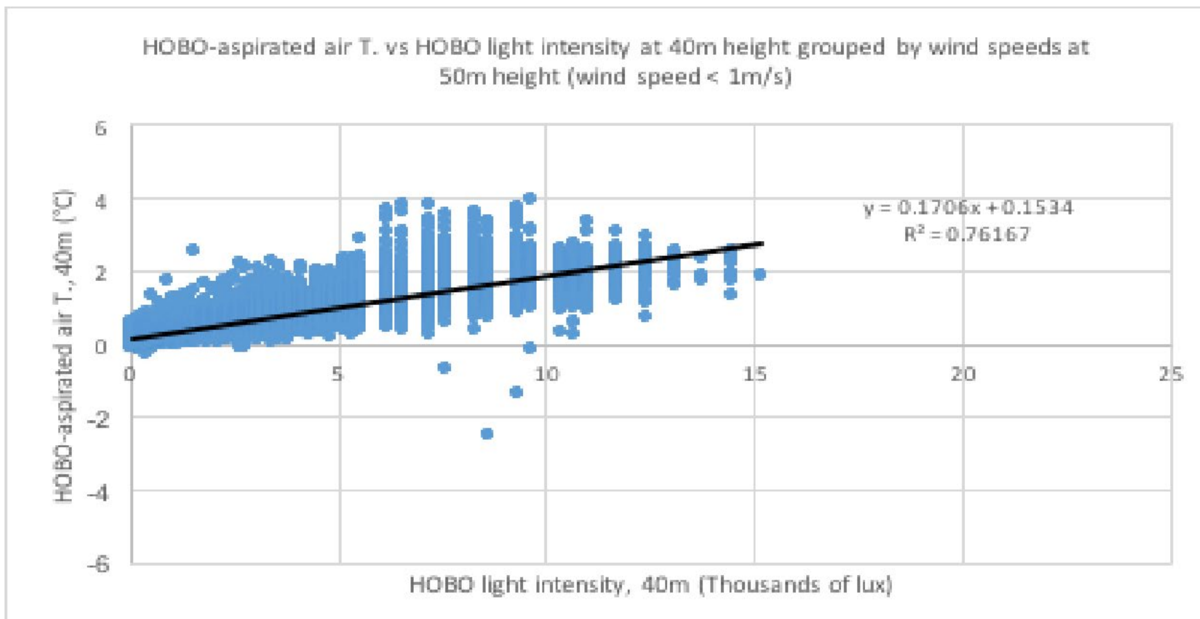

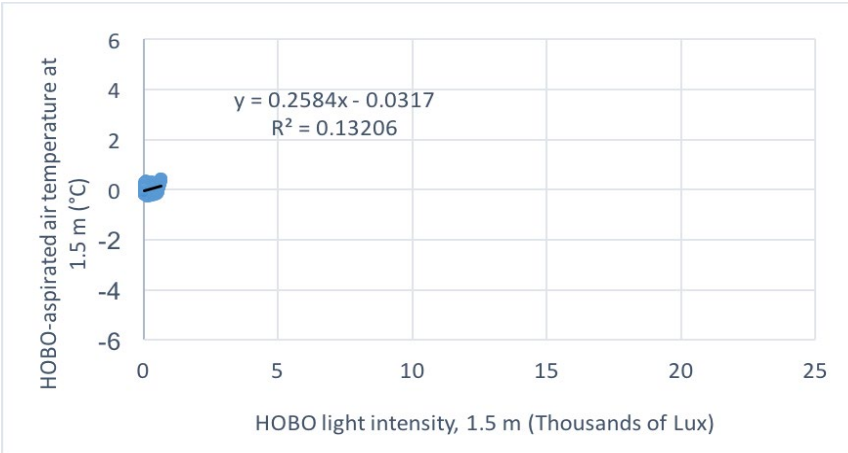

Figure 4.9a

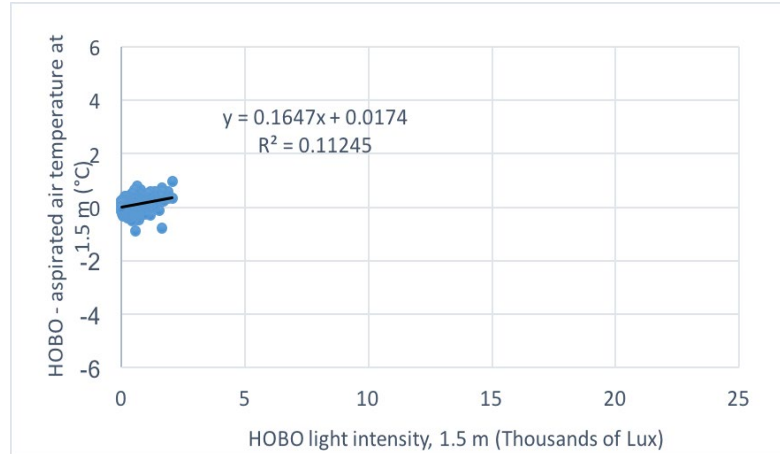

Figure 4.9b

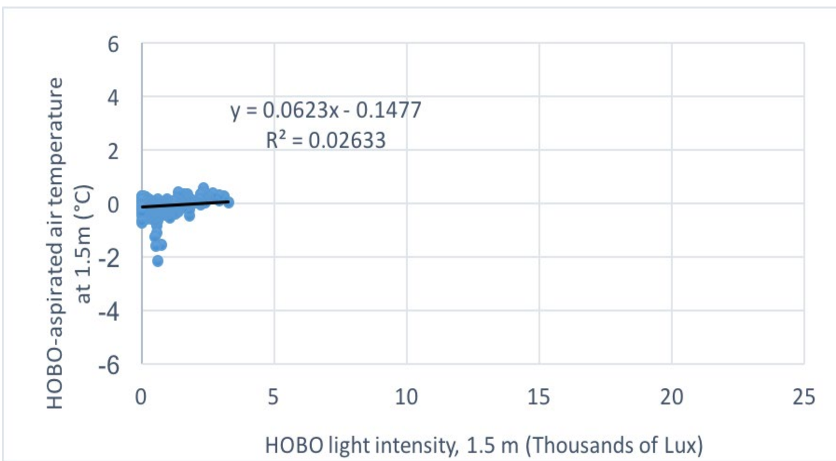

Figure 4.9c

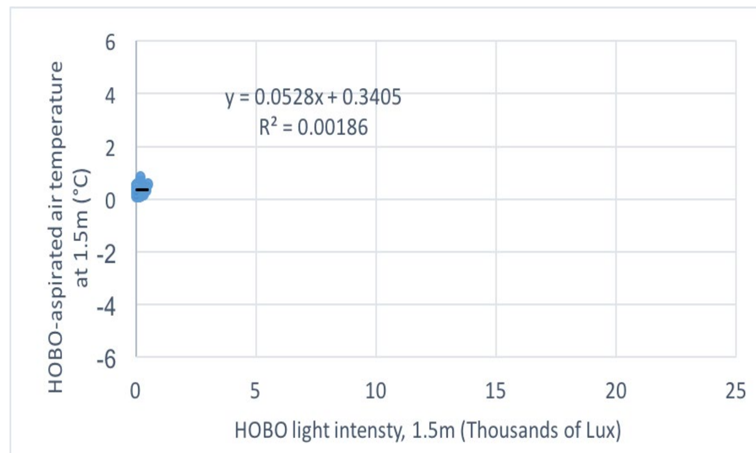

Figure 4.9d

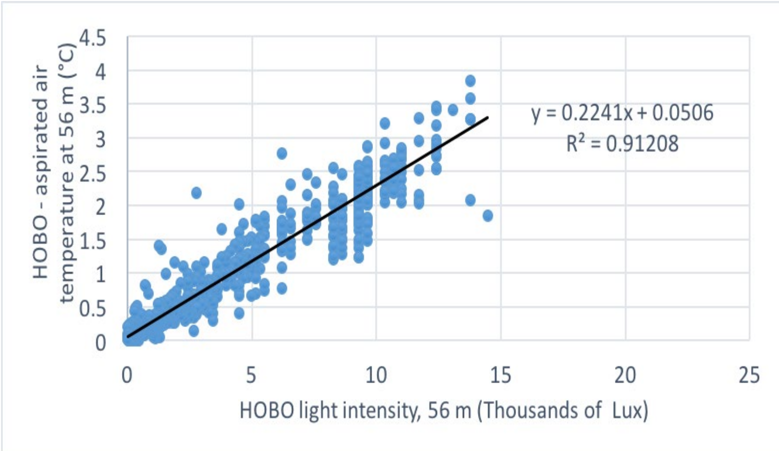

Figure 4.10a

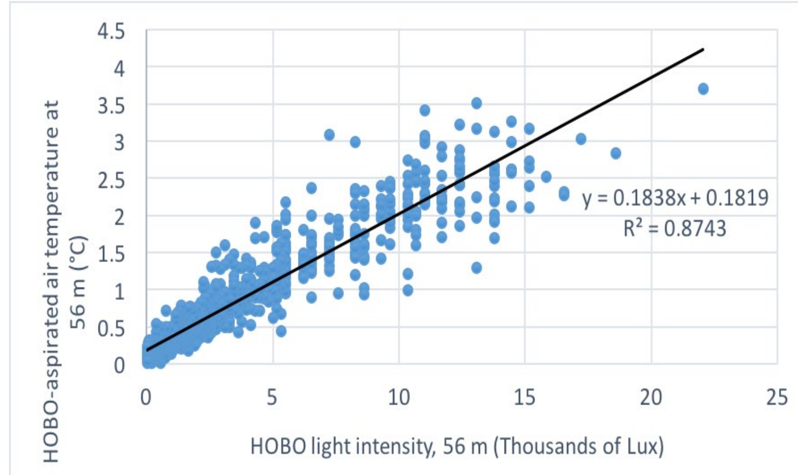

Figure 4.10b

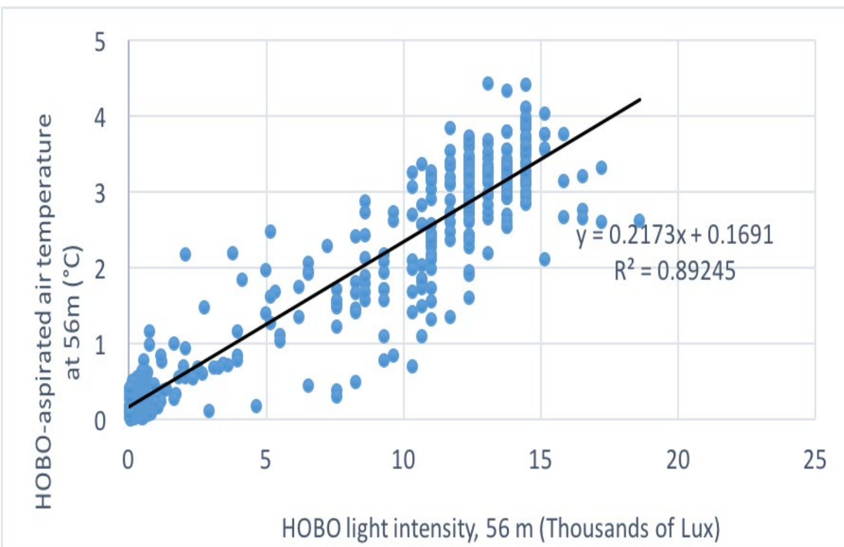

Figure 4.10c

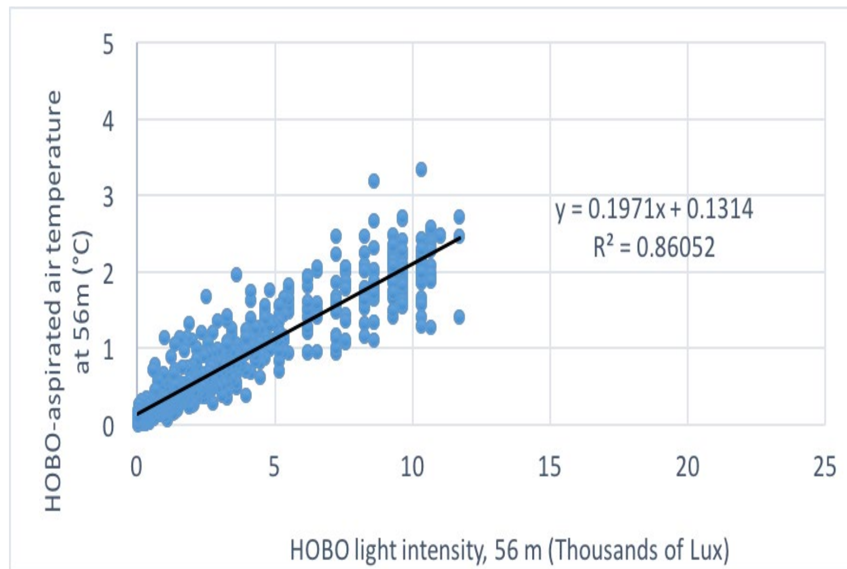

Figure 4.10d

Figure 4.11a

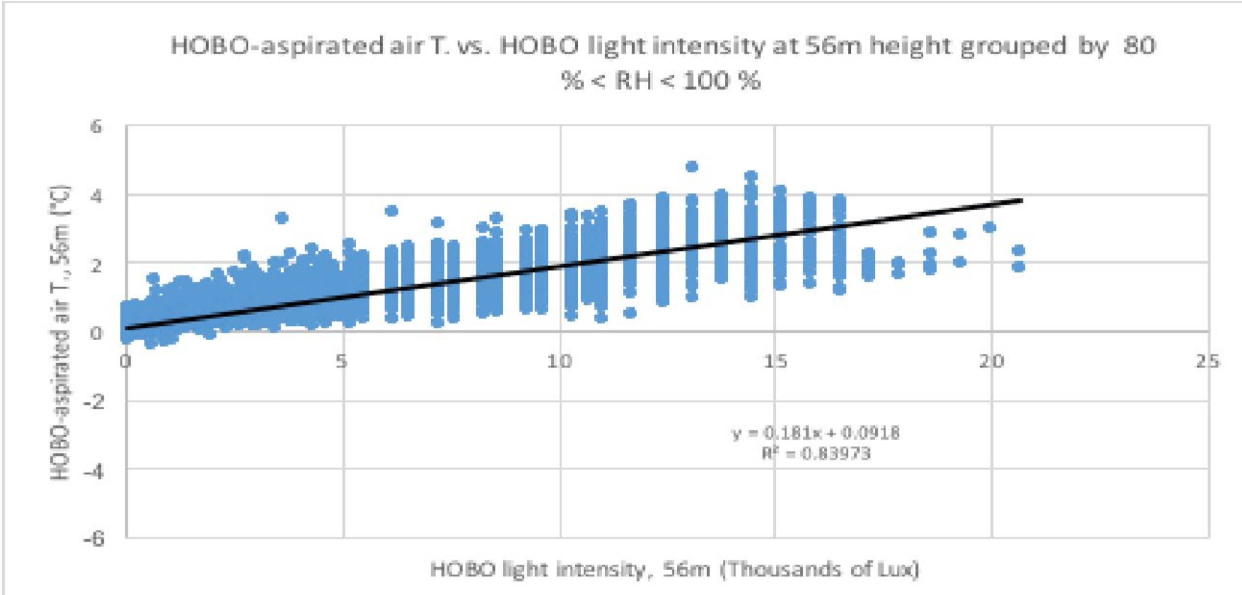

Figure 4.11b

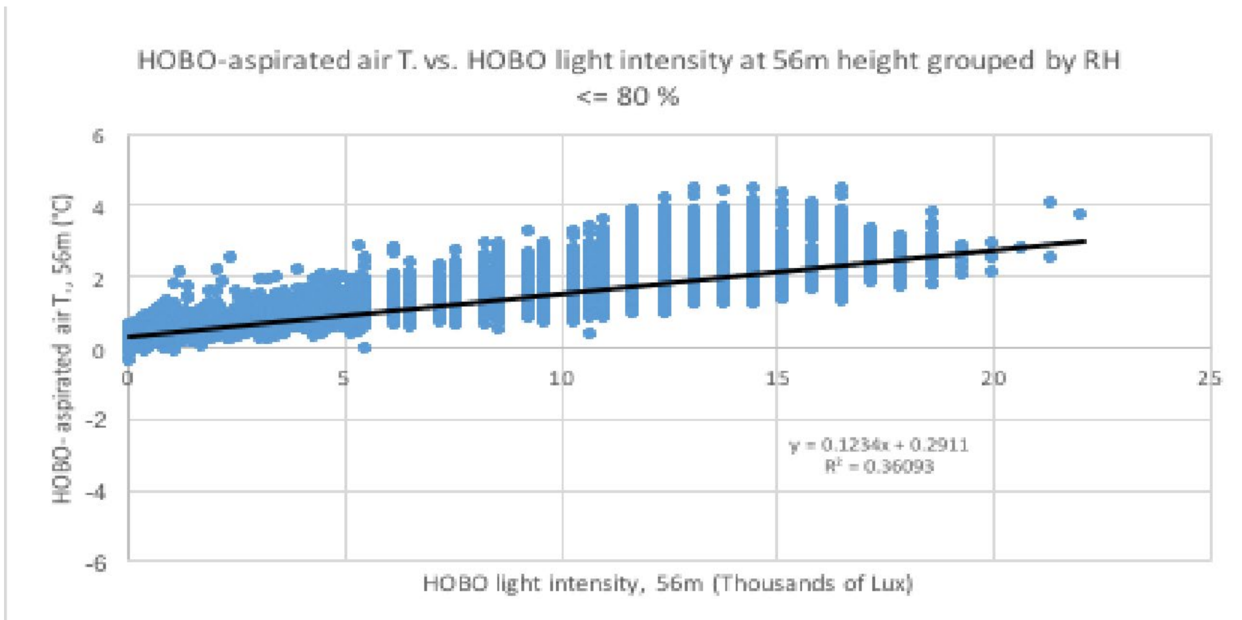

Figure 4.12a

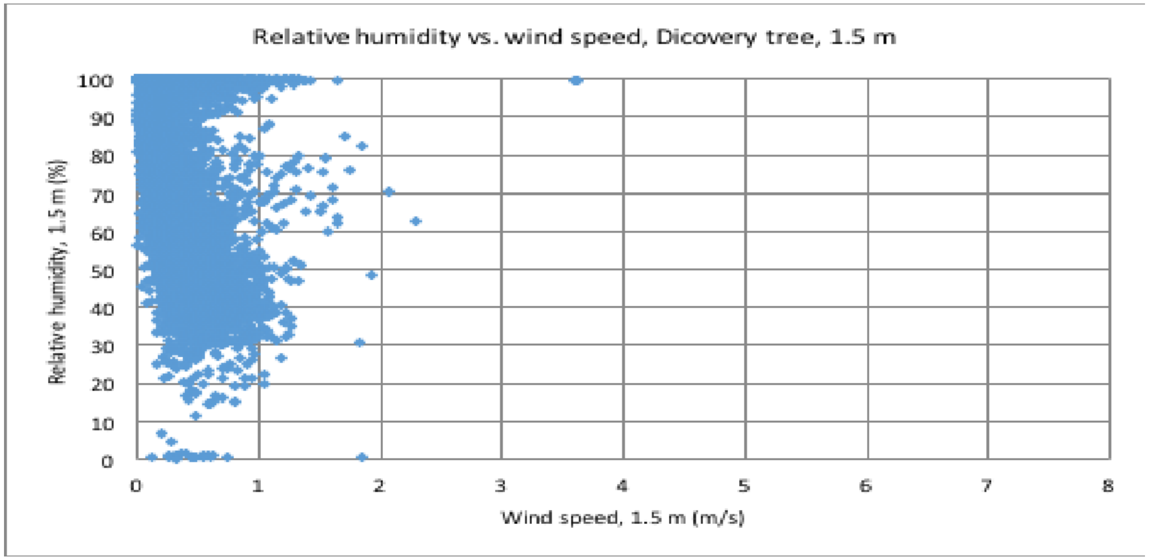

Figure 4.12b

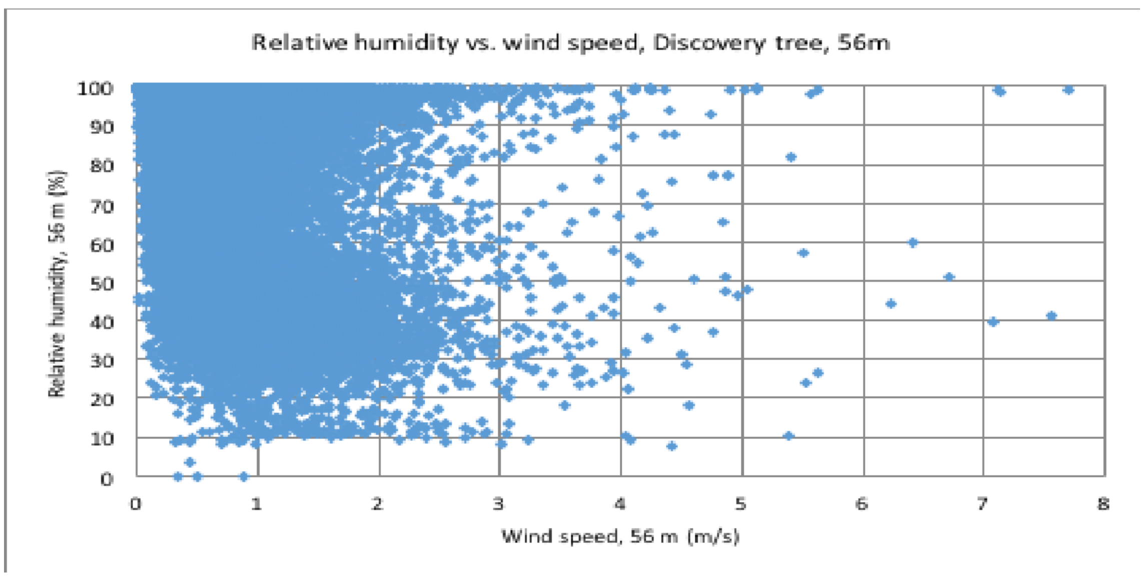

CHAPTER 5

Main findings and implications of the dissertation

5.1. Objective of the dissertation.

The objective of this dissertation was to understand the physical mechanisms affecting drainage flow and inversion events in a complex forested mountain landscape.

5.2. Effect of sun angle and topographic shading on vertical temperature profile in an old-growth Douglas-fir tree

Chapter 2 examined the effect of sun angle and topographic shading on diurnal heating and cooling and the vertical profile of temperature in Discovery tree. The main findings of this work are as follows. Sun angle and landscape shading influenced inversions. Although it was predicted that sun angle would be the main driver of inversion evolution at all times, the analysis showed that the importance of sun angle diminishes whereas the importance of landscape shading in inversion evolution increases during early morning and late afternoon (when the sun angle is low). The reason is that other factors such as upward ground heat flux and canopy heat storage become more important in the canopy energy budget than sun angle during the early morning and late afternoon hours. Trees promote mixing during night-time hours, counter to predictions. Trees promote inversions during day-time hours, counter to predictions.

The analysis in Ch2 is important because it has implications for understanding of ecosystem processes including carbon and water exchange. Diversity of flora and fauna also varies with vertical temperature gradients in the forest. The analysis in Ch2 also is important because it has implications for micrometeorology. The vertical temperature gradient is an index or proxy for behavior of inversions at the micro scale (<50 m).

5.3. Effects of sun angle and topographic shading on inversion dynamics in a mountain landscape

Chapter 3 examined effects of sun angle and topographic shading on inversion dynamics in a mountain landscape. The main findings were as follows. The proportion of the landscape in high shade influences the frequency and strength of inversions. The average solar radiation inputs influence the frequency and strength of inversions.

The analysis in Chapter 3 is important because it has implications for understanding of ecosystem processes. The landscape is composed of illuminated and shaded facets, which create differential wind and energy surfaces, which produce strong but localized winds, and affect the distribution of fauna and flora. These processes would be expected to produce variation in carbon and water exchange, and to contribute to high diversity by creating a variety of habitats. The analysis in Chapter 3 also is important because it has implications for understanding of local meteorology. Cold air pooling dynamics depend on physiography. The results reveal the hierarchy of processes operating to affect cold air pooling and inversions at different spatial scales.

5.4. Effects of light and wind on air temperature measurement in low-cost temperature sensors

Chapter 4 quantified the effect of light and wind on air temperature measurement in low-cost HOBO sensors with PVC shields. The main findings were as follows. The difference in measured air temperature between the HOBO sensor and an aspirated sensor was linearly positively related to light intensity (lux). The difference in measured air temperature was reduced at high wind speeds. Correction factors were developed.

The analysis in Chapter 4 is important because developing a correction factor may help to measure temperatures correctly using low-cost sensors in a spatially heterogeneous environment (both vertical and horizontal). The correction factors can be extended to correct sensors deployed horizontally, assuming horizontal homogeneity (same height) and same type of ecosystem (old growth forest).

5.5. Overall conclusions

Overall this dissertation showed that at low sun angles, other elements than net radiation, including shading of the surrounding landscape, influenced the energy budget of a 66-m tall Douglas-fir tree, producing conditions opposite to those predicted by radiation alone. In addition, the interaction of sun angle with landscape shading strongly influenced the strength and persistence of inversion events in the Andrews Forest. HOBO sensors experience radiation-induced temperature errors, and this error is reduced when the wind speed is high, and correction factors can be developed to remove some of this error.

APPENDIX FIGURES

2011

Figures A3.1 and A3.2_ Hourly air temperature differences, Vanmet – Primet,2011, daytime Hours(radiation >0) and nighttime hours (radiation = 0) respectively.

Figure A3.1

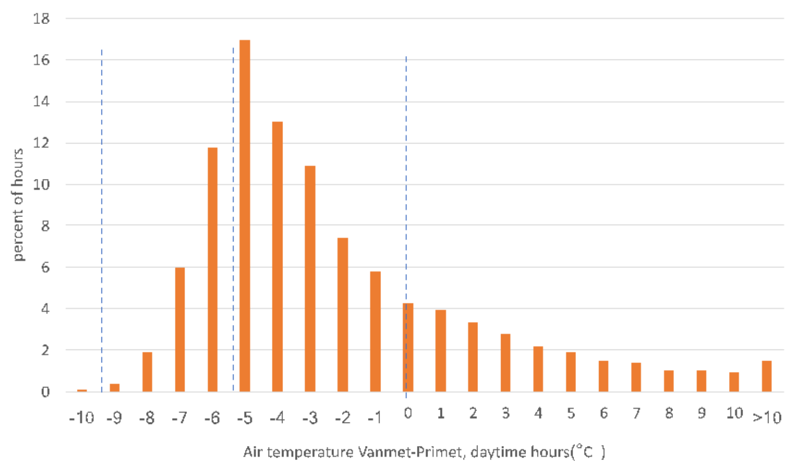

Figure A3.2

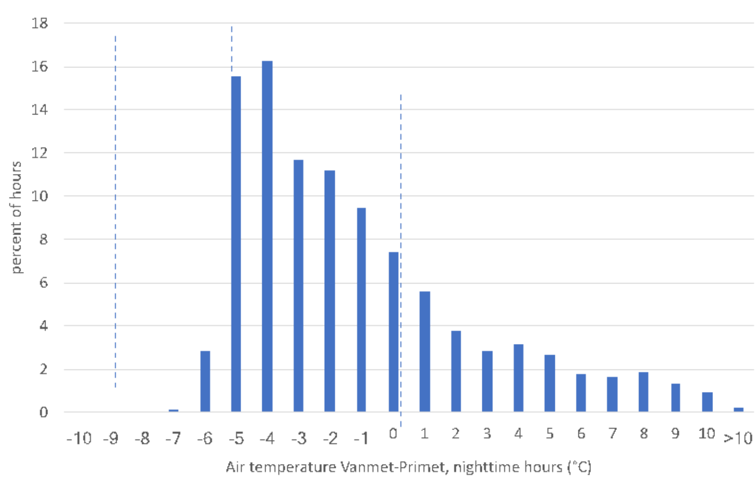

Figures A3.3-A3.6_ Daytime hourly wind speed and direction, Primet and Vanmet, 2011. (Fig A3.3) Wind speed, Primet (m/s), (Fig A3.4) Wind direction, Primet (degrees), (Fig A3.5) Wind speed, Vanmet (m/s), (Fig A3.6) Wind direction, Vanmet (degrees).

Figure A3.3

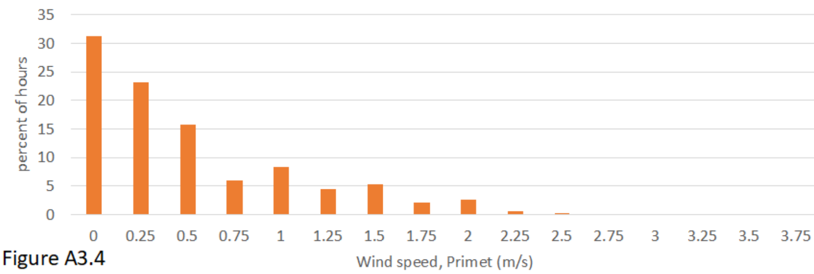

Figure A3.4

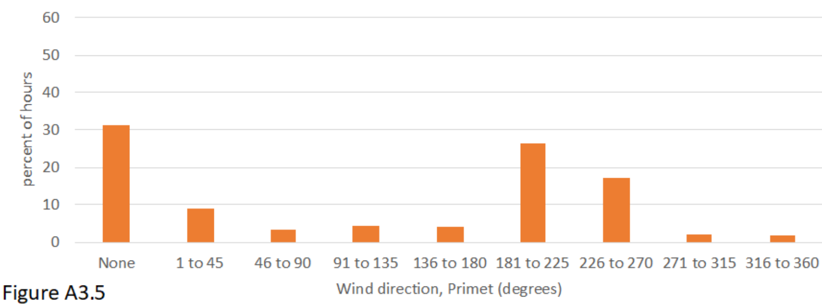

Figure A3.5

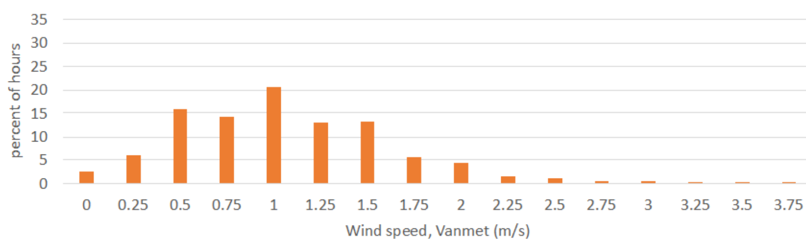

Figure A3.6

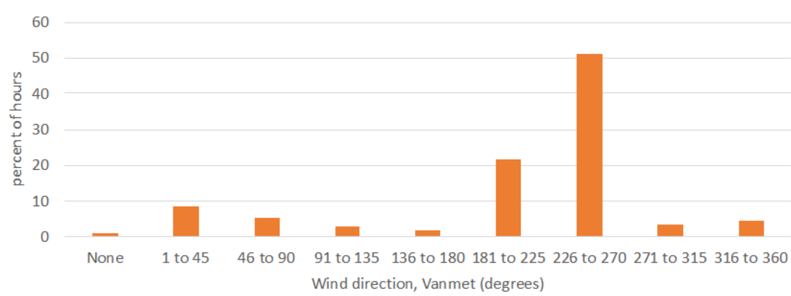

Figures A3.7- A3.10. Nighttime hourly wind speed and direction, Primet and Vanmet, 2011. (Fig. A3.7) Wind speed, Primet (m/s), (Fig. A3.8) Wind direction, Primet (degrees), (Fig. A3.9) Wind speed, Vanmet (m/s), (Fig. A3.10) Wind direction, Vanmet (degrees).

Figure A3.7

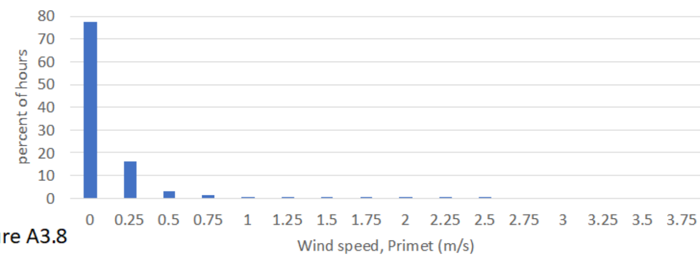

Figure A3.8

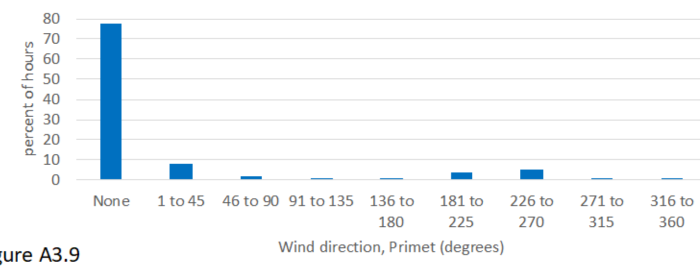

Figure A3.9

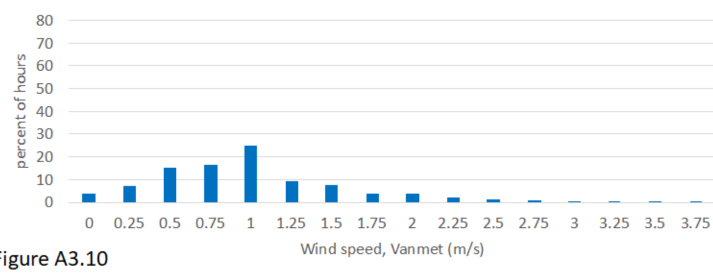

Figure A3.10

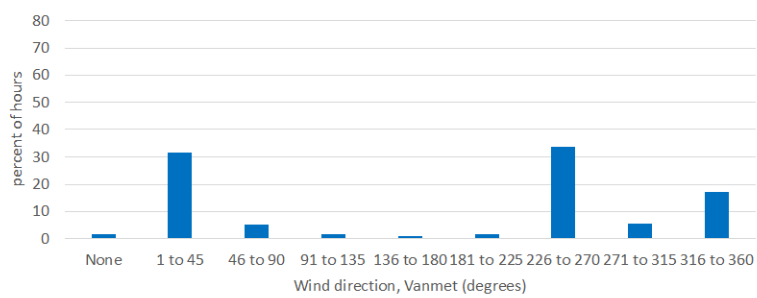

Figures A3.11 and A3.12. Hourly air temperature differences, Vanmet-Primet, for Jan, Apr, Jul, and Oct, 2011. (Fig. A3.11) daytime hours (radiation > 0), (Fig. A3.12) nighttime hours (radiation = 0).

Figure A3.11

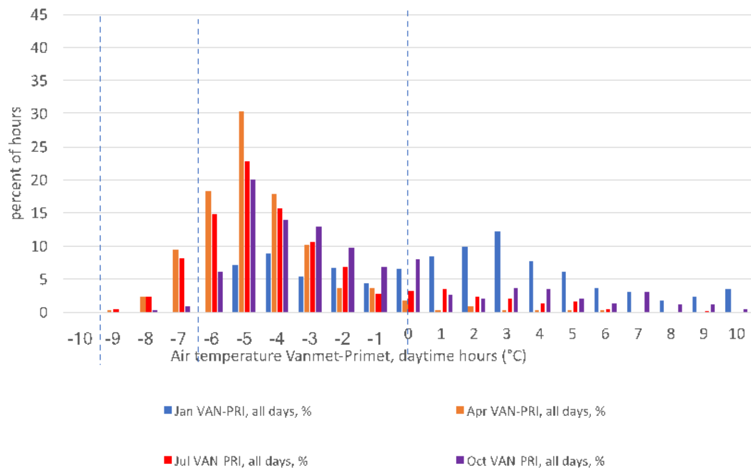

Figure A3.12

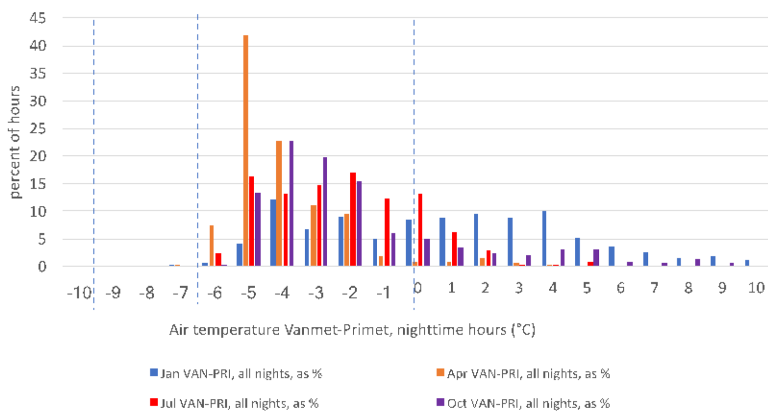

Figures A3.13-A3.16_ Daytime hourly wind speed and wind direction, Primet and Vanmet, Jan, Apr, Jul, and Oct, 2011. (Fig. A3.13) Wind speed, Primet (m/s), (Fig. A3.14) Wind direction, Primet (degrees), (Fig. A3.15) Wind speed, Vanmet (m/s), (Fig. A3.16) Wind direction, Vanmet (degrees)

Figure A3.13

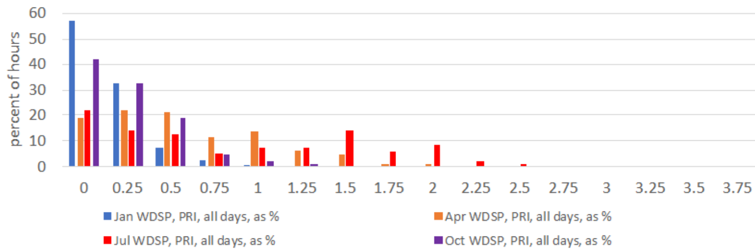

Figure A3.14

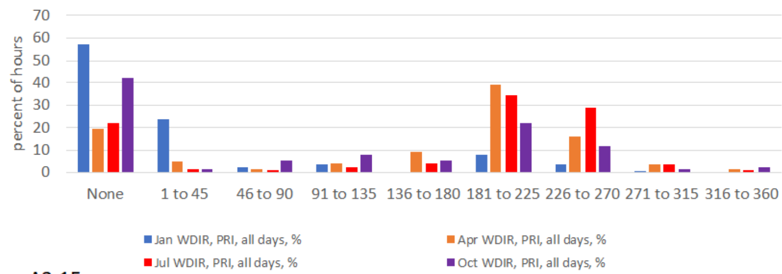

Figure A3.15

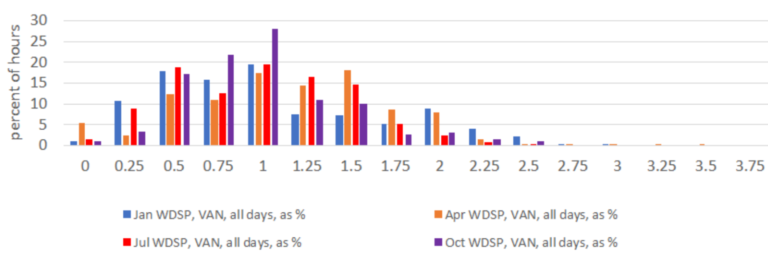

Figure A3.16

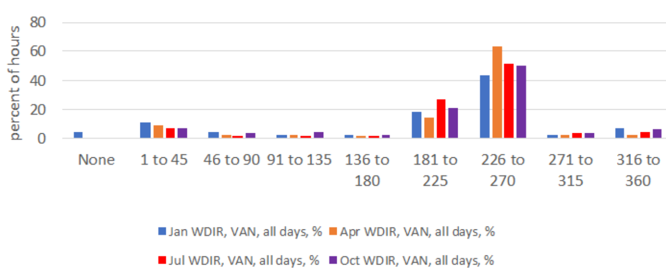

Figures A3.17-A3.20_ Nighttime hourly wind speed and wind direction, Primet and Vanmet, Jan, Apr, Jul, and Oct, 2011. (Fig. A3.17) Wind speed, Primet (m/s), (Fig. A3.18) Wind direction, Primet (degrees), (Fig.A3.19) Wind speed, Vanmet (m/s), (Fig.A3.20) Wind direction, Vanmet (degrees)

Figure A3.17

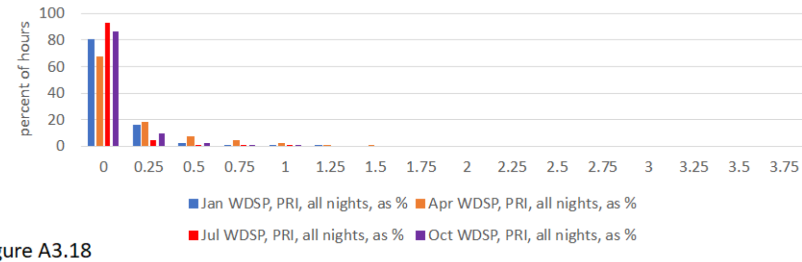

Figure A3.18

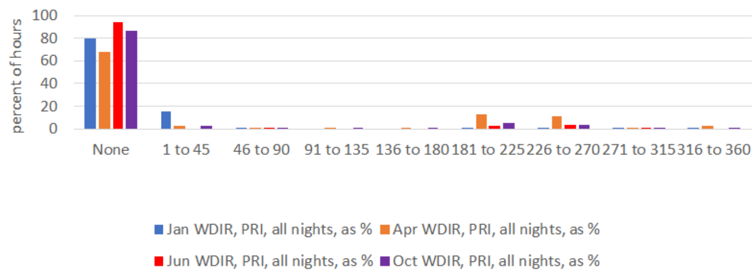

Figure A3.19

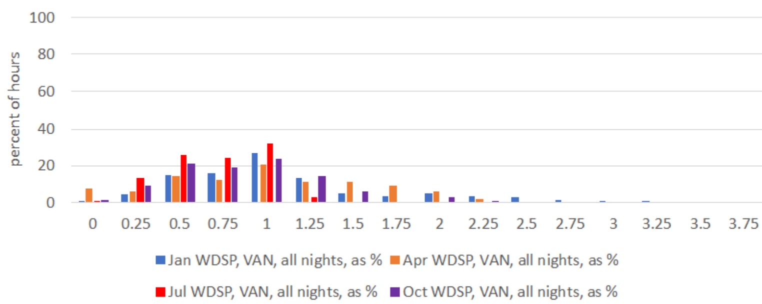

Figure A3.20

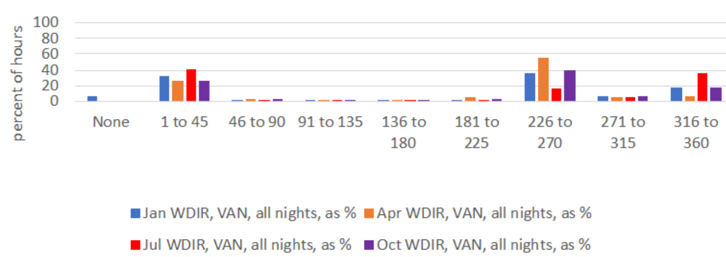

2003

Figures A3.21 and A3.22_ Hourly air temperature differences, Vanmet – Primet,2003, daytime hours(radiation >0) and nighttime hours (radiation = 0) respectively.

Figure A3.21

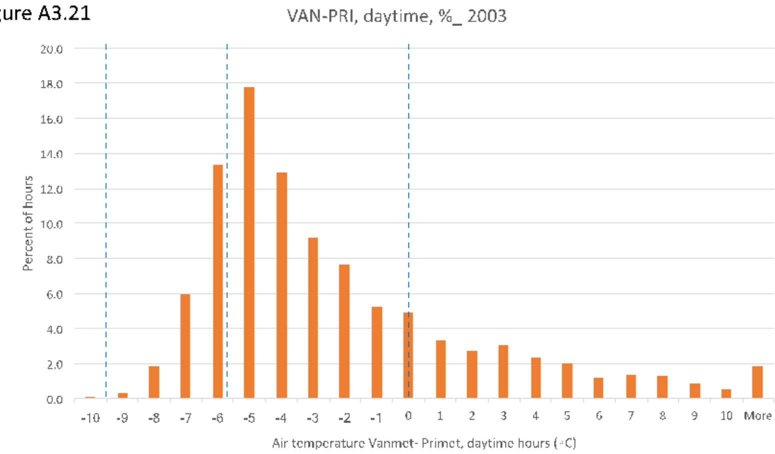

Figure A3.22

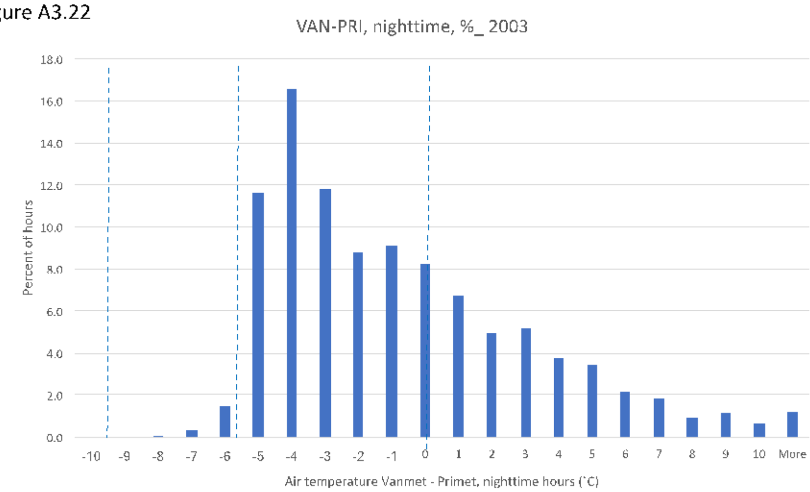

Figures A3.23-A3.26_ Daytime hourly wind speed and direction, Primet and Vanmet, 2003. (Fig A3.23) Wind speed, Primet (m/s), (Fig A3.24) Wind direction, Primet (degrees), (Fig A3.25) Wind speed, Vanmet (m/s), (Fig A3.26) Wind direction, Vanmet (degrees).

Figure A3.23

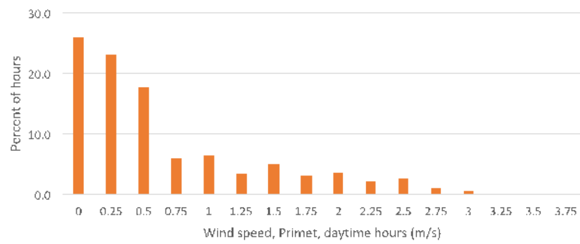

Figure A3.24

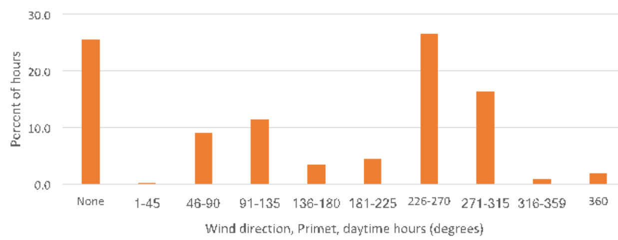

Figure A3.25

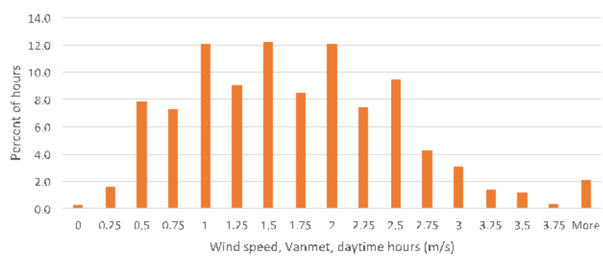

Figure A3.26

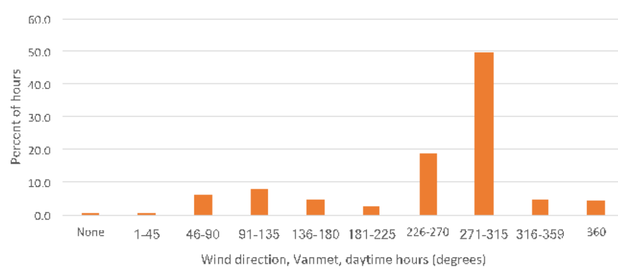

Figures A3.27- A3.30. Nighttime hourly wind speed and direction, Primet and Vanmet, 2003. (Fig. A3.27) Wind speed, Primet (m/s), (Fig. A3.28) Wind direction, Primet (degrees), (Fig. A3.29) Wind speed, Vanmet (m/s), (Fig. A3.30) Wind direction, Vanmet (degrees).

Figure A3.27

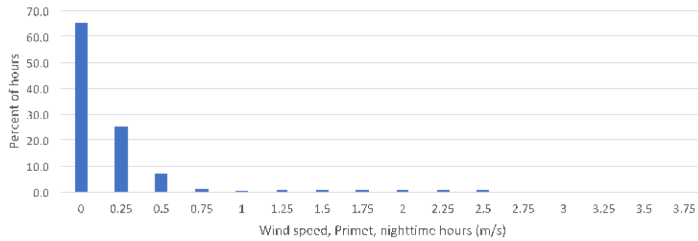

Figure A3.28

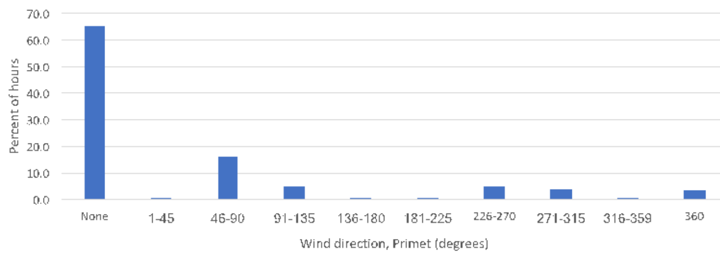

Figure A3.29

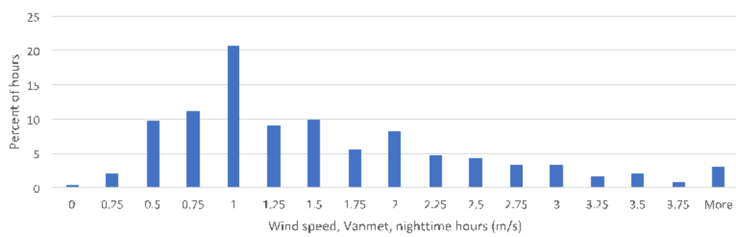

Figure A3.30

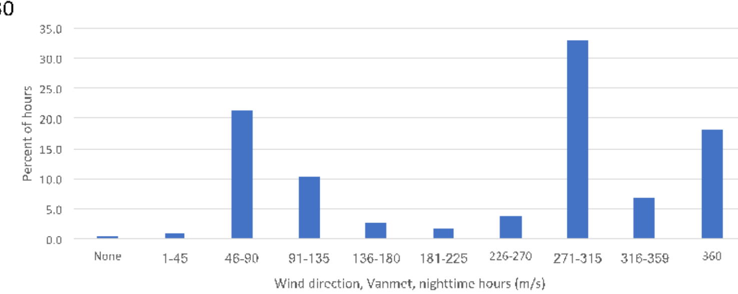

Figures A3.31 and A3.32_ Hourly air temperature differences, Vanmet-Primet, for Jan, Apr, Jul, and Oct, 2003. (Fig. A3.31) daytime hours (radiation > 0), (Fig. A3.32) nighttime hours (radiation = 0).

Figure A3.31

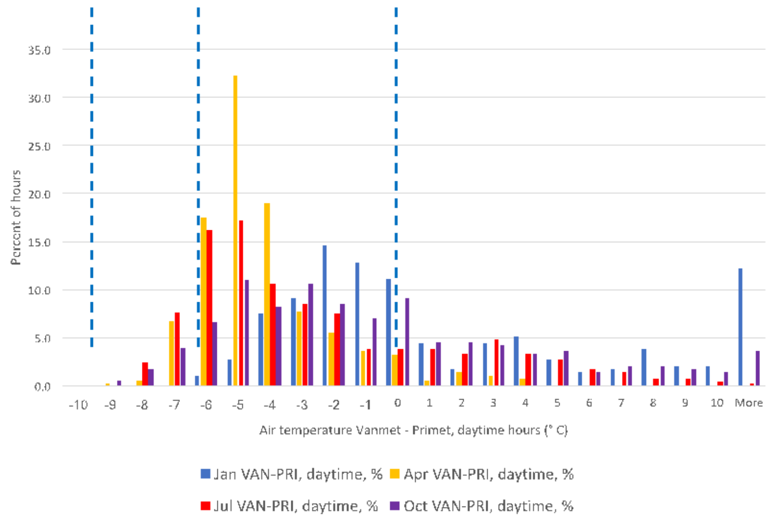

Figure A3.32

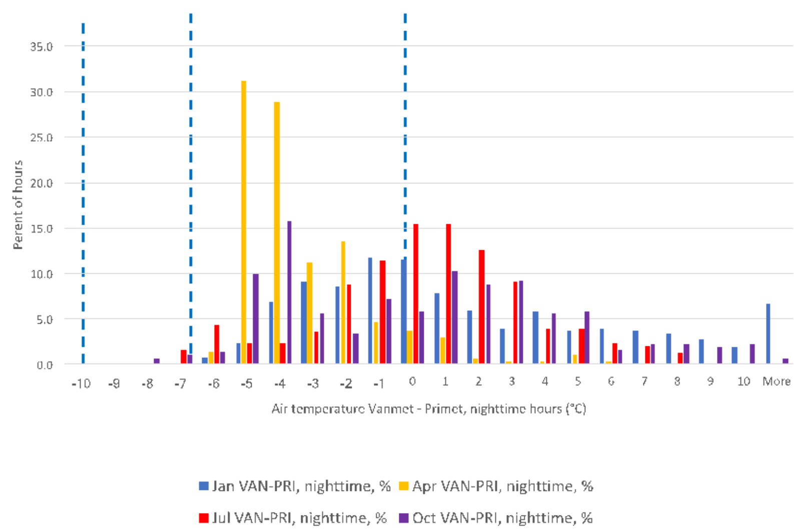

Figures A3.33-A3.36_ Daytime hourly wind speed and wind direction, Primet and Vanmet, Jan, Apr, Jul, and Oct, 2003. (Fig. A3.33) Wind speed, Primet (m/s), (Fig. A3.34) Wind direction, Primet (degrees), (Fig. A3.35) Wind speed, Vanmet (m/s), (Fig. A3.36) Wind direction, Vanmet (degrees)

Figure A3.33

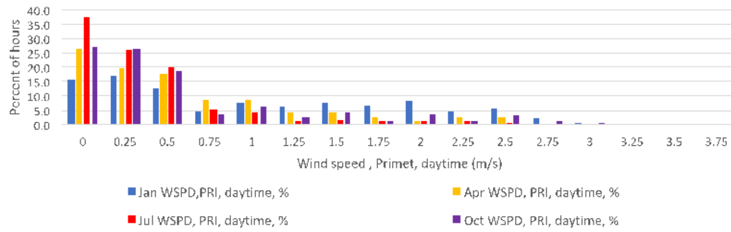

Figure A3.34

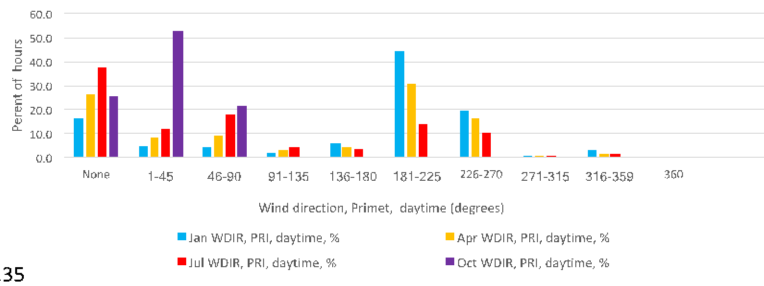

Figure A3.35

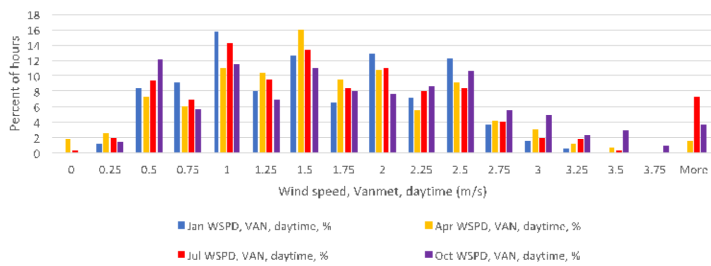

Figure A3.36

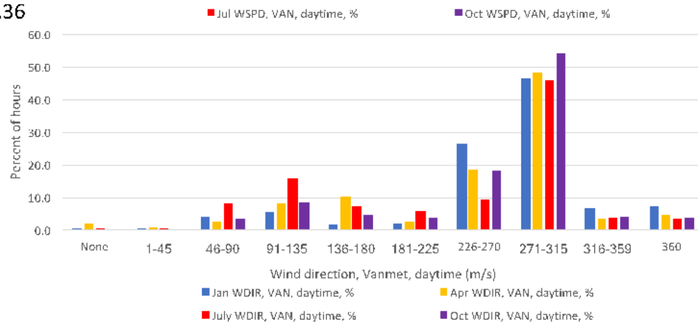

Figures A3.37-A3.40_ Nighttime hourly wind speed and wind direction, Primet and Vanmet, Jan, Apr, Jul, and Oct, 2003. (Fig. A3.37) Wind speed, Primet (m/s), (Fig. A3.38) Wind direction, Primet (degrees), (Fig. A3.39) Wind speed, Vanmet (m/s), (Fig. A3.40) Wind direction, Vanmet (degrees)

Figure A3.37

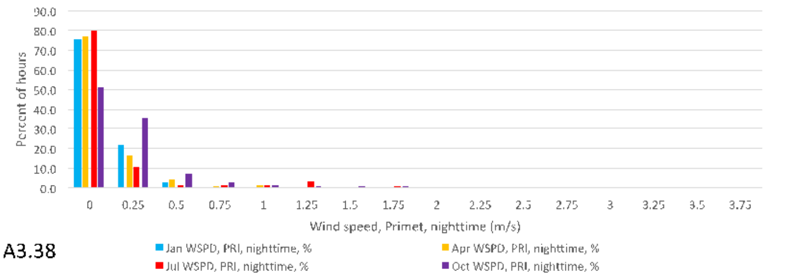

Figure A3.38

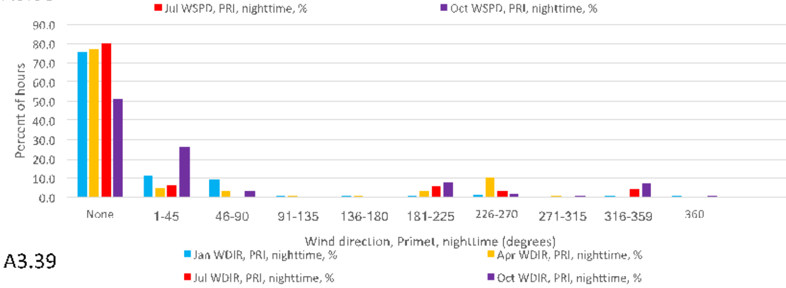

Figure A3.39

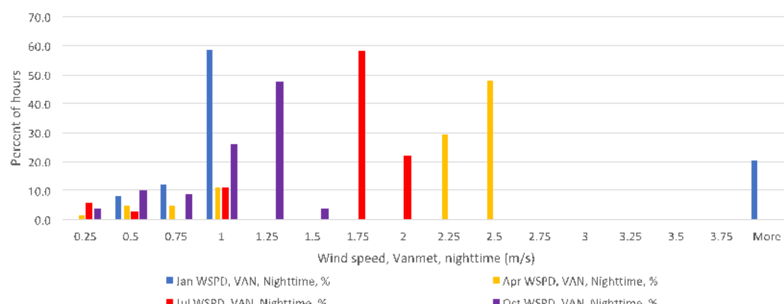

Figure A3.40

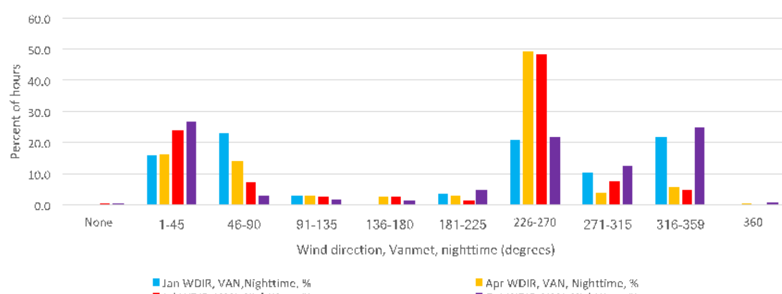

2014

Figures A3.41 and A3.42_ Hourly air temperature differences, Vanmet – Primet,2014, daytime hours(radiation >0) and nighttime hours (radiation = 0) respectively.

Figure A3.41

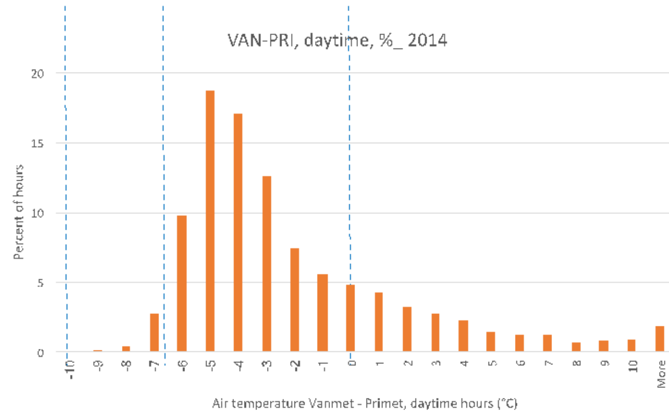

Figure A3.42

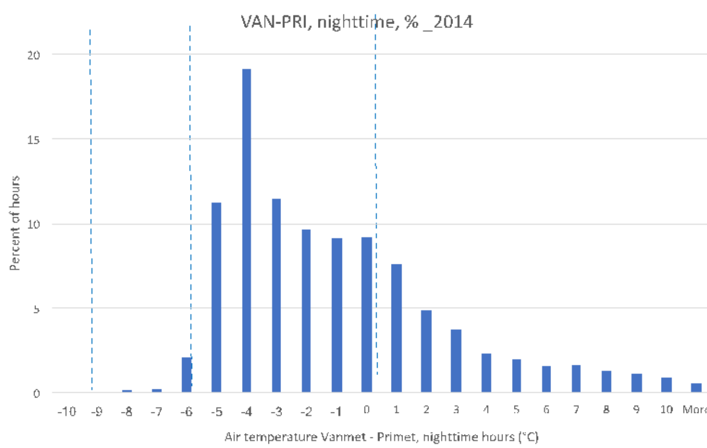

Figures A3.43-A3.46_ Daytime hourly wind speed and direction, Primet and Vanmet, 2014. (Fig A3.43) Wind speed, Primet (m/s), (Fig A3.44) Wind direction, Primet (degrees), (Fig A3.45) Wind speed, Vanmet (m/s), (Fig A3.46) Wind direction, Vanmet (degrees).

Figure A3.43

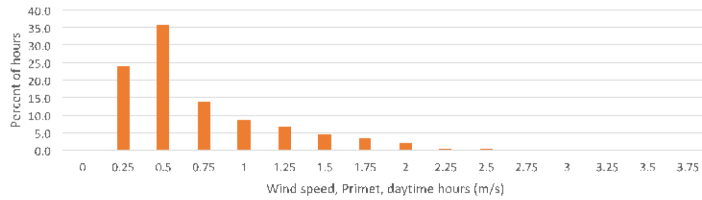

Figure A3.44

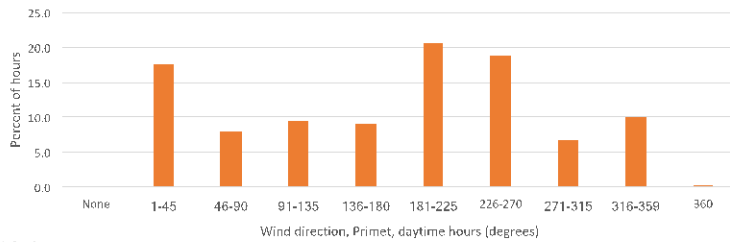

Figure A3.45

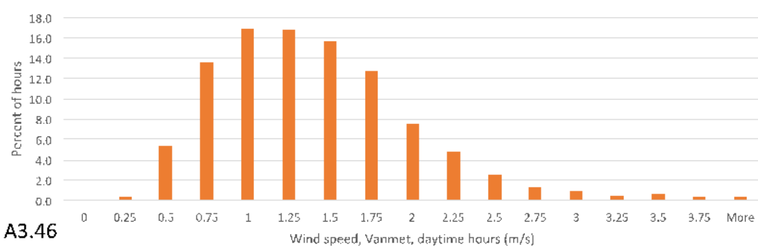

Figure A3.46

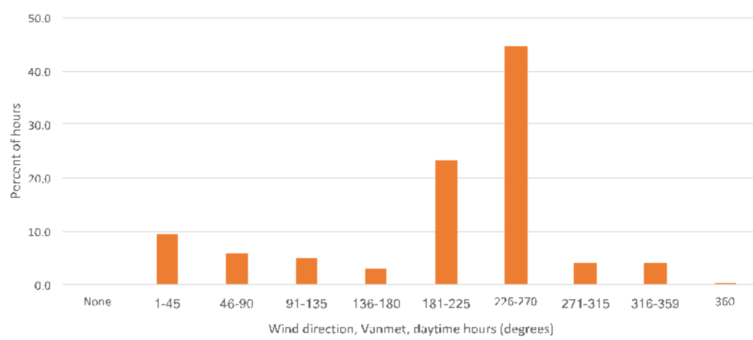

Figures A3.47-A3.50_ Nighttime hourly wind speed and direction, Primet and Vanmet, 2014. (Fig A3.47) Wind speed, Primet (m/s), (Fig A3.48) Wind direction, Primet (degrees), (Fig A3.49) Wind speed, Vanmet (m/s), (Fig A3.50) Wind direction, Vanmet (degrees).

Figure A3.47

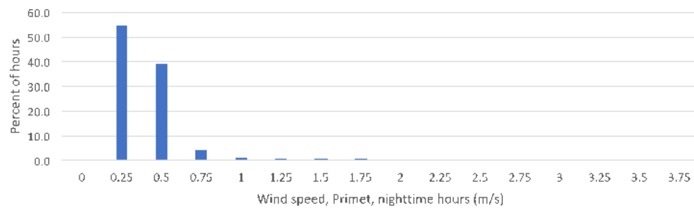

Figure A3.48

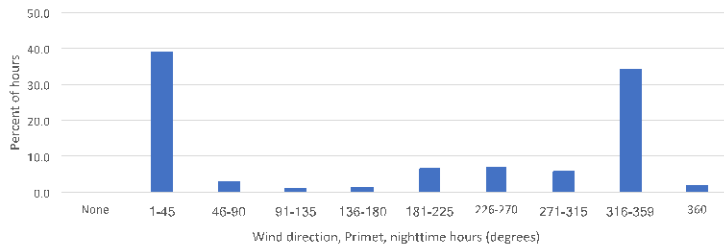

Figure A3.49

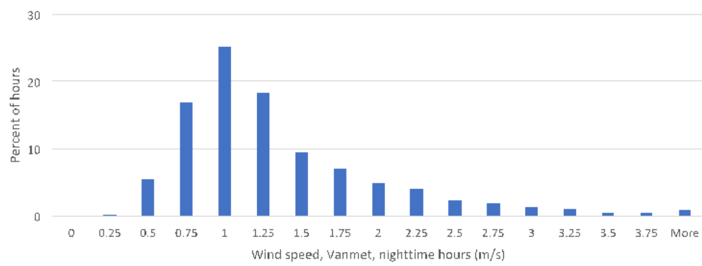

Figure A3.50

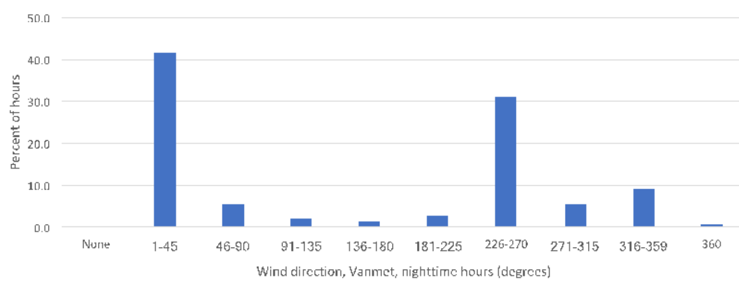

Figures A3.51 and A3.52_ Hourly air temperature differences, Vanmet-Primet, for Jan, Apr, Jul, and Oct, 2014. (Fig. A3.51) daytime hours (radiation > 0), (Fig. A3.52) nighttime hours (radiation = 0).

Figure A3.51

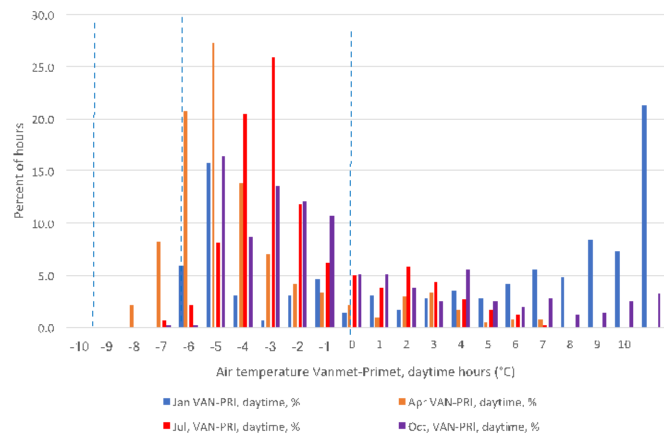

Figure A3.52

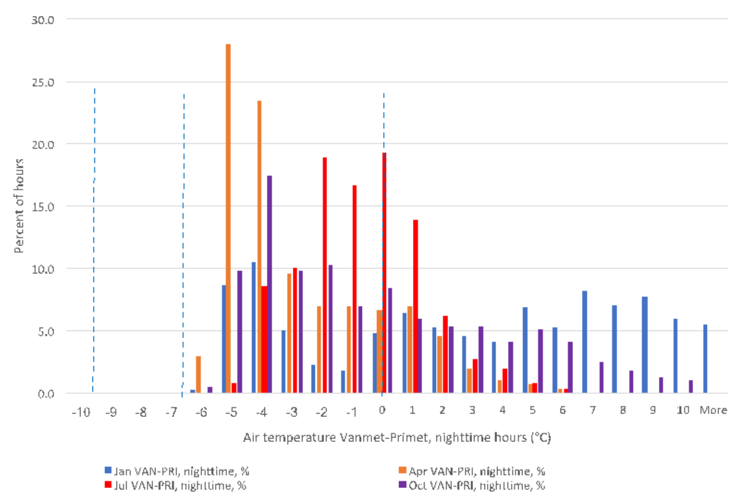

Figures A3.53-A3.56_ Daytime hourly wind speed and wind direction, Primet and Vanmet, Jan, Apr, Jul, and Oct, 2014. (Fig. A3.53) Wind speed, Primet (m/s), (Fig. A3.54) Wind direction, Primet (degrees), (Fig. A3.55) Wind speed, Vanmet (m/s), (Fig. A3.56) Wind direction, Vanmet (degrees)

Figure A3.53

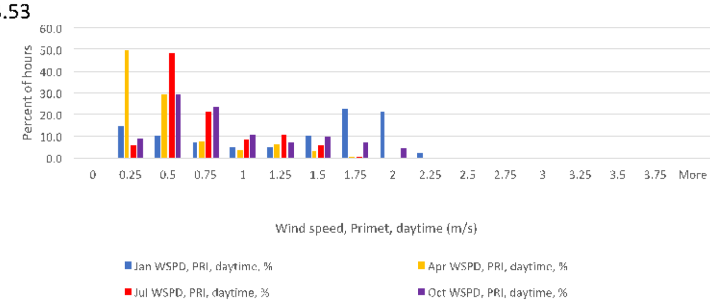

Figure A3.54

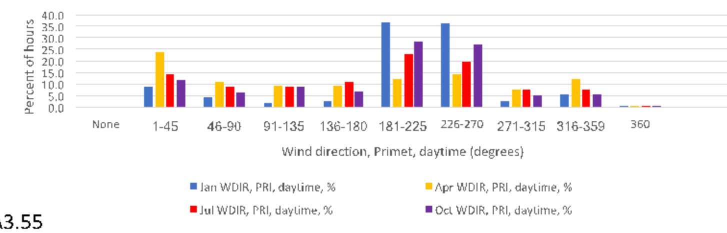

Figure A3.55

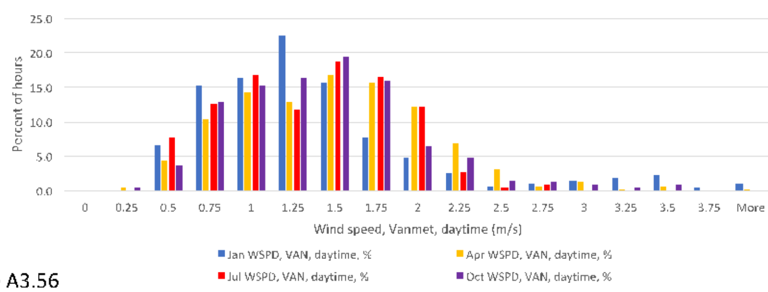

Figure A3.56

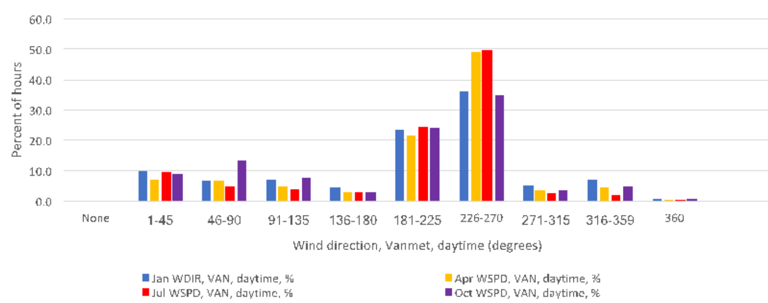

Figures A3.57-A3.60_ Nighttime hourly wind speed and wind direction, Primet and Vanmet, Jan, Apr, Jul, and Oct, 2014. (Fig. A3.57) Wind speed, Primet (m/s), (Fig. A3.58) Wind direction, Primet (degrees), (Fig. A3.59) Wind speed, Vanmet (m/s), (Fig. A3.60) Wind direction, Vanmet (degrees)

Figure A3.57

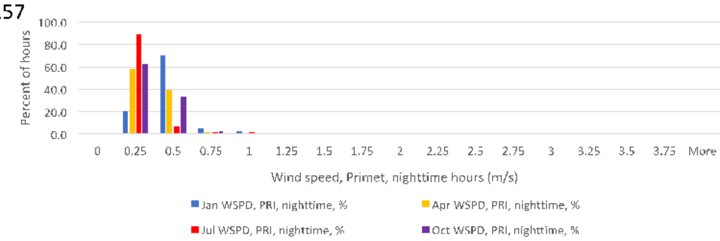

Figure A3.58

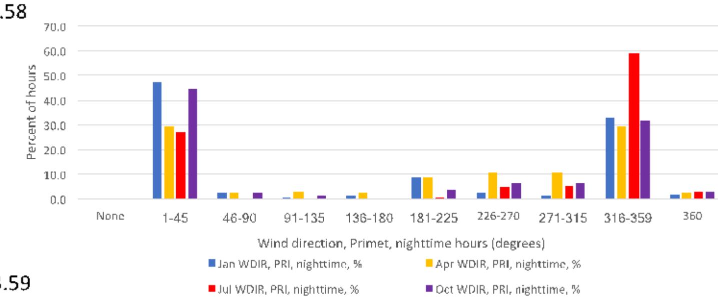

Figure A3.59

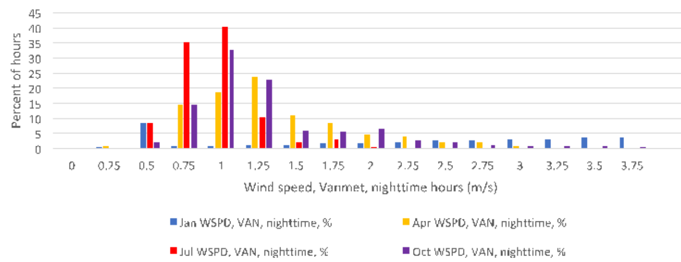

Figure A3.60

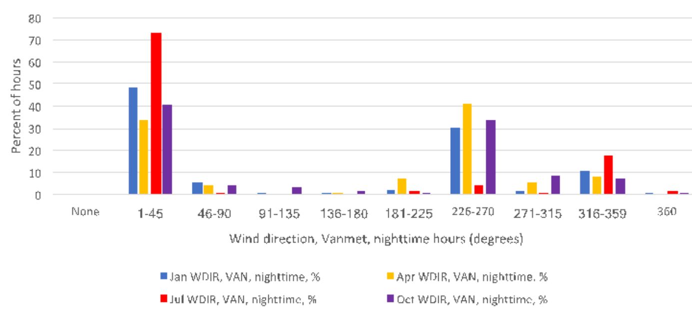

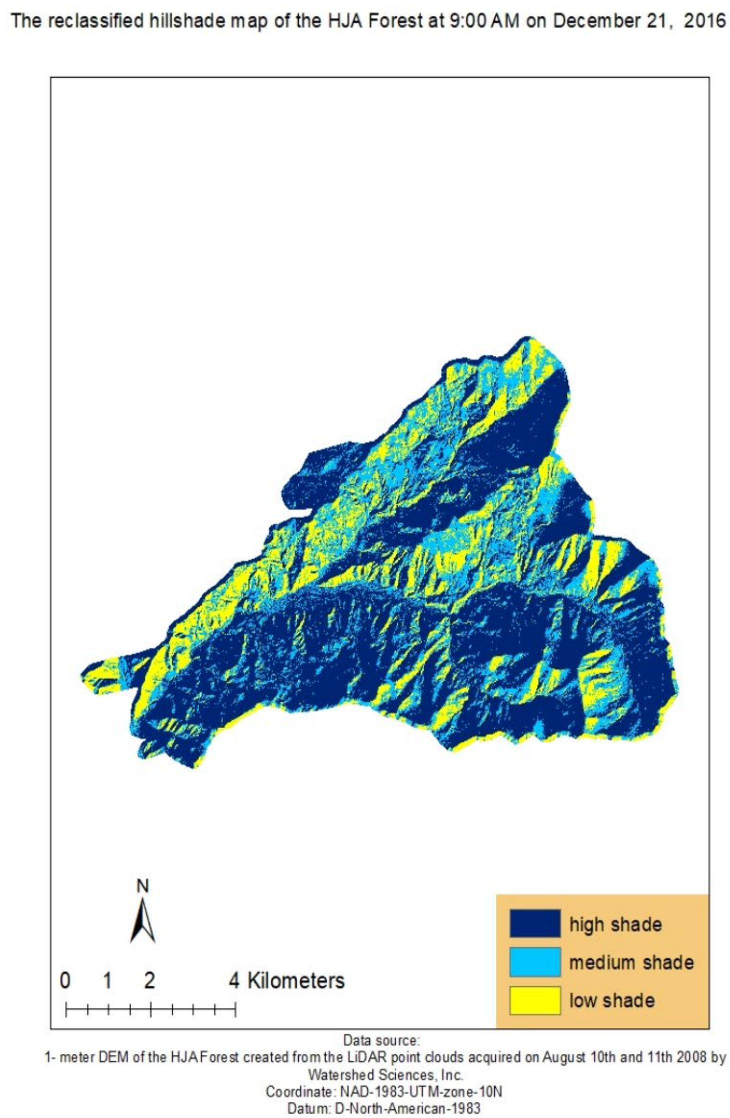

Figure A3.61_a. Reclassified hillshade map of the HJA Forest at 9:00 AM on December 21, 2016

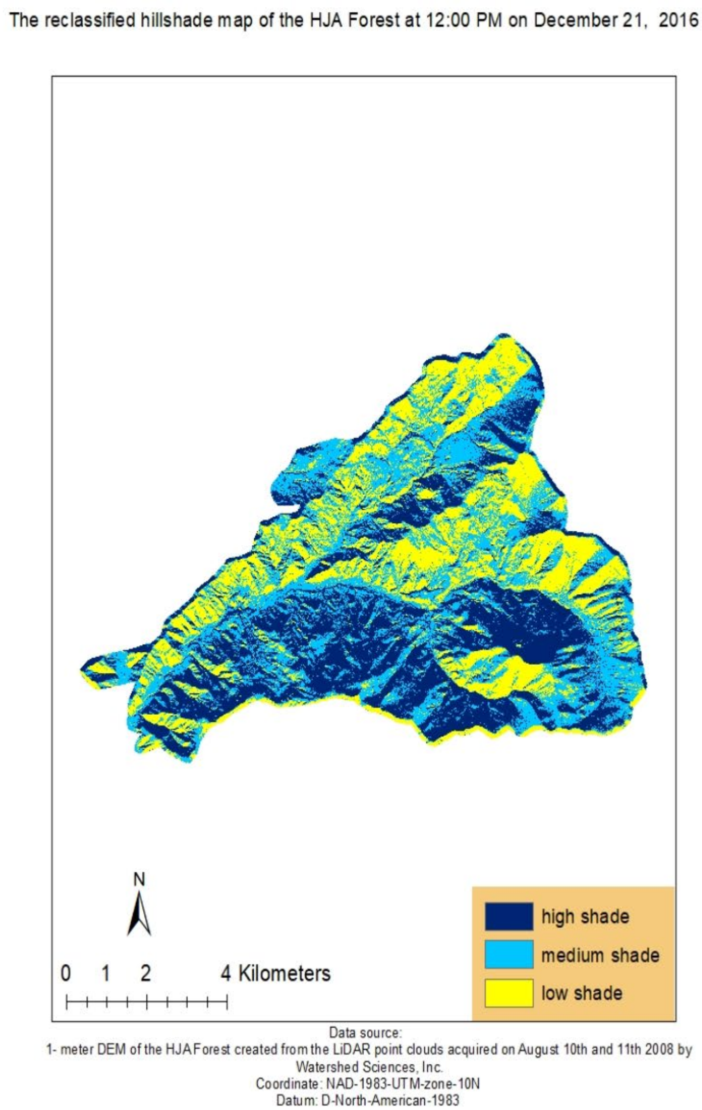

Figure A3.61_b. Reclassified hillshade map of the HJA Forest at 12:00 PM on December 21, 2016

The reclassified hillshade map of the HJA Forest at 3:00 PM on December 21, 2016

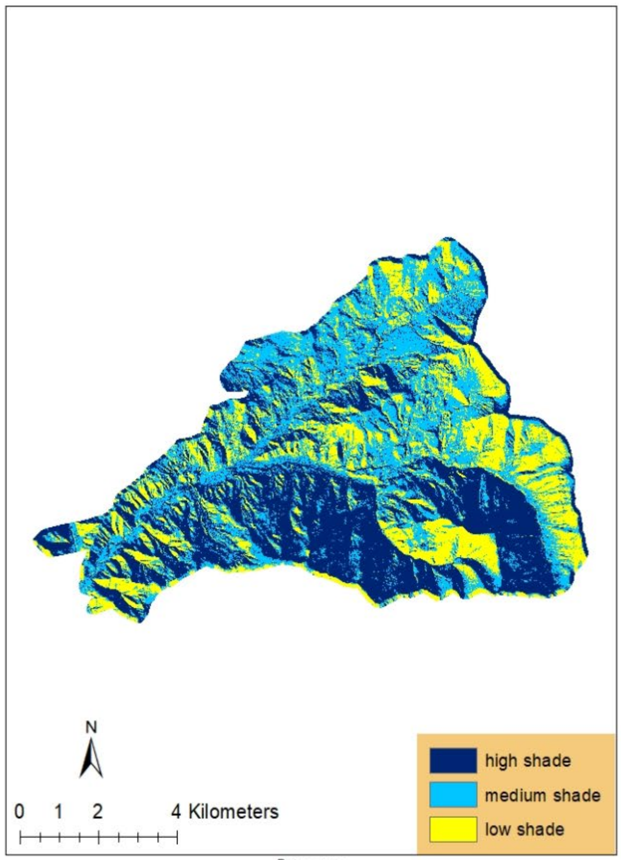

Data source:
1- meter DEM of the HJA Forest created from the LiDAR point clouds acquired on August 10th and 11th 2008 by Watershed Sciences, Inc.
Coordinate: NAD-1983-UTM-zone-10N
Datum: D-North-American-1983

Figure A3.61_c. Reclassified hillshade map of the HJA Forest at 3:00 PM on December 21, 2016

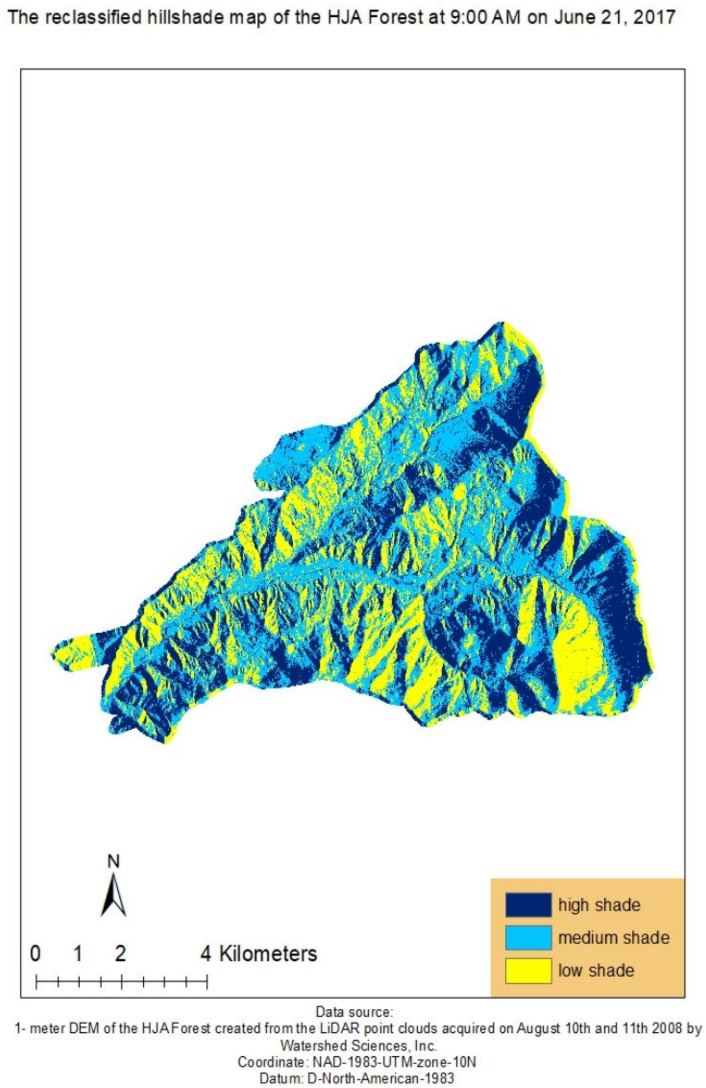

Figure A3.62_a. Reclassified hillshade map of the HJA Forest at 9:00 AM on June 21, 2017

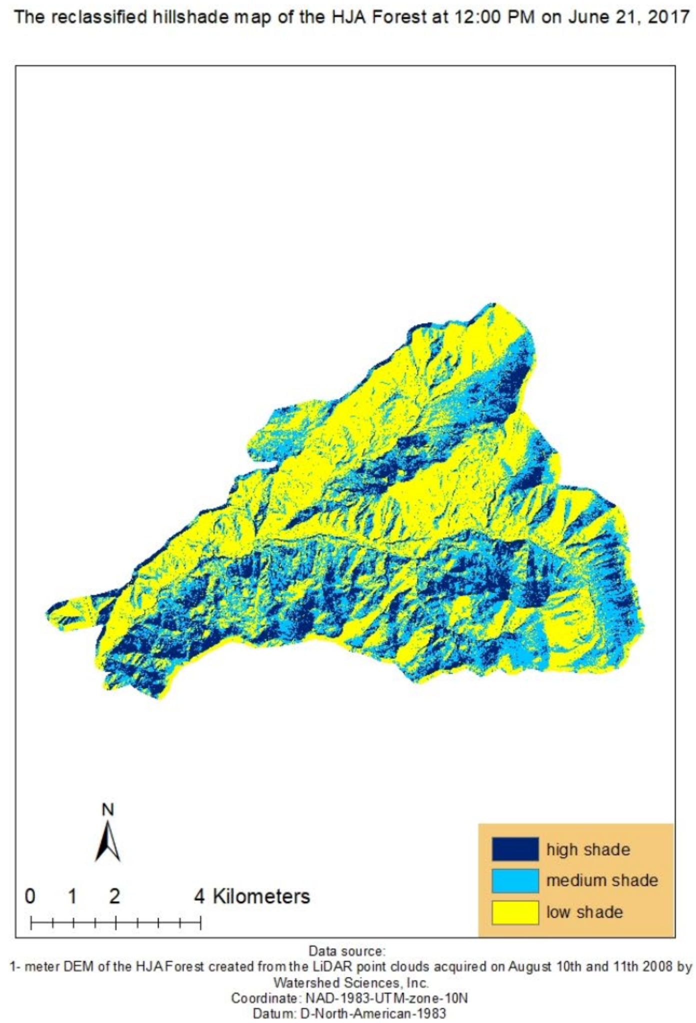

Figure A3.62_b. Reclassified hillshade map of the HJA Forest at 12:00 PM on June 21, 2017

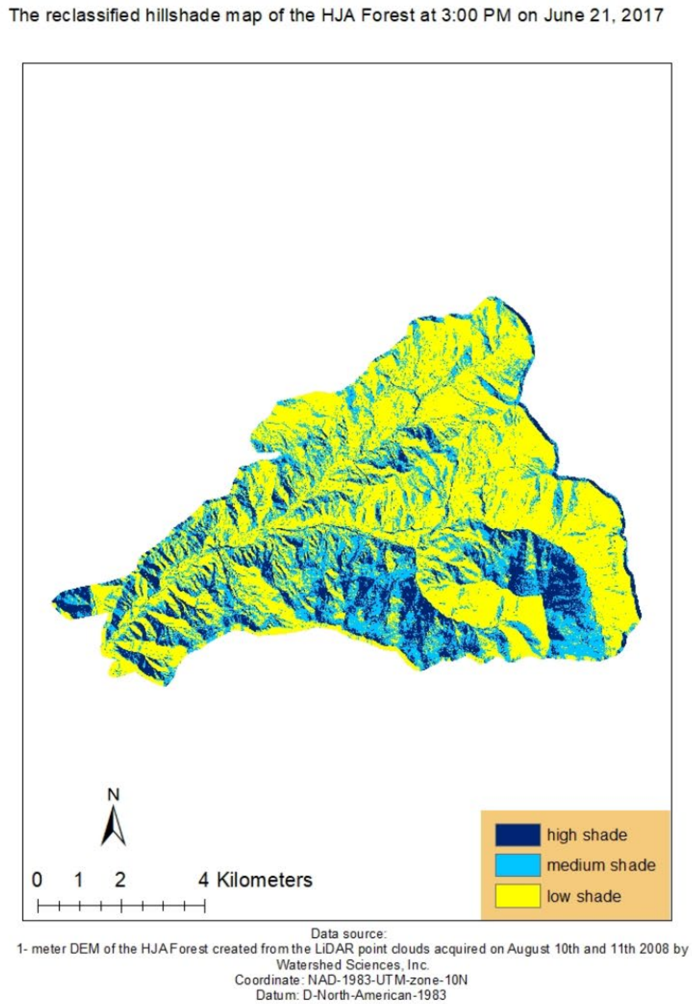

Figure A3.62_c. Reclassified hillshade map of the HJA Forest at 3:00 PM on June 21, 2017

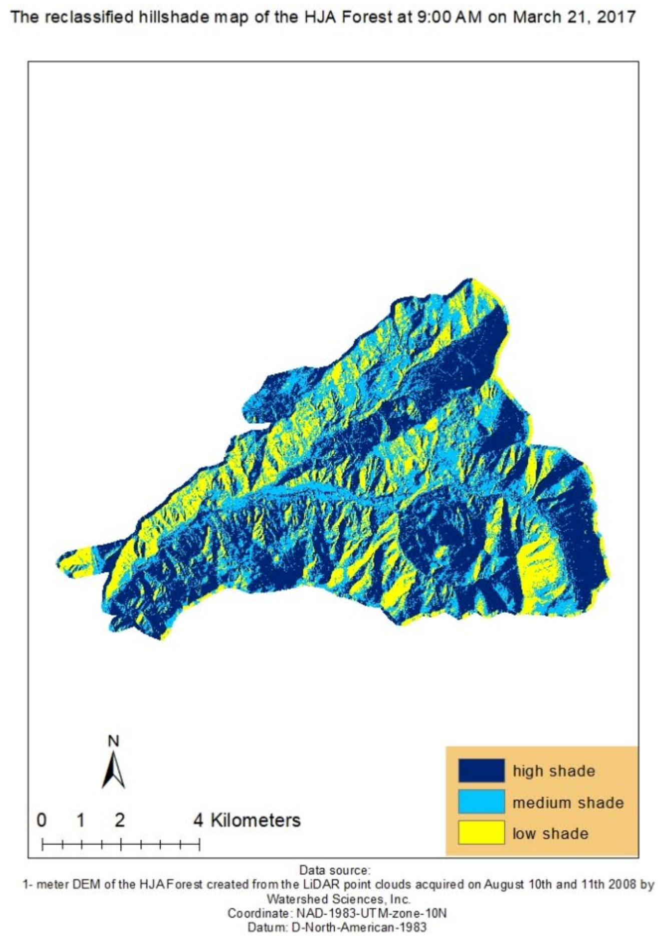

Figure A3.63_a. Reclassified hillshade map of the HJA Forest at 9:00 AM on March 21, 2017

The reclassified hillshade map of the HJA Forest at 12:00 PM on March 21, 2017

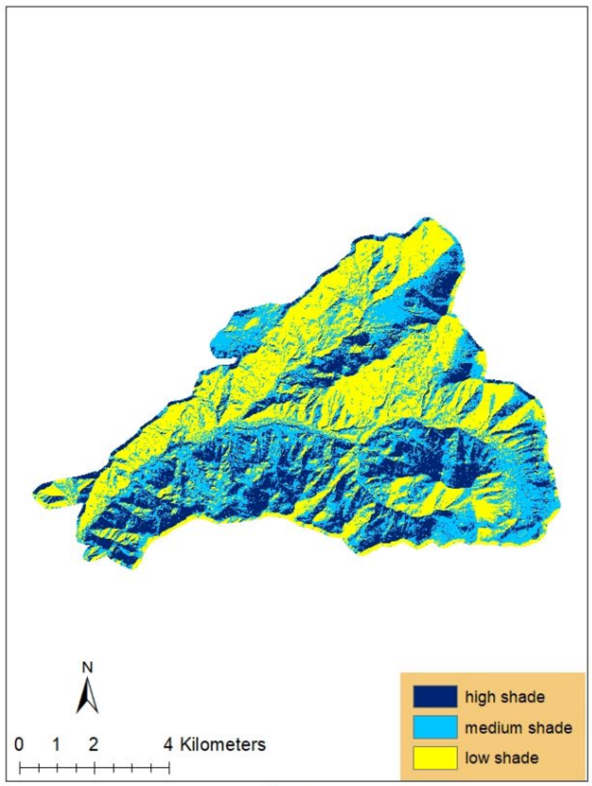

Data source:
1- meter DEM of the HJA Forest created from the LiDAR point clouds acquired on August 10th and 11th 2008 by Watershed Sciences, Inc.
Coordinate: NAD-1983-UTM-zone-10N
Datum: D-North-American-1983

Figure A3.63_b. Reclassified hillshade map of the HJA Forest at 12:00 PM on March 21, 2017

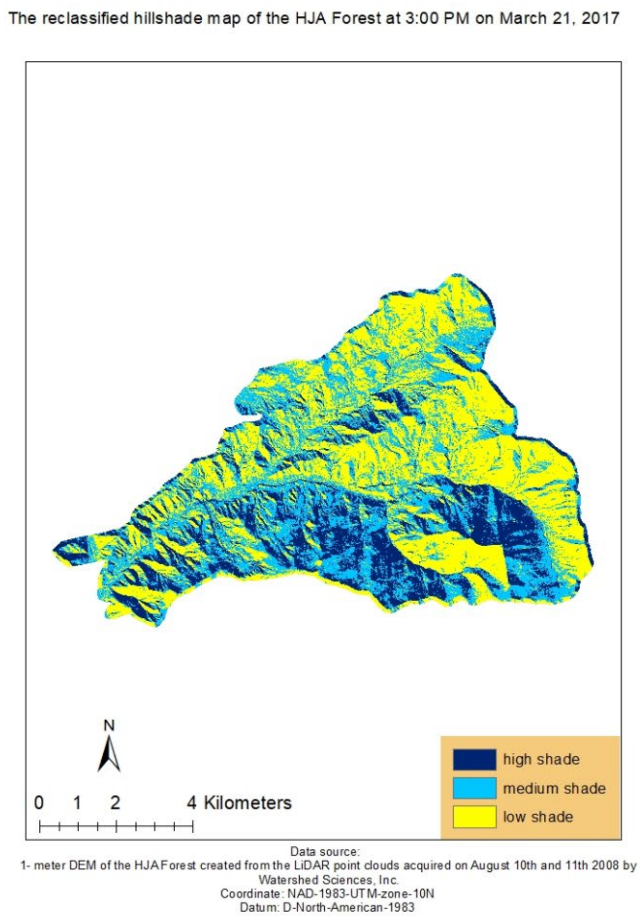

Figure A3.63_c. Reclassified hillshade map of the HJA Forest at 3:00 PM on March 21, 2017

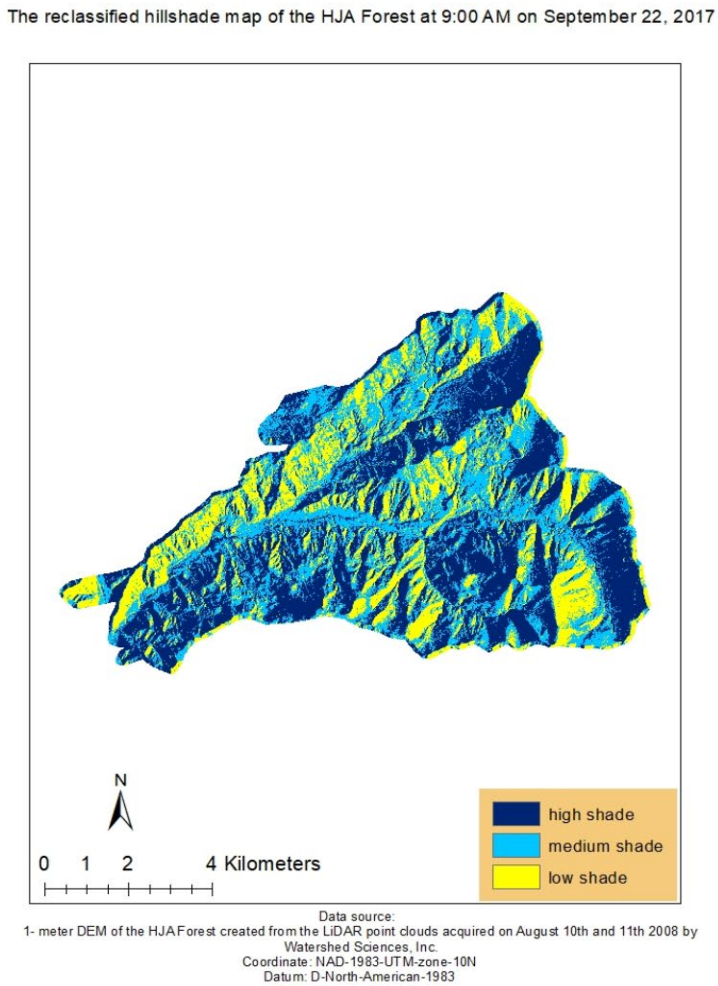

Figure A3.64_a. Reclassified hillshade map of the HJA Forest at 9:00 AM on September 22, 2017

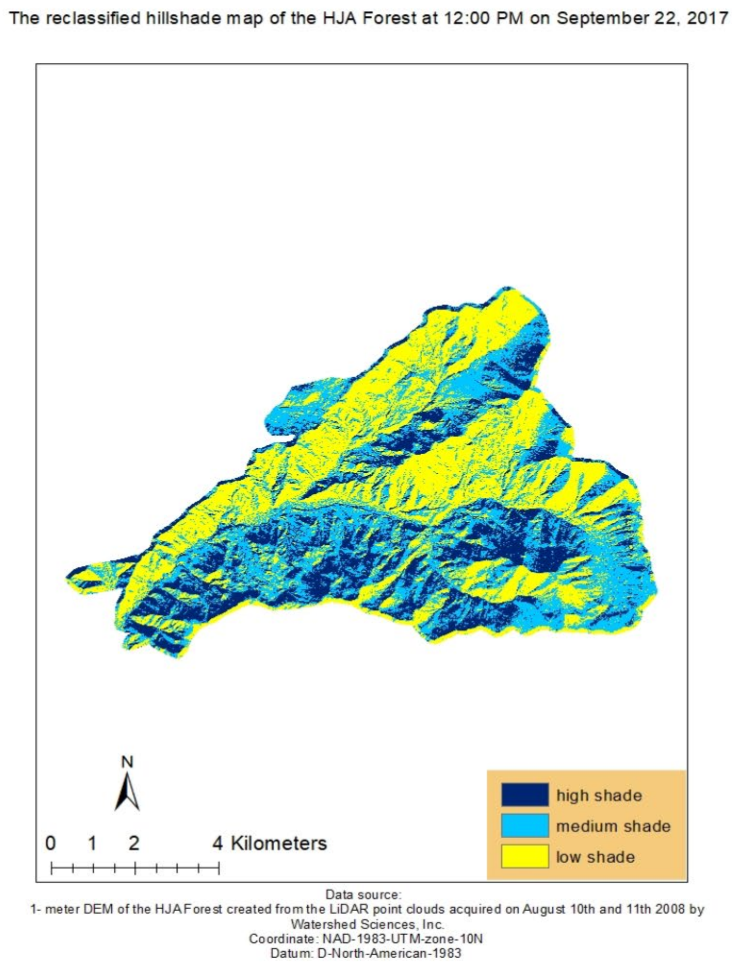

Figure A3.64_b. Reclassified hillshade map of the HJA Forest at 12:00 PM on September 22, 2017

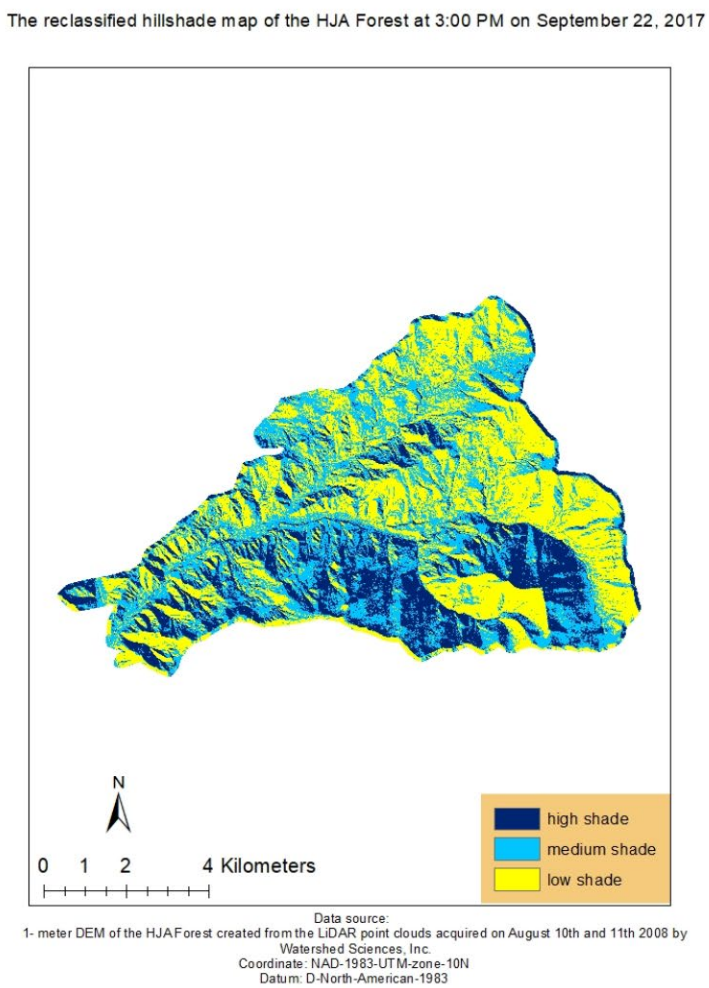

Figure A3.64_c. Reclassified hillshade map of the HJA Forest at 3:00 PM on September 22, 2017